



UNIVERSITY *of the*
WESTERN CAPE

Graphene supported antimony nanoparticles on carbon electrodes for stripping analysis of environmental samples

By

Bongiwe Silwana

MSc Chemistry (*Cum Laude*)

UNIVERSITY *of the*

Submitted in fulfilment of the requirements for the degree

DOCTOR OF PHILOSOPHY

in the

Department of Chemistry

Faculty of Science

University of the Western Cape

February, 2015

Supervisors: Dr V.S. Somerset

Prof. E.I. Iwuoha

Declaration

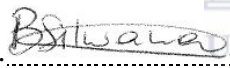
I declare that:

“Graphene supported antimony nanoparticles on screen-printed carbon electrodes for stripping analysis of environmental samples”

is my own work, that has not been submitted for any degree or examination in any other university, and that all the sources I have used or quoted have been indicated and acknowledged by complete references.

Bongiwe Silwana

Signature:

 UNIVERSITY of the
WESTERN CAPE

Date:

.....1st February 2016.....

Dedication

I dedicate this thesis to my mother, Nonkosi Constance Silwana, hoping I have fulfilled her ambitions and expectations wherever she is (RIP). Secondly, to my late son, Olwethu Silwana or "Ollie" as we have called him. I thought my studies will be a source of inspiration to you so that you can achieve whatever you set your mind to do. Then I learned another lesson in life! We may make our plans, but God has the last word. You are sadly missed (RIP).



Acknowledgements

I would like to express my sincere gratitude and appreciation to my supervisors Prof. E. Iwuoha and Dr V.S. Somerset. My deepest gratitude goes to Prof. E. Iwuoha for giving me an opportunity to pursue my PhD studies. I acknowledge his excellent input, insightful comments and encouraging words during our first annual meetings, which have improved me to be confident in front of the audiences. My special thanks to Dr V.S. Somerset for his guidance, support and encouragement during my study. He has been there, in front of my eyes for last six and a half years, motivating and inspiring every bit of me towards new possibilities in life. He is a living role model to me, taking up new challenges every day, tackling them with all his grit and determination and always thriving to come out victorious. He granted me an enormous freedom in my field of interest and, at the same time, provided the right guidance to make sure that my effort was always on the right path. Despite his busy schedule, he is always accessible for any help that I needed. My special words of thanks also goes to Prof. P.G.L. Baker for always being so kind, helpful and motivating. I appreciate the financial support from NRF throughout my studies. I acknowledge the Council of Scientific and Industrial Research (CSIR) in Stellenbosch for providing me with research facilities. I acknowledge the great help of my colleague Dr C. Van der Horst, a great research partner but overall a friend that has helped me in this study. I express gratitude to all my colleagues, the SensorLab group for their wholehearted support, encouragement and co-operation. My warmest thanks go to my late mother and my family for their understanding, endless support, patience, helps and encouragement during my whole life and one for myself, who I am very proud of. I thank the Almighty God for giving me the strength and patience to work through all these years so that today I can stand proud with my head held high.

List of Abbreviations and Acronyms

AAS	Atomic absorption spectrometric
AFM	Atomic Force Microscope
AdDPCSV	Adsorptive differential pulse cathodic stripping voltammetry
Ag/AgCl	Silver silver chloride
ASV	Anodic stripping voltammetry
μA	Micro amperes
BiFE	Bismuth film electrode
CMEs	Chemical modified electrodes
CNTs	Carbon nanotubes
CVAAS	Cold vapour atomic absorption spectroscopy
CPEs	Carbon paste electrodes
CPs	Conducting polymers
CSV	Cathodic stripping voltammetry
CV	Cyclic voltammetry
DME	Dropping mercury electrode
DMF	Dimethylformamide
DMG	Dimethylglyoxime
EDX	Energy- dispersive X-ray
EIS	Electrochemical impedance spectroscopy
FAAS	Flame atomic absorption spectroscopy
FTIR	Fourier transformed infrared
GCE	Glassy carbon electrode
GC-MS	Gas chromatography-Mass spectrometry
GFAAS	Graphite furnace atomic absorption spectroscopy
GO	Graphene Oxide
$\mu\text{g kg}^{-1}$	Micro grams per kilograms
HGAAS	Hydride generation atomic absorption spectroscopy
HR-TEM	High resolution transmission electron microscope
ICP-MS	Inductive coupled plasma mass spectrometry
ICP-OES	Inductively coupled plasma optical emission spectrometry
L	Ligand
La	Crystalline size
LOD	Limit of detection
LOQ	Limit of Quantification
LR	Linear range
Me	Metal
MWCNT	Multi-walled carbon nanotube
NAA	Neutron activation analysis
NPs	Nanoparticles
PB	Phosphate buffer
PGMs	Platinum group metals

PVA	Polyvinylalcohol
Ppb	Parts per billion
Ppm	Parts per million
PtNPs	Platinum nanoparticles
rGO	Reduced graphene oxide
rGO/SbNPs	Reduced graphene oxide antimony nanoparticles
Redox	Reduction –Oxidation
Rpm	Rotations per minute
RSD	Relative standard deviation
SbNPs	Antimony nanoparticles
SCE	Saturated calomel electrode
SPCE	Screen printed carbon electrode
SWASV	Square wave anodic stripping voltammetry
SWCNT	Single-walled carbon nanotube
UV-Vis	Ultra violet-visible
WHO	World Health Organisation
WRC	Water Research Commission



List of Publications and Presentations

Publications

B. Silwana, C. van der Horst, E. Iwuoha and V. Somerset. (2016). Reduced Graphene Oxide Impregnated Antimony Nanoparticle Sensor for Electroanalysis of Platinum Group Metals. *Journal of Electroanalysis*. DOI: [10.1002/elan.201501071](https://doi.org/10.1002/elan.201501071).

B. Silwana, C. van der Horst, E. Iwuoha and V. Somerset. (2016). A sensitive reduced graphene oxide-antimony nanofilm sensor for simultaneous determination of PGMs. *Journal of Nanoresearch*. (Accepted).

B. Silwana, C. van der Horst, E. Iwuoha and V. Somerset. (2015). Synthesis, characterisation and electrochemical evaluation of reduced graphene oxide modified antimony nanoparticles. *Thin Solid Films*, 592: 124–134.

Charlton van der Horst, **Bongiwe Silwana**, Emmanuel Iwuoha and Vernon Somerset. (2015). Synthesis and characterisation of bismuth-silver bimetallic nanoparticles for electrochemical sensor applications. *Analytical Letters*, 48(8): 1–22.

Charlton van der Horst, **Bongiwe Silwana**, Emmanuel Iwuoha and Vernon Somerset. (2015). Bismuth-silver bimetallic nanosensor application for the voltammetric analysis of dust and soil samples. *Journal of Electroanalytical Chemistry*, 752: 1–11.

V. Somerset, C. Van der Horst, **B. Silwana**, C. Walters and E. Iwuoha (2015). Biomonitoring and evaluation of metal concentrations in sediment and crab samples from the North-West Province of South Africa. *Water, Air, & Soil Pollution*, 226(43): 1–25.

Bongiwe Silwana, Charlton van der Horst, Emmanuel Iwuoha and Vernon Somerset. (2014). Amperometric determination of cadmium, lead, and mercury metal ions using a novel polymer immobilised horseradish peroxidase biosensor system. *Journal of Environmental Science and Health*, A49: 1501–1511.

Bongiwe Silwana, Charlton van der Horst, Emmanuel Iwuoha and Vernon Somerset. (2014). Screen-printed carbon electrodes modified with a bismuth film for stripping voltammetric analysis of platinum group metals in environmental samples. *Electrochimica Acta*, 128: 119 – 127.

B. Silwana, C. van der Horst, E. Iwuoha and V. Somerset. (2013). Inhibitive determination of metal ions using a horseradish peroxidase amperometric biosensor. In T. Rinken (Ed.), *State of the Art in Biosensors - Book 2*. (pp 105-120). INTECH, Croatia. ISBN 980-953-307-691-6.

C. van der Horst, **B. Silwana**, E. Iwuoha and V. Somerset. (2012) Stripping voltammetric determination of palladium, platinum and rhodium in freshwater and sediment samples from South African water resources. *Journal of Environmental Science and Health*, A47: 2084 – 2093.

V Somerset, C van der Horst, **B Silwana**, C Walters, E Iwuoha, S le Roux. (2012). Development of Analytical Sensors for the Identification and Quantification of Metals in Environmental Samples. Water Research Commission (WRC). *Report Number: 2013/1/12*.

Oral and Poster Presentations at Conferences

Bongiwe Silwana, Charlton van der Horst, Emmanuel Iwuoha and Vernon Somerset. Electrochemical method development based on a graphene nanocomposite for detection of platinum metals in roadside soil and dust samples. Paper presented at the 7th Society of Environmental Toxicology and Chemistry (SETAC) Africa Conference, Langebaan, South Africa, 5 - 8 October, 2015. [Poster presentation]

Bongiwe Silwana, Charlton van der Horst, Emmanuel Iwuoha and Vernon Somerset. Screen-printed carbon electrodes modified with a bismuth film for stripping voltammetric analysis of environmental samples. Paper presented at the 2nd International Symposium on Electrochemistry, Electrochemistry for Energy, University of the Western Cape, Bellville, South Africa, 19 – 20 July 2012. [Poster presentation]

Bongiwe Silwana, Charlton van der Horst, Vernon Somerset and Emmanuel Iwuoha. Screen-printed carbon electrodes modified with a bismuth film for stripping voltammetric analysis of environmental samples. Paper presented at the 13th WaterNet/WARFSA/GWP-SA International Symposium on Integrated Water Resource Management, Birchwood Hotel and OR Tambo Conference Centre, Johannesburg, South Africa, 31 October – 2 November 2012. [Oral presentation]

Bongiwe Silwana, Emmanuel Iwuoha, Charlton Van der Horst, Vernon Somerset. Bismuth film coated SPCE for Electrochemical Stripping Measurement of Platinum Group Metals. Paper presented at the 13th Topical Meeting of the International Society of Electrochemistry (ISE). Theme: Advances in Electrochemical Materials, Science and Manufacturing. CSIR International Conference Centre, Pretoria, South Africa, 7 - 10 April, 2013. [Oral presentation]

Bongiwe Silwana, Charlton van der Horst, Emmanuel Iwuoha and Vernon Somerset. Screen-printed carbon electrodes modified with a bismuth film for stripping voltammetric analysis of environmental samples. Paper presented at the Third Regional Conference of the Southern African Young Water Professionals. Conservatorium, University of Stellenbosch, Stellenbosch, South Africa, 16 – 18 July, 2013 [Poster presentation]

Bongiwe Silwana, Charlton van der Horst, Emmanuel Iwuoha and Vernon Somerset. Assessment and analysis of platinum group metals in environmental freshwater samples. Paper presented at the SANCIAHS2014 Conference, School of Public Health Building, University of Western Cape, Bellville, Cape Town, 01 to 03 September 2014. [Poster presentation]

B. Silwana, C. van der Horst, E. Iwuoha and V. Somerset. Spectroscopic and voltammetric analysis of platinum group metals in environmental samples: II. Sensor application in freshwater analysis. . Paper presented at the 17th International Conference on Heavy Metals in the Environment. Guiyang, China, 23-25 September 2014. [Poster presentation]

Bongiwe Silwana, Charlton van der Horstand Emmanuel Iwuoha and Vernon Somerset. Bimetallic Electrochemical Sensor based on the nanocomposite of rGO-SbNPs for the detection of platinum group metals. Paper presented at the 3rd International Symposium on Electrochemistry. Materials, Analytical and Physical Electrochemistry Today (MAPET15). University of the Western Cape, Bellville, South Africa, 26 – 28 May 2015. [Poster presentation]

Table of Contents

Dedication	ii
Acknowledgements	iii
List of Abbreviations and Acronyms	iv
List of Publications and Presentations	vi
Table of Contents	viii
List of Figures	xiv
List of Tables	xxi
Abstract	xxiii
1.1 Introduction	25
1.2 Carbon	30
1.3 Nanomaterials	31
1.3.1 What distinguishes nanomaterial from bulk material?	31
1.3.2 Nanoparticle production and synthesis	32
1.4 Graphene based nanocomposite	34
1.5 Electrodes modified by nanomaterials	34
1.6 Nanoparticles in Electro-analysis	35
1.7 Novelty of Research	35
1.8 Research Hypothesis	36
1.9 Aim and Objectives	36
1.9.1 Aims	36
1.9.2 Objectives	36
1.9.3 Approach	37
1.10 Chapter Outline	40
2.1. Introduction	41
2.2. Electrochemical sensors	42
2.3. Chemically modified electrodes	44
2.4. Carbon based electrodes in electroanalysis	45
2.4.1 Glassy like carbon	48

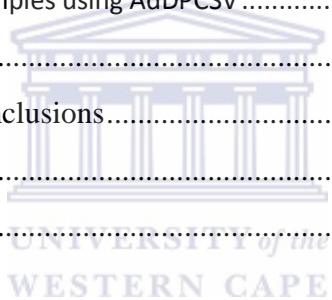
2.4.2. Screen printed electrode (SPE)	48
2.4.3. Graphene	51
2.4.3.1. Origin and development of Graphene.....	51
2.4.3.2. Synthesis and Surface Sensitive Electronic Properties	52
2.4.3.3. Graphene Fabrication.....	54
2.5. Applications of Graphene in Electrochemical Sensing ... Error! Bookmark not defined.	
2.5.1 Graohene as Biosensor	58
2.6. Nanomaterial.....	58
2.6.1. Nanoparticle	58
2.6.2. Nanocomposite.....	61
2.7. Nanoparticle in electrochemical sensor design.....	62
2.8. Flexible metalnanoparticle films.....	63
2.9. Synthesis of metallic nanoparticles.....	64
2.9.1. Ex situ synthesis	65
2.9.2. In situ synthesis.....	66
2.10. Stabilisation of nanoparticles.....	66
2.10.1. Steric stabilisation	67
2.10.2. Electrostatic stabilisation.....	68
2.11. Nanofabrication methods	70
2.11.1. Top Down.....	71
2.11.2. Bottom Up	71
2.12. Antimony nanoparticles (SbNPs)	71
2.13. Nanoparticles characterisation techniques.....	72
2.13.1. Optical Microscopes.....	73
2.13.2. Raman Spectroscopy	74
2.13.3 X-Ray Diffraction (XRD).....	75
2.13.4 Ultraviolet-Visible (UV-VIS) Spectroscopy	77
2.13.5 Fourier transform infrared (FT-IR) Spectroscopy	78
2.13.6 Electron Microscopy.....	80
2.13.6.1. Scanning Electron Microscopy (SEM).....	81
2.13.6.2. Energy Dispersive X-ray Spectroscopy (EDX)	82
2.13.6.3. Transmission Electron Microscopy (TEM).....	83

2.13.6.4	Atomic Force Microscope (AFM)	84
2.13.7.	Electrochemical Characterisation Processes	86
2.13.7.1.	Electrochemical Impedance Spectroscopy (EIS)	86
2.13.7.2.	Cyclic Voltammetry (CV)	88
2.14.	Thin Film Deposition	90
2.14.1.	Electrodeposition	90
2.14.2.	Sol gel deposition and Spin Coating	91
2.14.2.1.	Steps in sol gel process	91
2.15.	Adsorption at Electrode Surfaces.....	95
2.16	Environmental Pollution with Heavy Metals.....	96
2.17.	Behaviour of Heavy Metals in Soil.....	98
2.17.1.	Bioaccumulation	98
2.17.2.	Solubility and Mobility.....	101
2.18.	Environmental concerns.....	101
2.19.	Methods of Detection for Heavy Metals.....	101
2.19.1.	Inductive Coupled Plasma Mass Spectroscopy(ICP-MS)	102
2.19.2	Voltammetry.....	103
2.19.2.1	Stripping voltammetry.....	104
2.19.2.2	Anodic stripping voltammetry.....	105
2.19.2.3	Cathodic stripping voltammetry.....	106
2.19.2.4	Adsorptive stripping voltammetry	106
2.20.	Challenges in stripping analysis.....	107
2.25	Summary	108
3.1	Introduction.....	109
3.2	Material Synthesis.....	110
3.2.1	Synthesis of rGO.....	110
3.2.2	Synthesis of Antimony nanoparticles.....	115
3.2.3	Synthesis of Reduced Graphene Oxide Antimony Nanoparticles.....	118
3.3	Characterisation Methods	121
3.3.1	Electron Microscope.....	122
3.3.1.1	High resolution Scanning Electron Microscope (HR-SEM)	122
3.3.1.2	Transmission Electron Microscope (TEM)	124
3.3.1.3	Energy Dispersive X-ray Analysis (EDX)	126
3.3.1.4	Atomic Force Microscope (AFM).....	128

3.3.2	Optical Microscopes.....	130
3.3.2.1	Ultraviolet-visible spectroscopy (UV-VIS).....	130
3.3.2.2	Fourier Transformed Infrared spectroscopy (FTIR).....	133
3.3.2.3	Raman Spectra.....	135
3.3.3	Electrochemical and Impedance Characterisation	138
3.3.3.1	Cyclic Voltammetry	138
3.3.3.2	Electrochemical Impedance Spectroscopy (EIS).....	140
3.4	Detection Methods	142
3.4.1	ICP–AES Analysis	142
3.4.2	ICP–MS Analysis.....	143
3.4.3.	Stripping Voltammetry.....	144
4.1	Introduction.....	146
4.2	Experimental section.....	147
4.2.1	Chemicals and reagents.....	147
4.2.2	Synthesis of reduced graphene oxide	147
4.2.3	Synthesis of Antimony nanoparticles.....	148
4.2.4	Preparation of nanocomposite	148
4.2.5	Preparation of the electrodes.....	149
4.3.	Results and discussion	150
4.3.1	Scanning Electron Microscope (SEM).....	150
4.3.2	Transmission Electron Microscope	152
4.3.3	Fourier Transmittance Infra–Red Spectroscopy	155
4.3.5	Raman Spectra	157
4.3.5	UV Vis Spectra.....	159
4.4	Electrode reactions and Electrode Capacitance	161
4.5.	Comparative studies on electrochemical activity	162
4.5.1.	Cyclic Voltammetry	162
4.5.1.1	Effects of scan rates.....	165
4.5.2	Impedance Spectroscopy.....	166
4.6	Summary	170
5.1	Introduction.....	172
5.2	Materials and Methods.....	172

5.2.1	Reagents	172
5.2.2	Instrumentation	173
5.2.3	Preparation of graphene impregnated with antimony nanoparticles	173
5.3.	Results and discussion	174
5.3.1	Voltammetric evaluation of graphene-antimony nanomaterials	174
5.3.2	Effect of Supporting Electrolyte.....	175
5.3.3	rGO-SbNPs Redox Chemistry in 0.1M HCl.	177
5.4	Electrochemical calculations	180
5.4.1	Brown-Anson analysis	180
5.4.1.1.	Number of electrons in nanocomposite matrices.....	180
5.4.1.2	Surface concentration of the nanoparticle on carbon electrodes	181
5.4.1.3	Electron transport diffusion coefficient for carbon nanoparticle electrodes.....	182
5.4.1.4	Thickness of the nanoparticle carbon electrodes films.....	183
5.5	Redox behaviour of GCE/rGO-SbNPs sensor in acetate buffer solution	184
5.6	Summary	190
6.1	Introduction.....	191
6.2	Materials and Methods.....	191
6.2.1	Chemicals and reagents.....	191
6.2.2	Apparatus	192
6.2.3	Preparation of nanocomposite	193
6.2.4.	Preparation of the electrodes.....	193
6.2.5	Analytical procedure for the determination of PGMs.....	193
6.3.	Results and Discussion	194
6.3.1	Influence of Supporting Electrolytes	194
6.3.2	Complexing reagent	196
6.3.3	Influence of pH.....	196
6.3.4	Deposition potential optimisation studies	197
6.3.5	Deposition time optimisation studies	201
6.3.6	Stirring Period optimisation studies.....	203
6.3.7	Stability testing of the GCE/rGO-SbNPs sensor	204
6.3.8	Analytical features of the adsorptive stripping voltammetry procedure.....	206

6.3.9	Calibration curves.....	207
6.3.10	Comparison of calculated results for different sensor platforms.....	216
6.3.11	Repeatability.....	218
6.3.12	Interference studies of PGMs.....	221
6.4	Application of Analytical Techniques in Real Samples.....	227
6.4.1	Study Area.....	227
6.4.2	Sample Analysis Procedures.....	228
6.4.2.1	ICP-MS spectrophotometric analysis.....	229
6.4.2.2	Adsorptive stripping voltammetry analysis on GCE/rGO-SbNPs sensor.....	230
6.4.3	PGMs analysis in soil samples by using ICP-MS.....	231
6.4.4	PGMs analysis in dust samples using ICP-MS.....	234
6.4.5	PGMs analysis in soil samples using AdDPCSV.....	238
6.4.6	PGMs analysis in dust samples using AdDPCSV.....	240
6.5	Summary.....	242
7.1	General Discussion and Conclusions.....	244
7.2	Future Recommendations.....	247
8.1	References.....	249



List of Figures

	<u>Discription of Figure</u>	<u>Page</u>
1.	A simple model of metal in soil. (Adapted from Chatreewomgsin , Thesis, 2000)	27
2.	Various approaches undertaken for synthesis of metal nanostructures (Adapted from SPIE photonics West, 2009).....	33
3.	Structural model of glass-like carbon as proposed by Jenkins in 1971. This model is able to explain most of the properties exhibit by glass-like carbon up to this day (Craig <i>et al.</i> , 2006).....	49
4.	Typical Dropsen screen- printed carbon electrode (Dropsens, 2010)	50
5.	Hybridisation states of carbon structures that could be constructed using graphene (Yang <i>et al.</i> , 2013)	56
6.	Overview of applications and properties of graphene (Hibino, 2012).....	57
7.	Electrostatic and steric stabilisation of nanoparticles. (Balante <i>et al.</i> , 2011)	68
8.	Schematic representations of the ‘bottom-up’ and ‘top-down’ approaches of nanomaterials (http://www.gitam.edu/eresource/nano/nanotecnology/synthesis_and_processing_of_nano.htm)	71
9.	Schematic of general X-ray system (Fultz, 2013)	77
10.	Simplified schematic representation of the main parts of UV-VIS spectrophotometer showing the light sources the monochromator, reference and sample holder and the detector(http://www.files.chem.vt.edu/chem-ed/spec/uv-vis/array_spectrometer.html)	79
11.	Interaction of the electron beam with the specimen (http://ncmn.unl.edu/cfem/microscopy/interact.shtml)	81
12.	The three main classes of interactions in AFM(http://spm.phy.bris.ac.uk/techniques/AFM/ . accessed November 2013)	87
13.	Schematics of an electrolytic cell for plating metal "M" from a solution of the metal salt "MA"(http://electrochem.cwru.edu/ed/encycl/).....	91

14.	Schematics of a sol gel deposition technique (Mehrotra, 1992).....	92
15.	The four stages of spin coating (Raut <i>et al.</i> , 2011).....	94
16.	The schematics of a dip coating process (Attia <i>et al.</i> , 2002).....	95
17.	The schematics of a drop casting process (Adapted from Neogi <i>et al.</i> , 2014)	96
18.	Three different forms of mass transport for electroactive species in in solution to the electrode surface (Bard and Faulkner, 2001)	97
19.	Schematic overview over metal release, precipitation and adsorption processes (Hedberg, 2010)	98
20.	Schematic representations of standard three electrode set up (http://chemwiki.ucdavis.edu/Analytical_Chemistry/Analytical_Chemistry_2.0/11_Electrochemical_Methods/11D%3A_Voltammetric_Methods)	105
21.	Schematic representation of the synthetic route of rGO-SbNPs by direct reduction of the metal ions under reflux.....	120
22.	Schematic drawing of a scanning electron microscope (www.asu.edu).....	123
23.	Schematic drawing of a transmission electron microscope (www.nanoscience.gatech.edu).....	125
24.	Interaction of the atom with an electron beam (Goldstein, 2003).....	127
25.	Diagram showing the working of and AFM cantilever (www.geobacter.org , Microbial Nanowires.....)	129
26.	Schematic diagram of a single-beam UV-Vis spectrometre (http://www.files.chem.vt.edu/chem-ed/spec/uv-vis/singlebeam.html -).....	131
27.	Illustration of the electronic transitions process during light absorption (www2.chemistry.msu.edu/faculty/reusch/VirtTxtJml/Spectrpy/UV-vis/spectrum.htm).....	132
28.	Schematic illustration of an FTIR system (Du Toit, 2002).....	135
29.	Schematic illustration of a Raman set up system (Halvorson, 2010).....	136
30.	Schematic diagram showing the different scattering processes in which	

	an incident photon may take part(Adapted from reference Hollas, 2004)....	137
31.	Schematic representations of standard three – electrode and experimental set up for the electrochemical characterization. 1. Working electrode; 2. Reference electrode; 3. Counter electrode. (http://compton.chem.ox.ac.uk/index.php?title=research&topic=fund).....	140
32	Schematic descriptions of principles of electrochemical impedance spectroscopy with representation of impedance data in a) Nyquist and b) Bode Nyquist plot format (Brett, 1993).....	142
33.	A diagram showing the cross section of the different components of modern quadrupole ICP-MS (Wum, 2012).....	144
34.	Steps in Adsorptive Stripping voltammetry Electroanalysis (Adapted from Wang <i>et al.</i> , 1996).....	145
35.	Scheme illustrating the examination and characterization of rGO-SbNPs composites.....	150
36.	SEM image of (a) rGO, (b) SbNPs and (c) rGO-SbNPs with images showing ethanol dispersions of SbNPs, rGO-SbNPs and rGO.....	152
37.	HRTEM images of (a) rGO (b) SbNPs and (c). rGO-SbNPs and the corresponding nanoparticles size distribution.....	154
38.	Typical EDX plot obtained for rGO-SbNPs nanoparticles.....	156
39.	Results obtained for the individual FT-IR spectra of GO, SbNPs, rGO-SbNPs and rGO compounds.....	157
40.	Comparative Raman spectra of rGO, rGO-SbNPs and SbNPs compounds.....	158
41.	UV-Vis absorption spectra ofSbNPs, rGO and rGO-SbNPs compounds.....	161
42.	Schematic illustration of transport and kinetic phenomena in electrolytic reactions, drawn along with its equivalent impedance circuit.....	162
43.	The CVs obtained for a GCE, compared to rGO modified electrode, SbNPs modified electrode and to arGO-SbNPs modified. The potential was scanned between 0.6 and -1.0 V (vs. Ag/AgCl) in a 0.1 M HCl solution.....	164

44.	The results obtained for voltammetric scan rate studies of the rGO-SbNPs/GC sensor in a 0.1 M HCl solution at scan rates from 20 to 200 mV s ⁻¹ . The potential was scanned between 0.6 to -1.0 V (vs. Ag/AgCl)	166
45.	Nyquist Impedance and nyquist admittance plots for the rGO-SbNPs compounds in 0.1 M HCl solution.....	168
46.	Overlay of (a) activated and unactivated SPCE, (b) activated and modified SPCE, (c) activated, unactivated, modified SPCE, (d) GC/rGO-SbNPs and SPC/rGO-SbNPs electrodes in 0.2 M NaOAc (pH = 4.8) solution.....	175
47.	Cyclic voltammograms for the GCE/rGO-SbNPs sensor in different electrolytes at a scan rate of 10 mV s ⁻¹ in: 0.2M NH ₃ buffer (pH = 9.2); 0.2 M NaOAc buffer (pH = 4.8); 4 x10 ⁻³ M LiClO ₄ ; 0.2 M PBS buffer (pH = 7.4); 1 mM K ₃ Fe(CN) ₆ and 0.1 M HCl solutions.....	177
48.	Cyclic voltammograms of rGO-SbNPs evaluated at modified (a) GCE, and (c) SPCE in aqueous 0.1 M HCl electrolyte; while in (b) and (d) the graphs of peak current vs. square root of scan rate is shown.....	178
49.	Cyclic voltammetric results obtained for the scan rate studies performed on a GCE/rGO-SbNPs sensor in the presence of Pt(II), Pd(II) and Rh(III) in a 0.2 M NaOAc buffer solution with 1 × 10 ⁻⁵ DMG.....	186
50.	The dependence of peak current ratio with scan rate of Pd(II), Pt(II) and Rh(III) on the GCE/rGO-SbNPs, evaluated in 0.2 M NaOAc buffer solution.....	190
51.	Effect of different buffers at concentration on cyclic voltammograms of the GCE/rGO-SbNPs sensor at a scan rate of 10 mV s ⁻¹ in: (a) 0.2 M NH ₃ buffer (pH = 9.2); (b) 0.2 M NaOAc buffer (pH = 4.8); and (c) 0.2 M PB (pH = 7.4) buffer solution.....	196
52.	Influence of the pH value on the stripping current of	

	GCE/rGO-SbNPs and SPCE/rGO-SbNPs in 0.2 M NaOAc buffer (pH = 4.8) solutions.....	198
53.	Results obtained for effects of deposition potential (E_d) upon the peak current responses to 1 ng L^{-1} of Pd(II) (A), Pt(II) (C), Rh(II) (E) on GCE/rGO-SbNPs and Pd(II)(B), Pt(II) (D), Rh(II) (F) on SPCE/rGO-SbNPs evaluated in the presence of 0.2 M NaOAc buffer (pH = 5.2).....	200
54.	Effects of t_d upon the response to 1 ng L^{-1} (A) Pd(II), (C) Pt(II), (E) Rh(III) on a GCE/rGO-SbNPs sensor and (B) Pd(II), (D) Pt(II), (F)Rh(III) in the presence of 0.2 M NaOAc buffer (pH = 5.2) solutions.....	202
55.	Influence of electrode rotation rate on Pd(II),Pt(II) and Rh(III) stripping peak currents obtained in a 1 ng L^{-1} of PGMs, 0.2 M NaOAc (pH = 5.2) solution, containing $1 \times 10^{-5} \text{ M}$ DMG solution, $E_d = -1.2 \text{ V}$ (vs. Ag/AgCl); $t_d = 120 \text{ s}$	204
56.	Results obtained for stability testing of the GCE/rGO-SbNPs sensor in 0.2 M NaOAc buffer (pH = 5.2) solution containing 0.1 ng L^{-1} of selected PGMs with $1 \times 10^{-5} \text{ M}$ DMG concentration, $E_d = -1.2 \text{ V}$ (vs. Ag/AgCl) and $t_d = 120 \text{ s}$	206
57.	Results obtained for the AdDPCSV analysis for the increasing concentrations of Pd(HDMG) ₂ evaluated using the GCE/rGO-SbNPs and SPCE/rGO-SbNPs sensors, respectively in 0.2 M NaOAc buffer (pH = 5.2) solution with 0.00, 40, 80, 120, 160, 200, 240, 280, 360, 400 Pd(II) pg L^{-1} concentrations; with $E_d = -0.7 \text{ V}$ (vs. Ag/AgCl); $t_d = 90\text{s}$ for SPCE/rGO-SbNPs sensor and $E_d = -1.2 \text{ V}$; $t_d = 120\text{s}$ for GCE/rGO-SbNPs sensor	209
58.	Results obtained for the AdDPCSV analysis for the increasing concentrations of Pt(HDMG) ₂ evaluated using the GCE/rGO-SbNPs and SPCE/rGO-SbNPs sensors, respectively in 0.2 M NaOAc buffer (pH = 5.2) solution with 0.00, 40, 80, 120, 160, 200, 240, 280, 360, 400 Pt(II) pg L^{-1} concentrations; with $E_d = -0.7 \text{ V}$; $t_d = 90\text{s}$ for SPCE/rGO-SbNPs sensor and $E_d = -1.2 \text{ V}$	

	(vs. Ag/AgCl); $t_d = 120$ s for GCE/rGO-SbNPs sensor.....	210
59.	Results obtained for the AdDPCSV analysis for the increasing concentrations of Rh(HDMG) ₃ evaluated using the GCE/rGO-SbNPs and SPCE/rGO-SbNPs sensors, respectively in 0.2 M NaOAc buffer (pH = 5.2) solution with 0.00, 40, 80, 120, 160, 200, 240, 280, 360, 400 Rh(III) pg L ⁻¹ concentrations; with $E_d = -0.7$ V ; $t_d = 90$ s for SPCE/rGO-SbNPs sensor and $E_d = -1.2$ V; $t_d = 120$ s for GCE/rGO-SbNPs sensor.....	211
60.	Adsorptive differential pulse cathodic stripping voltammetry (AdDPCSV) analysis for the simultaneous determination of Pd-Rh-(HDMG) _x complexes at 0.00, 120,160, 200, 240, 280, 320, 360, 400 pg L ⁻¹ concentrations using a GCE/rGO-SbNPs sensor; $E_d = -1.2$ V (vs Ag/AgCl. and $t_d = 120$ s with a corresponding linear calibration curve also shown.....	213
61.	Adsorptive differential pulse cathodic stripping voltammetry (AdDPCSV) analysis for the simultaneous determination of Pt-Rh-(HDMG) _x complexes at 0.00, 120,160, 200, 240, 280, 320, 360, 400 pg L ⁻¹ concentrations using a GCE/rGO-SbNPs sensor; $E_d = -1.2$ V (vs. Ag/AgCl) and $t_d = 120$ s with a corresponding linear calibration curve also shown.....	214
62.	Adsorptive differential pulse cathodic stripping voltammetry (AdDPCSV) analysis for the simultaneous determination of Pt-Pd-Rh-(HDMG) _x complexes at 0.00, 120,160, 200, 240, 280, 320, 360, 400 pg L ⁻¹ concentrations using a GCE/rGO-SbNPs sensor; $E_d = -1.2$ V (vs. Ag/AgCl) and $t_d = 120$ s with a corresponding linear calibration curve also shown.....	215
63.	The AdDPSV results obtained for the effect of interfering ions on the stripping voltammetric results for Pd(HDMG) ₂ using the GCE/rGO-SbNPs sensor in ratio 1:4 (PGM: interference) with 0.2 M NaOAc buffer (pH = 5.2) solution containing 1×10^{-5} DMG solution.....	223

64.	<p>The AdDPCSV results obtained for the effect of interfering ions on the stripping voltammetric results for Pt(HDMG)₂ using the GCE/rGO-SbNPs sensor in ratio 1:4 (PGM: interference) with 0.2 M NaOAc buffer (pH = 5.2) solution containing 1×10^{-5} DMG solution.....</p>	225
65.	<p>The AdDPSV results obtained for the effect of interfering ions on the stripping voltammetric results for Rh(HDMG)₃ using the GCE/rGO-SbNPs sensor in ratio 1:4 (PGM: interference) with 0.2 M NaOAc buffer (pH = 5.2) solution containing 1×10^{-5} DMG solution.....</p>	226
66.	<p>Maps showing the location of the sampling sites on the Bottelary Road and Old Paarl Road, major routes into the town of Stellenbosch, South Africa.....</p>	229



List of Tables

<u>Discription of Table</u>	<u>Page</u>
Table 1. Criteria for the design and development of electrochemical sensors for environmental monitoring (Brett, 2001).	44
Table 2. Properties of graphene (Hibino, 2012).	53
Table 3. Different functions of nanoparticles in electrochemical sensor systems (adapted from Luo et al., 2006).	63
Table 4. The characteristics of different type of electrochemical reaction (Adapted from Birke et al., 1981).	89
Table 5. Characterisation Procedures used during sensor development.	121
Table 6. Summary of the values obtained for $E_{p,a}$ and $E_{p,c}$ peak potential, I_p and ΔE by GCE modified with rGO, SbNPs and rGO-SbNPS compounds using CV.	164
Table 7. Circuit elements for R_p , R_s , C_{dl} and CPE obtained by fitting equivalent circuit in Figure 42.	168
Table 8. Kinetics parameters of rGO, SbNP and rGO-SbNPs modified electrodes obtained in 0.1 M HCl solution.	170
Table 9. Summary of results for the slope and R^2 for carbon nanoparticle electrodes investigated.	179
Table 10. Summaries of results for the number of electrons for different nanoparticle carbon electrodes matrices at the scan rate 40 mV s^{-1}	181
Table 11. Summaries of results for the surface concentration of carbon nanoparticle electrodes.	182
Table 12. Summaries of results for electron transport diffusion coefficients in nanoparticle matrices.	183
Table 13. Summaries of results for the thickness of the nanoparticle film.	184
Table 14. Results for the E_{pa} and E_{pc} , ΔE_p , and $E_{1/2}$ for the PGMs collected in 0.2 M NaOAc (pH = 5.2) solution at the GCE/rGO-SbNPs sensor surface.	187
Table 15. Summary of the optimal conditions for PGMs determination with the respective GCE/rGO-SbNPs and SPCE/rGO-SbNPs sensor platforms and DMG as complexing agent.	206

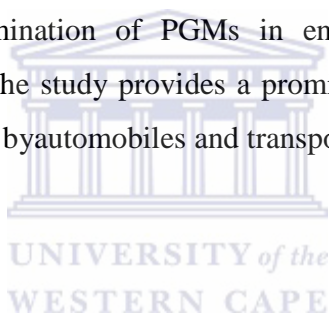
Table 16.	Summary of the comparative current responses and potentials for the cathodic reduction of Pd(HDMG) ₂ , Pt(HDMG) ₂ and Rh(HDMG) ₃ at the GCE/rGO-SbNPs and SPCE/rGO-SbNPs sensors, respectively.	211
Table 17.	Calibration data for the determination of PGMs in the presence of [DMG] = 1 × 10 ⁻⁵ M as chelating agent, using the GCE/rGO-SbNPs and SPCE/rGO-SbNPs sensor, with a supporting electrolyte of NaOAc buffer (pH = 5.2) solution.	215
Table 18.	Results obtained for the analytical parameters of applying the individual GCE/rGO-SbNPs and SPCE/rGO-SbNPs sensors in the AdDPCSV analysis of Pd(HDMG) ₂ , Pt(HDMG) ₂ and Rh(HDMG) ₃ in 0.2 M acetate buffer (pH = 5.2) solution as the supporting electrolyte.	217
Table 19.	Mean values for recovery of PGMs standard solution (n = 3).	219
Table 20.	Comparison of results obtained in the present study with other data in which modified stripping voltammetric techniques were applied for the determination of PGMs in standard solutions or environmental samples are listed.	220
Table 21.	Results obtained for the interferences and resulting % signal change in 0.2 M NaOAc buffer (pH = 5.2) solution as the supporting electrolyte.....	226
Table 22.	Results obtained for the total concentrations of PGMs in the in soil samples, using the acid digestion procedure and ICP-MS analysis.....	231
Table 23.	Results obtained for the sequential extraction of total metal concentrations in soil samples obtained using ICP-MS spectrophotometric analysis.....	232
Table 24.	Results obtained for the total concentrations of PGMs obtained in the direct acid digestion of the dust samples.....	234
Table 25.	Results obtained for the sequential extraction of the dust samples and analysis using ICP-MS spectrophotometry.....	236
Table 26.	Results obtained for the sequential extraction of speciation metal concentrations in soil samples obtained using AdDPSV analysis.	239
Table 27.	Results obtained for the sequential extraction of speciation metal concentrations in dust samples obtained using AdDPCSV analysis.....	240

Abstract

Platinum Group Metals (PGMs), particularly palladium (Pd), platinum (Pt) and rhodium (Rh) have been identified as pollutants in the environment due to their increased use in catalytic converters and mining in South Africa (as well as worldwide). Joining the continuous efforts to alleviate this dilemma, a new electrochemical sensor based on a nanoparticle film transducer has been developed to assess the level of these metals in the environment. The main goal of this study was to exploit the capabilities of nanostructured material for the development and application of an adsorptive stripping voltammetric method for reliable quantification of PGMs in environmental samples. In the study reported in this thesis, glassy carbon electrode (GCE) and screen-printed carbon electrode (SPCE) surfaces were modified with conducting films of nanostructured reduced graphene oxide-antimony nanoparticles (rGO-SbNPs) for application as electrochemical sensors.

The rGO-SbNPs nanocomposite was prepared by Hummer's synthesis of antimony nanoparticles in reaction medium containing reduced graphene oxide. Sensors were constructed by drop coating of the surfaces of the carbon electrodes with rGO-SbNPs films followed by air-drying. The nanocomposite material was characterised by: scanning and transmission electron microscopies; FTIR, UV-Vis and Raman spectroscopies; dc voltammetry; and electrochemical impedance spectroscopy. The real surface area of both electrodes were studied and estimated to be $1.66 \times 10^6 \text{ mol cm}^{-2}$ and $4.09 \times 10^3 \text{ mol cm}^{-2}$ for SPCE/rGO-SbNPs and GCE/rGO-SbNPs, respectively. The film thickness was also evaluated and estimated to be 0.36 cm and 1.69×10^{-6} cm for SPCE/rGO-SbNPs and GCE/rGO-SbNPs, respectively. Referring to these results, the SPCE/rGO-SbNPs sensor had a better sensitivity than the GCE/rGO-SbNPs sensor. The electroanalytical properties of the PGMs were first studied by cyclic voltammetry followed by in-depth stripping voltammetric analysis. The development of the stripping voltammetry methodology involved the optimisation of experimental conditions such as selection of adequate supporting electrolyte, choice of pH and /or concentration of supporting electrolytes, deposition potential, deposition time, stirring conditions. The detection of Pd(II), Pt(II) and Rh(III) in environmental samples were performed SPCE/rGO-SbNPs and GCE/rGO-SbNPs at the optimised experimental conditions.

For the GCE/rGO-SbNPs sensor, the detection limit was found to be 0.45, 0.49 and 0.49 $\mu\text{g L}^{-1}$ (S/N = 3) for Pd(II), Pt(II) and Rh(III), respectively. For the SPCE/rGO-SbNPs sensor, the detection limit was found to be 0.42, 0.26 and 0.34 $\mu\text{g L}^{-1}$ (S/N = 3) for Pd(II), Pt(II) and Rh(III), respectively. The proposed adsorptive differential pulse cathodic stripping voltammetric (AdDPCSV) method was found to be sensitive, accurate, precise, fast and robust for the determination of PGMs in soil and dust samples. The simultaneous determination of PGMs was also investigated with promising results obtained. The AdDPCSV sensor performance was compared with that of inductive coupled plasma mass spectroscopy (ICP-MS) for the determination of PGM ions in soil and dust samples. It was found that though the metals could be determined by ICP-MS technique, it was limited from the standpoints of sensitivity, ease of operation and versatility compared to the AdDPCSV sensor. This study has showcased the successful construction and application of novel SPCE/rGO-SbNPs and GCE/rGO-SbNPs AdDPCSV sensors for the determination of PGMs in environmental samples (specifically roadside dust and soil samples). The study provides a promising analytical tool for monitoring PGMs pollutants that are produced by automobiles and transported in the environment.



Chapter 1

Introduction

1.1 Introduction

The pollution involving heavy metal (HMs) ions is one of great significance in ecochemistry and ecotoxicology because of their toxicity at low levels and create environmental problems throughout the world. The ability of heavy metals associated with platinum group metals to accumulate and cause toxicity in biological systems - humans, animals, microorganisms and plants has been reported (Somerset *et al.*, 2015; Doumett *et al.*, 2008; Nouri *et al.*, 2006; D'amore *et al.*, 2005). All heavy metal (HMs) occur naturally in soils, at least in trace quantities but has also various sources. The main sources of soil contamination include agricultural and industrial pollution (Birwland, 1999). The chemical analysis of soil is important for environmental monitoring and legislation. Many of the differences between toxicities associated with metals can be explained by properties such as solubility, oxidation state, absorbability, transport and complexes (Stohs and Bagchi, 2000). Metals exist in different forms in the environmental and biological samples. Different chemical forms have different electrochemical, chemical properties as well as different toxicity effects on human. For the investigation of heavy metals in soils Wu *et al.* (2007) found that the inter-correlation between heavy metals and active soil components (such as Fe oxides, organic matter, and clay) is the major predictive mechanism.

It has been shown that voltammetric techniques are well suited for speciation studies due to their sensitivities to the chemical forms of metals. The anthropogenic forms of HMs mainly exists on the surfaces of soils as reactive forms. HMs in soils can be dissolved in the soil solution or bound to exchange sites. This fraction is seen to be phytoavailable. HMs that are either adsorbed to or complexed with organic matter (OM), secondary oxides, minerals and other chemical compounds may also become phytoavailable within time. In general, their availability depends on soil parameters and processes (Chang *et al.*, 2014; Kabata-Pendias, 2011).

Figure 1 shows a typical model of metal speciation in soil based on extraction techniques. Generally, there are several kinds of binding sites between metal species and soil components. Some metals may be loosely bound as presented in a water-soluble form. Alkaline and alkaline earth metal ions prefer to form electrostatic interactions with negative surface charges. These metals are classified as exchangeable fractions. Under certain conditions, some may precipitate as carbonate compounds. Metal oxides and organic matter are two major components in soils that can play an important role in metal adsorption. Strong interactions normally occur in these fractions due to inner-sphere complex formations.

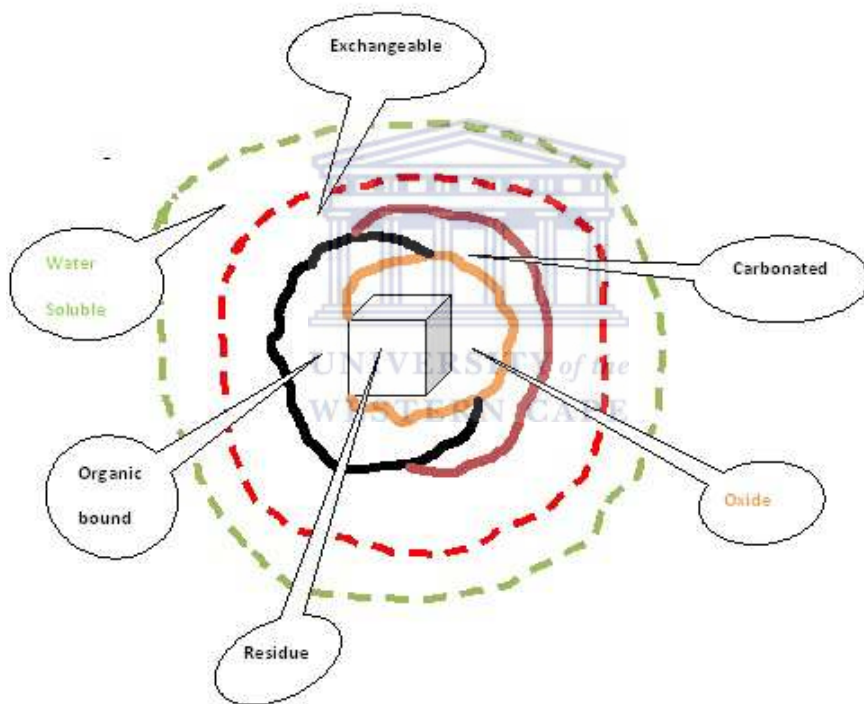


Figure 1. A simple model of metal fractions in soils (Adapted from Urai Chatreewongsin, PhD Thesis, 2000).

Quantitative determination of these metal ions in different environmental samples is a vital task. The detection of heavy metals has proven difficult with classical and recently developed analytical methods. The methods that are currently widely used are spectroscopic methods including atomic absorption, emission spectroscopy, plasma mass spectroscopy, etc.

and are also commercially available. They allow low detect limits, selectivity, reliability and accuracy, but they often require sophisticated and skilled laboratory staff. On the other hand these methods are unable to detect very low analyte concentrations particularly for platinum group metals since they are found at very low concentrations in the environment. Moreover, a main and common disadvantage of all these classical methods is that none of them can quantify the concentration of bioavailable heavy metals, as they only quantify the analytical total. Thus these techniques are hardly available for on-site analysis. Due to the large amounts of toxic metal ions commonly used and their impact on the environment and health, it is important to develop a prompt, accurate method of analysis. Electrochemical methods, like ion selective electrodes, polarography and voltammetric methods, are more user-friendly and require less complex instrumentation (Pujol *et al.*, 2014; Vyskčil *et al.*, 2011; Anderson *et al.*, 2000).

Electroanalysis can be classified as a special area of electrochemistry, which is aimed at identification and quantification of chemical substance(s) in the sample using electrochemical methods. Undoubtedly, as a discipline that includes the identification, quantification, and monitoring of various species in the environment, it is also one of the largest areas of electroanalysis (Rajeshwar *et al.*, 1994; Wang, 1994; Esteban & Casassas, 1994). The ability to build micro- and nanostructures on electrode surfaces has given rise to new electrochemical devices in which the properties of the electrode are tailored for specific purposes (Murray, 1992). In principle, this is a very attractive prospective for developing electrochemical sensors suited especially for environmental analysis in complex matrices, where the presence of numerous interferences hinders the reliable use of “classical” electrodes.

It is well known that geometry, surface structure and material constituting an electrode have a profound effect on the electrochemical behavior of electroactive species and as a consequence influence the electrochemical response. The size of working electrodes also affects the response of the electrode, due to mass transport effects of the active species to and from the electrode. Electrochemical sensors have a wide range of applications owing to their small size, low power requirements and the need for little or no sample pretreatment (Brett, 2001). Electrochemical sensor has shown promise for being inherently sensitive, capable of detecting a target analyte in a complex matrix even under turbid conditions. Additionally, electrochemical sensors has allowed for less operator involvement through a lowered requisite for sample pretreatment, a significant advantage for the development of in-line monitoring technology. The

ability to miniaturise the analytical recognition interface has further resulted in the development of diagnostics technology that is portable. Real-time monitoring of a target analyte can be performed either as a quantitative or qualitative assessment. The incorporation of electrochemical sensors provides useful information on the state, concentration and nature of a target analyte. The effects external conditions have on its stability, whether the intention is to synthesis the target analyte.

Chemically modified electrodes represent a modern approach to electrode systems. Such deliberate alteration of electrode surfaces can thus meet the needs of many electro-analytical problems, and may form the basis for new analytical applications and different sensing devices (Uslu *et al.*, 2007). A continuous search for improved methods and materials that could overcome the challenges pertaining to sensor development therefore ensues.

Nanomaterials, in particular graphene have shown unmatched promise as electrode materials for incorporation into electrochemical sensors. The attraction of using these nanomaterials is based on taking advantage of their enhanced conductive properties, as well as their capacity to increase surface areas significantly given their nano dimensional size. These properties afford greater sensitivities as well as enhanced reproducibility and re-usability. Due to its excellent electronic, thermal and mechanical properties graphene, a single atom thick sheet of hexagonally arrayed sp^2 bonded carbon atoms, has recently been attracting a lot of attention since it was first produced experimentally in 2004 (Willemse *et al.*, 2011). It is suggested to be a very important material in device applications. On the other hand insertion of the nanoparticles on the graphene based matrix is an important study for the exploration of their properties and applications.

This excellent merger of scientifically significant and industrially applicable properties in the graphene-based systems draws equal interests from scientists and engineers. The carbon backbone of graphene provides possibilities for surface chemical modification. This aspect of graphene was thoroughly investigated and exploited by building advanced composites of graphene (Dhand *et al.*, 2013). Graphene based electrodes have shown superior performance in terms of catalytic activity and microscopic scale conductivity than carbon nanotubes based ones. This indicates that the opportunities in electrochemistry encountered by carbon nanotubes might be available for graphene (Yin *et al.*, 2013; Tapas *et al.*, 2012; Shao *et al.*, 2009).

Major fundamentals and technological advances need to be made towards enhancing the sensitivity, selectivity and the reliability of the trace metal ion electrochemical sensors. The emergence of nanotechnology may open new horizons and satisfy the above target. Nanocomposite material will be attractive because of their unique electrical, chemical and physical properties (*i.e.* size, strength, composition, conductivity, magnetism, mechanical and light absorbing and emitting).

Graphene is the most studied nanomaterial and has been especially targeted for developing electrochemical sensors and biosensors. The main attractive property of antimony-based sensors is the low toxicity of antimony and its compounds while their performance closely resembles that of their mercury counterparts. Therefore, antimony incorporated on graphene can serve as environmentally friendly replacements for mercury electrodes in stripping analysis (Zhang *et al.*, 2014).

In this study, incorporation of antimony nanoparticles on graphene sheets has been demonstrated to reveal special features in new hybrids that will be utilised in environment sample analysis. The work in this thesis involves synthesis of a nanocomposite of graphene and antimony, followed by the characterisation of the newly synthesised nanocomposite and utilising the nanomaterials in sensor construction for the quantification of selected metal ions in environmental samples.

1.2 Carbon

Carbon is one of the most common elements on earth. Until the discovery of fullerenes in 1985, the science and chemistry of the carbon atom was thought to be well known (www.scienceclarified.com/Ca-Ch/Carbon-Family.html). Previous to this discovery, carbon was known to form graphite and diamond, as well as amorphous materials like charcoal. Perhaps the most important consequence of the discovery of the fullerene is that it opened the door for matter to be studied at the nanoscale. Six years later, in 1991, another big surprise was found – the carbon nanotube (Iijima, 1991). One of its most frequent allotropes, *e.g.* graphite, has been known and used for thousands of years. It consists of planes of carbon atoms arranged in a honeycomb structure that are weakly bonded together. To isolate one of these sheets of carbon

atoms and keeping it from rolling itself up was for a long time considered impossible. However, in 2004 researches from the University of Manchester, A. Geim and K. Novoselov, achieved exactly this (Geim *et al.*, 2007; Novoselov *et al.*, 2004). They used a surprisingly simple method, commonly referred to as the "scotch tape method", to gently peel the single atomic layers of carbon atoms in graphite apart. This way, graphene, a new and strictly two-dimensional material was born. From that moment on the interest in graphene has boomed, and already in 2010 the discoverers were awarded the Nobel Prize in physics for their groundbreaking research (Geim *et al.*, 2007; Novoselov *et al.*, 2004). With a new material come new opportunities to re-examine old problems as well as pose new ones.

These forms of carbon have led to a burst of research in nanomaterials. Depending on the lattice structure of each of these carbons-based materials, different material properties are observed at the nanoscale level. In this study, we focus on nanostructured composite (*i.e.* graphene and antimony nanoparticles).

1.3 Nanomaterials

1.3.1 What distinguishes nanomaterial from bulk material?

Most micro-structured materials have similar properties to the corresponding bulk materials. The properties of materials with nanometre dimensions are significantly different from those of atoms and bulk materials. When matter is reduced into nanoscale structures, new unique physical properties emerge that are not seen in bulk material. The smaller a particle becomes, the more the proportion of surface atoms increases. As particles decrease in size the number of surface atoms becomes equal to or even exceeds the number of inner-core atoms. For a typical bulk material the surface is negligibly small in comparison to the total volume. Among the characteristics of nanomaterials that distinguish them from bulk materials, it is important to note the following: (1) large fraction of surface atoms; (2) high surface energy; (3) spatial confinement; (4) reduced numbers of imperfections that do not exist in the corresponding bulk materials (Korotcenkov, 2008; Cao, 2004).

The use of nanomaterials provides the following advantages. First, all nanomaterials consist of very small particles. This is the first advantage of nanomaterials and nanotechnologies, promoting attainment of super miniaturisation. Because they are small, nanostructures can be

packed very closely together. As a result, on a given unit of area one can locate more functional nano-devices, which is very important for nano-electronics. Their high packing density has the potential to bring higher area and volume capacity to information storage and higher speed to information processing (because electrons require much less time to move between components). Thus, new electronic device concepts, smaller and faster circuits, more sophisticated functions, and greatly reduced power consumption can all be achieved simultaneously by controlling nanostructure interactions and complexity (Roco *et al.*, 1999).

Second, because of their small dimensions, nanomaterials have large specific surface areas, accelerating interactions between them and the environment in which they are located. For example, nanoparticles with a radius of 2.5 nm and a density of 5 gcm^{-3} have a surface of $240 \text{ m}^2\text{g}^{-1}$ when assuming a ball-like shape. For comparison, a dense (compact) material with a weight of 1 g and the same density has a surface area of $2 \times 10^{-6} \text{ m}^2$. Thus, nanoparticles have a much larger surface area per unit of mass compared with larger particles. Because growth and catalytic chemical reactions occur at surfaces, this means that materials in nanoparticle form will be much more reactive than the same mass of material made up of larger particles. A strong increase in the participation of surface atoms in the physical and chemical properties of nanomaterials is another consequence of a decrease in particle size. It is known that the volume of an object decreases as the third power of its linear dimensions, but the surface area decreases only as its second power (Chaturvedi *et al.*, 2012).

Therefore, when materials are in the form of nanoparticles, their surface area-to-volume ratio, *i.e.* the ratio between surface and bulk atoms, increases. This effect is especially strong when the sizes of nanomaterials are comparable to the Debye length. Simple calculations show that a particle of size 30 nm has 5% of its atoms on its surface; at 10 nm, 20% of its atoms; and at 3 nm, 50% of its atoms (Royal Society, 2004).

It is known that atoms on the surface of nanoparticles have unusual properties and (relatively speaking) there are a lot of them. These surface atoms make nanoparticles very different from just small particles, because not all bonds of surface atoms with neighbouring atoms are enabled. For atoms on uneven surfaces, non-saturation of the bonds is even higher. For this reason, corner atoms normally have the highest affinity to form bonds to adsorb molecules, followed by edge and in-plane surface atoms, a fact that is of great importance for catalytic activity. Alternatively, because of their low stabilisation due to low coordination, edge and in

particular corner atoms are often missing on single crystals, even in thermodynamic equilibrium (Roychowdhury, 2014; Roduner, 2006). Recently, size-dependent variation in oxidation state and lattice parameter has been reported for cerium oxide nanoparticles (Deshpande *et al.*, 2005).

1.3.2 Nanoparticle production and synthesis

Manufactured nanoparticles are produced by using top-down methods (e.g. lithography, grinding, ball milling, etc.) or by bottom-up methods, via crystal growth of ions or atoms (see Figure 2). Synthetic approaches comprise of two main classes: the top-down and bottom-up approach, and are summarised in Figure 2 below.

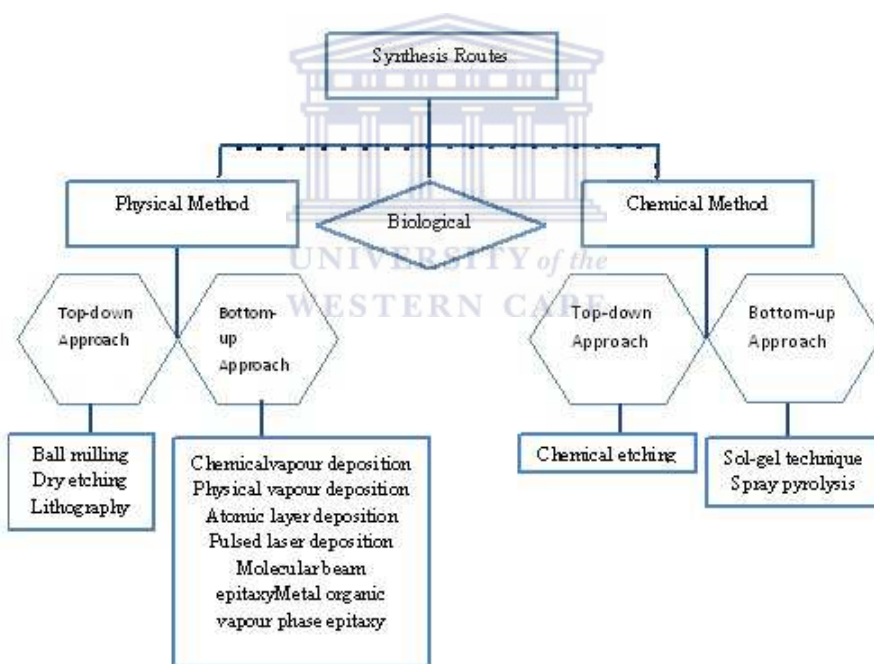


Figure 2. Various approaches undertaken for synthesis of metal nanostructures (Adapted from SPIE photonics West, 2009).

Both approaches play very important roles in modern industry and most likely in nanotechnology as well. There are advantages and disadvantages in both approaches. Among others, the biggest problem with top-down approach is the imperfection of the surface structure.

For example, nanowires made by lithography are not smooth and may contain a lot of impurities and structural defects on surface. Such imperfections would have a significant impact on physical properties and surface chemistry of nanostructures and nanomaterials, since the surface over volume ratio in nanostructures and nanomaterials is very large. Bottom-up approach is often emphasised in nanotechnology literature, though bottom-up is nothing new in materials synthesis. Typical material synthesis is to build atom by atom on a very large scale, and has been in industrial use for over a century. Examples include the production of salt and nitrate in chemical industry, the growth of single crystals and deposition of films in electronic industry. For most materials, there is no difference in physical properties of materials regardless of the synthesis routes, provided that chemical composition, crystallinity, and microstructure of the material in question are identical (Cao, 2004).

These processes can be controlled in such a way that many different types of structures are produced. The size range that holds so much interest is typically from 100 nm down to the atomic level (approximately 0.2 nm), because at just a few nm, nanoparticles show properties that are very different to those observed in the bulk. Decreasing the particle size, gives rise to an increased specific surface area, leading to better catalytic properties. At the small scale, the dominance of quantum effects changes the optical, magnetic or electrical properties of bulk material and is responsible to the main causes of change in NP behaviour (RS/RAEng, 2004). Manufactured nanoparticles generally consist of a single-core, mixed-core or composite of inorganic metal, metal oxides or carbon. They can be embedded in materials such as glass or annealed onto surfaces, depending on the required use (Kendall and Kosseva, 2005; Liz-Marzan & Lado-Tourino, 1996). However, aqueous suspensions of metal nanoparticles often have an oxide (or oxy-hydroxide) layer formed on the outer surface and may possess similar surface chemistries to other metal oxide NPs, but due to their small size may possess a larger number of metal atoms on the surface than in the bulk material (Louxand Savage, 2008; Christian *et al.*, 2008).

1.4 Graphene based nanocomposite

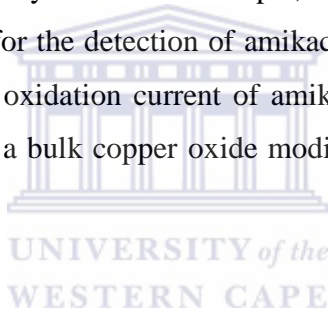
The functionalisation of graphene and its analogues aims the improvement of dispersibility, since graphene is hydrophobic in nature and the processability is very important for many applications. On the other hand, the combination of unique properties of graphene and GO, rGO (*e.g.* conductivity – pristine graphene, mechanical and thermal properties, large surface specific area *etc.*) with those of other components (organic or inorganic reagents) leads to new properties and extent of applicative area. Since graphene discovery, graphene – inorganic nanostructure composites (*i.e.* metallic and semiconducting nanoparticles) have been extensively studied, due to their tested performances and potential application in catalysis, optics and optoelectronics, supercapacitors, fuel cells, batteries, bio/sensing *etc.*

1.5 Electrodes modified by nanomaterials

An important advantage of electroanalytical techniques is the possibility to modify the working electrode with different types of advanced materials to increase the affinity for the analyte, to lower the limits of detection and to avoid interferences. In particular, during the last years nanomaterials appeared to be very promising for application in the field of sensors and biosensors. Among different types of nanomaterials, carbon nanotubes; metal and semi-conductive nanoparticles show very interesting properties and features for electrochemical performances and were chosen for the modification of electrodes to be used in selected trace electroanalytical applications (Compagnone *et al.*, 2014). Nanomaterials have been introduced in the development of new kinds of electrochemical sensors with improved performances. NPs in particular have been used and exploited for two main types of actions: 1) catalysis of electrochemical reactions and 2) acting as direct reactant. Many NPs, especially metal NPs have excellent catalytic properties combining, as they do, the intrinsic catalytic properties of the metal with the nanoparticulate properties of high surface area/volume ratio. The introduction of NPs with catalytic properties into electrochemical sensors and biosensors can decrease overpotentials of many analytically important electrochemical reactions, and even realize the reversibility of some redox reactions, which are irreversible at common electrodes (Cass, 1990).

1.6 Nanoparticles in Electro-analysis

Metallic nanoparticles are of great interest because of the modification of properties observed due to size effects, modifying the catalytic, electronic, and optical properties of the monometallic NPs. (Chushak and Bartell, 2003; Tomas, 2003; Bronstein *et al.*, 2000). A wide variety of metallic nanoparticles have been studied in order to assess the applications of these materials in electro-analysis, e.g. Raj and co-workers developed an electrochemical sensor for the selective detection of dopamine in the presence of ascorbic acid, which was based on the catalytic effect of AuNPs on the ascorbic acid oxidation (Raj *et al.*, 2003). You *et al.* (2003) prepared a highly sensitive H₂O₂ sensor based on the modification of a carbon film electrode with PtNPs. Some of the non-metal NPs that have special catalytic properties can also be applied in electrochemical analysis systems. For example, a carbon paste electrode doped with copper oxide NPs was developed for the detection of amikacin based on the catalytic properties of the copper oxide NPs, and the oxidation current of amikacin at the prepared electrode was about 40 times higher than that at a bulk copper oxide modified carbon paste electrode (Zen *et al.*, 2004).



1.7 Novelty of Research

The nanostructured sensor developed here is the first modifier of reduced graphene oxide impregnated antimony nanoparticle based on a GC and SPC electrodes for electrochemical electrochemical detection. The novelty is further showcased in the nanocomposite of rGO-SbNPs utilised for the detection of PGMs using a GCE and disposable SPCE set-up. The reduced graphene oxide impregnated antimony nanoparticle-based electrochemical detection system provides a new, simple, fast, and field-ready technology as an alternative to the traditional spectroscopic technique with comparable sensitivity.

1.8 Research Hypothesis

A reduced graphene oxide impregnated antimony nanoparticle sensor can be used as a modifier to fabricate GCE and SPCE electrodes. The rGO-SbNPs could enhance the electrode's electrochemical properties and used in stripping voltammetry to detect platinum group metals (PGMs) in the presence of chelating agent in road dust and soil samples.

1.9 Aim and Objectives

1.9.1 Aims

Based on the main hypothesis the following aims and objectives are identified:

The overarching goal of this work is to produce nanostructure electrochemical sensor based on graphene and antimony nanoparticles. The work sought to establish the properties through the utilisation of nanostructured materials and explore the application and enhancement of electrochemical sensor technology for the improved detection of PGMs (Pd(II), Pt(II), Rh(III)), in the presence of suitable complexing agent. The aims will be met by pursuing the following objectives.

1.9.2 Objectives

The following objectives were set to accomplish the aim of this study:

- (i) The sampling and chemical analysis of soil and dust samples collected along the road side in the Boland region of Western Cape, South Africa. The elements included are palladium, platinum and rhodium.
- (ii) To develop an improved techniques for pollutants detection in environmental samples using stripping voltammetry.

- (iii) To impregnate graphene with Sb nanoparticles (SbNPs) as well as specific binding of PVA in order to form a hetero-structure that displays, not only the useful properties of both parent materials, but also the novel nanoscale properties that emerge from their unique interface.
- (iv) The development of SPCE/rGO-SbNPs and GCE/rGO-SbNPs electrochemical sensors and their characterisation by cyclic voltammetry (CV), Raman spectroscopy, scanning electron microscopy (SEM), high resolution transmittance electron microscopy (HR-TEM), Energy Dispersive X-ray (EDX), ultra violet visible (UV-Vis) spectroscopy, Fourier transform infrared spectroscopy, (FTIR) and electrochemical impedance spectroscopy (EIS).
- (v) The optimisation of the operational parameters of the SPCE/rGO-SbNPs and GCE/rGO-SbNPs sensor systems and the testing of their applications in the determination of heavy metals and platinum group metals in standard solutions.
- (vi) The application of the SPCE/rGO-SbNPs and GCE/rGO-SbNPs sensor systems in the determination of heavy metals and platinum group metals in environmental (soil and road side dust) samples.
- (vii) To compare the differences between classification of SPCE and GCE and the classification based on detection limit, linearity and reproducibility of the method.
- (viii) Comparison of spectroscopic and stripping voltammetry methods of determining heavy metals and platinum group metals standards and the performance of recovery studies to test the accuracy.

1.9.3 Approach

The determination of PGMs in environmental samples is one of the most difficult analytical tasks owing to extremely low concentrations being determined and numerous interfering effects from matrix elements with the detection of the metals by the available instrumental techniques. The availability of the representative sample, quantitative transformation of the metals into solution, their separation from interfering elements and the choice of instrumental detection technique of the required detection limit affect the quality of the obtained results. Because of the complexity of the sophisticated techniques that are used today for PGMs detection. This work aims to improve detection of platinum group metals by synthesising reduced graphene oxide impregnated antimony nanoparticles (rGO-SbNPs) in the presence of polyvinyl alcohol (PVA) as a stabiliser. From the analytical point of view, the wide and increasing success of chemically modified electrodes (CME) may be explained by the offered possibility to purposely design the surface of conventional electrodes. By combining the intrinsic properties of the modifier and a given electrochemical reaction. The ability to miniaturise the analytical recognition interface has further resulted in the development of diagnostics technology that is simple, robust and portable. The incorporation of electrochemical sensors based on nanoparticles remains a concept that is interesting to deal with. My interest in this study is very broad. First, as explained above, the issue of synthesis of the rGO-SbNPs. Secondly, my synthesised material will be modified on carbon electrodes (GCE and SPCE). rGO-SbNPs were deposited onto the GCE and SPCE using a drop coating method. At a later stage my developed nanoparticle sensor will be applied in the soil and dust samples.

1.10 Chapter Outline

Execution of this study was divided into different chapters as outlined and described below.

- Chapter 1 Begins with a brief overview of the existing nanomaterials, heavy metal pollution and electrochemical sensors, including an introduction into this thesis with the main objectives, research hypothesis and the layout of the thesis.
- Chapter 2 Presents an extensive literature review on the electrochemical technology, the history and synthesis of one dimensional nanomaterials, with special attention to the methods used to fabricate the nanomaterials used in this research. The mechanical, electrical, and thermal properties of the aforementioned materials are discussed, as well as why each is an ideal candidate for the particular chosen application.
- Chapter 3 Corresponds to the experimental design and methodology, providing information on reagents, protocols, procedures, synthesis and instruments used in the thesis. Basic theory of the science of microscopic and analytical techniques is also presented for the synthesised nanomaterials and the sensor operation.
- Chapter 4 Discuss the results obtained on the characterisation of the synthesised material by scanning electron microscope (SEM), high resolution transmission microscope (HR- TEM), Energy Dispersive X-ray EDX, ultra violet visible spectroscopy (UV-VIS), FTIR, as well as electrochemical method (CV and EIS).
- Chapter 5 Provides the demonstration that a reduced graphene oxide (rGO) layer, containing antimony nanoparticles (SbNPs) can act as a transducer layer on screen-printed carbon and glassy carbon electrode surfaces. The rGO-SbNPs nanocomposite was characterised using various voltammetric techniques. The electrochemical properties of GCE/rGO-SbNPs are compared with SPCE/rGO-SbNPs. The materials, methods, and results of the functionalised graphene containing

antimony based nanomaterials for environmental sensing is also presented. The information on electroanalytical properties of the PGMs is studied. Oxidation, reduction and electrochemical sensing are all topics highlighted and discussed in this chapter.

Chapter 6 Presents the materials, methods, and results of the development of graphene antimony nanoparticle for stripping voltammetry application of environmental samples. Several optimisation parameters are also discussed in this chapter. It is the section reporting the results obtained in comparison of GCE and SPCE modified with rGO-SbNPs. Also given are the results obtained in application of the adsorptive differential pulse cathodic stripping voltammetry and inductive coupled plasma mass spectroscopy (ICP-MS) to the unknown samples.

Chapter 7 Summary, Conclusions, Recommendation and Future work.

Chapter 8 References



Chapter 2

Literature Review

2.1. Introduction

This chapter covers relevant literature in research on the presence and environmental concerns of heavy metals associated with platinum group metals (PGMs) in the environment. It further covers relevant literature on electroanalytical techniques for the monitoring these metals in sample matrices. A range of analytical techniques have been applied to the analysis and detection of heavy metals associated with PGMs in samples and include flame atomic absorption spectroscopy (FLAAS), inductive coupled plasma optical-emission spectroscopy (ICP-OES), inductive coupled plasma mass-spectroscopy (ICP-MS) and neutron activation analysis (NAA). Various structural characterisation methods that are most widely used in characterising nanomaterials and nanostructures are also discussed. This chapter also includes a historical overview of previous research and a description of the evaluation of various techniques, and some ways of monitoring these pollutants from the environment. The challenges of developing simple and inexpensive techniques is one of the most important matter, research in this field is concerned with the development of the modified electroanalytical sensors for monitoring heavy metal ions in environmental samples. As a result of mismanagement, environmental samples available in developed economies are polluted and contaminated to varying levels. It is, of course, also necessary to consider the problem from an economical point of view due to mass application of instrumentation techniques. Highly sensitive physical methods are using very expensive instrumentation, which frequently cannot be used as field equipment, from a practical and cost perspective. The intention of this chapter is to provide readers with the basic information on the literature of nanoparticles together with techniques used for characterisation and quantification of heavy metals.

The instrumentation for environmental monitoring should be easy to operate and not only require personnel with university training to do so. The requirement is met especially sensors, in

particular: electrochemical sensors, are rapidly being recognised in many sectors due to their track record of comparable sensitivity, selectivity, reproducibility as well as being capable of integration into a wide range of applications. What is predominantly in the favour of electrochemical sensors is the capacity to miniaturise the technology which is highly sought after for the development of portable sensor technology (Ferarri *et al.*, 2015).

In recent times, the carbon-based electrode materials are nearly ubiquitous in the electrochemical laboratory because of their availability in various forms and shapes, and usefulness over the relatively wide potential range in cathodic and anodic area (Uslu *et al.*, 2007; Wang *et al.*, 2006; Wang *et al.*, 2000). The most commonly used carbon-based material in the analytical laboratory known for its chemical stability and relatively large over-potential of oxygen and hydrogen evolutions is glassy carbon electrode (GCE) (Harris, 2005; Kessinger, 1996; Kinoshita, 1996). Important advances in electrochemical technology have fostered the development of alternative methods to monitor the generation of pollutants which damages the environment. The feasibility of zero emission of pollutants during production processes was difficult to envisage in over 30 years ago. In practice, this strategy is difficult with spectroscopic methods because these pollutants occur at very low concentration levels. Electrochemical sensors have contributed to methodologies for monitoring of these pollutants. Electrochemical technologies also proposed for electricity storage generated in power plants and renewable sources of energy during period of low demand. This stored energy can then be used in peak periods of high demand (Hadjipaschalis *et al.*, 2009).

2.2. Electrochemical sensors

An overview of analytical chemistry development demonstrates that electrochemical sensors represent the most rapidly growing class of chemical sensors. A chemical sensor is defined in Eggins (2002) as a device which responds to a particular biological analyte or chemical species in a selective way through a chemical reaction and can be used for the qualitative and quantitative determination of the analyte. Ideally, a chemical sensor provides a certain type of response directly related to the quantity of a specific chemical species. All chemical sensors consist of a transducer, which transforms the response into a detectable signal

on modern instrumentation, and a chemically selective layer, which isolates the response of the analyte from its immediate environment (Janata, 2001). Chemical sensors are categorised into electrochemical, optical, mass sensitive and heat sensitive depending on the type of transducer.

An electrochemical sensor is a device that transforms electrochemical information into an analytically useful signal. Electrochemical sensors usually composed of two basic components, a chemical (molecular) recognition system which is the most important part of a sensor and a physicochemical transducer which is a device that converts the chemical response into a signal that can be detected by modern electrical instrumentations. These two parts form a working (or sensing) electrode. A reference electrode and sometimes a counter electrode are also used in electrical measurements. Electrochemical sensors rely on the redox activity of a target analyte. A variety of electrochemical techniques exist, such as potentiometric, amperometric/voltammetry and coulometric. Electrochemical sensors combine the sensitivity and the selectivity within a small analytical device. Compared to conventional analytical methods (e.g., spectroscopy, chromatography) electrochemical sensors can be modified and adapted for the analysis of target analyte (Ozel *et al.*, 2015; Ispas *et al.*, 2012; Perry *et al.*, 2009; Wilson & Ammam, 2007). The choice of which electrochemical technique to adopt is based on knowledge of the analyte of interest as well as related contributing factors notwithstanding the desired outcome. Amperometric sensors exploit the use of a potential applied between a reference and a working electrode, to cause the oxidation or reduction of an electroactive species, and measured the resultant current. The performance of amperometric sensors is strongly influenced by the working electrode material. Consequently, much effort has been devoted to electrode fabrication and maintenance. Although classical electrochemical measurements of analytes started in 1922, when Heyrovsky invented the dropping mercury electrode, for which he received a Nobel Prize, solid electrodes constructed of noble metals and various forms of carbon have been the sensors of choice in recent years. The impressive progress in this area, and its growing impact on electroanalytical chemistry, is more recent. Research into electrochemical sensors is proceeding in a number of directions (Ciucu, 2014; Stradiotto *et al.*, 2003). A number of critical design criteria that should be considered when designing and developing robust electrochemical sensors for environmental monitoring are listed in Table 1. These are especially true for the development of submersible sensors where microfabrication, portability, analytical response, sensitivity,

selectivity, biofouling, reversibility and power consumption issues are of major concern (Hanrahan *et al.*, 2004).

Table 1. Criteria for the design and development of electrochemical sensors for environmental monitoring (Brett, 2001).

Macro vs. miniaturised fabrication design
Overall cost, simplicity/complexity of design
Robustness, reliability
Sensitivity and selectivity
Reversibility and stability
Speed
Artefact minimisation
Speciation capabilities
Automation, data acquisition
Single vs. multicomponent analysis capabilities
Low power consumption

2.3. Chemically modified electrodes

When considering an electrode designed for power generation, conversion or detection of analyte one is interested in the following desired attributes: (i) surface development (ii) improved electrocatalysis and sensitivity (iii) freedom from surface fouling and (iv) exclusion of side reactions that might compete with the studied electrode process. All of above mentioned are together hard to come by when only bare electrodes are taken into account. To overcome these limitations researchers started to experiment with new, often complex materials and dedicated catalysts. Using them they started to create so called chemically modified electrodes. Surface active compounds, present in a sample, may interfere to direct metal determination. Adsorption of organic matter onto the working electrode may hinder the diffusion of metal ions and thus diminish or eliminate the diffusion current and cause a nonlinear relationship between stripping current and deposition time. These substances may also adsorb on the electrode surface and disturb deposition of the analyte (Jia *et al.*, 2007; Economou and Fielden, 2003).

Chemically modified electrodes (CMEs) represent a modern approach to electrode systems. Such deliberate alteration of electrode surfaces can thus meet the needs of many electroanalytical problems, and may form the basis for new analytical applications and different

sensing devices. The usefulness of the chemically modified electrodes is critically dependent on its ability to transduce a concentration or the nature of an analyte in a predictable and reproducible manner. However, it is to be expected that the response will depend on the preparation method of the chemically modified electrode, and in particular, factors such as surface coverage, film composition and morphology. The pioneering work in that field was presented by Lane and Hubbard (1973). Since that time the branch of electrochemistry studying these newly developed electrodes has seen remarkable growth, and numerous important results were achieved (Uslu *et al.*, 2007). With the advent of nanotechnology various new materials such as carbon-based nanomaterials, metal and metal oxide nanoparticles, have emerged. There are various ways in which the CMEs can benefit analytical applications. These include the acceleration of electron transfer reactions, preferential accumulation or selective membrane permeation. Such steps can impart higher sensitivity, selectivity or stability (Baldwin and Thomsen, 1991; Murray *et al.*, 1987).

2.4. Carbon based Electrodes in Electroanalysis

Carbon is the most commonly used electrode material for electroanalytical chemistry. It is available in a variety of forms: graphite, glassy carbon, carbon fibre, nanotubes, and amorphous powders. These traditional carbon electrodes are important in electrochemistry because of low cost, simple preparation methods, possibility of achieving large surface area, and a relatively wide potential window of water stability (Rao *et al.*, 2005). Despite these advantages, they have several drawbacks such as fouling due to surface adsorption limiting their long term stability, inability to detect compounds that oxidise at high anodic potentials, not suitable for use in aggressive environments. Another allotropic form of carbon is diamond (Noked *et al.*, 2011; Qureshi *et al.*, 2009). Diamond is showing the typical sp^3 structure of carbon atoms and graphite presenting a honeycomb sp^2 configuration. Carbon possesses the ability to hybridise into sp , sp^2 and sp^3 configurations, depending on the bonding with neighbouring atoms. This possibility is due to the narrow band gap between $2s$ and $2p$ electron shells. These hybrid states are responsible for the different characteristics of various organic species, which open the possibility to fabricate a wide range of different carbon-based materials

(Leary and Westwood, 2011). The union between the properties of sp^2 carbon and the unique behaviour of nanoscale compounds allows the production of carbon-based nanomaterials with distinct characteristics in terms of size, surface area, strength, optical and electrical properties (Wanekaya, 2011; Mauter and Elimelech, 2008). All these advantages make them suitable for the production of modified electrodes (Svancara *et al.*, 2009; Wang, 2009). Carbon related materials offer great advantages as supports.

First, recent advances in the field have allowed the preparation of carbon nanostructures with well-defined porosities and high surface areas. Second, the carbonaceous surface can be conveniently modified through different approaches (e.g. ozonolysis, plasma, doping with heteroatoms, acid or basic treatment) to stabilise catalyst–support interactions (Tasis *et al.*, 2006). Despite the conventional use of microporous carbons as supports for metal nanoparticles, there have been recent advances in the preparation of a range of carbonaceous materials as flexible supports (Huang *et al.*, 2008; Wang *et al.*, 2007). The principal carbon-based nanomaterials used for the modification of electrodes are fullerenes, graphene, nanofibers and nanotubes (Kochmann *et al.*, 2012; Ratinac *et al.*, 2011; Tessonnier *et al.*, 2009; Gooding, 2005).

Fullerenes are composed only by carbon atoms in different structures, as hollow spheres, ellipsoids and tubes and they are applied in the electrochemical field particularly in amperometric enzymatic sensors.

Graphene is a single layer of graphite and it is classified as a zero-gap semiconductor with ballistic transport of charge carriers, electrons or holes. It can be easily functionalised and it presents very good thermal conductivity and stability, high surface-to-volume ratio and high electron transfer rate. Their electrochemical properties and applications to the sensoristic field will be discussed later in this chapter.

Nanofibers are usually synthesised by vapour-growth and are composed by graphene sheets held together by Van der Waals forces, arranged as stacked cones, cups or plates around the fiber axis, presenting more reactive sites. They have an average diameter between 5 and 500 nm and their structure depends on the nature of the catalyst metal.

Nanotubes represent the most famous, but also the most debated carbon-based nanomaterial in electroanalysis. Budarin *et al.*, (2008) have recently reported the preparation of a wide range of supported metal nanoparticles on a novel family of mesoporous carbonaceous materials called Starbon prepared from controlled carbonisation (under nitrogen atmosphere) of

mesoporous starch. Endo *et al.* (2003) have also described the preparation of Pt nanoparticles (<3 nm) using carbon-fiber-type materials and interestingly, a carbon cup-stack motif to effectively trap the growing nanoparticles between the cups. Platinum nanoparticles were observed inside and outside of the carbon-fiber structure.

Carbon nanotubes have also been investigated as supports for metal nanoparticles (Terrones, 2004; Wildgoose *et al.*, 2006). Their intrinsic properties include high surface areas, unique physical properties and morphologies, high electrical conductivity and inherent size and hollow geometry that make them extremely attractive as supports for heterogeneous catalysts (Wang *et al.*, 2008). For the purpose of this study more details will be based on graphene.

2.4.1. Glass-like carbon

Glass-like carbons are derived through the carbonisation, or thermal degradation, of organic polymers in inert atmospheres. The structure in Figure 3 is comprised of a structure of interwoven ribbons of the graphite structure. This structure means glassy carbon is a much harder form of graphite, and it is impermeable to liquids or gases. The resultant carbon has a glass-like appearance in the sense that is smooth, shiny and exhibits a conchoidal fracture. Because of its appearance, glass-like carbon has also been referred historically as vitreous carbon or glassy carbon. It is impermeable to gases and extremely inert, with a remarkable resistance to chemical attack from strong acids such as nitric, sulphuric, hydrofluoric or chromic and other corrosive agents such as bromine. Even when it does react with oxygen it only does so at high temperatures. Its rates of oxidation in oxygen, carbon dioxide or water vapour are lower than those of any other carbon. It has a hardness of 6 to 7 on Mohs scale, a value comparable to that of quartz. X-ray diffraction studies have shown that glass-like carbon presents an extremely small pore size of a closed nature and an amorphous structure (Iwashita *et al.*, 2004).

Glass-like carbon also has a wider electrochemical stability window than platinum and gold, which makes it ideal in electrochemistry experiments. Even when the overall properties of the resulting carbon depend on the nature of the precursor used, they do not change very significantly and the above values could be employed as an initial reference. A consensus on the crystalline structure of glass-like carbon has not been reached yet. The most widely accepted

model is the one that considers this type of carbon as made up of tangled and wrinkled aromatic ribbon molecules that are randomly cross-linked by carbon covalent bonds. The ribbon molecules form a networked structure, the unit of which is a stack of high strained aromatic ribbon molecules. Such structure of crystallites reflects the features of thermosetting resins structure which are commonly used as precursors for glass-like carbons. This model explains the high variety of experimental results obtained so far on glass-like carbons including its impermeability, brittleness and conductivity (Dekanski *et al.*, 2001).



Figure 3. Structural model of glass-like carbon as proposed by Jenkins in 1971. This model is able to explain most of the properties exhibit by glass-like carbon up to this day (Craig *et al.*, 2006).

2.4.2. Screen printed electrode (SPE)

Screen-printed electrodes are complete electrochemical cells (Figure 4), since they are usually composed by three electrodes: a working electrode of the desired material, a pseudo-reference electrode, usually of silver, and a counter electrode, normally of carbon.

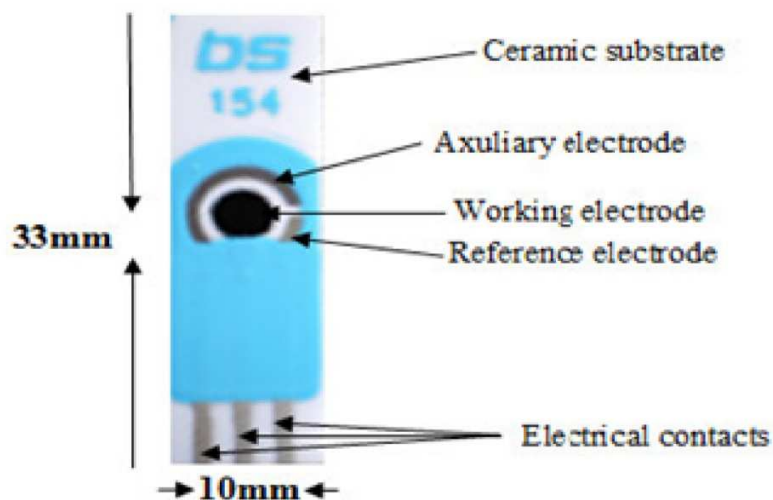


Figure 4. Typical Dropsense screen-printed carbon electrode (Dropsens, 2010).

Screen-printed electrodes (SPEs) are increasingly being used for inexpensive, reproducible and sensitive disposable electrochemical sensors for determination of trace levels of pollutant and toxic compounds in environmental and biological fluids sample (Wring *et al.*, 1991). A disposable sensor has several advantages, such as preventing contamination between samples, constant sensitivity and high reproducibility of different printed sensors (Kim *et al.*, 2002). SPEs can be designed in different ways and configurations, according to specific aims, for example with two working electrodes or as array of electrodes. These devices present several advantages with respect to conventional bulk electrodes: easiness of use, low cost, good precision and accuracy, high sensitivities and low detection limits, portability, disposability, the possibility to work with small amounts of samples and the adaptability to specific target analytes (Mettters *et al.*, 2011). Screen-printed electrodes (SPEs) may also constitute an interesting, reliable and low-cost choice to be used as electrochemical detector for chromatography, particularly high performace liquid chromatography (HPLC). They can also be modified with various types of compounds, such as nanomaterials, metal nanoparticles, mediators and metal oxide, like bismuth oxide, paving the way for interesting potential applications in clinical and environmental fields, in aqueous or non-aqueous solvents. SPEs find application in routine water quality tests, for the monitoring of pH, dissolved oxygen, nitrite and phosphate, in environmental

pollutant analysis of organic compounds, such as phenols, pesticides, herbicides and poly-aromatic hydrocarbons (Li *et al.*, 2012). The determination of heavy metals, such as Pb(II), Cd(II), Hg(II) and As(III), gas pollutants (CO, NO_x and VOCs) and in the medical field for the detection of bacteria, drugs and antibiotic residues (Laschi *et al.*, 2000; Alvarez-Icaza and Bilitewski, 1993). In this thesis, screen-printed carbon electrodes and glassy carbon electrode were studied to find sensitive electroanalytical methodologies for the determination of various organic and inorganic pollutants in environmental samples.

2.4.3. Graphene

Graphene has become the focus of an extensive collection of experimental and theoretical studies. Early work focused on graphene as the base unit of graphite, and more recently graphene has garnered further attention as the structural basis for fullerenes and carbon nanotubes (Ajayan, 1999; Saito *et al.*, 1998; Dresselhaus *et al.*, 1996). However, for decades graphene was perceived primarily as a structure for academic treatment of other, practical materials. It was predicted, and almost universally agreed, that such two dimensional materials as graphene could not exist in a stable form in isolation from bulk support structures. The benefits of graphene are many and the limitations few, but one fundamental property which limits the widespread introduction of graphene electronic devices is the absence of an electronic band gap (Neto *et al.*, 2009; Chen *et al.*, 2008; Geim *et al.*, 2007). Graphene, with zero energy gap between the highest occupied molecular orbit and the lowest unoccupied molecular orbit (HOMO-LUMO), offers a unique two-dimensional (2-D) environment for fast electron transport and has potential applications in electronic devices (Chen *et al.*, 2009, Novoselov *et al.*, 2004). Other consequences of the band structure is the opacity which is wavelength independent (Nair *et al.*, 2008), and thermal conductivity (Yu *et al.*, 2007). The four edges of a graphene sheet provide significant number of centres for fast heterogeneous electron transfer when compared to single-walled carbon nanotubes (SWCNTs) for which heterogeneous electron transfer occurs only at the two ends of the nanotube (Chen *et al.*, 2009; Pumera, 2009). Consequently, graphene sheets may have wider applicability in electrochemistry (Stoller *et al.*, 2008). The properties of graphene are very interesting, including very large surface area (at 2630 m²/g, twice of single-walled carbon nanotubes), high mechanical strength (200 times greater than steel), high elasticity and thermal

conductivity (Stoller *et al.*, 2008). The widely accepted mechanism for the synthesis of inorganic nanostructures decorated graphene is the attraction of the positively-charged metal ions by the polarised bonds of the functional groups on the graphene oxide(GO). The attachment of the metal ions to the surface and edges of the GO results in a redox reaction and the formation of nucleation sites. Eventually it leads to the growth of nanostructures on the 2-D graphene sheets (Stoller *et al.*, 2008).

2.4.3.1. Origin and development of Graphene

Graphene and Graphite are the two-dimensional layer consisting of sp^2 hybridised carbon atoms in hexagonal configuration found in pencil lead. Graphite is a layered material formed by stacks of graphene sheets separated by 0.3 nm and held together by weak van der Waals forces. The weak interaction between the sheets allows them to slide relatively easily across one another. This gives pencils their writing ability and graphite its lubricating properties, however the nature of this interaction between layers is not entirely understood. The experimental work that predates the mainstream introduction of graphene to the scientific community in 2004, and the manner in which this work has evolved to create the recent flurry of activity surrounding the study of monolayer, bilayer, and trilayer graphene. Graphene is a single layer graphite material with very interesting electronic properties, including very large surface area (at 2630 m^2/g , twice of single-walled carbon nanotubes), high mechanical strength (200 times greater than steel), high elasticity and thermal conductivity (Stoller *et al.*, 2008). In general; graphene is now well known for its possible applications in various fields. Furthermore, the oxidised rings of functionalised and defective graphene sheets contain abundant C–O–C (epoxide) and C–OH groups, while the sheets are terminated with C–OH and –COOH groups (Yang *et al.*, 2009, Wang *et al.*, 2008). Nevertheless, several of these applications are still not feasible due to the challenges in the large scale production of pure graphene sheets. Defects of graphene may change its electronic and chemical properties (Boukhvalov, 2008). The functionalised and defective graphene sheets are more hydrophilic and can be easily dispersed in solvents with long-term stability. Moreover, they are more easily produced in mass quantities as compared with the carbon nanotubes. They may be used to prepare some novel graphene-based nanocomposite films, which could facilitate the

further manipulation and processing of these materials for developing novel electronic devices, such as chemical sensors and biosensors (Paredes *et al.*, 2008).

2.4.3.2. Synthesis and Surface Sensitive Electronic Properties

The properties of graphene suggest several exciting electronic applications including high-frequency oscillators, field effect transistors, transparent flexible touch screens, and solar energy processing panels (Guo *et al.*, 2011; Watcharotone *et al.*, 2007; Berger *et al.*, 2004). Potential advanced material applications include mechanically robust and yet light-weight material applications including hydrogen visualisation templates for transmission electron microscopy (TEM), components of satellites and aircraft technology. The breaking strength of graphene is more than 100 times greater than that of steel. From an electrical aspect, the carrier mobility of graphene at room temperature is more than 100 times higher than that of silicon. Furthermore, graphene is an ultra-wide-band optical material that interacts strongly with light of a widerange of wavelengths. These properties of graphene suggest that various applications are possible. Its typical properties are summarised in Table 2. As graphene presents so many unique physical properties, how to produce such material has become a critical issue. Currently, graphene has mainly been made by three different methods. The first is micromechanical exfoliation. Based on the results reported to date, it has been suggested that graphene represents a promising material for electro-analytical applications due to its high electrical conductivity and ability to promote rapid electron transfer. However, it should be noted that recent studies by Goh and Pumera (2010) suggest that graphene modified electrodes do not provide significant advantages over graphite microparticle modified electrodes for electro-analytical applications interms of either sensitivity or reproducibility. Excellent electrochemical performance has been attributed to the high density of edge-plane-like sites or defects in graphene and a density of state argument, which also is said to apply to carbon nanotubes (McCreery, 2008). Studies by Pumera and co-workers suggested that the presence of oxygen containing functional groups also may affect the activity of graphene modified electrodes (Pumera *et al.*, 2009). The conclusion of high electrochemical activity of graphene has been reached largely on the basis of observation of small peak to peak separations, low overpotentials, and large currents detected in transient cyclic voltammograms, and assuming that theories based on the semi-infinite linear diffusion mass

transport model are applicable. Early work on the synthesis and etching of graphene nanostructures came from the laboratory of Sumio Iijima, who would later be credited with the discovery of carbon nanotubes (Gupta, 2014). In early studies of few-layer graphene by Iijima and co-workers (Iijima *et al.*, 1991). Graphene has been synthesised in various ways and on different substrates. One interesting method for synthesis of graphene conductor sheets is based on (chemical, physical or electrochemical preparation) insulator graphene oxides as precursor to form graphene conductor structures properties of graphene according to the methodology employed in their fabrication (Kosynkin *et al.*, 2009). Several studies emphasised changes in structural scientifically clear understanding of the different methods for graphene synthesis is essential to realize the optimum potentiality of graphene in a large variety of its applications. The size and quality of the graphene produced depends on the techniques used and the next sub-sections are devoted to some of the commonly used methods, their merits and demerits. Chemical reduction of GO is one of the established procedures to make graphene in large volume. Many primary products with either high conductivity or good solubility have been made by chemical reduction, intercalation, or thermal annealing, but most of these procedures create either highly functionalised materials (~3% heteroatom except C and O) or materials with a surface polymer coating (Gao *et al.*, 2009).

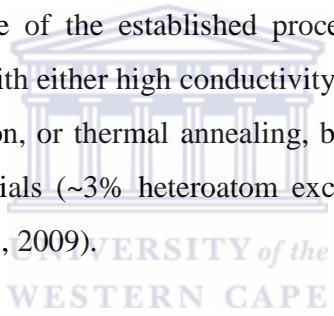


Table 2. Properties of graphene (Hibino, 2012).

Property	Value	Comparison with other materials	References
Breaking strength	42 Nm ⁻¹	More than 100 times greater than steel	Lee <i>et al.</i> , 2008; Royal Swedish Academy of Sciences, 2010
Elastic limit	~20%		Kim <i>et al.</i> , 2009
Carrier mobility at room temperature	200,000 cm ² V ⁻¹ s ⁻¹	More than 100 times higher than Si	Chen <i>et al.</i> , 2008
Thermal conductivity	~5000 Wm ⁻¹ K ⁻¹	More than 10 times higher than Cu	Ghosh <i>et al.</i> , 2010
Maximum current density	>108 Acm ⁻¹	~100 times larger than Cu	Murali <i>et al.</i> , 2009
Optical absorption coefficient	2.3%	~50 times higher than GaAs	Bao and Loh, 2012; Nair <i>et al.</i> , 2008;

2.4.3.3. Graphene Fabrication

On papers, graphene has therefore existed for a long time as a theoretical building block for other graphitic materials. However, it was predicted, and therefore for a long time believed, that a 2D crystal like graphene could not be stable at room temperature (Geim *et al.*, 2007). The most common method of graphene fabrication is exfoliation which finds its roots with a technique that has been around for centuries – writing with a graphite pencil. By writing with a pencil you create many graphene sheets spread over your paper. Unfortunately this method is uncontrollable and you are typically left with many sheets of varying thicknesses. If you want to study a single graphene sheet you need to locate it. The problem amounts to trying to find a needle in a haystack. A way around this problem was solved by Andre Geim's group in Manchester (Novoselov *et al.*, 2004; Geim *et al.*, 2004). By gently rubbing or pressing a freshly cleaved graphite crystal on oxidised silicon wafer graphene flakes with the correct thickness of oxide, single atomic layers are visible under an optical microscope due to thin film interference effects (Hill *et al.*, 2007; Jiang *et al.*, 2005). This technique simplifies the process of finding single graphene sheets but obviously limits this fabrication scheme to devices for research purposes. For the case of suspended graphene sheets, this process may take ~ 1 hour to find relatively thin ~ 1-5 nm thick suspended graphene devices but could take several days or weeks to find a suitable single suspended layer. There are recent attempts to improve the quality and yield of exfoliation techniques. These include stamping methods which use silicon pillars to transfer graphene flakes and electrostatic voltage assisted exfoliation which uses electrostatic forces to controllably separate graphene from bulk crystals (Liang *et al.*, 2007). These are very recent developments and only time will tell whether they yield significant improvement over standard exfoliation. Another common graphene fabrication technique is to disperse graphene from solution (Hwang *et al.*, 2007). In this method graphite flakes are sonicated in a solution and then dispersed onto a wafer. An atomic force microscopy (AFM) is used to locate individual sheets making this technique very time consuming relative to the optical detection scheme. Long sonication times are needed to break the graphite down and this typically results in small flakes. Recently a similar technique was used to fabricate graphene ribbons with nanoscale widths (Wang *et al.*, 2008). One of the difficulties in dispersing graphene from solution is separating the

layers without breaking them. Away around this is to intercalate the graphite and dissolve it in a solvent. When the intercalant dissolves it separates the graphene sheets. This technique was shown to work effectively for graphene oxide. However, the success of similar techniques on graphene is limited due to the chemistry required to keep individual graphene sheets from aggregating in solution. The technique which currently seems to have the greatest potential for mass production is the direct growth of graphene. Typically this is accomplished by heating a SiC wafer which results in the partial graphitisation of the upper layer (Song *et al.*, 2004). However, controlling the number of layers as well as the grain sizes is difficult with this technique limiting the mobilities achieved so far with this form of graphene (Song *et al.*, 2006). Furthermore, isolating single sheets is problematic and additional lithography is required to pattern electrostatic gates on top of the graphene. Making suspended mechanical structures from grown graphene has yet to be demonstrated. Chemical vapour deposition (CVD) and molecular beam epitaxy (MBE) are two other potential routes to graphene growth. For the time being, exfoliation remains the preferred method for most of the experimental research groups around the world. However, as in diamond, wide spread applicability of graphene is limited by the crude and time consuming methods currently used to fabricate and isolate single graphene sheets. The research community is currently in need of a reliable and reproducible graphene fabrication method if graphene is ever to move beyond being a laboratory curiosity. Figure 5 illustrates the carbon structures constructed from graphene.

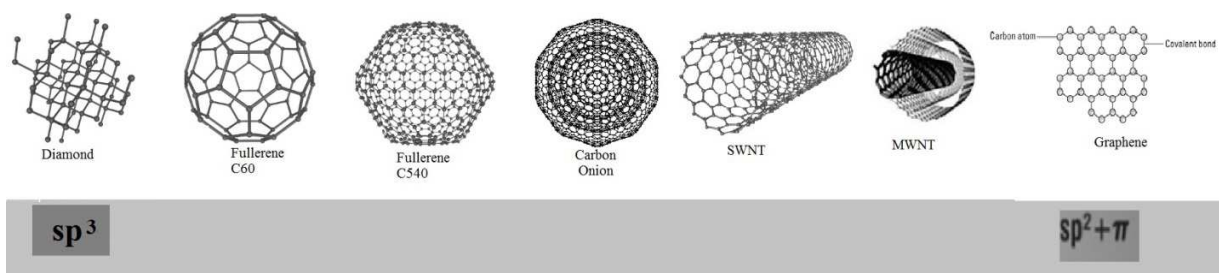


Figure 5. Hybridisation states of carbon structures that could be constructed using graphene (Yang *et al.*, 2013).

2.5. Application of graphene in electrochemical Sensing

Graphene is also promising for photonics devices such as modulators and photodetectors. In general, the range of potential applications is very wide and includes sensors, interconnects capacitors, heat dissipaters, gas barriers, and membranes as seen in Figure 6.

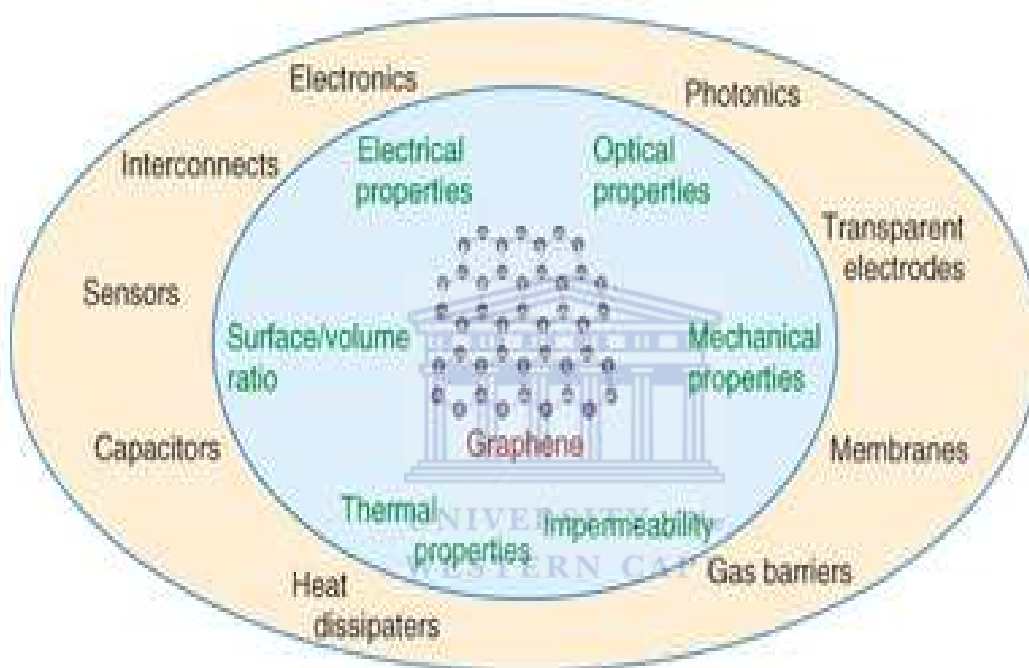


Figure 6. Overview of applications and properties of graphene (Hibino, 2012).

Graphene exhibits improved electrochemical response when compared with other electrodes such as glassy carbon electrodes, graphite and CNTs. Zhou *et al.* (2009) have shown that graphene exhibits a wide electrochemical potential window of ca. 2.5V in 0.1M phosphate buffered saline solution (PBS) at (pH = 7.0). Other groups have explored the electrochemical properties of reduced graphene oxide (rGO) and graphene-based nanomaterials (Wang *et al.*, 2009; Zhou *et al.*, 2009). These studies used different probes such as nucleic acids, potassium ferricyanide, dopamine and acetaminophen. Carbon nanotubes have shown the ability to detect gases when decorated with nanoparticles (Sippel-Oakley *et al.*, 2005; Star *et al.*, 2004; Kong *et*

al., 2000;). Graphene-based sensors also exhibit an electrical response to gaseous CO, H₂O, NO₂, and NH₃. Sensors based on graphene operate by measuring a change in resistivity resulting from the adsorption of gas molecules (Schedin *et al.*, 2007). Robinson and co-workers demonstrated a molecular sensor based on rGO capable of detecting toxic gases at parts per billion (ppb) sensitivity. In comparison to CNT-based sensors, rGO-based sensors show similar performance with greatly reduced noise (Robinson *et al.*, 2008). Detection of organic vapours like nonanol, octanic acid, and trimethyl amine was reported by Dan *et al.* (2009). Furthermore, Schedin *et al.* (2007) achieved single molecule detection with an electrical sensor made of few-layered graphene.

2.5.1 Graphene as a Biosensor

The same mechanism allows graphene and its derivatives to be used in biosensors. Graphene nanocomposite materials have also served as a basis for constructing enzymatic biosensors. Huang and co-workers prepared a composite based on rGO, gold nanoparticles and catalase for use in an amperometric sensor for H₂O₂. This approach has similar detection limit (50 nM) and linear range (0.3-600 μM), but sensitivity is low (13.4 μA mM⁻¹, -0.3 V vs. SCE) (Huang *et al.*, 2011). Two other reports confirm that gold nanoparticles improve detection limits and linear ranges (Fang *et al.*, 2010; Zhou *et al.*, 2010). The electrochemical response of hydrogen peroxide (H₂O₂) on an rGO electrode has been studied which resulted in improved performance compared to glassy carbon, graphite and CNTs (Takahashi *et al.*, 2013). A similar effect was observed in the electrochemical behaviour of the small molecule reducing agent nicotinamide adenine dinucleotide (NADH) on graphene modified electrodes (Keeley *et al.*, 2011; Tang *et al.*, 2009). In both the cases, the superior electrolytic activity of graphene is attributed to the high density of edge-plane-like defective sites on graphene. The enhanced oxidation of NADH on graphene modified electrodes is strongly confirmed when compared with bare edge plane pyrolytic graphite electrode (EPPGE). High density of the edge-plane-like defective sites contributes to enhanced oxidation/reduction of biomolecules. A multilayer graphene nanoflake film electrode demonstrated highly resolved simultaneous detection of uric acid, ascorbic acid, and dopamine with the detection limit as low as 0.17 μM (Zhou *et al.*, 2009).

It was reported that graphene exhibited better sensing capability of dopamine than CNTs in resolving ascorbic acid, dopamine, and serotonin (Alwarappan *et al.*, 2009). In a similar study, graphene exhibited high sensitivity to dopamine with a linear range of 5–200 μM and a better performance compared to multiwalled CNTs (Wang *et al.*, 2009). This performance is attributed to high conductivity, large surface area, and π - π bond interaction between dopamine and graphene.

2.6. Nanomaterial

2.6.1. Nanoparticle

Over the last three decades nanoparticles have received an increasing amount of research interest. Metal nanoparticles (NPs) find widespread application as a result of their unique physical and chemical properties. NPs have generated considerable interest in catalysis and electrocatalysis, where they provide a high surface area to mass ratio and can be tailored to promote particular reaction pathways. The activity of NPs can be analysed especially well using electrochemistry, which probes interfacial chemistry directly (Kleijn *et al.*, 2014). The use of NPs or nanoscale electrodes in electrochemistry has been the subject with a focus on electroanalysis, nanoscale electrodes and nanopores] or NP synthesis (Oja *et al.*, 2013; Zhang *et al.*, 2012, Rassaei, *et al.*, 2011).

Nanostructured materials have potential application in many other areas such as biological detection, controlled drug delivery, low-threshold laser, optical filters, microelectronics, magnetic devices, electronics, and various sensor applications, among others (van der Horst *et al.*, 2015; Kostoff *et al.*, 2008; Andrievskii, 2003). This is due to the unique size dependent properties of nanoparticles, which are often thought of as a separate and intermediate state of matter lying between individual atoms and bulk material. The properties of nanoparticles arise as a consequence of the confinement of the electron wavefunction and of the extremely high proportion of surface atoms, both of these factors are directly dependent on the size of the nanoparticle (Nicolais and Carotenuto *et al.*, 2005). Indeed the possibilities to control the properties, by tuning the size of the nanoparticle, has constant physical properties regardless

of mass, nanoparticles offer unique opportunities for control by varying the diameter and have manipulated electronic, magnetic and optical properties. These effects arise because the energy levels for small particles are not continuous, as in bulk materials, but discrete, due to confinement of the electron wavefunction. Nanoparticles of a large range of transition metals and metal oxides have been found to exhibit advantageous size dependent catalytic properties and being investigated intensively. The shape, coordination and stabilisation of these nanoparticles have been found to affect the catalysis and are therefore also the subject of much current research. As with many other applications of nanoparticles, catalysis often requires a suitable support/substrate for the nanoparticles. This should ideally provide a convenient means to utilise the nanoparticles, while protecting them from aggregation and allowing simple recovery. A key aspect to the study and employment of NPs as electrocatalysts is the preparation and characterisation of nanoparticulate electrodes, which often consist of NPs dispersed on a (typically non-electrocatalytic) support material. In such electrodes, the NP support plays a number of roles. First and foremost, from a practical point of view, the support electrode acts as a conductive bridge, contacting the NPs to an external electronic circuit. Second, the support acts to disperse the NPs, to limit agglomeration, and maintain the high surface-to-volume ratio desired. Finally, the interaction between the support material and the NPs can be employed to modify the electrocatalytic activity of the NPs (Kleijn *et al.*, 2014; Hayden *et al.*, 2007). There is therefore currently much interest in finding effective methods of producing supported nanoparticle catalytic materials using substrates such as inorganic oxides, alumina, silica and titania, as well as polymers (Prasad, 2004; Heilmann, 2003; Shipway *et al.*, 2000). Supported nanoparticles can be confined by porous materials, polymeric networks, carbon nanotubes, or polyelectrolytes. Confined nanoparticles benefit from this high colloidal stability and can be separated from the reaction medium on demand (Campelo *et al.*, 2009; Wildgoose *et al.*, 2006). By employing a core-shell structure it is possible to combine the properties of the core e.g. optical, or magnetic properties with the properties of the shell e.g. stimuli responsiveness, or improved stabilisation of nanoparticles. For example, if magnetic particles are used as core, they can be easily removed after the reaction by utilising their magnetic properties (Du *et al.*, 2011; Wu *et al.*, 2010).

2.6.2. Nanocomposite

Assemblies of different materials that form an entity in the nanometer range are often referred to as nanocomposites. Nanocomposite is defined as a composite materials having more than one phase and atleast one dimensions of at least one component in the nanometer size scale (< 100 nm. Although the term nanocomposite represent a new and exciting field in material science and technology, the nanocomposites have actually been used for centuries by the nature. Using natural materials and polymers such as carbohydrates, lipids and proteins, nature makes strong nanocomposites such as bones, shells and wood (Hussain *et al.*, 2006; Ajayan *et al.*, 2003).). However in recent years the characterization and control of structures at the nanoscale have been studied, investigated and exploited by the learning from the natural surroundings.

Nanoparticle mixed with conventional polymers, metal oxides, or metals, resulting in a special class of hybrid material known as nanocomposites. Nanocomposites are basically a mixture of two immiscible materials in which at least one has nanoscale dimensions. They can be fabricated not only with different nanostructured materials but also with various biomolecules and polymers to possess unique hybrid properties characteristic of neither the incorporated component nor the host matrix. Furthermore, based on the nanomaterials dimensional morphology, nanocomposites can be classified as 1-D, 2-D, and 3-D structures (Alexandre and Dubois, 2000). When the three dimensions are of the order of nanometres, we are dealing with isodimensional nanoparticles, such as spherical silica nanoparticles obtained by in situ sol-gel methods or by polymerisation promoted directly from the surface, but which also can include semiconductor nanoclusters and other structures. Due to their large aspect ratios (i.e., size-to-volume ratios), submicrometer size, and unique properties, nanosensors, nanoprobes, and other nanosystems are revolutionising the fields of chemical and biological analysis.

Graphene nanocomposites were often decorated with metals such as palladium and platinum resulting in sensors for hydrogen. Zhang and co-workers reported on the use of plain reduced graphene oxide (rGO) for hydrogen sensing with a resistance measurement, but the sensitivity was poor yielding a signal change of only 0.4% R/R_0 for 500 ppm hydrogen (Zhang *et al.*, 2011). If rGO is combined with a conductive polymer such as polyaniline, the sensitivity is enhanced by a factor of 10 compared to rGO only. The signal change is 3.9% (R/R_0 units) for 600 ppm of hydrogen, and 12.9% (R/R_0) for 0.5% hydrogen. Kumar and co-worker used a palladium-platinum alloy on rGO for their resistance measurements to improve response and recovery times of the respective hydrogen sensor (Kumar *et al.*, 2011). Compared to a similar

method reported by Lange *et al.* (2011), response times are reduced to 2-20 s, but the signal response is decreased (only 4.3% R/R0 for 2% H₂). Kaniyoor *et al.* (2011; 2009) have combined multi-walled carbon nanotubes with rGO (1:1 w/w) and decorated this material with platinum nanoparticles. This increases the response to 1-5% hydrogen by a factor of 2 compared to platinum decorated nanotubes. Such sensors work at temperatures up to 160 °C. Yi *et al.* (2011) reported on a sensor based on ZnO nanorods and graphene on metal foils for conductive sensing of vapors. Gong *et al.* (2010) have developed a nanocomposite consisting of rGO protected by poly(vinyl pyrrolidone), chitosan and gold nanoparticles for sensing Hg²⁺ by anodic stripping voltammetry. This sensor has a sensitivity of 708.3 ppb, and its detection limit (6 ppt) is far below the guideline value of drinking water set by the WHO (1 ppb).

Catalysis, separation, sorption, and fuel cells are other important fields for nanocomposite applications. The constituents of nanocomposites include various nanofillers such as nanoparticles, nanowires, and nanotubes of materials such as metal oxides, polymers, carbon, noble metals, and others. Because the constituents of nanocomposites have different structures, composition, and properties (electrophysical, optical, catalytic, etc.), they serve various functions. Thus, materials built from them can be multi-functional. Thus, applications utilising nanocomposites may have clear advantages over those utilising homogeneous materials (Ajayan *et al.*, 2003). Depending on the type of filler, i.e., the nanoscale material of the nanocomposites, for sensing applications they are divided into metal oxide based nanocomposites, polymer-based nanocomposites, carbon-based nanocomposites, and metal-based nanocomposites. Moreover, nanocomposites offer useful new properties compared to conventional materials. Therefore, nanocomposites are generally used when a combination of properties is required that cannot be found in a single material. For example, by combining an organic polymer with an inorganic material, the properties of the polymer, *i.e.* flexibility, toughness, and processibility, and the properties of the inorganic material, *i.e.*, hardness, good chemical stability, better barrier properties, and brittleness, one can produce a composite which will have all these properties. For example, the conventional micro-composite approach as applied to enhance polymer properties uses micro sized clay particle aggregates as filler to reinforce the polymer. However, the mechanical properties of the individual micrometre-size layered particles of clay do not function reactively in these systems.

In addition, such composites can lose optical transparency. The nanocomposite approach gives much better results. The use of nanosized particles strongly improves the mechanical properties of polymers. Moreover, because the size of the individual clay particles in these systems is much smaller than the wavelength of visible light, these nanocomposites are optically clear and transparent (Gao, 2004). Therefore, interfaces in nanocomposites play an important role in the overall properties of the system. Moreover, special properties of nanocomposite materials often arise from interactions between phases at the interfaces.

2.7. Nanoparticle in electrochemical sensor design.

Nanoparticles constitute a crucial and technology intensive area of research and development in the burgeoning field of nanotechnology. The attraction of nanoparticles lies in the myriad attractive characteristics which can be achieved by reducing suitable materials from the bulk to the nanometre size, these characteristics ranging from increased surface/volume ratio to novel quantum confinement effects. Examples of property enhancements include magnetic, optical, biosensing, thermoelectric, semiconducting and catalytic, energy storage and thermal properties. Industries that are interested in novel nanoparticles include data storage, plasmonic, photonic, microelectronic, energy, pharmaceutical, biomedical, and cosmetics. An interesting aspect of nanoparticles is the wide range of materials classes in which nanoparticles are useful including semiconductor, dielectric, and metallic, ceramic, composite and polymer nanoparticles. In the last decades, nanostructured materials have received much attention due the possibility to develop new architectures applied in electrochemical sensing and biosensing devices due to their unique chemical and physical properties (Lost *et al.*, 2011).

Many kinds of nanoparticles, such as metal, oxide and semiconductor nanoparticles have been used for constructing electrochemical sensors and biosensors, and these nanoparticles play different roles in different sensing systems. The important functions provided by nanoparticles include the immobilisation of biomolecules, the catalysis of electrochemical reactions, the enhancement of electron transfer between electrode surfaces and proteins, labelling of biomolecules and even acting (Luo *et al.*, 2006). Although these nanoparticles play different

roles in different electrochemical sensing systems based on their unique properties, the basic functions of nanoparticles can be mainly classified as:

- immobilisation of biomolecules,
- catalysis of electrochemical reactions,
- enhancement of electron transfer,
- labelling biomolecules,
- acting as reactant.

The roles that different nanoparticles have played in electrochemical sensor systems are summarised in Table 3.

Table 3. Different functions of nanoparticles in electrochemical sensor systems (adapted from Luo *et al.*, 2006).

Functions	Properties used	Typical nanoparticles	Sensor advantages	Typical examples
Biomolecule immobilised	Biocompatibility	Metal nanoparticles	Improved stability	Antibody
Immobilisation nanoparticles	large surface area	(Au, Ag); Oxide nanoparticles		onto Au remains stable for 100 days (Zhuo <i>et al.</i> , 2005)
Catalysis of Reactions	High surface energy	Metal nanoparticles (Au, Pt)	Improved sensitivity and selectivity	H ₂ O ₂ sensor based Prussian Blue Nanoparticles (Fiorito <i>et al.</i> , 2005)
Enhancement of electron transfer glucose	High surface tiny dimensions	Metal nanoparticles (Au, Ag); oxide nanoparticles (TiO ₂ , ZrO ₂)	Improved sensitivity; direct electrochemistry of proteins	Electron transfer rate oxidase enhanced of 5000 s ⁻¹ for oxidase enhanced by gold nanoparticles (Xiao <i>et al.</i> , 2003)
Labelling Biomolecules nanoparticles	Small size modifiability	Semiconductor nanoparticles (CdS, PbS) metal nanoparticles; (Au, Ag);	Improved sensitivity; indirect detection	DNA sensor labeled with Ag achieves detection of 0.5 pM (Cai <i>et al.</i> , 2002)
Acting as Reactant	Chemical activity	Oxide nanoparticles (MnO ₂)	New response mechanism	Lactate biosensor with MnO ₂ nanoparticles response 50 times more sensitive than without (Xu <i>et al.</i> , 2005)

2.8. Flexible metal nanoparticle films

In the past several years, metal nanoparticles (NPs) are of great scientific interest because they effectively bridge between bulk materials and atomic/molecular structures (El-Sayed, 2004; Schmid and Corain, 2003; Brust and Kiely, 2002; McConnell *et al.*, 2000; Shipway *et al.*, 2000a; Zhang, 1997). The electronic properties of metal NPs are neither those of bulk metal nor those of molecular compounds. Instead, they are dominated by collective oscillations of free electrons (so-called surface plasmon resonances), which depend not only on the material's electron density but also on the particles size and shape and on the distance between close-neighbour particles (Schmid and Corain, 2003; Shipway *et al.*, 2000a; Landman *et al.*, 1992). In particular noble metal nanoparticles (e.g., Au and Ag) have generated extensive interest due to their unique electronic, optical and catalytic properties. Alignment of metal nanoparticles into thin films is of great importance for diversified applications. Metal nanoparticles have a large surface-area-to-volume ratio as compared to the bulk equivalents, making them particularly attractive candidates for catalytic applications. Their main features also include a unique transition between molecular and metallic states (providing a local density of states (LDOS)), a short-range ordering and increasing number of kinks, corners and edges (Guo *et al.*, 2006). Furthermore, recent advances in controlling the particle size and shape have opened the possibility to optimise the geometry of the particles for enhanced activity, providing the optimum size and surface properties for specific reactions. Decreasing metal cluster or nanoparticle size also results in an increase in the available surface of the system. The relationship between this surface, intraparticle metal-metal bonding, the particle shape and atom-packing geometry ultimately determines the efficacy of these nanoparticles in their catalytic applications (White *et al.*, 2008).

2.9. Synthesis of metallic nanoparticles

Metal nanoparticles (NPs) can be easily synthesised, and many different types are commercially available. Nanoparticles with controlled size and shape can be synthesised either by physical methods such as vapour deposition and laser ablation or by chemical methods (Zabet-Khosousi and Dhirani, 2008; Burda *et al.*, 2005; Masala and Seshadri, 2004). There are various liquid phase methods for preparing NPs such as the chemical reduction, sol-gel, and reversed

micelle, hot-soap, pyrolysis, and spray pyrolysis methods. We will focus on the chemical methods, since they can easily provide NPs capped with organic ligands. Metal NPs, independently how they have been synthesised, is stabilised by a “protective layer”. In the case of synthesis without stabilising agent the protective layer is made by the electric double layer (electrostatic stabilisation) which gives stable dispersion but very dilute. With such kind of stabilisation it is very difficult to extract the particles and redisperse in another solvent. It is necessary to use polymers as steric capping agent for obtaining colloidal solution with higher concentration and for extracting the NPs (Okuyama *et al.*, 2004). This has fuelled investigation into the preparation of metal polymer nanocomposites. These composites most commonly take the form of thin polymer films or powders, as this is normally the simplest structure to prepare, and also good for exploiting the desired properties. Preparation techniques can be classified as *in situ* and *ex situ* methods.

2.9.1. *Ex situ* synthesis



In the *ex situ* process, the metal NPs are prepared first, traditionally by the controlled precipitation and concurrent stabilisation of the incipient colloids. This can be done by the reduction of a metal salt dissolved in an appropriate solvent, often containing a polymer stabiliser. Alternatively, it can be prepared by controlled micelle, reverse micelle, or micro-emulsion reactions. The particles produced by these methods are often surface modified to prevent aggregation, either covalently by metal-thiol bonds or by coating with a suitable polymer shell. These particles then need to be introduced into polymers. This is accomplished by mixing with a solution of the polymer, or monomer, which can then be spin cast etc., according to standard polymer processing techniques. However, this method is limited by problems of dispersion. It is necessary to surface modify the particles, therefore altering their properties, in order to disperse them. Even with this step it is difficult to produce well dispersed composites, and ascertain degree of aggregation remains. Also, this route is limited to compatible polymer-particle-solvent systems (Nicolais and Carotenuto, 2005; Goia, 2004; Hutter, 2004; Carotenuto and Nicolais, 2003).

2.9.2. *In situ* synthesis

In the *in situ* methods the monomer is polymerised, with metal ions introduced before or after polymerisation. Then the metal ions in the polymer matrix are reduced, chemically, thermally, or by UV irradiation, to form NPs. The *in situ* methods that have been used for the manufacture of metal NPs polymer composites consist of much more varied techniques. *In situ* methods, though often less simple and straightforward as *ex situ*, are commonly considered to produce better quality and more controlled nanocomposite materials.

2.10. Stabilisation of nanoparticles

Although metal nanoparticles (NPs) are catalytically active, one major drawback of these particles is their tendency to agglomerate. No matter how they may have been created, nanoparticles generally require some form of stabilisation to prevent them from coalescing, agglomerating or aggregating, which can detrimentally affect their properties and application. To prevent aggregation various approaches are pursued to stabilise NPs. These stabilisers should not interfere with the catalysed reaction or block the surface of the catalyst. Furthermore, the catalyst should be easily removed from product after the reaction. The capping ligands play an important role in the synthesis of metal NPs. They can control the particles size and can stabilise them against aggregation. For example, molecules that bind strongly to the NP cores or that provide great steric hindrance can slow down the NPs growth, resulting in small NPs. However, the ligand molecules also greatly influence the physical and chemical properties of the resulting NPs including solubility, reactivity, stability and optical properties (Burda *et al.*, 2005). Therefore it would be desirable to be able to choose freely the NPs capping ligand. Indeed, it is possible to modify the capping ligands of the monolayer-capped nanoparticles (MCNPs) after the synthesis by a ligand substitution reaction (Hostetler *et al.*, 1999).

Homogeneously distributed NPs can be stabilised by electrostatic or steric approaches (Zahmakiran and Ozkar, 2011). Metal oxide NPs are more stable, but unprotected metal NPs are subject to strong attractive forces especially at short inter-particle distances. The NPs are attracted together by van der Waals forces and, because of their metallic lattice structure it can

easily coalesce. Capping the metal NPs with an organic monolayer can protect and stabilise them as well as enhance and tailor their surface sensitive properties. The design and successful preparation of monolayer-capped NPs (MCNPs), in which versatile molecular functionalities are used to influence the chemical characteristics. One method of stabilising NPs is simply to deposit, infuse or embed the NPs into a solid substrate/host material. This matrix must, of course, be suitable for the application that the NPs are intended for. However, if the nanoparticles are required or synthesis or use in solution, then other techniques must be used. The two possible routes for the stabilisation of NPs in solution are electrostatic stabilisation and steric stabilisation. The two stabilisation routes are illustrated in Figure 7.

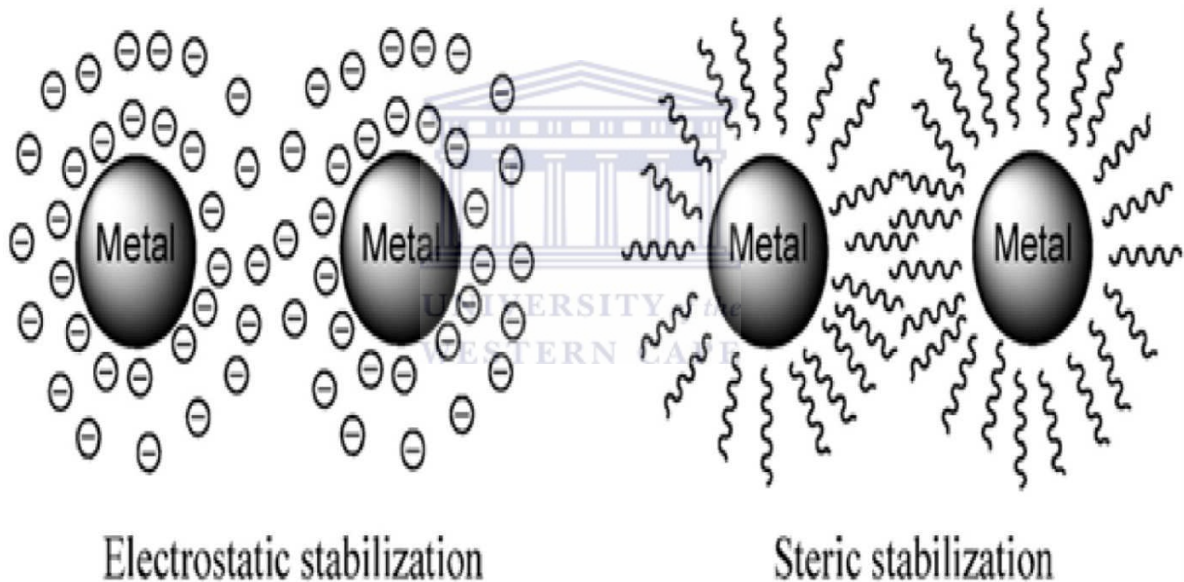


Figure 7. Electrostatic and steric stabilisation of nanoparticles (Balanta *et al.*, 2011).

2.10.1. Steric stabilisation

Steric stabilisation, also called polymeric stabilisation is a method widely used in stabilisation of colloidal dispersions and thoroughly discussed by Yu *et al.* (1998) and Duen and

Lieber (2000), though it is less well understood as compared with electrostatic stabilisation method. Polymeric stabilisation does offer several advantages over electrostatic stabilisation. Steric stabilisation is achieved by the coordination of sterically demanding molecules such as polymers, surfactants or ligands that act as protective shields on the metallic surface. Compared to electrostatic stabilisation mechanism, polymeric stabilisation offers an additional advantage in the synthesis of NPs, particularly when narrow size distribution is required. Polymer layer adsorbed on the surface of NPs serves as a diffusion barrier to the growth species, resulting in a diffusion-limited growth in the subsequent growth of nuclei. In this way, nanometallic cores are separated from each other and agglomeration is prevented (Figure 7). This can occur because of the electron deficient nature of the metal surface. Metal ions in the bulk of a lattice are commonly surrounded on all sides by the delocalised electrons in the structure. This leaves the metallic ions on the lattice surface, especially the curved surface of a nanoparticle, comparatively electron deficient. Therefore it is necessary for steric protecting agents to have suitable electron donating groups. These groups coordinate to the surface of the metal NPs. The main classes of protective groups are polymers and block copolymers, usually with P, N, O and S donors (e.g. phosphanes, amines, esters/ethers, thioethers), or solvents such as tetrahydrofuran and methanol that have electron rich groups. The steric protecting agent, in order to function effectively, must not only be attracted to the nanoparticle surface, but also be adequately solvated by the dispersing fluid (Volpe *et al.*, 2003).

2.10.2. Electrostatic stabilisation

This method is often used in the more traditional routes to NPs synthesis, especially for well controlled particle size distribution. Each metallic NP is surrounded by an electrical double layer, which causes repulsion between neighbouring NPs. This electrical double layer forms because of the attraction to the surface of the NPs of negative ions present in the solution. These negative ions are attracted to positive metal ions at the surface of the metallic lattice of the NPs. This helps to stabilise and control the growth of the forming NPs. The negative ions species can be byproducts of the metal feedstock (the metal salt), the reducing agent, or just species present in the solution. This Coulombic repulsion between the particles caused by the electrical double

layer formed by ions adsorbed at the particle surface (e.g. sodium citrate) (Bonnemann and Richards, 2009).

2.11. Nanofabrication methods

The fundamental processes used to achieve nanoscale structures, that are pivotal to this area of research, can generally be sorted into two groups, 'bottom-up' processes and 'top-down' processes (Figure 8). Top-down approach refers to slicing or successive cutting of a bulk material to get nanosized particles, whereas bottom-up techniques construct structures from smaller objects in a form of fabrication. An example of a top-down process is nanolithography, which includes both photolithography and electron beam (or "e-beam") lithography, a slower technique but with higher resolution than photolithography. Bottom-up techniques can be used to produce even smaller scale structures with greater resolution through the positioning of objects that are smaller than the nanoscale fabrication. Molecular self-assembly is a bottom-up technique that can generate structures with features of only a few nanometres over areas of hundreds of nanometres. The term "self-assembly" is reserved for the spontaneous formation of supramolecular architecture from its molecular constituents and is distinguished from self-organisation, which relates to structures formed in systems far from thermodynamic equilibrium (Barth *et al.*, 2005).

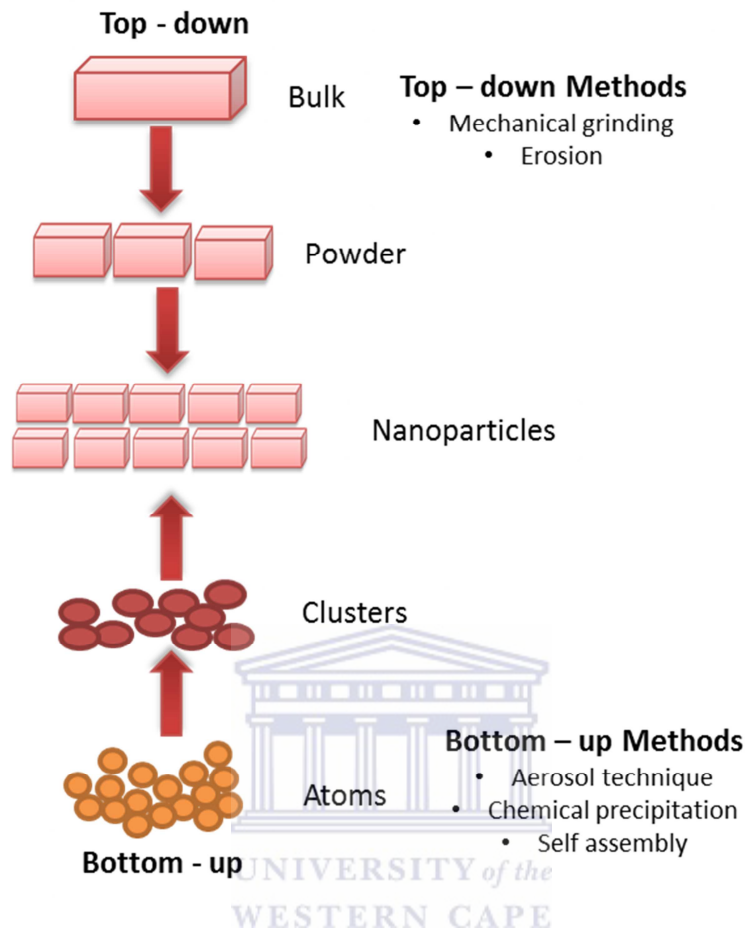


Figure 8. Schematic representations of the ‘bottom-up’ and ‘top-down’ approaches of nanomaterials (http://www.gitam.edu/eresource/nano/nanotechnology/synthesis_and_processing_of_nano.htm).

2.11.1. Top Down

The top down method involves the systematic breakdown of a bulk material into smaller pieces using some form of grinding mechanism. This is advantageous in that it is simple to perform and avoids the use of volatile and toxic compounds often found in the bottom-up techniques. However, the quality of the NPs produced by grinding is widely accepted to be poor in comparison with the material produced by modern bottom up methods. The main drawbacks include contamination problems from grinding equipment, low particle surface areas, irregular shape and size distributions and high energy requirements needed to produce relatively small

particles. Aside from these disadvantages though, it must be noted that the nanomaterial produced from grinding still finds use, due to the simplicity of its production, in applications including catalytic, magnetic and structural purposes (Hassel, 2014).

2.11.2. Bottom Up

The bottom up approach uses atomic or molecular feed-stocks as the source of the material to be chemically converted into larger NPs. This has the advantage of being potentially much more controllable than the top down approach. By controlling the chemical reactions, and the environment of the growing NPs, then the size, shape and composition of the NPs may all be affected. For this reason nanoparticles produced by bottom up, chemically based and designed, reactions are normally seen as being of higher quality and having greater potential for use in advanced applications. This has led to the development of a host of common bottom up strategies for the synthesis of NPs. Many of these general techniques can be adapted to be performed in gas, liquid, solid or even supercritical states, hence the applicability of bottom up strategies to a wide range of end products. Most of the bottom up strategies requires appropriate organometallic complexes or metal salts to be used as chemical precursors, which are decomposed or reduced in a controlled manner resulting in particle nucleation and growth (Hassel, 2014). One of the key differences that can be used to subdivide these strategies into different categories is the method by which the precursor is decomposed or reduced. It is beyond the scope of this thesis to describe the entire current and historical bottom up synthesis methods of NPs, as there are a great number of variations.

Instead, the thesis will describe the synthesis and method used for characterisation of NPsto provides a suitable overview, with specific attention being paid to graphene and antimony.

2.12. Antimony nanoparticles (SbNPs)

In the last six decades mercury (Hg) electrodes were the most extensively used for electrochemical stripping analysis of several metal ions and some selected organic species. However, due to the toxicity of Hg many other electrode materials have been suggested as

substitutes for Hg, e.g. different modifications of carbon, gold, platinum, silver, iridium, several alloys and amalgams etc. (Somerset *et al.*, 2010). The successful application of bismuth has therefore naturally led to investigation of other elements with similar properties such as antimony, gallium and tin (Hocevar *et al.*, 2007; Tyszczyk *et al.*, 2007; Economou *et al.*, 2005). Antimony is positioned above bismuth in group 15 of the periodic table, and is therefore a metalloid of more non-metallic character than bismuth. Both of them, and their alloys, are of interest because of their small effective mass and large mean-free length, which makes their nanostructures interesting for studying quantum confinement effects (Heremans *et al.*, 2000; Huber *et al.*, 2000). In addition, these nanomaterials are suggested to perform enhanced thermoelectric effect comparing with their bulk materials (Amy *et al.*, 2003; Joseph *et al.*, 2002). Recently, some studies involved the syntheses of antimony NPs. The synthesis was mainly based on the electrodeposition, the solvothermal, and self-assembled technique. However, it is still a challenge to develop a rapid technique to prepare antimony NPs. Antimony NPs can be manufactured using a facile electrochemical method. Bulk antimony electrode is dispersed under highly cathodic polarisation in different media at room temperature without the need for precursor ions or organic capping agents. The as-prepared antimony NPs have to be immediately transferred into Sb–Sb₂O₃ core–shell NPs during post treatment and characterisation as surface oxidation of antimony NPs by oxygen in the air occurs (Martin-Gonzalez *et al.*, 2003).

In adsorptive stripping voltammetry (AdSV) the metal ions must be converted into stable complexes with adequate surface-active ligands to be adsorbed on the working electrode by means of a non-electrolytic process prior to the voltammetric scan, and the detection limit of AdSV is also usually better than that of ASV (Arancibia *et al.*, 2012).

2.13. Nanoparticles characterisation techniques

One of the critical challenges faced currently by researchers in the nanotechnology and nanoscience fields is the inability and the lack of instruments to observe measure and manipulate the materials at the nanometre level by manifesting at the macroscopic level. In the past, the studies have been focused mainly on the collective behaviours and properties of a large number of nanostructured materials. Many great techniques are being used to characterise

nanocomposite. Characterisation is necessary to establish understanding and control of NPs synthesis and their applications. We discuss here some of the most important ones which are used on regular basis. Characterisation and manipulation of individual nanostructures require not only extreme sensitivity and accuracy, but also atomic-level resolution. It therefore leads to various microscopes that will play a central role in characterisation and measurements of nanostructured materials and nanostructures.

2.13.1. Optical Microscopes

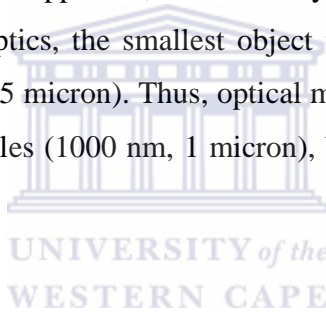
Optical spectroscopy has been widely used for the characterisation of nanomaterials, and the techniques can be generally categorised into two groups: absorption and emission spectroscopy and vibrational spectroscopy. For manipulation and imaging of nanoscale objects, optical microscopy has limited resolution since the objects are often smaller than the wavelength of the light. The achievable resolution for a wavelength (λ) is often given by the diffraction limit (δ). Optical systems of any kind that use lenses and mirrors to form an image are limited in their resolution, even with the best designs. The ability to make fine structural details is expressed in terms of numerical aperture (NA). The numerical aperture can be expressed as $n\sin\theta$, where n is the refractive index of the medium between the sample and the objective lens through which the light passes ($n_{\text{air}} = 1.00$; $n_{\text{water}} = 1.33$; $n_{\text{oil}} = 1.4$), and θ is the acceptance angle of the lens ($\sin\theta = 1$ if the angle is 90°). The limits of the objective lens are such that θ cannot be greater than 90 degrees, and the object space, even if filled with oil, can only reach a numerical aperture (NA) of 1.4. The resolving power of the light microscope is also limited by the wavelength of the light used for illumination. To explain this more, the resolving power of the optical system can be expressed as:

$$R = \frac{\lambda}{2NA} \quad (\text{Eqn. 2.1})$$

Where R is the distance between distinguishable points (nm), λ is the wavelength of the illumination source (nm), and NA is the numerical aperture of the objective lens. Reducing the wavelength from red to violet (700 to 400 nm) can improve the resolution, as can using an oil immersion lens ($n > 1$), but only so far. The optimal resolving power for a light microscope is obtained with ultraviolet illumination ($\lambda = 365$) if a system with the optimal NA is used (1.4). In this example, R is calculated to be 130.4 nm.

$$R = \frac{365}{2 \times 1.4}, R = 130.4 \text{ nm} \quad (\text{Eqn. 2.2})$$

Using ultraviolet light is one approach, but it is very expensive. In general, with optical microscopy, even with the best optics, the smallest object that can be measured using visible light is limited to about 500 nm (0.5 micron). Thus, optical microscopy can be used to determine the size of micrometer sized particles (1000 nm, 1 micron), but not nanoparticles (1 to 100 nm) (Poole and Owens, 2003).



2.13.2. Raman Spectroscopy

Raman spectroscopy is a vibrational technique and differs from the infrared spectroscopy by an indirect coupling of high-frequency radiation, such as visible light, with vibrations of chemical bonds. Raman spectroscopy is an analytical technique which operates in a same manner as other spectroscopic techniques as it also involves the interaction of molecules with light (or energy). However, in contrast to other spectroscopic techniques, Raman spectroscopy is concerned with the scattering of radiation by the sample rather than the absorption process. Similar to infrared spectroscopy, Raman spectroscopy is a useful technique in chemical industry as it provides structural information about the molecules based on the vibrational energy bands. This technique is based on the Raman Effect which is the result of inelastic light scattering. Raman spectrum is very sensitive to the lengths, strengths and arrangements of chemical bonds

in a material, but less sensitive to the chemical composition. When the incident photon interacts with the chemical bond, the chemical bond is excited to a higher energy state (Orhring, 1992).

2.13.3 X-Ray Diffraction (XRD)

XRD is a routine technique used by mineralogists and solid states chemists for characterisation of crystalline solids and determination of the structure. X-Rays are usually obtained by bombarding a metal target with a beam of high-voltage electrons inside a vacuum tube. Choice of the metal target and the applied voltage determines the output wavelength. X-Rays of a given wavelength are diffracted only for certain orientations of the sample. If the structures are arranged in an orderly array or lattice, the interference effects with structures are sharpened. The information obtained from scattering at wide angles describes the spatial arrangements of the atoms, while low angle X-Ray scattering is useful in detecting larger periodicities. X-Ray diffraction patterns of non-orientated polymers are characterised by rings. As the specimen is oriented, these rings break into arcs, and this structure reaches the relatively sharp patterns at high degrees of orientation. Due to its easiness and availability, this technique is commonly used to research the nanocomposite structures. However, the XRD can only detect the periodically stacked montmorillonite layers; disordered (not parallel stacked) or exfoliated layers cannot be detected, thus the only intercalated structures, where individual silicate layers are separated by 2-3 nm, give rise in XRD while others remain silent (Manias, 2001).

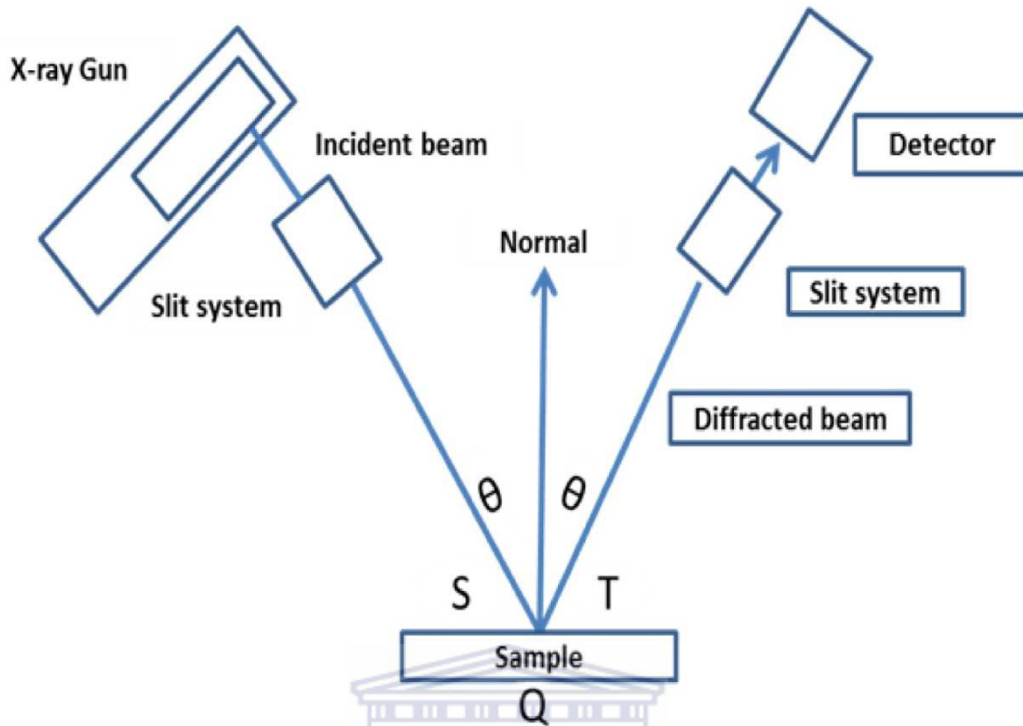


Figure 9. Schematic of general X-ray system (Fultz, 2013).

XRD measurements can characterise these structures if diffraction peaks are observed in the low-angle region, indicating the d-spacing of ordered-intercalated or delaminated nanocomposites. A schematic representation of the theory can be seen in Figure 9, where X-Ray beams of wavelength, λ , are incident on the planes of the layers at an angle, θ . These rays are scattered by atoms while constructive interference of them occur at the same angle, θ , to other planes. A whole number, n , of wavelengths are equal to the distance between SQ+QT. Angles of SQ and QT is 46 (Mitchell, 2004).

$$n\lambda = \overline{SQ} + \overline{QT} \quad (\text{Eqn. 2.3})$$

$$n\lambda = d_{nkl} \sin \theta + d_{nkl} \sin \theta \quad (\text{Eqn.2.4})$$

$$= 2d_{nkl} \sin \theta \quad (\text{Eqn. 2.5})$$

Equation 2.5 is known as Bragg's law, also n is order of reflection which may be any integer consistent with $\sin \theta$ not exceeding unity. Thus, we have a simple expression relating the x-ray wavelength and interatomic spacing to the angle of the diffracted beam (Mitchell, 2004).

2.13.4 Ultraviolet-Visible (UV-VIS) Spectroscopy

Ultraviolet visible spectroscopy (UV-VIS) spectroscopy offers a relative straightforward and effective way for quantitatively characterisation both organic and inorganic compounds. As it operates on the principles of absorption of photons that promotes the molecules to an excited state it is an ideal technique for determination of electronic properties such as band gap of material. UV-VIS can be performed on metal NPs dispersed in a solvent or embedded in an insulator matrix. The wavelength of the maximum absorption depends on the type, shape, size and the environmental surrounding of the NPs (Kreibig and Vollmer, 1995). Figure 10 gives a diagram representation of main parts of UV-VIS spectrophotometer. It should be noted that the strong UV-VIS absorption band observed for metal NPs are known as localised surface plasmon resonance is not present in the spectrum of their bulk metal counterparts (Mock *et al.*, 2003). Furthermore, size depending optical properties can also be observed in a UV-VIS spectrum, particularly in the nano and atomic scales. These include peak broadening or shifts of absorption wavelength. When the size increases the plasmon absorption maximum is normally shifted to longer wavelength as bandwidth increases. The size dependence resonance is useful phenomenon for sensing application (Kreibig and Vollmer, 1995).

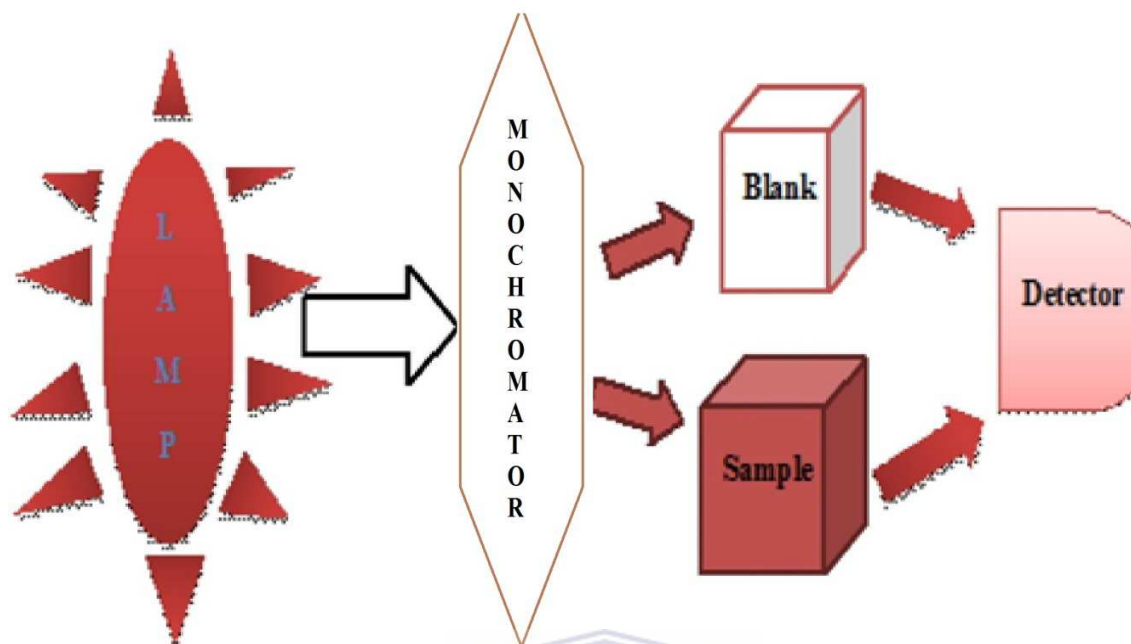
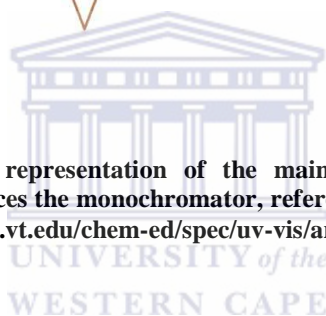


Figure 10. Simplified schematic representation of the main parts of UV-VIS spectrophotometer showing the light sources the monochromator, reference and sample holder and the detector (<http://www.files.chem.vt.edu/chem-ed/spec/uv-vis/array-spectrometer.html>).



2.13.5 Fourier transform infrared (FT-IR) Spectroscopy

Fourier transform infrared (FTIR) spectrometers have replaced dispersive instruments for most application due to their superior speed and sensitivity. They have greatly extended the capability of infrared spectroscopy and have been applied to many areas that are very difficult or nearly impossible to analyse by dispersive instruments. In FT-IR, all frequencies are examined simultaneously. It also allows valuation of infrared spectroscopy with far better resolution and signal to noise ratio than conventional spectroscopy. Infrared spectroscopy involves examination of the twisting bending, rotating and vibrational motions of atoms in a molecule. Molecules contain bonds of specific spatial orientation energy. These bonds are seldom completely rigid, and when is supplied, they may band, distort or stretch. A vary approximate model compares the vibration to that of a harmonic oscillator, such as an ideal spring (MacFarland and Van Duyne, 2003).

2.13.6 Electron Microscopy

Electron microscopes work on the principles similar to that of an optical microscope with the key difference that they use electrons and not photons as the source.

Limitation of resolving power by light microscopy can be modified and applied to the electron microscope by using De Broglie's formula. In 1924 Louis De Broglie suggested that the electron had a dual nature, with characteristics of a particle or a wave (Beaudry, 2010). The De Broglie wavelength, λ , for these “matter waves” is:

$$\lambda = \frac{h}{mv} \quad (\text{Eqn. 2.6})$$

In equation (6), h is Planck's constant (6.63×10^{-34} J s), m is the mass of the particle (9.11×10^{-31} kg for electrons) and v is the velocity in m s^{-1} . The wavelength of electrons in a beam produced from an electron gun can be computed from the accelerating potential, V , and the electron charge, e (1.60×10^{-19} C), using the classical expression:

$$E = Vxe = \frac{1}{2}(mv)^2 \quad (\text{Eqn. 2.7})$$

Therefore,

$$v = \left(\frac{2Ve}{m}\right)^{1/2} \quad (\text{Eqn.2.8})$$

Substituting into the DeBroglie equation and collecting all the constants (m , e , and h) for the wavelength gives:

$$\lambda = \frac{1.23}{\sqrt{v}} \text{ nm} \quad (\text{Eqn.2.9})$$

The equation above shows that the wavelength of an electron beam is a function of the accelerating voltage used. By increasing the accelerating voltage, a shorter wavelength is obtained. For an accelerating potential of 1 kV (1000 V), the wavelength associated with the electrons is 0.0388 nm, compared to the wavelength of violet light, about 400 nm. The shorter the wavelength the smaller is the limit of resolution of the microscope. Using such waves in a microscope results in a significant increase in resolution (Electron Microscope, 2001).

In the electron microscope accelerated electrons strike the object to be examined. Images are formed because the thicker portions of the sample absorb more of the electron stream than the thinner portions. Figure 11 illustrates a schematic interaction of the electron beam with the specimen.

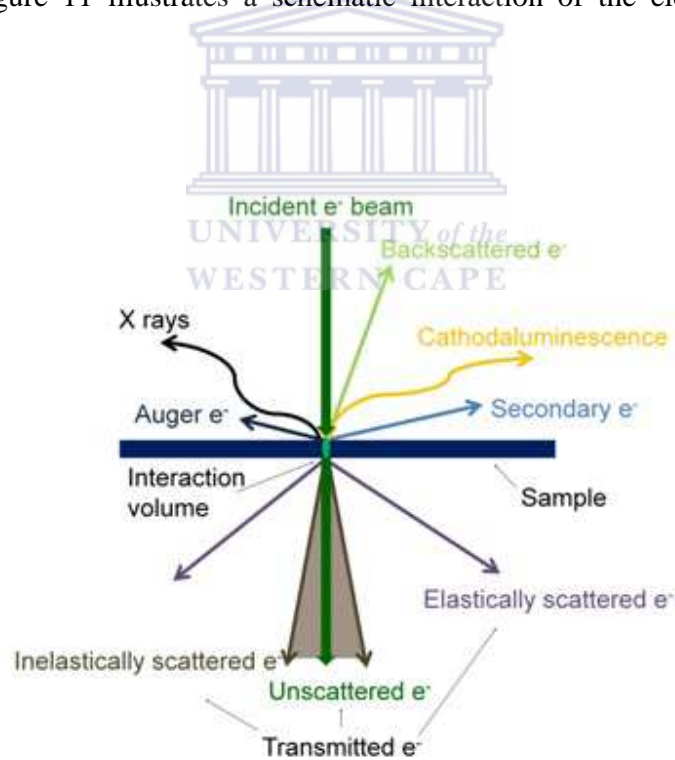


Figure 11. Interaction of the electron beam with the specimen. (<http://ncmn.unl.edu/cfem/microscopy/interact.shtml>).

2.13.6.1. Scanning Electron Microscopy (SEM)

Scanning electron microscopy (SEM) is a method for high-resolution imaging of surfaces. SEM comprise of cathode so called gun, which emits electrons, which in turn are being focused into a beam, and accelerated in the direction of the anode. With high enough voltage applied the velocity of electrons reaching anode can get to values close to the speed of light. Scanning electron microscope is also equipped with a system capable to deflect the beam in a controllable manner, making it possible to scan the surface of the studied material in pre-programmed fashion, and thus allow creating the resulting image line by line. The SEM uses electrons for imaging, like a light microscope which uses visible light. A finely focused electron beam scanned across the surface of the sample generates secondary electrons, backscattered electrons, and characteristic X-rays. These signals are collected by detectors to form images of the sample displayed on a cathode array tube screen. Scanning electron microscope typically is used for conductive samples.

SEM is one of the most widely used techniques in nanomaterials characterisation. This method is usually applied to get information about the grain size, surface roughness, porosity, particle size distributions, material homogeneity, and intermetallic distribution and diffusion (Bowman *et al.*, 1997). In scanning electron microscopy image is generated through analysis of the results of scattering of electronic beam on the surface of the studied sample. When formed and deflected beam hits the surface of the sample the results of these interactions is being recorded by the dedicated detector. After the interaction of the beam with the surface, several types of radiation can be generated: back scattered electrons, secondary electrons, X-rays and visible light. Back scattered electrons emission takes place when energy of the reflected electrons is almost identical to the energy of the beam electrons. Secondary electrons generation occurs when low energy electron is being emitted from the surface layer of the sample. Since the electrons are unable to flow through the sample the image produced from the data stored by the detector represents topography and composition of the surface only. In order to obtain higher quality images, the process is being carried out in the vacuum to prevent electrons from the beam from interacting with air. Scanning electron microscopy provides valuable information about the topography of the studied samples. Owing to that it was applied in this research for analysing various graphene antimony NPs based materials. Resolution of smaller objects can be provided

from electron microscopy, allowing direct observation of thin specimens, like single polymer crystals, and the electron diffraction patterns. It is carried out in the conditions of temperature well below the room temperature and source of accelerated voltages (higher than the usual 50000 – 100000V) in order to prevent of damage to single polymer crystals. In SEM, a fine beam electron is scanned across the surface of an opaque specimen. These photons are emitted when the beam hits to surface, then collected to provide a signal used to strengthen the intensity of the electron beam (Dunlap and Adaskaveg, 1997).

2.13.6.2. Energy Dispersive X-ray Spectroscopy (EDX)

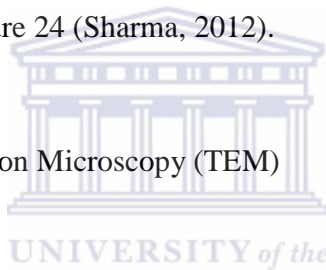
The ability to view three dimensional images of samples of interest does not always solve a problem in an analysis. Occasionally, further complimentary techniques are required to for example when there is a necessity to identify the different elements co-exists within the same sample. For such cases, a typically built in spectrometer called Energy Dispersive X-ray Spectrometer (EDS) will be extremely helpful. This is the most commonly x-ray spectroscopy microanalysis technique implemented in SEM or TEM. This non-invasive method is sometimes referred as EDS or EDAX analysis and used in conjunction with SEM or TEM but does not stand alone without the latter. It is a method that records the energy and intensity distributions of x-ray generated by the impact of electron beam on the surface of the sample and allow using that energy for qualitative and quantitative elemental analysis (Kirk and Hutchison, 2006).

To further explain, an electron beam hits a sample surface which will be pre-coated to make it conducting. The energy supplied by the electron beam is normally in the region of 10-20 kV. This energy supplies sufficient force for some electrons from the atoms on the sample surface to be knocked off. The vacation of electron from the atom inner shell then filled by the transfer of electrons from the atom outer shell. As the energy levels of the outer shell electrons are higher than that of the inner, the energy difference is then emitted as x-ray. During EDX analysis, the specimen is bombarded with an electron beam inside the scanning electron microscope. The bombarding electrons collide with the specimen atoms own electrons, knocking some of them off in the process. A position vacated by an ejected inner shell electron is eventually occupied by a higher-energy electron from an outer shell. To be able to do so,

however, the transferring outer electron must give up some of its energy by emitting an X-ray. Since that the every atom dissipates unique energy level for each electron transfer, identification of the atom from which the X-ray was emitted can be established (<http://www.nlectc.org/assistance/sem.html>).

The results from the EDX analysis is called EDX spectrum. In principle it shows a plot of frequency of x-ray emission has occurred for each energy level. As each peak is unique for each atoms, quantitative or qualitative analysis of element composition can be resolved. Higher peaks value simply means a higher concentration of the element. Not only that EDX is responsive towards the element according to each peak, it can also reveal the type of X-ray to which it corresponds as well. The interaction of the atom with an electron beam in a sample in EDX and the emitted X-rays have energies which are characteristic of the material from which they originate and therefore may be used to ascertain the chemical composition of a sample and can be represented in Chapter 3 as Figure 24 (Sharma, 2012).

2.13.6.3. Transmission Electron Microscopy (TEM)



Transmission Electron Microscopy(TEM) is a microscopy technique whereby a beam of electrons is transmitted through an ultra-thin specimen, interacting with the specimen as it passes through it. The energy of electrons in TEM determines the lateral spatial resolution and the relative degree of penetration of electrons in specific samples. In addition to the capability of structural characterisation, TEM has been explored for a wide range of applications in nanomaterials (Cao, 2004). This includes the determination of the crystal structure and lattice parameter of individual nanomaterials and the measurement of mechanical properties of individual nanotubes and nanowires (Wang, 2000). In most TEMs, the space for the sample holder is only about (5 mm) between the two objective lenses for the incoming and transmitted beam. Before reaching a CCD camera, the transmitted beam is sent through several magnification lenses to achieve the high magnification (500.000X is not unusual). The image formation in TEM can be based on several principles, but practically all images used in this work were made by phase contrast imaging, here called High Resolution Transmission Electron Microscopy (HRTEM). At sufficiently high brightness, electron sources can produce coherent

electron beams due to the point-like emitter surface area and small energy spread. The coherent electron beam can be considered as a spherical wave propagating from the emitter and out through the electron optical system, much like a laser beam would propagate through an optical system. The HRTEM images are based on the interference of the electron wavefront after it has passed through the sample and reach a CCD detector to give a phase contrast image of the sample (Reimer *et al.*, 1993).

2.13.6.4 Atomic Force Microscope (AFM)

Atomic Force Microscopy (AFM) is one of the most powerful tools for determining the surface topography of native molecules at subnanometre resolution. The AFM can be used to investigate any surface, even poorly or non-conducting ones, which broadens its potential applications significantly. The technique involves imaging a sample through the use of a probe, or tip, with a radius of 20 nm. The tip is held several nanometres above the surface using a feedback mechanism that measures surface–tip interactions on the scale of nano Newtons. Variations in tip height are recorded while the tip is scanned repeatedly across the sample, producing a topographic image of the surface (Butt *et al.*, 2005; Claesson, 1996). The instrument measures forces on a surface by scanning the sample with the tip attached to a flexible cantilever. The resolution obtained by AFM is determined in large part by the size of the probe tip used for imaging. The way the AFM operates is similar to the principle behind the record player in that the tip moves up and down in response to the surface features. An optical readout, or a piezoelectric crystal, translates the motion of the cantilever into an electronic signal.

Pyramidal or needle shaped silicon (Si) or silicon nitride (Si_3N_4) are the two main tips used in AFM. These probes have end radii of curvature as small as 10 nm but are often much larger (Van Cleef *et al.*, 1996; Sheng *et al.*, 1996). Advances are always being made to create a better tip, for example, SuperSharpSilicon™ tips are offering radii of typically 2 nm. The way in which image contrast is obtained in AFM can be achieved in many ways. The three main classes of interactions are contact mode, noncontact mode and tapping mode as seen in Figure 12. Contact mode, also known as repulsive mode, is the common method used in the AFM. The tip and sample remain in close contact while the scanning proceeds. One of the problems of remaining in contact with the sample is caused by excessive tracking forces applied by the probe

to the sample, which can damage the sample and distort image data. In noncontact mode the cantilever is oscillated in the attractive regime, meaning that the tip is quite close to the sample, but not touching it (Figure 12). Noncontact imaging generally provides low resolution, and it is a very difficult mode to operate with the AFM. Instead, the tapping mode can be used.

This technique allows users to obtain high resolution topographic imaging of sample surfaces that are easily damaged, poorly immobilized, or difficult to image by other AFM techniques. Tapping mode improves the AFM functionality by placing the tip in contact with the surface to provide high resolution and then lifting the tip off the surface to avoid dragging the tip across the surface. The advantage of the tapping mode technique is that it prevents the tip from sticking to the surface and causing damage during scanning. Another advantage of this technique is that the surface material is not pulled sideways by shear forces since the applied force is always vertical. One of the disadvantages of the tapping mode is that the tip-sample impact force in this mode is so great that it is destructive (<http://mrsec.wisc.edu/Edetc/index.html>).



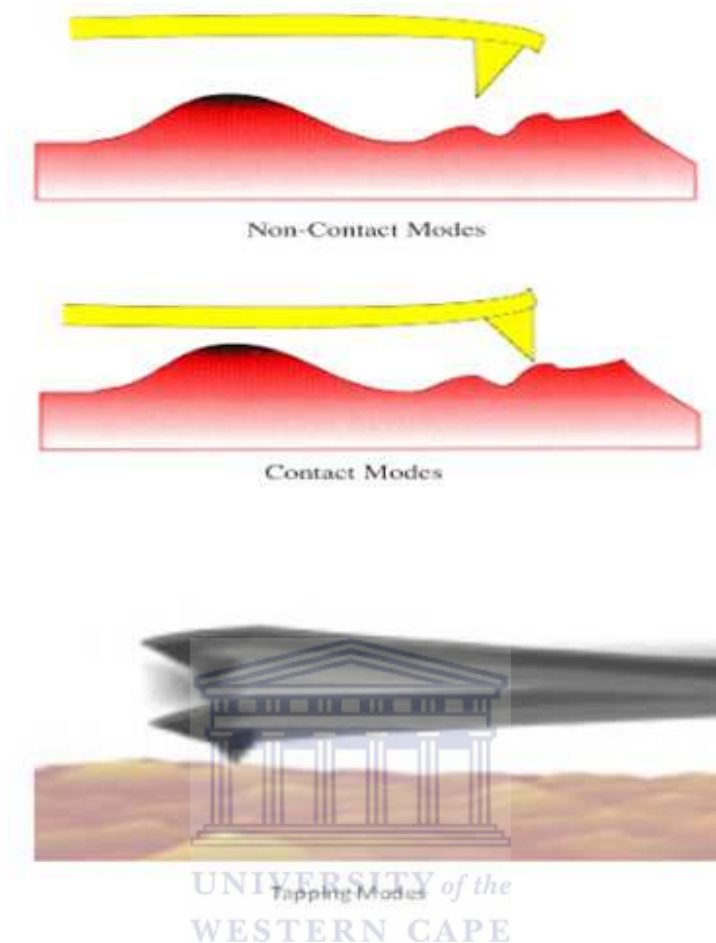


Figure 12. The three main classes of interactions in AFM (<http://spm.phy.bris.ac.uk/techniques/AFM/>, accessed November 2013).

2.13.7. Electrochemical Characterisation Processes

2.13.7.1. Electrochemical Impedance Spectroscopy (EIS).

The first publication of EIS dates to 1975 (Grieshaber *et al.*, 2008). Electrochemical impedance spectroscopy is a powerful method used to study electrochemical properties of systems and their interfaces with conductive electrodes (Krause, 2003, Brett, 1993; Westbroek *et al.*, 2005). EIS can be used in various applications, and this work focuses on its ability to characterise thin film formation and initially applied to the determination of the double-layer capacitance. Total

electrode impedance consists of the contributions of the electrolyte, the electrode solution interface and electrochemical reactions taking place on the electrode. The use of EIS tests to accompany other electrochemical results leads to a better understanding of the internal electrochemical processes.

Electrochemical impedance spectroscopy is a non –destructive material characterisation technique and is advantageous over other characterisation techniques due to it being economically favourable, simplistic, and portable, automated, provides time – dependent data and can operate in harsh environments. Impedance data can be graphically represented in two ways using Nyquist and Bode plot. The most widely used impedance data representation is the Nyquist plot or sometimes referred to as complex plane. Nyquist plot is the plot of the imaginary part (Z'') versus the real part (Z') of the impedance. Electrical equivalent circuits are used for the analysis of the impedance data, and within the circuit, simple electrical elements such as resistance (R) and capacitance (C) are connected to model the electrochemical process (Brett, 1993; Westbroek *et al.*, 2005). The resistance in the equivalent circuit represents the electrical conductivity of the electrolyte and the capacitance (double-layer capacitance) caused by the charge which is in excess at the electrode–electrolyte interface. The most widely used equivalent circuit for the analysis of the impedance data is the Randles equivalent circuit. During an impedimetric measurement, a frequency response analyser is used to impose an alternating current (AC) sinusoidal signal across a sample and the resulting current and voltage response is measured. The Randles equivalent circuit shows the solution or electrolyte resistance (R_E) connected in series to the parallel combination of charge transfer resistance (R_{ct}) and the double-layer capacitance (C_{dl}). In other systems the reaction rate might be controlled by transport phenomenon and this effect needs to be taken into consideration, the measured impedance can be explained by the component that depends on the conditions of transport or diffusion of electroactive species. This component is called Warburg impedance (Z_w) and is connected in series with the charge transfer resistance. Even though the Nyquist plot has been widely used for the graphic representation of impedance measurement, there is no indication of the frequency where the impedance was measured. Therefore, the use of different data representation of the impedance measurement which gives information about frequency where the impedance was measured is desirable. Bode plot is another form of impedance data representation which gives the frequency information at the measured impedance. Bode data representation is the plot of the

phase angle (θ) and the logarithm of impedance magnitude ($\log Z$) versus the logarithm of the frequency ($\log f$) as shown in Figure 32. Sometimes using Bode data representation one can plot the $\log Z'$ and $\log Z''$ versus $\log f$, and compare to Nyquist plot if both types of Bode plot are included all the information can be obtained for impedance measurements (Macdonald, 2006).

2.13.7.2. Cyclic Voltammetry (CV)

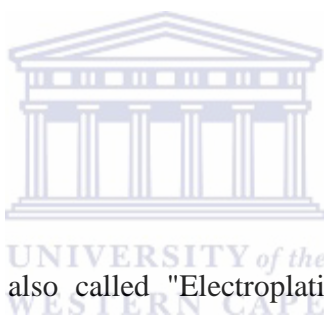
CV is a type of electrochemical measurement where the potential of the working electrode is ramped in a linear fashion versus time. After the end potential is reached, the potential is inverted. A cyclic potential sweep is imposed on an electrode and the current response is observed (Gosser, 1993). In a cyclic voltammogram, the current at the working electrode is plotted versus the applied potential. Depending on the analysis needed, one full cycle or a series of cycles is performed. The reduction or oxidation at the surface of the working electrode at a particular applied potential, results in mass transport of material to the electrode surface. The analytical advantages of cyclic voltammetry include a wide dynamic range, extreme sensitivity to low concentrations of ionic species, ease of use, and are a non-destructive method for characterising electron transfer mechanisms.

Cyclic voltammetry can be used to provide qualitative data on the system of interest, including kinetics of heterogeneous electron transfer, thermodynamics of a redox process, of coupled chemical reactions and of adsorption processes. Cyclic voltammetry can be particularly useful in the diagnostics of non ideal systems, such as those where the redox reaction is slow or coupled with a chemical reaction. The cyclic voltammetric technique entails a linear increase of potential to a particular switch potential where the voltage is changed back linearly to the starting value. A diagram of current generated versus the potential (voltammogram) can be plotted and used to identify the redox potential of the electroactive components and whether the redox reactions are reversible (Skoog *et al.*, 1996). The cyclic voltammogram shows characteristics of an analyte by several important parameters such as peak currents and peak potentials that can be used in the analysis of the cyclic voltammetric response either the reaction is reversible, irreversible or quasi-reversible as listed in Table 4.

Table 4. The characteristics of different type of electrochemical reaction (Adapted from Birke *et al.*, 1981).

Type of reaction	Characteristics
Reversible	<p>Cathodic and anodic peak potential are separated by $59/n$ mV.</p> <p>The position of peak voltage does not alter as a function of voltagescan rate.</p> <p>The ratio of the peak current is equal to one.</p> <p>The peak currents are proportional to square root of the scan rate.</p> <p>The anodic and cathodic peaks are independent of the scan rate.</p>
Irreversible	<p>Disappearance of a reverse peak.</p> <p>The shift of the peak potential with scan rate (20 – 100 mV/s).</p> <p>Peak current is lower than that obtained by reversible reaction.</p>
Quasi-reversible	<p>Larger separation of cathodic and anodic peak potential. ($> 57/ n$ mV) compared to those of reversible system.</p>

2.14. Thin Film Deposition



2.14.1. Electrodeposition

Electrodeposition is often also called "Electroplating", and the two terms are used interchangeably. As a matter of fact, "electroplating" can be considered to occur by the process of electrodeposition. This process involves: (i) oriented diffusion of charged growth species (typically positively charged cations) through a solution when an external electric field is applied, and (ii) reduction of the charged growth species at the growth or deposition surface which also serves as an electrode. In general, electrochemical deposition is only applicable to electrical conductive materials such as metals, alloys, semiconductors and electrical conductive polymers. After the initial deposition, the electrode is separated from the depositing solution by the deposit and the electrical current must go through the deposit to allow the deposition process to continue. Electrochemical deposition is widely used in making metallic coatings usually metallic, on a surface by the action of electric current (Mohammedi *et al.*, 2009; Salimi *et al.*, 2008). The deposition of a metallic coating onto an object is achieved by putting a negative charge on the object to be coated and immersing it into a solution which contains a salt of the metal to be deposited (in other words, the object to be plated is made the cathode of

an electrolytic cell). The metal cations of the salt carry a positive charge and are thus attracted to the object. When they reach the negatively charged object (that is to be electroplated), it provides electrons to reduce the positively charged ions to metallic form. Figure 13 is a schematic presentation of an electrolytic cell for electroplating a metal "M" from an aqueous (water) solution of metal salt "MA" (<http://electrochem.cwru.edu/ed/encycl/>).

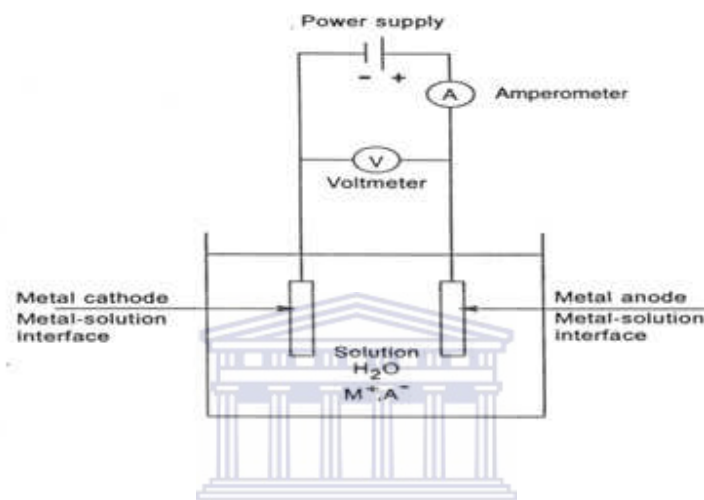


Figure 13. Schematics of an electrolytic cell for plating metal "M" from a solution of the metal salt "MA" (<http://electrochem.cwru.edu/ed/encycl/>).

2.14.2. Sol gel deposition and Spin Coating

In simple terms sol-gel processing involves the transition from a sol (very finely divided solid particles dispersed in a liquid which will not settle out) to a gel (a dispersion of a liquid throughout a solid matrix). It is a long-established process with the key controlling processing steps being sol formation and gelling, drying, curing and sintering. Starting materials used in the preparation of the sol are usually inorganic metal salts or metal organic compounds such as metal alkoxides. Typically, the precursor is subjected to a series of hydrolysis and polymerisation reactions to form a colloidal suspension. This suspension can be further processed to make materials in different forms from thin films and aerogels to nanocomposites and NPs. Typical sizes of NPs produced by this method are 5–30 nm (Walt, 2002; Zarzycki, 1997).

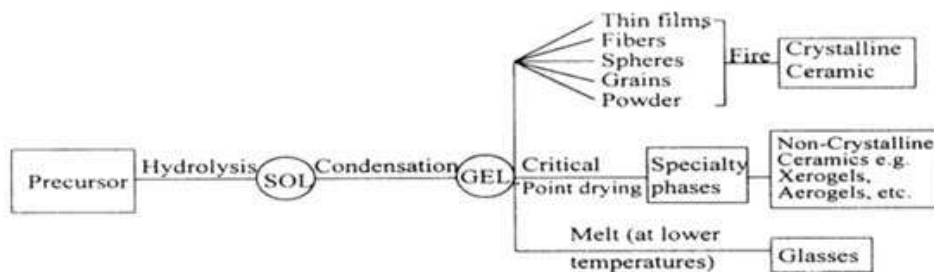


Figure 14. Schematics of a sol gel deposition technique (Mehrotra, 1992).

2.14.2.1. Steps in sol gel process

Prior to sol-gel transition or gelation, sol is a highly diluted suspension of nanoclusters in a solvent, and typically sol-gel films are made by coating sols onto substrates. Although some methods are available for applying liquid coatings to substrates, the best choice depends on several factors including solution viscosity, desired coating thickness and coating speed. Most commonly used methods for sol-gel film deposition are spin and dip-coating. The sol-gel process is a wet-chemical technique used for the fabrication of both glassy and ceramic materials (Brinker). In this process, the sol (or solution) evolves gradually towards the formation of a gel-like network containing both a liquid phase and a solid phase. The first patent based on sol-gel processing was granted to Jenaer Glaswer Schott and Gen (1939) for silicate sol-gel films formed by dip coating (Huang *et al.*, 2000). Coatings for rear-view mirrors and anti-reflective and architectural applications have been in commercial production since the 1960s. Today, sol-gel thin film coatings are used extensively for such diverse applications as protective and optical coatings, passivation and planarisation layers, sensors, high or low dielectric constant films, inorganic membranes, electro-optic and nonlinear optical films, electrochromics, semiconducting anti-static coatings, superconducting films, strengthening layers and ferroelectrics. The sol-gel technique offers a low-temperature method for synthesising materials that are either totally inorganic in nature or both inorganic and organic. Several methods can be used to make sol-gel

coatings with the sol-gel process. Spin coating and dip coating are two basic techniques used to deposit sol-gel coatings. Drop casting and spin coating are the easiest and most widely used methods (Torrey *et al.*, 2015).

2.14.2.1.1. Spin Coating

In the case of spin-coated layers, the rotational speed and angular acceleration of the sample during the deposition are also important parameters. Spin coating is used for many applications where relatively flat substrates or objects are coated with thin layers of material. For example, several cathode ray tube (CRT) manufacturers use the spin coating method to make anti-glare or anti-reflection coatings. In spin coating, the material to be made into coating is dissolved or dispersed into a solvent, and this coating solution is then deposited onto the surface and spun off to leave a uniform layer for subsequent processing stages and ultimate use. Example is the modification of indium tin oxide substrate with xerogel oxide film by spin coating a viscous gel (Wang *et al.*, 1989). There are four key stages in spin coating:

- Stage 1: The deposition of the coating fluid onto the substrate
- Stage 2: Aggressive fluid expulsion from the substrate surface by the rotational motion
- Stage 3: Gradual fluid thinning
- Stage 4: Coating thinning by solvent evaporation.

The coating thickness is inversely proportional to the square root of the rotation speed: thickness $\sim [1/\text{speed}]^{1/2}$. In addition, the coating solution properties (such as viscosity and liquid density) also affect coating thickness. Some spin coating systems are specifically designed for depositing scratch resistant coatings on ophthalmic lenses. These systems have multiple functions, including cleaning, providing the solution, spin coating and curing (either thermal or

ultraviolet). The temperature and atmosphere in the chamber environment can be precisely controlled to ensure high quality results (Figure15).

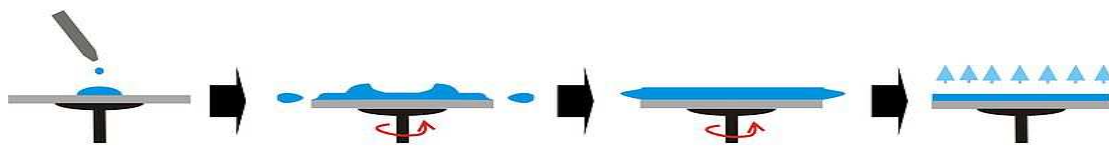


Figure 15. The four stages of spin coating (Raut *et al.*, 2011).

2.14.2.1.2. Dip Coating



Dip coating is a process where the substrate to be coated is immersed in a liquid and then withdrawn with a well-defined withdrawal speed under controlled temperature and atmospheric conditions (Abbaspour *et al.*, 2009). Vibration-free mountings and very smooth movement of the substrate is essential for dip systems. An accurate and uniform coating thickness depends on precise speed control and minimal vibration of the substrate and fluid surface. The coating thickness is mainly defined by the withdrawal speed, the solid content and the viscosity of the liquid. If the withdrawal speed is chosen such that the shear rates keep the system in the Newtonian regime, the coating thickness can be calculated by the Landau-Levich equation:

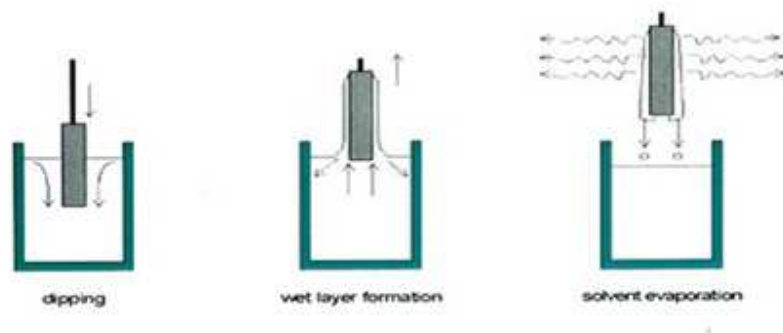
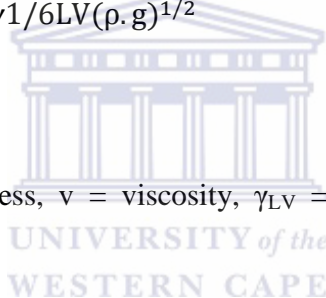


Figure 16. The schematics of a dip coating process (Attia *et al.*, 2002).

$$h = 0.94 \cdot \frac{(\eta \cdot V)^{2/3}}{\gamma^{1/6} LV (\rho \cdot g)^{1/2}} \quad \text{Eqn. 2.10}$$

Where h = coating thickness, v = viscosity, γ_{LV} = liquid-vapor surface tension, ρ = density, g = gravity.



2.14.2.1.3. Drop casting

Drop casting and spin coating are the easiest and most widely used methods for NP film deposition. This method is a major technique used in this study because of its simplicity, and advantage of setting a constant deposition potentials which guides against variation in the amount of nanomaterials. A solution containing organic semiconducting materials is dropped in a controlled fashion on an, ideally, horizontal substrates can be seen in Figure 17. When a solution of NPs is spread on a solid substrate by drop casting or spin coating, long-range dispersion forces between the NPs or between the NPs and the substrate cause the NPs to self-organise into mono- or multilayer structures when the solvent evaporates (Andres *et al.*, 1996). Drop-cast films typically exhibit well-packed NP domains with domain sizes ranging from a few hundred

nanometres to several micrometers. Domain sizes have been shown to depend on NP size distribution, NP concentration, and solvent dewetting or volatility. Drop casting is a technique that allows for creating thick organic films. However, there is minimal control over the thickness of resulting organic films, which is a major disadvantage of this technique.

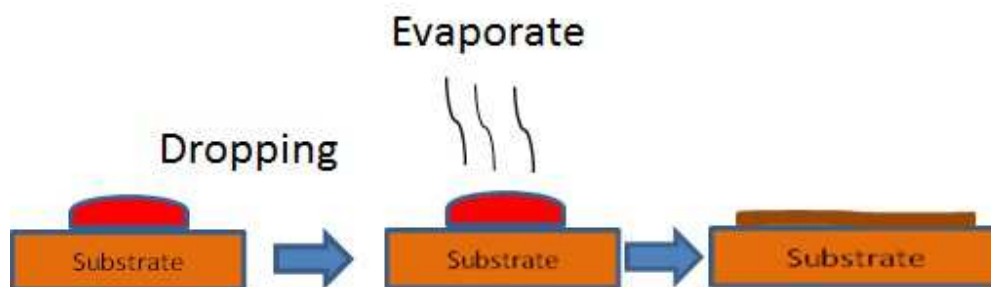


Figure 17. The schematics of a drop casting process (Adapted from Neogi *et al.*, 2014).

2.15. Adsorption at Electrode Surfaces

Adsorption is the binding of species from the solution phase to the electrode surface. The adsorbates may be atoms, ions, molecules, reactant, intermediate, or product of the electrode reaction regardless of whether they are organic or inorganic in their nature (Figure 18). In addition to covalent bonding-based technique, adsorption can also occur by means of electrostatic forces. This can be achieved if the electrode surface is electrostatically charged with either positive or negative which eventually attracts ions or dipoles with opposite charge to it. The accumulation species with counter charge enable adsorption via electrostatic method to be achieved. Whatever they are, adsorbates do affect the reaction rate as well as the mechanism involved at the electrode of interest. Adsorption of both organic and inorganic species involving either ions or even neutral molecules can occur at the electrode surface and in variety of environments (Bard and Faulkner, 2001).

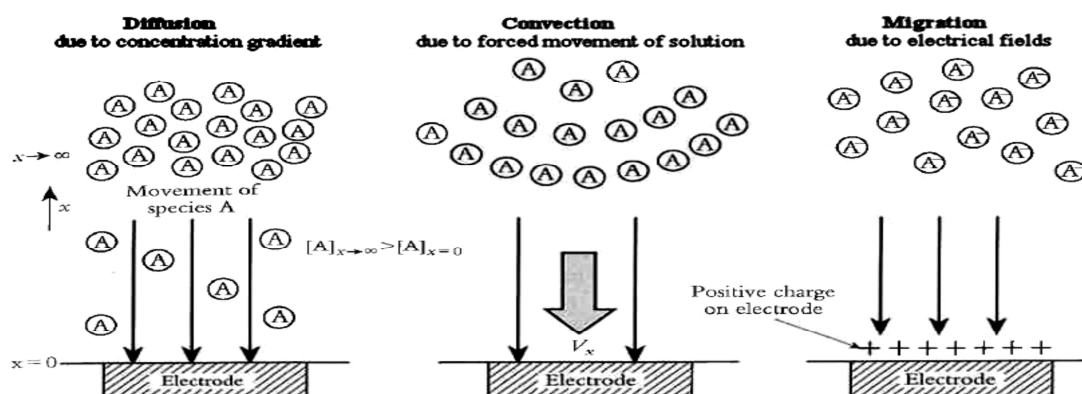


Figure 18. Three different forms of mass transport for electroactive species in solution to the electrode surface (Bard and Faulkner, 2001).

2.16 Environmental Pollution with Heavy Metals

Environmental problems related to metal ion pollution have a long history. Certain events in the past have induced government to address these problems in their environmental policy. As the results, the emissions from point sources have been reduced significantly over the past decades in many countries. Metals are considered as important toxic pollutants and there is extensive literature concerning their accumulation in ecosystems. Metals are continuously released into the biosphere by volcanoes, natural weathering of rocks but also by numerous anthropogenic activities, such as mining, combustion of fuels, industrial and urban sewage and agricultural practices. Heavy metals in the environment have the potential to contaminate soil and water, and they are characterised by relatively high stability and solubility in atmospheric precipitations (Lim *et al.*, 2008). Their high non-biodegradability and accumulation in human and animal organisms results in various diseases, genetic disorders, and deleterious ecological effects (Attar *et al.*, 2014). Figure 19 illustrates the complexity of metal release, precipitation and adsorption processes.

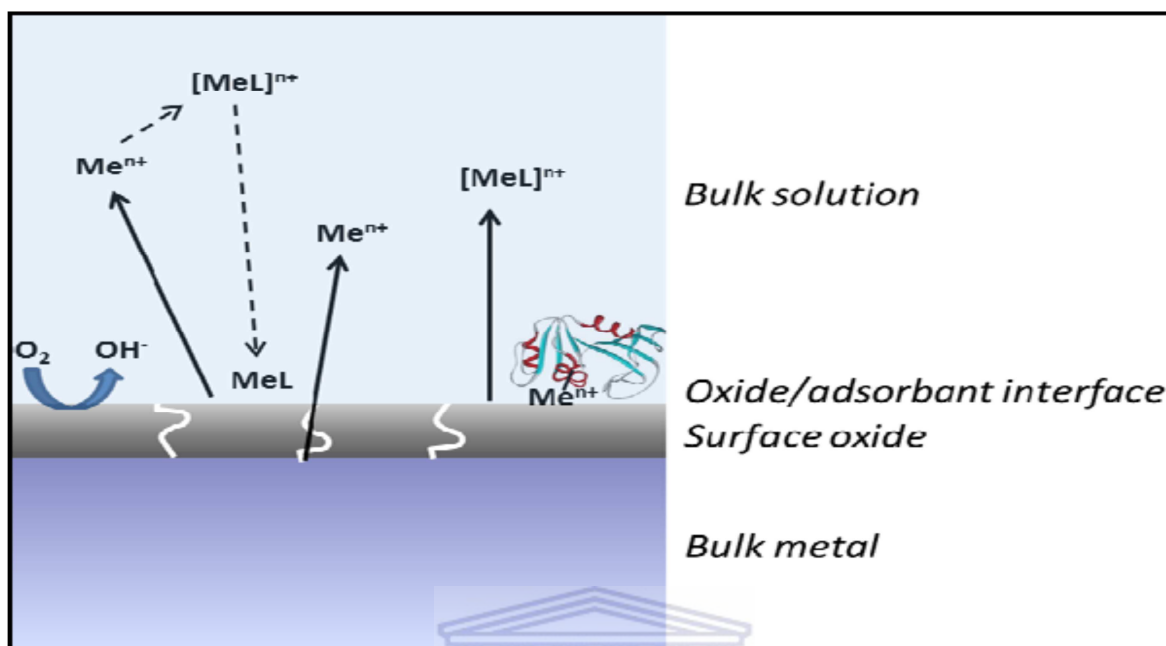


Figure 19. Schematic overview over metal release, precipitation and adsorption processes (Hedberg, 2010).

Metal (Me) can be released via many pathways, *i.e.* bulk corrosion (enabled by surface oxide defects), chemical or electrochemical dissolution of the surface oxide, complexation of surface metal atoms by ligands (L), such as complexing agents (e.g., citric acid) or proteins, and subsequent detachment of any metal complexes into the bulk solution. Within the bulk solution, any free or weakly complexed metal ions can complex to any free ligands and in some cases (often time dependent) precipitate as solid complexes, e.g. iron phosphates or carbonates. In special cases, precipitation is the dominant process as illustrated for released Fe into surface water solutions of pH 6 and 8 and different salt concentration in the licentiate thesis (Hedberg, 2010). On a global scale there is now abundant evidence that anthropogenic activities have polluted the environment with heavy metals from the poles to the tropics and from the mountains to the depths of the oceans. According to UNEP/GPA (2006a), an increasingly serious global problem is the management of electronic waste (e-waste), particularly the disposal of used computers and mobile phones, which contain over 1000 different materials, many of which are toxic to human (UNEP/GPA, 2006a). Monitoring of environmental pollution in the field requires

portable fast-response sensors that are robust and with sufficient sensitivity and long lifetime (Wang *et al.*, 2008). Due to increasing demand of the toxicity of these metals in soil, environmental companies and pollution monitoring agencies have expressed the need for reliable approved procedures for the determination of these elements (Farrel-Poe, 2000). Heavy metals are well known to inhibit the activity of enzymes and application of this phenomenon to the determination of these hazardous toxic elements offers several advantages such as simplicity and sensitivity (Rodriguez-Mozaz *et al.*, 2006). The analysis of heavy metal ions in environmental samples remains a challenging task since these metals ions are present at very low levels in the samples with some sample matrices being very complex in nature (Somerset *et al.*, 2009).

The world-wide emissions of metals to the atmosphere (thousands of tons per year) by natural sources is estimated as: Ni: 26, Pb: 19, Cu: 19, As: 7.8, Zn: 4, Cd: 1.0, Se: 0.4, (tx10³.yr⁻¹). Whereas, from anthropogenic sources: Pb: 450, Zn: 320, Ni: 47, Cu: 56, As: 24, Cd: 7.5, Se: 1.1 (thousand t yr⁻¹). It is obvious from these numbers that Pb, Zn, Ni and Cu are the most important metal pollutants from human activities. Metals are separated into the essentials and non-essentials in classes A and B, and in a borderline class².

A: Calcium (Ca), Magnesium (Mg), Manganese (Mn), Potassium (K), Sodium (Na), Strontium (Sr)

B: Cadmium (Cd), Copper (Cu), Mercury (Hg), Silver (Ag)

Borderline: Zinc (Zn), Lead (Pb), Iron (Fe), Chromium (Cr), Cobalt (Co) Nickel (Ni), Arsenic (As), Vanadium (V), Tin (Sn) (Clark *et al.*, 1997).

2.17. Behaviour of Heavy Metals in Soil

2.17.1. Bioaccumulation

Heavy metals are dangerous because they tend to bioaccumulate in biota. This means that the concentration of a chemical in a biological organism becomes higher relative to the environmental concentration (Kampa and Castanas, 2008). Heavy metal pollution of soil enhances plant uptake causing accumulation in plant tissues and eventual phytotoxicity and

change of plant community (Gimmler *et al.*, 2002). In environments with high nutrient levels, metal uptake can be inhibited because of complex formation between nutrient and metal ions (Gothberg *et al.*, 2004). Therefore, a better understanding of heavy metal sources, their accumulation in the soil and the effect of their presence in water and soil on plant systems seems to be a particularly important issue (Sharma *et al.*, 2004). Accumulation of heavy metals can also cause a considerable detrimental effect on soil ecosystems, environment and human health due to their mobilities and solubilities which determine their speciation (Kabata-Pendias, 1992). The soil to plant transfer factor is one of the important parameters used to estimate the possible accumulation of toxic elements, especially radio nuclides through food ingestion (El-Ghawi *et al.*, 2005). The toxicology and carcinogenicity of many heavy metals is another important environmental concern of the scientific community. Beside a direct intake via soil particles or air, the main pathway of heavy metal intake by human beings is via the food chain (Peralta-Videa *et al.*, 2009).

The extent of bioaccumulation of metals is dependent on the total amount, the bioavailability of each metal in the environmental medium and the route of uptake, storage and excretion mechanisms. The requirements of different organisms for essential metals vary substantially but optimal concentration ranges are narrow and frequently under careful homeostatic control. Excess metal concentration in an organism must be actively excreted, compartmentalised in cells or tissues, or metabolically immobilised. Some metal escape all these actions causing toxic and other adverse effects (Chapman *et al.*, 1996). Metals in the aquatic environment can bioaccumulate into organisms or biota either passively from water or by facilitated uptake. Evaluation of metal concentrations in biological systems must take into account certain other factors, such as temperature, redox conditions (dissolved oxygen concentration), ionic strength, organic complexation, concentrations of metal and ligand species that compete for uptake sites, pH, general physiologic behaviour, life cycle and life history (McKenna *et al.*, 1993). The equation that enables the calculation of the bioaccumulation ratio (BAR) of a contaminant (z) and has been defined as follows (Somerset *et al.*, 2015, Ferguson and Chandle, 1998; Mackay and Fraser, 2000; Ruus *et al.*, 2005):

$$BAR_z = \frac{C_{organism,pollut.}}{C_{organism,controlled}} \quad (\text{Eqn. 2.11})$$

With z being defined as a specific contaminant (pollutant), where $[C_{organism,pollutant}]$ the mean concentration of the pollutant (z) in the organism exposed to the contaminated sediment (pollutant) $[C_{organism,controlled}]$ the mean concentration of the pollutant (z) in the organism exposed to control sediment or sediment collected at a controlled site.

2.17.2. Solubility and Mobility

Among the negative impacts related to human activities, the mobilisation of heavy metals from their natural's reservoirs to the aquatic and terrestrial ecosystems has become a generalised problem almost worldwide (Han *et al.*, 2002; Koptsik *et al.*, 2003). Heavy metal solubility and mobility in soils are of environmental significance due to their potential toxicity to both humans and animals (Chirenje *et al.*, 2003). The transfer and the chemical stability of metal contaminants in soils and sediments are controlled by a complex series of biogeochemical processes depending on variables like pH, clay content and redox potential (Vanbroekhoven, 2006). Trace metal mobility is closely related to metal solubility, which is further regulated by adsorption, precipitation and ion exchange reactions in soils (Ma and Dong, 2004). The transfer of heavy metals from soils to plants is dependent on three factors: the total amount of potentially available elements (quantity factor), the activity as well as the ionic ratios of elements in the soil solution (intensity factor), and the rate of element transfer from solid to liquid phases and to plant roots (reaction kinetics). However, changes in soil solution chemistry, such as pH, redox potential and ionic strength, may also significantly shift the retention processes of trace metals by soils (Gerringa *et al.*, 2001). Reduction in redox potential may cause changes in metal oxidation state, formation of new low-soluble minerals, and reduction of Fe, resulting in release of associated metals. Metal solubility usually increases as the pH decreases, with the notable exception of metals present in the form of oxyanions or amphoteric species (Baumann *et al.*, 2002; Chuan *et al.*, 1996).

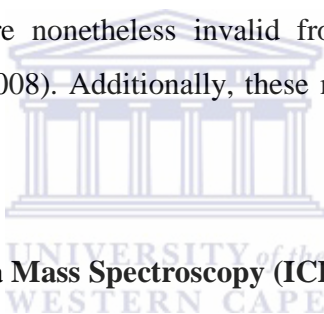
2.18. Environmental concerns

Ecotoxicologists and Environmental Scientists use the term “heavy metals” to refer to metals that have caused environmental problems. The metals which have been studied extensively the last decades are: Cd, Hg, Zn, Cu, Ni, Cr, Pb, Co, V, Ti, Fe, Mn, Ag and Sn (Tin). Some metals that have received more attention are Hg, Cd, and Pb, because of their highly toxic properties and their effects on the environment and the living organisms. Some metals such as Cr, As, Se, and Hg can be transformed to other oxidation states in soil, thus influencing their mobility and toxicity (McLean and Bledsoe, 1992). Many of these metals (eg. Hg, Cd, Ni, Pb, Cu, Zn, Cr, Co) are highly toxic both in elemental and soluble salt forms. High concentration of heavy metals in soils is toxic for soil organisms: bacteria, fungi and higher organisms (Woolhouse, 1993). In recent years, concerns have risen about the side effects of these compounds due to their intentional or accidental release in the environment. After the industrial revolution and the increase in chemical technologies, concerns for minimisation of pollutants and alternative “clean technologies”, have become the common European Union (EU) strategy. The whole control process started with tighter environmental legislation that were introduced in order to minimise the release of harmful pollutants either having immediate affects or long term ones. As a consequence from the chemical release, there is an increase of contaminated sites that need to be sampled. The medium that interests researchers inside and outside EU countries focuses on drinking water, air, groundwater, river water, seawater and soil. Different methods are usually required for the preparation of samples from such matrices, including extraction techniques and analysis (Grasselli, 1992).

2.19. Methods of Detection for Heavy Metals

In this section various methods for metal determination will be summarised. ICP-AES or MS and stripping voltammetry will be discussed in detailed. Some metal analysis methods can be applied directly to solid samples such as X-ray fluorescence (XRF), instrumental neutron activation (INAA) or direct current arc atomic emission spectroscopy (DCAAS). Most trace

level methods incorporate an aqueous extraction scheme (or organic extraction where the metal is complexed with organics). The extraction serves to separate the analyte of interest from the bulk sample and to help homogenise the analyte speciation for analysis. These methods include, flame, graphite furnace, cold vapour and hydride generation modifications of atomic absorption spectroscopy (FAAS, GFAAS, CVAAS, HGAAS, respectively), and also, inductively coupled plasma atomic emission spectroscopy (ICP-AES) and inductively coupled plasma mass spectroscopy (ICP-MS) (Alloway *et al.*, 1990, Fifield and Haines, 2000). Although the majority of applications can be satisfied by the use of ICP-MS and/or ICP-OES, expert trace metals chemists recognise that alternative procedures are required at times to satisfy unusual analytical challenges. Careful examination of each application must be done from a quality assurance perspective. There are situations when multi-element techniques that utilise the plasma as an ion source or light emission source are capable of producing values that appear to be valid from a quality control standpoint, but are nonetheless invalid from a quality assurance standpoint (Lewen *et al.*, 2004; Lira *et al.*, 2008). Additionally, these methods cannot be used for on-line and on-site field monitoring.



2.19.1. Inductive Coupled Plasma Mass Spectroscopy (ICP-MS)

ICP-MS is an atomic emission spectroscopic technique that uses plasma for atomization process. Plasma contains a remarkable fraction of electrons and positive ions which cancel out as well neutral molecules. The plasmas consist of highly energetic and ionised gases which are produced in inert gases like argon. They are useful for dissociation of atoms as well as excitation and ionisation to give atomic and ionic emissions. When compared to atomic absorption spectroscopy (AAS), ICP gives better detection limit but need highly skilled personnel to operate and extensive sample preparation. The major disadvantage of all spectroscopic method is that they provide no information on the oxidation state of an element or its speciation (Khopkar, 2009). ICP-MS can be applied to measure traces of nearly most of the elements in the periodic table and it is an extremely powerful analysis method for metal and non-metallic elemental measurements (Wuilloud and Altamirano, 2006; Hirner, 2006). The combinations of low detection limit, lower than part per trillion (ppt), and the short measurement time make it suitable

for many fields in both research and applied science and superior to other types of elemental analysis instruments such as atomic absorption spectrometer (AAS) and inductively coupled plasma –optical emission spectrometer (ICP-OES) (Ammann, 2007; Nelms, 2005; Thomas, 2004; Ray *et al.*, 2004; Moldovan *et al.*, 2004; Montaser, 1998). Examples of the fields where ICP-MS has been applied include environmental (Butler *et al.*, 2011), biomedical, forensic (Ulrich *et al.*, 2004), food industry, life sciences (Bettmer *et al.*, 2006) and many more. Samples used for ICP-MS analysis can be any state liquid, solid or gas.

2.19.2 Voltammetry

Electro-analytical methods are widely used in scientific studies and monitoring of industrial materials and the environment. One of the most widespread electro-analytical methods is voltammetry. Voltammetry is an electrochemical technique that is based on the measurement of the current response to an applied potential. It is a branch of electrochemistry in which the electrode potential, or the faradaic current or both are changed with time. Normally, there is an interrelationship between all three of these variables (Bond *et al.*, 1989). The principle of this technique is a measurement of the diffusion controlled current flowing in an electrolysis cell in which one electrode is polarisable (Fifield and Kealey, 2000). The current is proportional to the metal concentration in the sample. We apply a time-dependent potential to an electrochemical cell and measure the resulting current as a function of that potential. We call the resulting plot of current versus applied potential a voltammogram, and it is the electrochemical equivalent of a spectrum in spectroscopy, providing quantitative and qualitative information about the species involved in the oxidation or reduction reaction.

The earliest voltammetric technique is polarography, developed by Jaroslav Heyrovsky in the early 1920s, an achievement for which he was awarded the Nobel Prize in Chemistry in 1959. Since then, many different forms of voltammetry have been developed. This technique can measure any chemical species that is electroactive (Wang, 2000). Voltammetry has been an important and widespread analytical technique. Since 1950 to 1980 it was the dominating analytical method for the determination of several important trace metals and important organic compounds (Barek *et al.*, 2001a). Although the range of organic and inorganic compounds that can be measured by voltammetry is very broad, the major type of application is analysis of metal

ions (Buffle and Tercier-Waeber, 2000; Buffle and Tercier-Waeber, 2005). Some of the most important voltammetric techniques are briefly reviewed in the following subsections.

Nowadays, voltammetry unite large number of instrumental techniques such as anodic stripping voltammetry (ASV), cathodic stripping voltammetry (CSV), adsorbed voltammetry (DPAV), and differential pulse anodic stripping voltammetry (DPASV), which due to its large sensibility more and more suppresses classic techniques. One of the most important voltammetry appliances in environment analysis is for speciation testing. Speciation analysis is defined as determination of concentration of different chemicals forms of elements that make up the total concentration in sample. Since toxicity of every metal ion depends on physical – chemical form and that the most toxic form of metal ion is hydrated or free metal ion, it is important to do the chemicals peciation (Dube *et al.*, 2001).

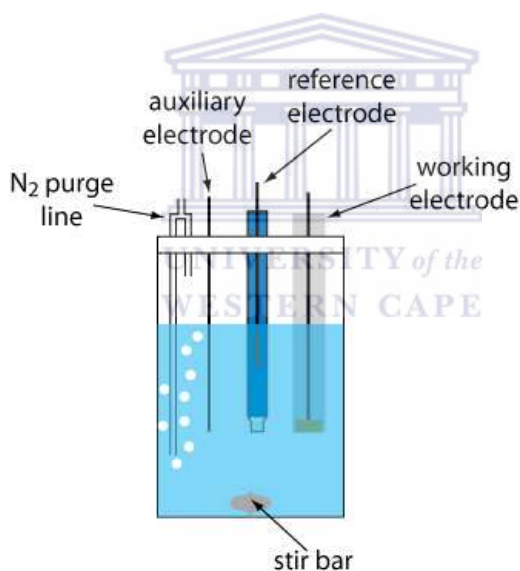


Figure 20. Schematic representations of standard three electrodes set up (Harvey, 2013).

2.19.2.1 Stripping voltammetry

Stripping analysis is a very sensitive electrochemical technique for measuring trace metals. Stripping analysis is a two-step technique. The first step involves the electrolytic

deposition of a small portion of the metal ions in solution onto the electrode surface to pre-concentrate metals. This is followed by the stripping (the measurement) step of the deposit, which involves the dissolution (stripping) of the deposit. Since the metals are pre-concentrated into the electrode by factors of 100 to 1000, detection limits are lowered by 2-3 orders of magnitude compared to solution-phase voltammetric measurements (Wang, 2000). Most stripping measurements require the addition of appropriate supporting electrolyte and removal of dissolved oxygen. The former is needed to decrease the resistance of the solution and to ensure that the metal ions of interest are transported toward the electrode by diffusion and not by electrical migration. Contamination of the sample by impurities in the reagents used for preparing the supporting electrolyte is a serious problem. Dissolved oxygen severely hampers the quantitation and must be removed. The pre-concentration (or accumulation) step can be adsorptive, cathodic or anodic. Beside the classic anodic stripping voltammetry, used for the determination of metals forming amalgam with mercury, adsorptive stripping voltammetry has also appeared and the application of modified electrodes has widely spread (Wang, 2000).

2.19.2.2 Anodic stripping voltammetry (ASV)

The term ASV is applied to the technique in which metal ions are accumulated by reduction at a hanging mercury drop electrode (HMDE) held at a suitable negative potential. The deposition potential is usually 0.3 to 0.5 V more negative than a standard potential for reduced metal ion to be determined. It is the most widely used form of stripping analysis. In this case, the metals are pre-concentrated by electrodeposition onto the electrode surface. The pre-concentration is done by cathodic deposition at a controlled time and potential. The deposition potential is usually by 0.3 V more negative than the least easily reduced metal ion to be determined. The metal ions reach the electrode surface by diffusion and convection, where they are reduced and concentrated. The convective transport is achieved by electrode rotation or solution stirring. The duration of the deposition step is selected according to the concentration level of the metal ion in question. Following the preselected time of the deposition, the forced convection is stopped and the potential is scanned anodically, either linearly or in a more sensitive potential time (pulse) waveform that discriminates against the charging background

current. During the anodic scan, the metals are reoxidised, stripped out from the electrode surface in an order that is a function of each metal standard potential. The voltammetric peak reflects the time dependant concentration gradient of the metal at the working electrode during the potential scan. Peak potential serves to identify the metals in the sample. The peak current depends upon various parameters of the deposition and stripping steps; as well as on the characteristics of the metal ion and the electrode geometry; and it is proportional to the concentration of the metal ions in the sample. Voltammetric measurements of numerous metal ions in various types of samples have been reported (Arancibia *et al.*, 2004; Shams *et al.*, 2004).

2.19.2.3 Cathodic stripping voltammetry (CSV)

CSV is the “mirror image” of ASV with two exceptions. First, it involves an anodic deposition of the analyte, secondly, stripping is accomplished by scanning cathodically toward a more negative potential. The term CSV was used originally for the indirect trace determination of organic compounds as mercury salt, involving anodic oxidation of mercury and subsequently cathodic reduction of mercury. The resulting reduction peak current provides the desired quantitative information. Cathodic stripping voltammetry is used to determine a wide range of organic compounds, and also inorganic compounds that form insoluble salts with the electrode material (Wang, 2000).

2.19.2.4 Adsorptive stripping voltammetry (AdSV)

AdSV significantly enhances the scope of stripping measurements towards numerous trace elements (Van den Berg, 1991). This method involves formation, adsorptive accumulation and reduction of a surface active complex of the metal. Most procedures involve the reduction of the metal in the adsorbed complex. The response of the surface confined species is directly proportional to its surface concentration (Wang, 2000). In case of adsorptive stripping voltammetry, the accumulation of the target metal ions is based on a selective chemical interaction. The target metal ions, complexed with different selective organic ligands, are usually

accumulated by adsorption onto the electrodesurface, and then the quantitative stripping response is obtained by reducing the metalions from its complexed form (Wang, 2000).

2.20. Challenges in stripping analysis

The major types of interferences in stripping analysis are overlapping stripping peaks, caused by similarity in the oxidation potentials of the metals, or the presence of organic surface active compounds that adsorb on the electrode surface and inhibit the metal deposition, and the formation of intermetallic compounds (Wang, 2000). The interference of overlapping stripping peaks can be minimised by introducing a separation step prior to the stripping measurement using a supporting electrolyte with a suitable complexing agent. This will shift the stripping peak potentials according to the stability, composition and concentration of the complexing agent using of surface active agents to mask or shift the stripping peaks and lowering the deposition potential until the metal with the more negative deposition potential is not deposited.

Interference of intermetallic compounds can be minimised by reducing a deposition time, adding a “third” element that forms a more stable intermetallic compound with one of the components of the binary system and by choosing a suitable supporting electrolyte (Cofre and Brink, 1992). In order to overcome the organic interferences, removal or destruction of organic matter by UV irradiation or ozone oxidation procedures may be considered prior to the stripping analysis of the organic-rich samples. For samples with low organic content, a standard addition method can be used (Monticelli *et al.*, 2009; Obata *et al.*, 2006).

2.21 Summary

Synthesis methods, characterisation methods, electrochemical and spectroscopic approaches for determination of heavy metals have been reviewed in this chapter. From this collection it can be seen that analytical studies in this field register a sharp increase in recent years. Some comprehensive tables present the reported available literature within the nanoparticles modified electrodes and summarises the criteria to be used especially with respect to the design and development of electrochemical sensor. Occasionally, some spectroscopic methods have been employed in analysis of heavy metal but depending to how rich is the sample. It was noted that determination of heavy metal ions has predominantly been performed by spectroscopic methods using ICP – AES or MS, with emerging research moving towards the greater variety of modified electrodes. The new applications of voltammetric techniques are promising contribution thanks to the low adsorption ability and the widest usable potential range with fast response times and wide linear concentration ranges. The use of sensors coated by nanoparticles with a very low detection limits and wide linear concentration ranges in the detection and determination of environmental pollutants is also discussed. Building on these facts, further advancement in this field can proceed in order to develop the nanoparticle electrochemical sensor for fast, simple, sensitive and selective determination of PGMs.

Chapter 3

Experimental Methods and Techniques

3.1 Introduction

This chapter outlines the experimental methods used to prepare and characterise the synthesised antimony nanoparticles and furthermore will describe several experimental techniques and procedures performed during this research project. Nanoparticles (NPs) characterisation is critical when conducting studies concerning synthesis and behaviour. Techniques applied can be both quantitative and qualitative in characteristics of size, particle coating, charge and aggregation. The detailed synthesis of nanoparticles that are used in this work to produce the nanocomposite of define first (rGO-SbNPs) will be presented. This chapter also gives the details of all the chemicals used in this work. Technical details, operation procedures and instrumentations are also the subjects of detailed discussion here. The experimental techniques for characterisation are broadly classified into three types as electrochemical, imaging and spectroscopic techniques. Spectroscopic analysis (e.g. ICP-AES or ICP-MS) and stripping voltammetry will be discussed in detailed as quantitative methods used in this work. The proposed electrochemical sensors described in this work, constructed from nanoparticles for the detection of PGMs. The possible mechanisms details for synthesis of nanoparticles and detection of heavy metals will also be presented.

3.2 Material Synthesis

3.2.1 Synthesis of rGO

Reduced graphene oxide (rGO) are produced from natural graphite flakes via simplified Hummer's method modified from literature (Basavaraja *et al.*, 2011; Goa *et al.*, 2011; Hirata *et al.*, 2004). Graphite is treated with a mixture of sulphuric acid, sodium nitrate and potassium permanganate (a very strong oxidiser). However, other methods have been developed recently that are reported to be more efficient, reaching levels of 70% oxidation, by using increased quantities of potassium permanganate, and adding phosphoric acid combined with the sulphuric acid, instead of adding sodium nitrate. Graphite is commonly chosen as the starting material due to its availability and low cost proportional amounts of oxidants, such as potassium permanganate, sodium nitrate, and concentrated sulphuric acid, are mixed in order with the graphite. These oxidisers work by reacting with the graphite and removing an electron in the chemical reaction. This reaction is known as a redox reaction, as the oxidising agent is reduced and the reactant is oxidised.

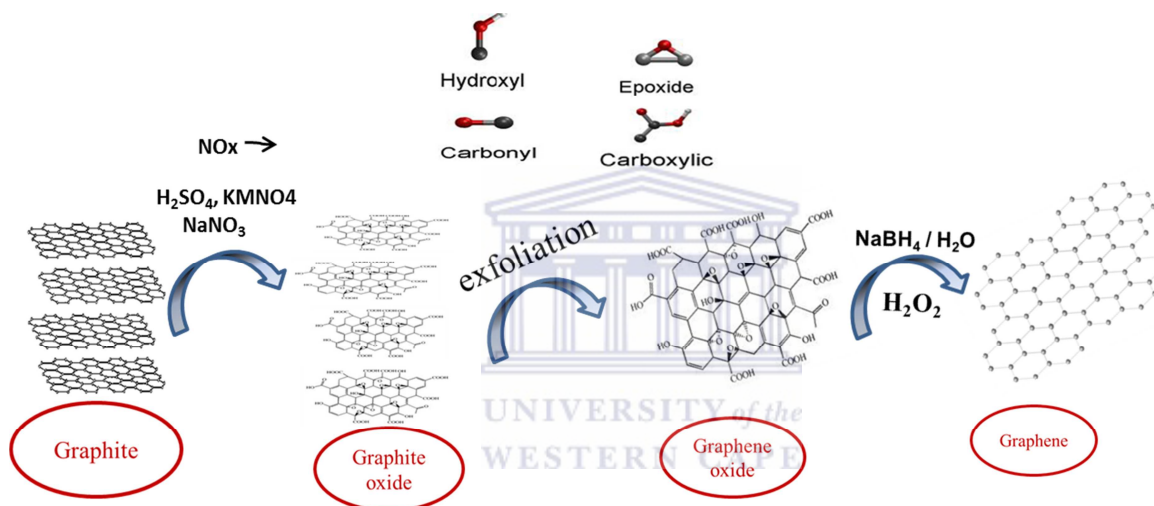
Subsequently, a three-phase procedure is conducted with low, mild, and high temperature reactions, each occurring separately at scheduled times. This process has been done under intensive stirring. The reactivity of MnO_4^- can only be activated in acidic solution, mainly described in the scheme reaction 3.2 (see below). The color of the mixture itself will stay dark because of the graphite but at the liquid border the formation of the green manganate dimer (Mn_2O_7) can be seen. The transformation of MnO_4^- into a more reactive form Mn_2O_7 will certainly help oxidise graphite, but the bimetallic form of manganese oxide has been reported to detonate when heated up to 55 °C, or when reacted with organic compounds. The graphite was oxidised to define graphite oxide through these procedures. Graphite oxide is a compound made up of carbon, hydrogen and oxygen molecules. A large number of oxygen-containing functional groups (epoxide, carbonyl, carboxylic and hydroxyl) have been introduced onto both sides of a single graphite sheet (namely, Graphite oxide) as seen in Scheme 3.1. The implantation of functional groups overcomes the inter-sheet van der Waals force and enlarges the interlayer spacing. Graphene oxide (GO) is effectively a by-product of this oxidation as when the oxidising

agents react with graphite, the interplanar spacing between the layers of graphite is increased. The completely oxidised compound can then be dispersed in a base solution such as water, and graphene oxide is then produced. As proposed in Scheme 3.1, graphite oxide and graphene oxide (GO) are very similar, chemically, but structurally they are very different. The difference in structure of GO and graphite oxide lies in a large amount of chemical functional groups attached to the carbon plane and structural defects within the plane, both of which can severely decrease the electrical conductivity. The main difference between graphite oxide and GO is the interplanar spacing between the individual atomic layers of the compounds, caused by water intercalation. This increased spacing, caused by the oxidation process, also disrupts the sp^2 bonding network, meaning that both graphite oxide and graphene oxide are often described as electrical insulators. The sheets in such an expanded structure are then easily pulled open using an external force such as sonication. That is, the expanded graphite is exfoliated into multi-layered or even single-layered sheets. Sonication can be a very time-efficient way of exfoliating graphite oxide, and it is extremely successful at exfoliating graphene (almost to levels of full exfoliation), but it can also heavily damage the graphene flakes, reducing them in surface size from microns to nanometres, and also produces a wide variety of graphene platelet sizes. As a result, the reduction of GO can be considered to be aimed at achieving two targets: the elimination of functional groups and the healing of structural defects. For the elimination of functional groups, there are also two effects that should be considered: whether the oxygen containing groups can be removed and whether the areas after removal can be restored to a long-range conjugated structure, so that there are pathways for carrier transport within the defined reduced graphene oxide (rGO) sheet.

Generally, the oxidised graphene sheets, or GO, acquire multiple defects and the degree of the defects is subject to the additive amount of oxidant and the oxidizing time (Kim *et al.*, 2012; Kuila *et al.*, 2012). Additional H_2O was added to dilute the solution, and 30% H_2O_2 was injected into the solution to completely react with the excess $KMnO_4$. Sodium borohydride was then added which then reduced GO into reduced graphene oxide, namely, rGO gradually precipitated out as a black solid. Reducing graphene oxide to produce reduced graphene oxide is an extremely vital process as it has a large impact on the quality of the rGO produced, and therefore will determine how close rGO will come, in terms of structure, to pristine graphene.

Mechanism

Since graphite is the source material, we first focus on its reactivity and chemistry. It is known that graphite does not directly react with most reagents but forms intercalation Compounds (Xia *et al.*, 2014). Graphite and graphene possess a bonding system with a high metallic character. Both sulfuric acid and sodium nitrate play an important role in the preparation of graphene oxide (Venugopal & Kim, 2011; Jenkins *et al.*, 2009).

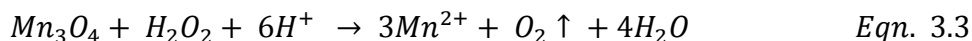
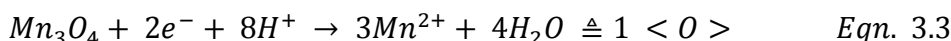
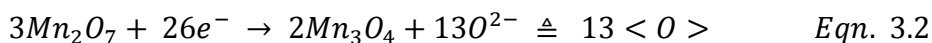


Scheme 1. Overview of the different stages on the route to reduced graphene oxide. The detailed procedure and mechanism are explained in the above sections.

In the first pathway the reaction is responsible for generating (intermediate) oxygen species which are consumed during the oxidation process. Altogether, there are three oxidation agents involved, namely KMnO_4 , NaNO_3 and H_2SO_4 . All of these are intercalated between the graphite layers which promote the oxidation effect (Chung *et al.*, 2002).

Adding permanganate to fuming sulfuric acid leads to *in situ* generation of Mn_2O_7 , a manganate dimer with a characteristic green color. It can be observed shortly after the addition of KMnO_4 along the inside of the glass vial where the mixture touches the glass. Equation 3.1 explains the instability of the dimer in water. If enough water is present in the reaction the

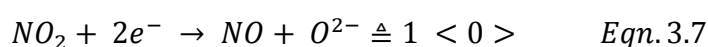
formation is reverted. The small quantity of water that is formally created in this reaction is absorbed by sulfuric acid (indicated by the “precipitation”-arrow) (Chung *et al.*, 2002).



Scheme 2 **Formation of dimanganeseheptoxide from KMnO_4 in the presence of a strong acid (adapted from Dreyer *et al.*, 2010).**

Mn_2O_7 generates a large oxidative potential when reduced to a mixed oxide with Mn(II) and Mn(III) cations. Due to the anhydrous environment of the reaction, the Equation 3.2 does not involve any protons nor water. Instead, a process similar to oxidation melting is assumed to occur. In the aqueous environment, the mixed manganese oxide spontaneously precipitates as reddish brown solid. It is resolved again either by stirring for a while or by heating the mixture like it is done in the procedure described later. The last process will further reduce the mixed manganese oxide to the Mn(II)-ion species.

Hydrogen peroxide is added as final step to overcome this issue. After addition, small bubbles will raise and the color of the solution gets clearer compared to the one before. It reduces the remaining manganese oxides and thus produces elementary (gaseous) oxygen as described by Equation 3.3. The generated oxygen gas of the last step leaves the reaction immediately and so it is not taken into account for the total oxygen balance. From the Equations 3.2 and 3.3 it is obvious that three Mn_2O_7 generate 15 (13 + 2.1) intermediate oxygen entities ($\langle \text{O} \rangle = 2e^-$). For this six KMnO_4 units are needed, i.e. 2.5 (15 O per 6 KMnO_4) oxygen entities are generated per unit. So, theoretically, 62.5% of the available oxygen could be used for the oxidation of graphite. However, some of the oxygen is involved in creating nitrogen oxide species (see next reactions) (Chung *et al.*, 2002).



NaNO₃ in fuming sulfuric acid is converted into HNO₃. Sulfuric acid is very hygroscopic and dehydrates nitric acid to form the anhydride N₂O₅ (Thiemann *et al.*, 2000). Eventually, the anhydride decomposes into NO₂ and O₂ gas. NO₂ and its dimer form, N₂O₄, oxidize graphite. The above equations sum up this process. For clarification, the dimer forms of the nitrogen oxide species (N₂O₄, N₂O₂) are omitted. The resulting nitrogen monoxide is oxidised again to form nitrogen dioxide which closes the loop. It is also common to use sodium nitrite instead of sodium nitrate (Satti *et al.*, 2010). In this case, HNO₂ is first formed which disproportionates to HNO₃ and NO. From this perspective, adding NaNO₂ instead of the nitrate does not make any difference. The chemistry of nitrogen oxide is complex and due to the oxidation potential in the present reaction all possible nitrogen oxide species (N_xO_y) are created as seen in Scheme 1. Their well-known toxicity has been subject to substantial research. Hence, some completely omit using any nitrate or nitrite in their synthesis (Marcano *et al.*, 2010; Kovtyukhova *et al.*, 1999).

The last part of the scheme 1 is very short and simple there is a strong reducing agent involved, NaBH₄ a mechanism for the elimination of oxygenated groups is proposed (Stankovich *et al.*, 2007). Though numerous strategies have been proposed to reduce GO, there are still many questions without clear answers. For example, can the functional groups of a GO sheet be fully eliminated? Can the lattice defects formed during oxidation be restored during reduction? Does a reduction process decrease or increase the defect density in a graphene sheet?

The answers and further improvements in GO reduction will rely on an improved understanding of reduction mechanisms. For the elimination of functional groups, there are also

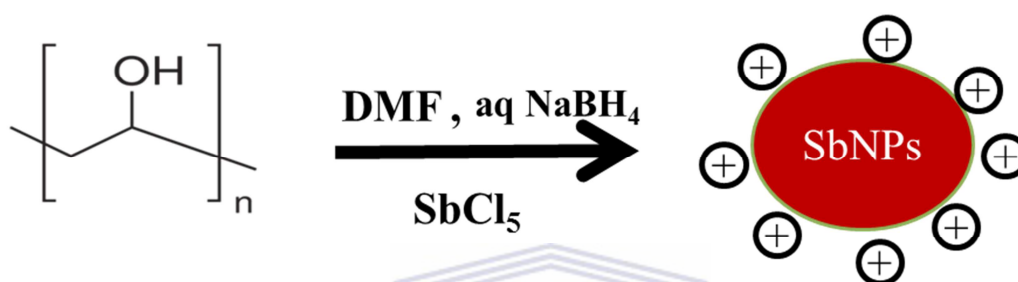
two effects that should be considered: whether the oxygen containing groups can be removed and whether the areas after removal can be restored to a long-range conjugated structure, so that there are pathways for carrier transport within the rGO sheet (Pei *et al.*, 2012).

In a typical synthesis, graphite powder (1, 2 μM) 2 g and NaNO_3 (1 g) were subjected to an oxidative treatment with potassium permanganate (KMnO_4) in concentrated sulphuric acid (120 mL) under stirring in an ice bath. KMnO_4 (7.5 g) was added slowly with stirring and cooling, so that the temperature of the mixture was not allowed to reach 20 °C (warning: this has to be done with extreme caution; the process is highly exothermic). The mixture was then stirred and the glass beaker was placed in a water bath maintained at 35 °C for two hours to complete the synthesis, and distilled water (920 mL) was added. Upon oxidation, graphite oxide was exfoliated to graphene oxide (GO), resulting in a brownish gel-like solution. In 15 min, the reaction was terminated by the addition of a large amount of distilled water (2 L) and 30% H_2O_2 solution (10 mL), to reduce the residual KMnO_4 . The colour changed from dark brown to bright yellow indicating the formation of graphene oxide. The mixture was filtered and washed with 1:10 HCl solution (3 L) in order to remove metal ions, then acetone and distilled water until the pH was neutral. The resulting graphene oxide (GO) was dried in vacuum oven to get a loose, light brown powder. Finally, reduced graphene oxide (rGO) was prepared by dispersing 10 mg of graphene oxide in 30 mL EtOH / water (9:1 v/v) with slowly added drop wise 2 mL of 0.118 M *aq.* NaBH_4 freshly prepared under vigorous stirring for 1 h. Thereafter, the mixture was ultrasonicated for 1 h. The rGO dispersion was then washed with ethanol and repeatedly with deionized water to remove the remaining NaBH_4 and dried at 60 °C for 4 h in a vacuum oven (Loryuenyong *et al.*, 2013, Kovtyukhova, *et al.*, 1999).

3.2.2 Synthesis of Antimony nanoparticles

Nanometer sized particles have different properties than their bulk. Their reduction potential is highly dependent on size of the particle. As the size of the particle decreases the density of states become more limited and this will cause the reduction potential to be shifted to lower negative values. Although metal nanoparticles are catalytically active, one major drawback of these particles is their tendency to agglomerate. To prevent aggregation various approaches

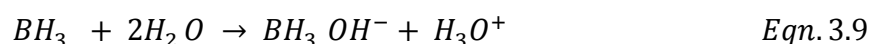
are pursued to stabilise nanoparticles. These stabilisers should not interfere with the catalysed reaction or block the surface of the catalyst. Furthermore, the catalyst should be easily removed from product after the reaction. In this thesis, metal nanoparticles are synthesised by a wet chemical approach with sodium borohydride using polyvinylalcohol (PVA) as a stabiliser. Scheme 3 shows the reaction of antimony metal nanoparticles (Pradham *et al.*, 2002).



Scheme 3. Scheme for the preparation of antimony nanoparticles in aqueous solution.

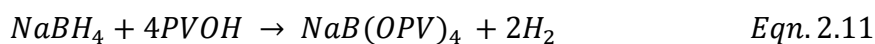
Antimony (Sb) in its aqueous form $\text{Sb}^{5+} \setminus \text{Sb}_{\text{bulk}}$ has a reduction of 0.69 V (vs. N.H.E) while Sb in nanometer sized has $\text{Sb}^{5+} \setminus \text{Sb}_{\text{atom}}$ reduction potential of -0.51 V (vs. N.H.E) (Schlenoff and Dubas, 2001). To convert the Sb ions to Sb metallic particles, the reduction potential should be overcome and this happen with the help of strong reducing agent like NaBH_4 (Pradham *et al.*, 2002). NaBH_4 has a reduction of -1.3 V (vs. N.H.E) (Schlenoff and Dubas, 2001, Pradham *et al.*, 2002). Once the nanoparticles are formed they will agglomerates causing reduction potential to increase in value till they reach the value of the bulk material and then they will stabilise. This is restricted by the surrounding matrix at which the chains and the tails of the polymer will define a new value for the reduction potential of the growing nanoparticles. NaBH_4 is a well-known reducing agent that is used in the production of the nanoparticles. It is regarded as a nucleophilic agent that can donate electrons to the nanoparticles. The dissolution of NaBH_4 in water will lead to separation of water molecules to its respective components OH^- and H^+ .

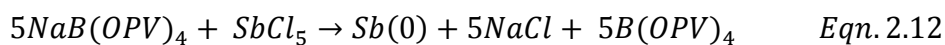
This will create an alkaline medium. The reducing power of NaBH₄ is controlled by formation of an intermediate compound that will appear during dissolution and allow the electron transfer to Sb ions to convert it into metallic nanoparticles.



From equation 3.9 we can see that the intermediate compound that is responsible for the reducing power or electron transfer is BH₃OH⁻. It is always accompanied by the liberation of hydrogen gas. As the intermediate compound get attached to Sb ions, and electron transfer will take place where the conduction band will filled and cause Fermi level to be shifted to higher negative values. This will induce a change in electronic density of the SbNPs forming new optical properties. The shift in Fermi level will manifest high sensitivity of nanoparticles towards oxidation. Polyanions act as well as a nucleophile that cause stabilisation of the growth of the nanoparticle. In reality there is no electron transfer to nanoparticles but the polymer can squeeze the energy level in a smaller volume and induce higher electronic density which will shift the Fermi level to higher negative potential level.

The general scheme for formation of antimony nanoparticles (SbNPs) is via reduction by sodium borohydride (NaBH₄) in the presence of defined poly vinyl alcohol (PVA) as stabiliser is given by the following reaction (Pradham *et al.*, 2002).





Typically, 3 g of PVA, 0.3 ml of SbCl₅, 10 mL of DMF and 0.25 mL of 1.8M NaBH₄ aqueous solution was added all at once in to the mixture of PVA, DMF and SbCl₅ constant stirring then allowed to age in darkness at room temperature for 8 days and later refluxed for 2 h. Finally the powder was washed, separated and dried at ambient temperatures for 2 h (Chin *et al.*, 2010).

3.2.3 Synthesis of Reduced Graphene Oxide Antimony Nanoparticles

Reduced graphene oxide (rGO) nanoparticles possess a number of advantages when compared to bare nanoparticles including less nanoparticle aggregation as well as the enhancement of electrical, electrochemical, and optical properties (Yang *et al.*, 2010). Ultimately, once reduced graphene oxide has been produced, there are ways that we can functionalise rGO for use in different applications. By treating rGO with other chemicals or by creating new compounds by combining rGO with other two dimensional materials, we can enhance the properties of the compound to suit commercial applications. The synthesis of defined (rGO–SbNPs) began with the preparation of Sb nanoparticles with subsequent aging treatment of the synthesised Sb nanoparticle solution at room temperature for about 8 days. In this case, preparation strategy for rGO–SbNPs nanocomposite is produced through direct use of rGO as shown in Figure 21. In the literature metal/graphene, the nanocomposites are produced through simultaneous reduction of GO and metal ions (Hu *et al.*, 2012; Moussa *et al.*, 2011; Wang *et al.*, 2011). In this synthesis rGO sheets are directly used, ethanol was used as a medium for the synthesis. Most oxidised functional groups are removed during the reduction of graphene oxide it is generally difficult to disperse the resulting graphene in solution, a stabilising agent is required to encourage the assembly of the nanostructure.

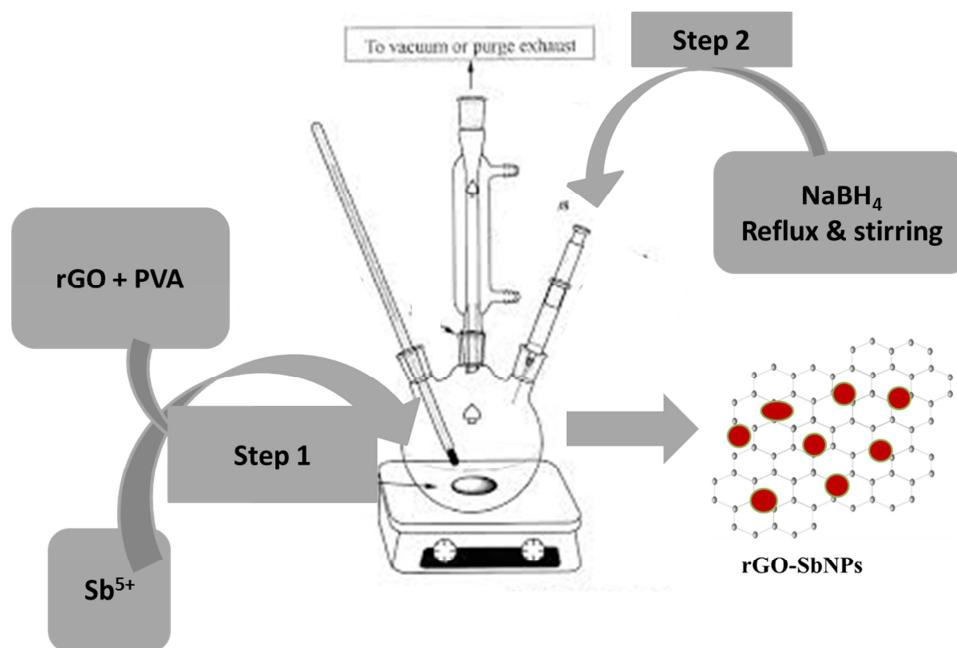
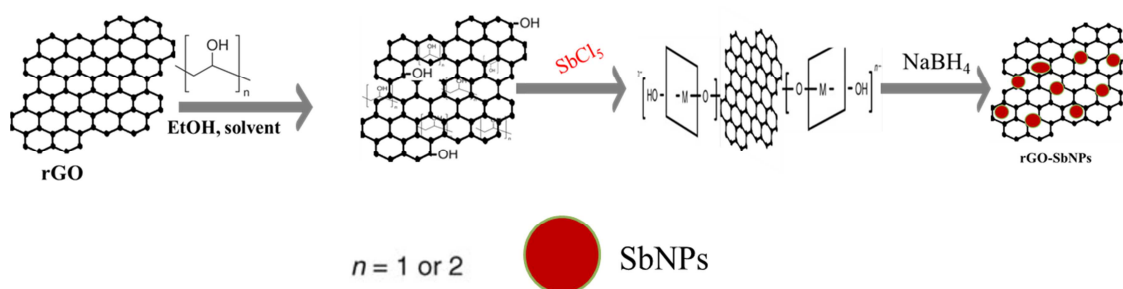


Figure 21. Schematic representation of the synthetic route of rGO-SbNPs by direct reduction of the metal ions under reflux.

Ethanol was used as a solvent so there is a possibility of unreacted PVA. The presence of unreacted PVA not only facilitates the dispersability of the resulting hybrids, but also contributes to the homogeneous distribution of SbNPs nanoparticles on the rGO sheets. By controlling the size of cracked rGO, a variety of nanomaterials with varying size including inorganic materials are used. In this study PVA and SbNPs were used in the synthesis of the rGO-SbNPs nanocomposite and to enhance their properties as well as to obtain new synergistic effects. The interaction between PVA and rGO was mainly by hydrogen bonds. In this case the non-covalent functionalisation of rGO, through weak interactions minimises the effect of alter sp^2 hybridised network because it does not interfere in any destruction of aromatic structure of graphene. The hydrogen in the O-H group of PVA is capable of forming bond with the hydrogen in the rGO ring. Now, PVA chains form linkage between the rGO ring via hydrogen bonding as shown in Scheme 4.



Scheme 4. Illustration of the proposed mechanism for SbNPs formation into rGO sheets.

Unfortunately, no one has studied the detailed reaction which takes place in the above mixture until this time. But the following is mechanism that might happen. The reaction occurs as the following steps, the initial step is the mixing of PVA and rGO followed by addition of SbCl_5 dropwise. The chains of residual PVA molecules lie on the surface of the rGO sheets, with the polymer groups extending into the solution to provide electrostatic repulsion that stabilises the suspension. These polymer groups also behave as both the active sites for the adsorption of Sb ions and the nucleation centres for Sb nanoparticles (Fenandez-Ujados *et al.*, 2013, Lu *et al.*, 2007).

In this way, Sb nanoparticles are grown and densely assembled on the graphene surface, as shown in reaction Scheme 4. The second step is conversion of the Sb ions to Sb metallic particles, the reduction potential should be overcome and this happened with the help of strong reducing agent like NaBH_4 . The negatively-charged functional groups on the surface of rGO induced the nucleation of positively charged metallic nanoparticle, resulting in the successful growth of metal nanoparticles on the rGO surface.

3.3 Characterisation Methods

Different of techniques can be used to characterise the nanoparticles depending on the kind of application. Table 5 shows several characterisation techniques and parameters that can be obtained from each.

Table 5. Characterisation Procedures used during sensor development.

Technique	Purpose
Fourier Transform Infra-Red (FTIR) Spectroscopy	Identify specific functional groups present in the molecules
Ultra Violet Visible (UV/VIS)	Determine particle formation and its properties
Raman Spectroscopy	Information such as defect density functionalisation and crystallographic orientation can be extracted.
High resolution scanning electron energy dispersive X-ray Spectroscopy (HRSEM)	Information about surface microscopy & roughness, porosity, particle size distribution and intermetallic distribution and diffusion.
High resolution transmission electron (HRTEM/EDS).	Determine surface topography and also the thickness of the studied sample.
Atomic Force Microscope (AFM)	Determine particle formation and its properties the thermodynamics of electrode
Cyclic voltammetry (CV) Electro impedance spectroscopy (EIS)	Electrochemical activity of new systems. Better understanding of the internal electrochemical processes.

3.3.1 Electron Microscope

3.3.1.1 High resolution Scanning Electron Microscope (HR-SEM)

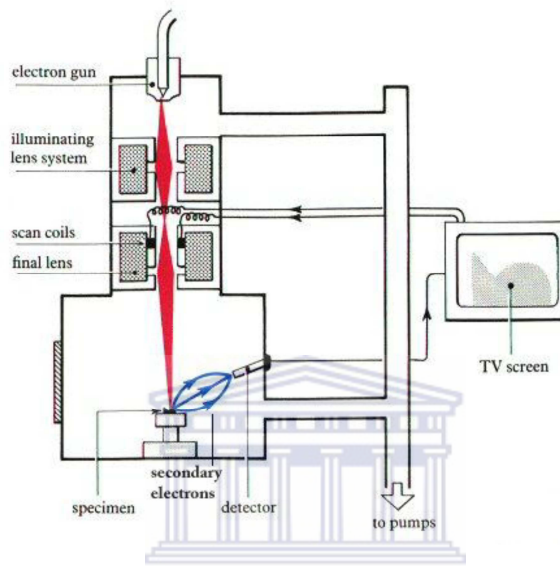


Figure 22. Schematic drawing of a scanning electron microscope (www.asu.edu).

Figure 22 shows the components of a scanning electron microscope (SEM) (www.asu.edu). Scanning electron microscope is an extremely useful tool for the study of the surface of the sample because it offers a better resolution than the optical microscope. In a scanning electron microscope (SEM) measurement, a focused electron beam (typically of energy between 5 and 20 keV) is incident upon the surface of a sample. It uses electrons emitted from tungsten or Lanthanum hexaboride (LaB_6) thermionic emitters for the visualisation of surface of the sample. The filament is heated resistively by a current to achieve a temperature between 2000-2700 K. This result in an emission of thermionic electrons from the tip over an area about $100 \mu\text{m} \times 150 \mu\text{m}$. The energy of this beam is deposited into a 'generation', or 'interaction', volume, the size and shape of which is dependent on a multitude of factors including incident beam energy, beam footprint on the sample surface, angle of incidence etc. From within this volume a number of signals originate including secondary electrons (produced in a variety of

ionisation events) and backscattered electrons which are the signals that contribute to the formation of a SEM image (Goldstein, 1992). If the sample is sufficiently thin, a signal can be detected below the sample and comprises primary electrons and both elastically and in elastically scattered electrons. Each point of the sample onto which the beam is focused, and from which information is collected, forms one pixel of a SEM image and may range from 1 nm to 10 μm in diameter. In order to create an image the primary beam is scanned across the surface of the sample in a raster pattern, and the information from each point displayed on the corresponding area of a screen. Thus the magnification, M , in a SEM is accomplished through the mapping of the sample scale, L_{sample} , onto the larger scale of the display, L_{display} :

$$M = \frac{L_{\text{sample}}}{L_{\text{display}}} \quad \text{Eqn. 3.13}$$

The main drawback of SEM is that it is unable to probe beyond the external structure. In contrast to this, the transmission of the primary beam in TEM readily yields additional information regarding the number and quality of the walls of a rGO and the condition of the inner channel, in addition to verifying the presence of material encapsulated within reduced graphene layers.

The High Resolution Scanning Electron Microscopy (HRSEM) images presented in this thesis were obtained using an Auriga Zeiss instrument with Gemini technology, employing a FEG Tip operated at an accelerating voltage of 3 Kv at the Electron Microscope Unit (EMU), of the University of the Western Cape. The working distance and magnification was altered according to the contrast and depth of field required. rGO, SbNPs and rGO-SbNPs samples were fitted into the vacuum chamber of the microscope (HRSEM, Zeiss Ultra 55 Field Emission – In-lens detection). High Resolution Scanning Electron Microscopy was used to probe the surface micro and macro structure, and determine the degree of agglomeration. Specifically few grams of sample were placed in a specially designed sample holder and this was mounted into the HRSEM instrument.

3.3.1.2 Transmission Electron Microscope (TEM)

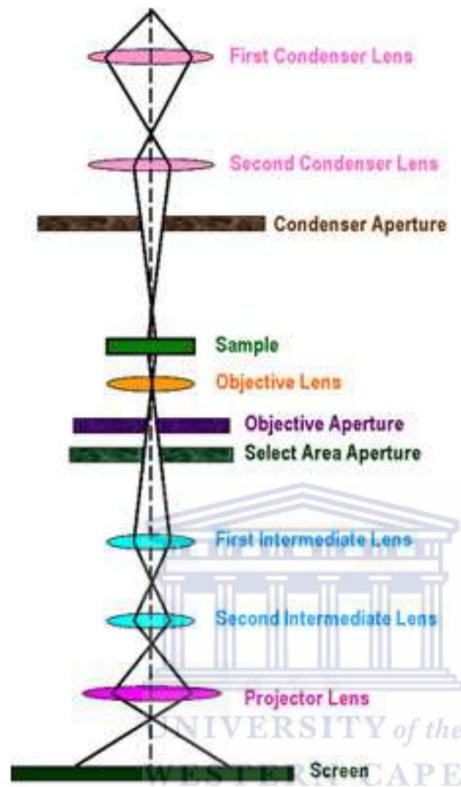
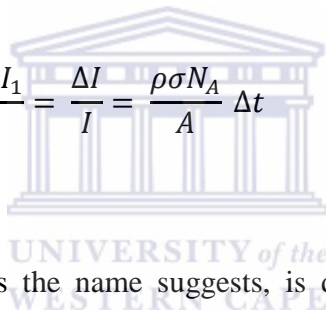


Figure 23. Schematic drawing of a transmission electron microscope (www.nanoscience.gatech.edu).

Figure 23 shows the components of a transmission electron microscope (TEM). TEM analysis has been used to visualise the change in the morphology of the rGO on exposure to the SbNPs. TEM has also been used for analysing the shape and size of the rGO-SbNPs synthesised using sodium borohydride. Transmission electron microscopy (TEM) is inherently different from SEM in that this technique involves the detection of primary electrons which have passed through a sufficiently thin sample. A TEM microscope is composed by an optical column, operated under high vacuum that enclose. Illumination system takes the electrons from the gun and transfers them to the specimen giving either a broad beam or a focused beam. In the ray-diagram, the parts above the specimen belong to illumination system. The diffraction pattern and image are formed at the back focus plane and image plane of the objective lens. If we take the

back focus plane as the objective plane of the intermediate lens and projector lens, we will obtain the diffraction pattern on the screen. The beam is of sufficiently high energy (typically > 100 keV) that the majority of the electrons can pass through the sample. As the electrons pass through the sample, the uniform intensity of the primary beam is made non-uniform by scattering. In order to convert the scattered electron intensity into some meaningful form of contrast and allow easy image interpretation, TEM images are usually formed from either the direct beam (bright field, BF, image) or diffracted beam (dark field, DF, image). The contrast between two adjacent areas of a TEM image, I_1 and I_2 , is usually one of two main types: mass-thickness contrast, which is of particular importance when imaging non-crystalline samples, and diffraction contrast. Mass-thickness contrast, C , arises from incoherent elastic scattering of the primary electrons and occurs in both BF and DF images using electrons scattered through low angles (William and Carter, 1996).

$$C = \frac{I_2 - I_1}{I_1} = \frac{\Delta I}{I} = \frac{\rho \sigma N_A}{A} \Delta t \quad \text{Eqn. 3.14}$$



Mass-thickness contrast, as the name suggests, is dependent on variations of sample thickness, Δt , and the single atom scattering cross-section, σ , which is a function of atomic number, Z . ρ is the density of the sample, A the atomic mass and N_A is the Avogadro constant. In simple terms the consequences of this are as follows: higher Z elements have a larger scattering cross-section than lighter elements and so scatter electrons away from the trajectory of the primary beam more effectively. Increased sample thickness has the same effect. Thus, areas of a sample with a relatively high Z and t will appear as dark areas on a BF image and bright areas on a DF image (William and Carter, 1996).

The main disadvantage of both SEM and TEM is that they are unable to yield information regarding the chemical composition of the structures seen in the images and so there is a need for supplementary techniques such as energy dispersive x-ray analysis (EDX), if a more complete picture of the sample is to be obtained (EDX may be carried out in an electron microscopy). Moreover, electron beam exposure has been shown to lead to sample degradation

and damage (Monthioux *et al.*, 2001), which may lead to difficulties in identifying weakly bound or sensitive species within the sample during subsequent analysis.

The High Resolution Transmission Electron Microscopy (HRTEM) and Energy Dispersive X-ray Analysis measurements of the rGO, SbNPs and rGO-SbNPs presented in this thesis were performed on the Tecnai G2 F20X-Twin MAT Field Emission Transmission Electron Microscope, equipped with EDSinstrument from FEI (Eindhoven, Netherlands) under an acceleration voltage of 200 kV in the Electron Microscope Unit, UWC Campus.

Samples were prepared by dispersion of a spatula-tip in 5 ml methanol solution, followed by sonication of the suspension. One drop of the suspension was deposited onto on a Cu TEM grid covered with a thin layer of amorphous carbon and allowed to air-dry. The methanol was allowed to evaporate at room temperature. Samples were mounted in a sample holder that was introduced into the shaft of the electron microscope. The initial goal for using TEM was to provide a clear indication of size and distribution of the nanoparticles embedded in the reduced graphene oxide antimony nanoparticles.

3.3.1.3 Energy Dispersive X-ray Analysis (EDX)

This analysis is performed coupled with imaging. The characteristic X-rays emitted after electron bombing from the specimen. This is fundamentally qualitative technique but a semi-quantitative is possible.

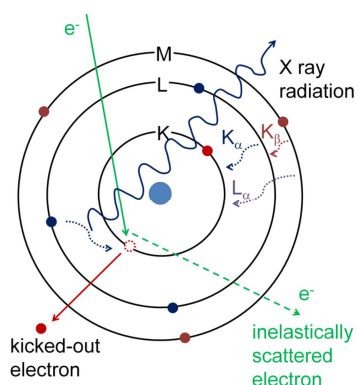


Figure 24. Interactions of the atom with an electron beam (Goldstein, 2003).

Figure 24 shows the interaction of the atom with an electron beam in a sample in EDX. The emitted x-rays have energies which are characteristic of the material from which they originate and therefore may be used to ascertain the chemical composition of a sample. The ability to view three dimensional images of samples of interest does not always solve a problem in an analysis. Occasionally, further complimentary techniques are required to for example when there is a necessity to identify the different elements co-exists within the same sample. For such cases; a typically built-in spectrometer called Energy Dispersive X-ray Spectrometer (EDS) will be extremely helpful. This non-invasive method is sometimes referred as EDS or EDX analysis and used in conjunction with SEM or TEM but does not stand alone without the latter. The energies of the emitted photons (energy dispersive x-ray analysis, EDX may be measured. EDX is frequently carried out within an electron microscope. The benefits of using a high energy electron beam as the excitation source is that highly localised volumes of the sample can be analysed due to the ability to precisely focus the electron beam; specific points of interest in a SEM or TEM image can be chemically characterised. This is a particularly useful tool when analysing the nanocomposite of rGO and SbNPs since any contaminants present can be identified and eliminated (Sharma, 2012).

To further explain, an electron beam hits a sample surface which will be pre-coated to make it conducting. The energy supplied by the electron beam is normally in the region of 10-20 keV. This energy supplies sufficient force for some electrons from the atoms on the sample surface to be knocked off. The vacation of electron from the atom inner shell then filled by the transfer of electrons from the atom outer shell. As the energy levels of the outer shell electrons are higher than that of the inner, the energy difference is then emitted as x-ray. During EDX analysis, the specimen is bombarded with an electron beam inside the scanning electron microscope. The bombarding electrons collide with the specimen atoms' own electrons, knocking some of them off in the process. A position vacated by an ejected inner shell electron is eventually occupied by a higher-energy electron from an outer shell. To be able to do so, however, the transferring outer electron must give up some of its energy by emitting an X-ray. Since that the every atom dissipates unique energy level for each electron transfer, identification of the atom from which the x-ray was emitted can be established. The results from the EDX analysis is called EDX spectrum. In principle it shows a plot of frequency of x-ray emission has occurred for each energy level. As each peak is unique for each atoms, quantitative or qualitative

analysis of elemental composition can be resolved. Higher peaks value simply means a higher concentration of the element is. Not only that EDX is responsive towards the element according to each peak, it can also reveal the type of X-ray to which it corresponds as well. Each emission from one electron orbital to another carries difference values of energy level.

In this study, EDX analysis was used mainly to determine the presence of rGO, SbNPs and rGO-SbNPs in the sample materials. In an HRTEM, a fixed accelerating voltage of 20 kV was used in order to obtain high signal intensity.

3.3.1.4 Atomic Force Microscope (AFM).

Figure 25 shows the working of Atomic Force Microscope (AFM). Compared to other conventional optical microscopes, for instance, Scanning Electron Microscopy (SEM), which offers imaging resolution in the order of a few nm, AFM allows a better resolution in atomic scales taken in a three dimensions. AFM can examine almost any type of sample including ceramics, composites, polymers, as well as bio-samples in air or solutions with demonstrated nanoscaled resolution.

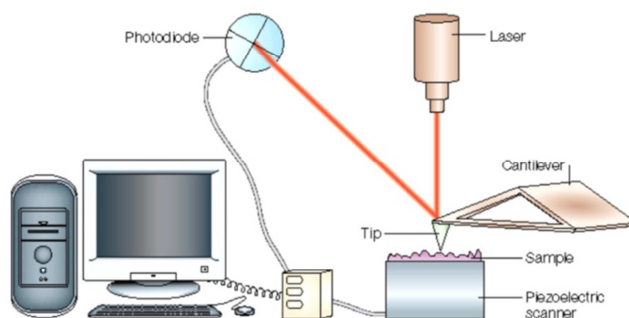


Figure 25. Diagram showing the working of and AFM cantilever (www.geobacter.org. Microbial Nanowires).

The principles of on how the AFM works are very simple. Atomic force microscopy is a surface analysis technique which consists of a cantilever with a tip having 30-50 nm radius and a laser detection system. The tip scans the surface of a specimen and the tip-sample interactions produce a deflection of the cantilever that is recorded by a laser deflection system. The lateral resolution depends on the size of the tip. The height detection system can resolve step height in the z-direction down to the few Ångström. The AFM can be used in contact and non-contact mode. In contact mode, the tip drags on the surface of specimen and the deflection in tip due to surface profile is recorded as signal. This technique is destructive for soft matter and harmful for the tip while scanning hard material. In non contact mode, the tip oscillates at a certain frequency above the surface of a specimen. The deflection in tip is produced due to van der Waals forces or electrostatic forces or dipole-dipole interactions (Morita *et al.*, 2002).

Contact mode AFM is one of the most widely used method in scanning probes which works based on rastering a sharp tip across the sample. The force works on the tip is repulsive. Initially, the AFM tip needs to be moved manually very close to the vicinity of the sample. The piezoelectric scanner then will automatically adjust the position between the cantilever tip and the sample based on the pre-setup distance value decided beforehand. Now that the sample is in direct contact with the sample surface, it will then be scanned by a piezoelectric scanner by means of either moving the sample or tip relative to each other. Every deflection resulted from the scanning causes the laser beam at the back of the cantilever tip to be reflected off to a split photodiode. This photodiode acts as a sensor which records all the deflections produced from the scanning. In order to maintain a constant distance between the cantilever tip and the sample, a feed loop is used in where the scanning direction is adjusted in the z direction. By having a feedback loop, damages caused to the sample from crashing of the cantilever tip could be minimized although cannot be totally eliminated. The measured cantilever deflections are used to generate a map of the surface topography. Although contact mode AFM offers fast scanning rate and proven to be very useful when having samples with rough surface area, often the force imposed end up causing damages or deformation of soft samples and distortion of the image as a consequence. This problem is always encountered with softer materials, such as biological samples, polymers, and even some seemingly hard materials, such as silicon wafers. This problem is however resolved by imaging in liquid form.

3.3.2 Optical Microscopes

3.3.2.1 Ultraviolet-visible spectroscopy (UV-VIS)

Figure 26 shows the working of UV-Vis spectrometer. Ultraviolet-visible spectroscopy (UV-VIS) uses light in the visible and adjacent near ultraviolet (UV) ranges.

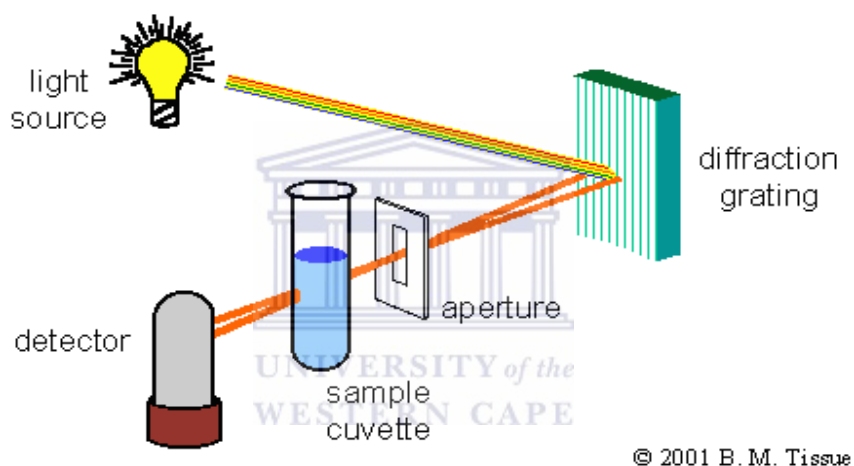


Figure 26 Schematic diagram of a single-beam UV-Vis spectrometer (<http://www.files.chem.vt.edu/chem-ed/spec/uv-vis/singlebeam.html/>)

The UV-Vis radiation source has wavelengths in the range of 200 to 800 nm, with the UV range going from 200 - 400 nm and the visible range extending from 400 - 800 nm. At these wavelengths, molecules undergo electronic transitions. Since the absorption of ultraviolet or visible radiation by a molecule leads transition among electronic energy levels of the molecule, it is also often called as electronic spectroscopy. The information provided by this spectroscopy when combined with the information provided by NMR and IR spectral data leads to valuable structural proposals. In this technique, the light passes through the sample to be analysed, and some of the light is absorbed by the sample. Thus, the sample has to be thin enough such that some of the light is transmitted. Another factor is that the sample must be placed onto a

supporting substrate, for example, quartz, that is transparent at the wavelengths of light used. When visible or ultraviolet light is absorbed by the valence electrons of the material, these electrons are promoted from their ground states to higher energy excited states (Figure 27). The energies of the orbital involved in electronic transitions have fixed values (www2.chemistry.msu.edu/faculty/reusch/VirtTxtJml/Spectrpy/UV-vis/spectrum.htm).

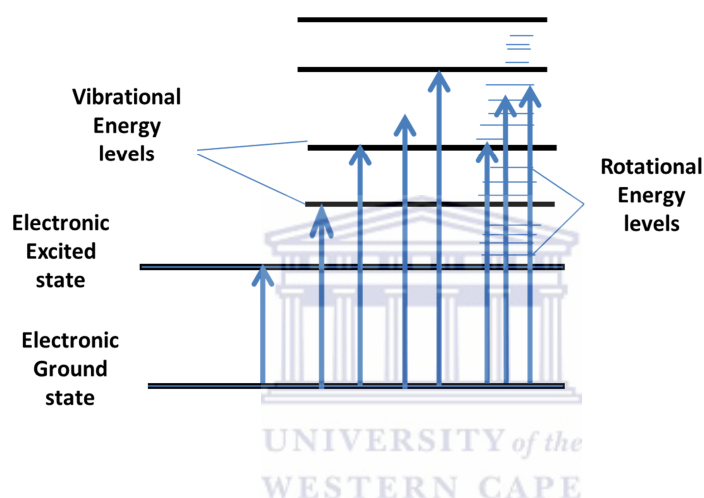


Figure 27. Illustration of the electronic transitions process during light absorption (www2.chemistry.msu.edu/faculty/reusch/VirtTxtJml/Spectrpy/UV-vis/spectrum.htm).

Any molecular system possesses three types of energy namely electronic (E_{ele}), vibrational (E_{vib}) and rotational (E_{rot}) with decreasing magnitude in same order for a system. Absorption of energy leads to transition of electron from ground state to excited state. The absorption peak thus obtained is broad, smooth and never very sharp due to the fact that the electronic absorption is accompanied with a corresponding change in the vibrational and rotational energies as well. The relationship between the energy absorbed in an electronic transition and the frequency, ν , wavelength, λ and wave number, $\tilde{\nu}$ of the radiation producing the transition is (Denney and Sinclair, 1993):

$$\Delta E = h\nu = hc/\lambda = h - \nu . c \quad \text{Eqn. 3.15}$$

where, h is Planck's constant, c is the velocity of light and ΔE is the energy absorbed in an electronic transition in a molecule from a low-energy state (ground state) to a high energy state (excited state). The position of absorption maxima for a molecule depends on the difference in the energy of the ground state level to that of excited state; larger the difference between the energies, higher is the frequency of absorption and thus smaller will be the wavelength. Absorption band shows two important characteristics; position of the band which depends on the energy difference between electronic level and intensity which depends on the interaction between the radiation and electronic system as well as on the energy difference between the ground and excited state. A convenient expression, which relates the absorbance with the path length that the radiation travels within the system and the concentration of the species, can be derived from the Lambert-Beer law and is given as

$$A = a \cdot b \cdot c \quad \text{Eqn. 3.16}$$

Where, A is measured absorbance, a is the absorptivity, b is the path length and c is the concentration of the analyte (Denney and Sinclair, 1993).

For the purposes of this study, UV-Vis spectroscopy was employed to investigate the stoichiometry of rGO-SbNPs, a typical single beam Thermo Scientific Helios Omega range UV-VIS spectrometer with vision PC Software was used for spectroscopic characterisation. In general, the radiation from the source was passed through a filter or a suitable monochromator to get a band or a monochromatic radiation. It was then passed through the sample (or the reference) and the transmitted radiation was detected by the photo detector. Typically, two operations were performed, first, the cuvette was filled with the reference solution and the absorbance reading from 200 - 1000 nm range was recorded. Second, the cuvette was taken out and rinsed and filled with sample solution and the process was repeated. The spectrum of the sample was obtained by subtracting the spectrum of the reference from that of the sample solution. The signal so obtained was sent as a read out or was recorded. The wavelength at which the maximum absorption occurs is known as λ_{max} . At this fixed wavelength, the absorbance

changes in accordance with concentration, since the absorbance is proportional to the concentration of the absorbing species given by the Beer-Lambert law (Mehta, 2012).

For the purpose of this study UV-VIS was used for characterisation of nanoparticles. The sample were dissolved in *N,N'*-dimethylformamide (DMF) and placed in 1 cm quartz cuvettes and their UV-VIS spectra recorded. The visible spectrum was measured with the use of a halogen bulb, while the UV part of the spectrum was measured using a Deuterium lamp. The light from both sources travel along fibre optic cables and measurements were conducted on the spectral range 200 to 1000 nm. The obtained spectra were then used to characterise the absorption bands and analyse the nanoparticle samples for similarities and differences in structure (Somerset *et al*, 2010).

3.3.2.2 Fourier Transformed Infrared spectroscopy (FTIR)

Figure 28 represent the schematic diagram showing the three basic spectrometer components in FTIR spectroscopy. Infrared spectroscopy yields similar results as Raman spectroscopy, but complementary information. Infrared spectroscopy (IR) is a widely applied research technique that provides qualitative information about the studied sample mainly by allowing identifying specific functional groups present in the molecules.

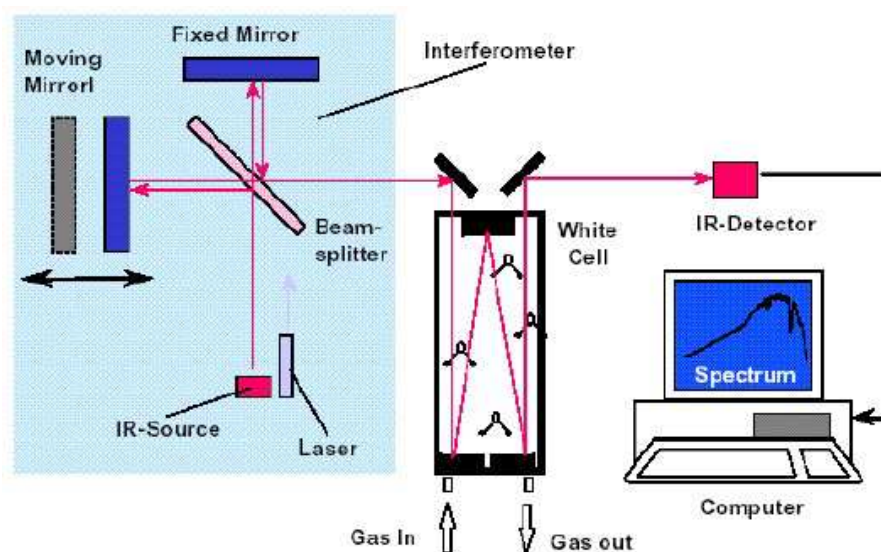


Figure 28. Schematic illustration of an FTIR system (Du Toit, 2002).

Typically, an infrared (IR) spectrum is obtained by passing IR radiation through a sample and determining what fraction of the incident radiation is absorbed at a particular energy. The energy at which any peak in an absorption spectrum appears corresponds to the frequency of a vibration of a part of a sample molecule (Stuart, 1996). Upon amplification of the signal, in which high-frequency contributions have been eliminated by a filter, the data are converted to a digital form by an analog-to-digital converter and then transferred to the computer for Fourier transformation to be carried out (Stuart, 1996). One of the great advantages of infrared spectroscopy is that virtually any sample in nearly any state can be studied. Liquids, solutions, pastes, powders, films, fibres, gases and surfaces can all be examined by a judicious choice of sampling technique. The IR spectrum is usually presented as a graph of absorbance (A) or % transmittance (T), the percentage of the energy of the radiation of a particular wavelength that is not adsorbed by the sample – versus radiation’s wavenumber. The absorbance and transmittance fulfill Beer-Lambert law (Stuart, 1996).

For the purpose of this study a Bruker® IFS 66/S FTIR spectrometer was used to characterise all the samples synthesised in this study. The samples were prepared by chemical methods using a bottom up approach, followed by dissolution in a 5 ml DMF solution and drop coat 5µL to the surface of the electrode. This process was left overnight for drying. The FTIR

spectra were recorded in the region $4000 - 100 \text{ cm}^{-1}$. This method allowed for characterisation of the vibrations in the molecules by measuring the absorption of light of certain energies that correspond to the vibrational excitation of the molecules from lower to higher states (Somerset *et al.*, 2010).

3.3.2.3 Raman Spectra

Raman spectroscopy was used to study vibrational, rotational, and other low frequency modes in a system. It relies on inelastic scattering, or Raman scattering of monochromatic light, usually from a laser in the visible, near infrared, or near ultraviolet range. The main generic apparatus of a Raman spectroscopy experiment are: excitation source (laser), optical components, spectrometer, and the processing system (CCD detector and computer). A typical Raman experimental setup is shown in Figure 29. Almost all experiments utilise some variation of this basic setup (Chalmers & Griffiths., 2002).

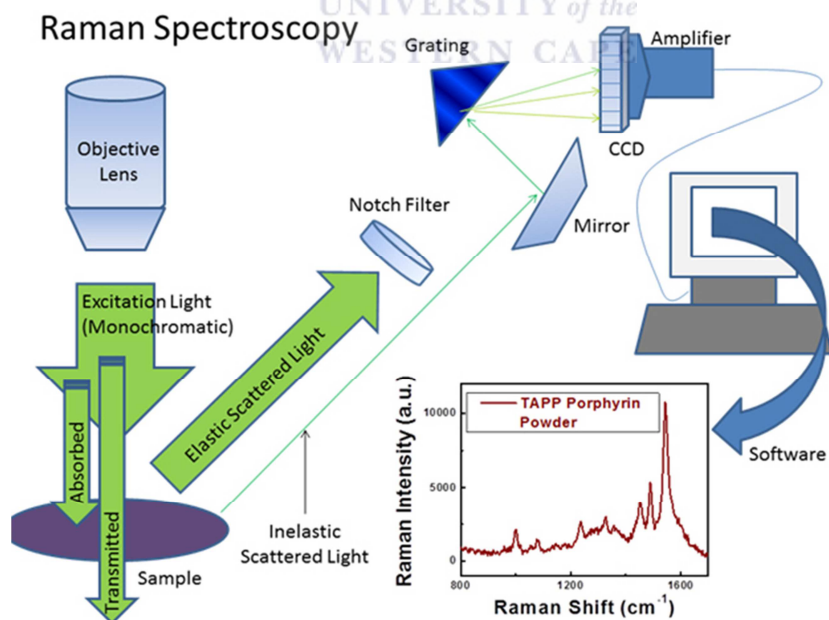


Figure 29. Schematic illustration of a Raman set up system (Halvorson, 2010).

The laser light interacts with phonons (quantised modes of vibration) or other excitations in the system, resulting in the energy of the laser photons being shifted up or down. The shift in energy gives information about the vibrational modes in the system. The resolution of the Raman spectra can be enhanced by accumulated scans with a longer exposed time. In the study of graphene and graphene-related materials, carbon atoms are only bonded into a sp^2 arrangement forming C-C single bonds, which infrared spectroscopy is unable to detect. This makes Raman spectroscopy really helpful in determining ordered and disordered crystal graphitic structures as supporting evidence for the formation of graphene nanosheets and, also, to distinguish antimony nanoparticles and reduced graphene-antimony nanoparticles. In Figure 30 schematic diagrams showing the different scattering process in which an incident photon may take part. When light is incident on a sample, absorption, transmission and scattering may occur. Scattering may occur such that there is no change in the wavelength of the incident radiation (Rayleigh scattering) or there may be a small positive or negative change in the frequency of the scattered radiation (Hollas, 2004).

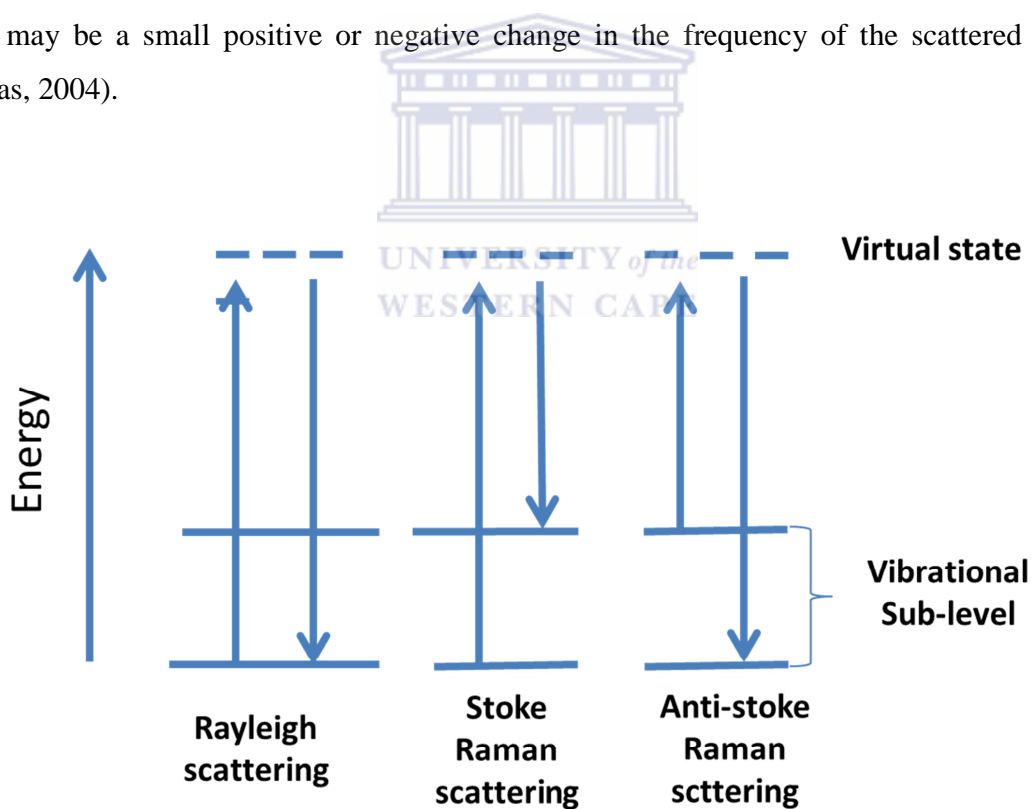


Figure 30. Schematic diagram showing the different scattering processes in which an incident photon may take part (Adapted from reference Hollas, 2004).

This small change in frequency occurs due to the Raman Effect and was first postulated by Smekai in 1923 and first observed experimentally in liquids in 1928 (McCreery, 2000). The origin of the Raman effect may be conceived as a scattering of incident photons through a 'virtual state' (Figure 30). The change in the frequency of the scattered radiation is associated with the exchange of quanta of vibrational energy between the incident photons and the lattice. Energy may be either lost by the photons to the lattice (Stokes line) or gained (Anti-Stokes line). Stokes lines occur when the scattered photons have less energy than the incident photons and the difference in the energy will create a phonon. These Stokes lines will have a longer or redder wavelength than the incident light. In general the Stokes lines are considerably more intense than the anti-Stokes lines at standard temperature, since the lowest vibrational states have more occupation probability. Stokes radiation is usually used since it is higher in intensity than the Anti-Stokes radiation due to the higher population of lower vibrational states at typical sample temperatures. The magnitude of the 'Stokes-shift' is therefore a measure of the (quadrupole-active) vibrational excitations of the sample and a Raman spectrum can be used to infer structural information about the sample (Ferraro, 2003).

The energy levels of molecules are explored by examining the frequencies present in the radiation scattered by molecules. During a scattering event, (1) an electron is excited from the ground to an excited (often virtual) state by absorbing a photon, (2) stimulated emission of a photon induced by a second photon occurs, as the excited state transforms back to a specific vibrational level in the ground state. About 1 in 10⁷ of the incident photons collide with molecules, give up some their energy, and emerge with a lower frequency (Atkins, 1998). These photons produce what are referred to as Stokes lines in the spectrum of the scattered radiation shown in Figure 30. A small fraction of the scattered fraction photons gains energy in striking a molecule in the sample and emerges with a higher frequency; these photons produce what are referred to as anti-Stokes lines in the spectrum of the scattered radiation. If the scattered photons have the same frequency as the incident photons, this is called Rayleigh scattering. There are a number of types of Raman spectroscopy such as resonance Raman, stimulated Raman, surface enhance Raman, tip-enhance Raman and polarised Raman (Ferraro, 2003).

The Raman spectroscopy measurements presented in Chapter 4 were carried out at our laboratory, SensorLab, UWC using a Dilor XY-multi-channel Raman spectrometer, with a 514.5 nm Argon ion excitation laser. In order to reduce heating effects and degradation of the samples

the laser power was set at 100 mW, thereby only probing at about 100 nm depth of the sample surface. The samples were prepared by drop deposition of each of the suspensions onto a separate glass microscope slide. These samples were examined without further preparation. The Raman scattering measurements were performed in ambient atmosphere and at room temperature. The sample was simply placed on the sample holder followed by taking a signal. At least three spectra were taken at different regions of each sample to ensure that the spectra really are typical of the sample (Qi and Berger, 2006).

3.3.3 Electrochemical Characterisation

3.3.3.1 Cyclic Voltammetry

In the research project reported in this thesis, we learned how to use voltammetry to determine an analyte's concentration in a variety of different samples. We also use voltammetry to characterize an analyte's properties, including verifying its electrochemical reversibility, determining the number of electrons transferred during its oxidation or reduction, and determining its equilibrium constant in a coupled chemical reaction. Cyclic Voltammetry was used as a characterisation technique. All CV tests were conducted on an electrochemistry workstation. Figure 31 shows schematic representation of standard three electrodes set up.

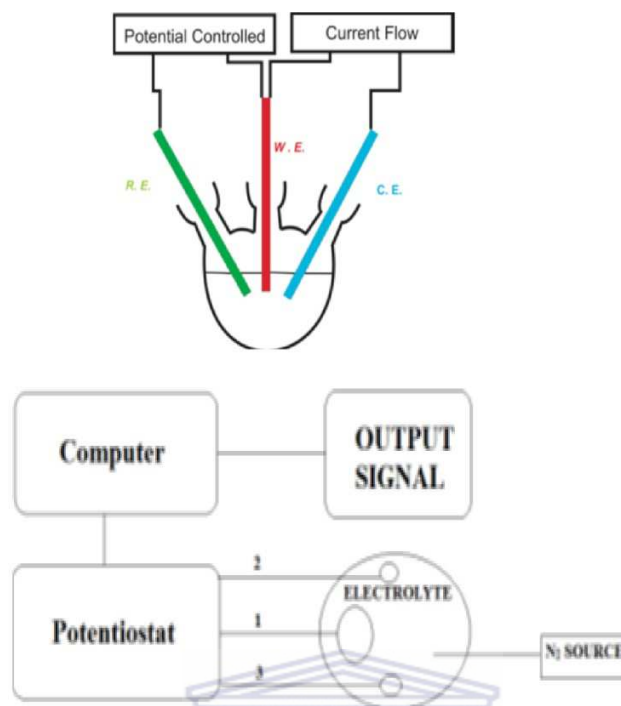
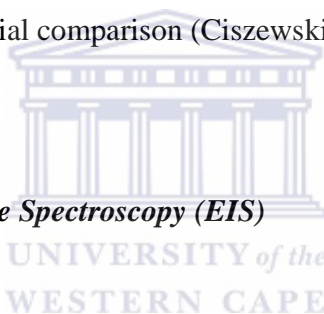


Figure 31. Schematic representations of standard three – electrode and experimental set up for the electrochemical characterisation. 1. Working electrode; 2. Reference electrode; 3. Counter electrode. (<http://compton.chem.ox.ac.uk/index.php?title=research&topic=fund>).

In cyclic voltammetry we complete a scan in both directions. Cyclic voltammetry experiments are conducted in quiescent solutions using large (millimetric dimension) electrodes such that diffusion normal to the electrode is the major form of mass transport. Because we carry out cyclic voltammetry in an unstirred solution, the resulting cyclic voltammogram should have peak currents instead of limiting currents. The voltammogram has separate peaks for the oxidation reaction and the reduction reaction, each characterized by a peak potential and a peak current. A standard three electrode cell with a platinum counter electrode and an Ag/AgCl reference electrode in 0.1 M HCl prepared with deionised water ($>18 \text{ M}\Omega \text{ cm}$). The rGO-SbNPs film was cycled between 0.6 and -1.2 V (vs. Ag/AgCl) in order to make the film hydrophilic and achieve steady state voltammograms. This step as primarily used for rGO-SbNPs catalyst films that required at least 10 CV cycles before exhibiting hydrophilicity. rGO-SbNPs on the other hand are easily wettable due to the presence of positively charged antimony groups on the surface and to the existence of more edge plane sites. When we oxidise an analyte at the working

electrode, the resulting electrons pass through the potentiostat to the auxiliary electrode, reducing the solvent or some other component of the solution matrix. If we reduce the analyte at the working electrode, the current flows from the auxiliary electrode to the cathode. In either case, the current from redox reactions at the working electrode and the auxiliary electrodes is called a faradaic current. A faradaic current due to the analyte's reduction is a cathodic current, and its sign is positive. An anodic current is due to an oxidation reaction at the working electrode, and its sign is negative. Although the potential at the working electrode determines if a faradaic current flows, the magnitude of the current is determined by the rate of the resulting oxidation or reduction reaction. Two factors contribute to the rate of the electrochemical reaction: the rate at which the reactants and products are transported to and from the electrode, what we call mass transport and the rate at which electrons pass between the electrode and the reactants and products in solution. Voltammetry results will also give some support to the impedance spectroscopy analysis for the material comparison (Ciszewski *et al.*, 2014).



3.3.3.2 Electrochemical Impedance Spectroscopy (EIS)

In brief, EIS operates by applying a small sinusoidal potential or current perturbation to the electrochemical interface while simultaneously measuring its response (Figure 32).

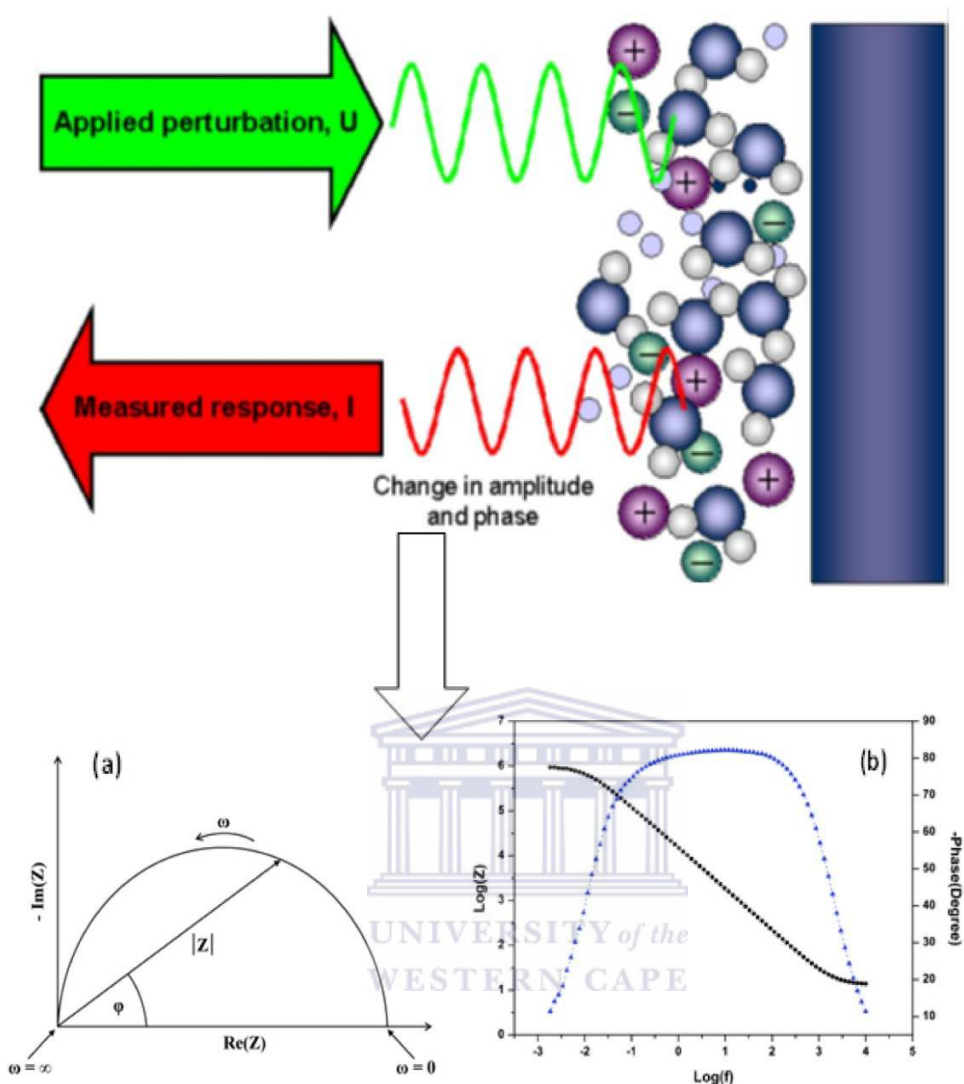
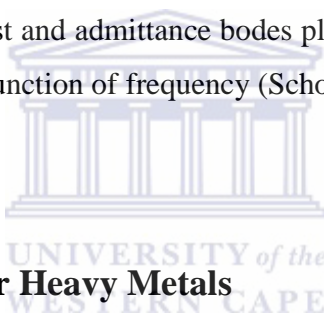


Figure 32. Schematic descriptions of principles of electrochemical impedance spectroscopy with representation of impedance data in a) Nyquist and b) Bode Nyquist plot format (Brett, 1993).

This method represents a powerful tool for the investigation of electrical properties of the material and interface at the working electrode. It is used for study of the kinetics of charges in the bulk and in the interface region, charge transfer of ionic or mixed ionic conductors, corrosion inhibition and capacitance of coating (Scholz, 2005). The resistive and capacitive characteristics of the interface can be evaluated by analysing the impedance response in a wide frequency range, provided that the analytical constraints are fulfilled. The strength of EIS lies in the fact that it is essentially a steady-state technique that is capable of accessing electrochemical processes whose relaxation times vary over many orders of magnitude (Bockris, 1999).

Impedance spectroscopy works by measuring changes to such a signal due to the impedance of the half cell. By measuring at various frequencies we can get an impedance spectrum. These measurements can then be analyzed by fitting to an equivalent electrical circuit model. Data from an impedance spectrum can be shown as either a Nyquist plot. A Bode plot shows the absolute impedance ($|Z|$) and the phase (θ) frequency on the x-axis. It can also be used to show the real impedance (Z') and the imaginary impedance (Z'') against frequency. A cell was used with a platinum wire as a counter electrode, GCE and SPCE substrate as the working electrode and with Ag/AgCl as a reference electrode. The measuring technique principles state that a small time dependent perturbation is given to an electrochemical signal at which the response is linear to record the response signal and to neglect harmonic generation and frequency mixed products. EIS was used at an open circuit dc potential = 0 mV, with a superimposed 5 mV AC potential was applied and scanned a frequency range lying between 0.1 Hz and 1000000 Hz. The outputs were plotted in Nyquist and admittance bodes plot showing a variation of phase and the Impedance of the sample as a function of frequency (Scholz, 2005).



3.4 Detection Methods For Heavy Metals

3.4.1 ICP–AES Analysis

In atomic emission spectroscopy (AES) the sample solution is nebulised and sprayed into an atomiser: flame, inductively coupled plasma, direct current arc, or graphite furnace. The energy source in this case, must cause not only atomisation, but also excitation of electrons to elicit electromagnetic emissions. The emission intensity is dependent upon the analyte concentration. The emission spectrum of each element has a unique complex characterisation; a monochromator capable of scanning wavelengths is required. A polychromator may also be used for multiple element analysis. In this sense AES differs from AAS because sequential or simultaneous of multiple elements is possible. AES has advantages over AAS in cost and convenience when the number of elements surpasses ten at a time. Since AES utilises higher

energy sources there is greater atomisation of the sample thus matrix interferences are lowered; however, at increased temperatures more elements will emit spectra at higher temperatures so spectrometers must be more elaborate (Alloway *et al.*, 1990; Fifield and Haines, 2000).

3.4.2 ICP–MS Analysis

With mass spectroscopy, the sample is ionised in one of a number of ways. The ions are then separated by passing them through a magnetic field in a vacuum, and detected according to their charge to mass ratio.

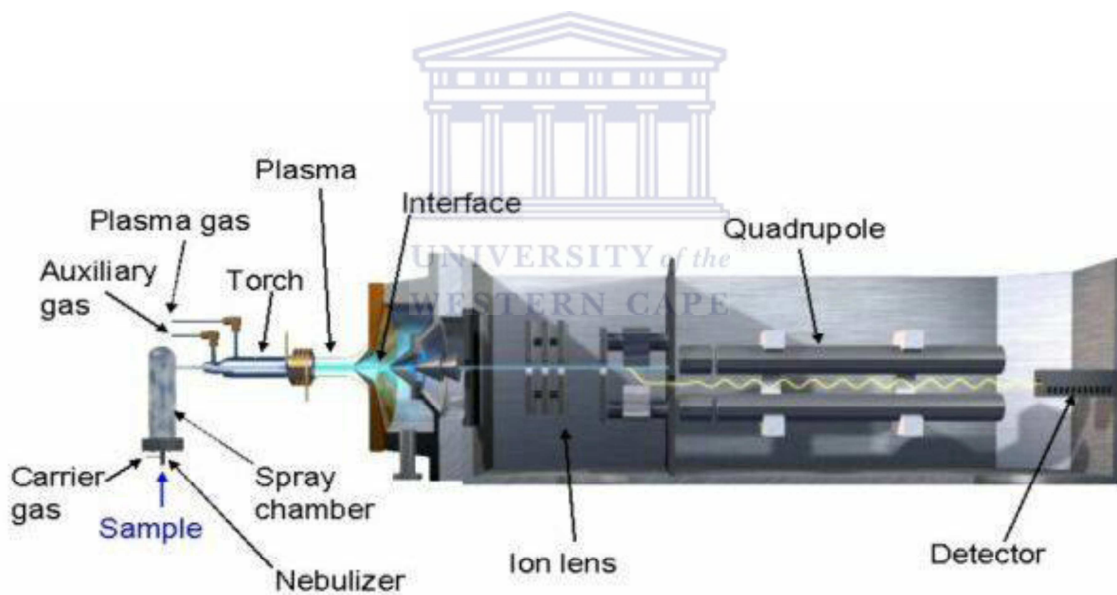


Figure 33. A diagram showing the cross section of the different components of modern quadrupole ICP-MS (Wum, 2012).

An inductively coupled plasma (ICP) as ion source is used primarily for the analysis of heavy metals. The plasma is at a temperature of more than 10000 K composed of a mixture of native argon and ions with free electrons. A large fraction of the sample introduced will be

ionised in this environment. The sample is usually introduced via nebulisation (a fine spray) after extraction into a liquid phase such as aqueous acid. The technique is highly sensitive. Mass Spectroscopy can also be used for molecular identification. If an ionization process is less severe molecules are broken into ionised fragments in ratios dependent on the molecular structure. These can be separated in the magnetic field and measured together to generate a distinctive spectrum (with a peak for each fragment). For this technique to be feasible complex molecular compositions need to be separated first. For this, gas chromatography (for volatiles) or high performance liquid chromatography (for dissolved species) can be used (Wum, 2012).

3.4.3. Stripping Voltammetry

Stripping voltammetry is a sensitive electroanalytical technique for the determination of trace amount of metals in solution.

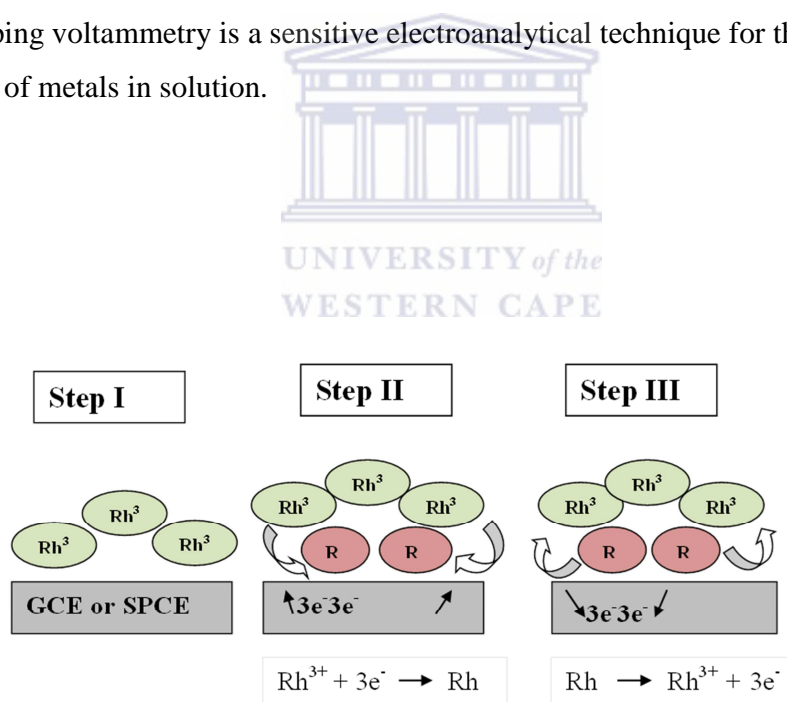


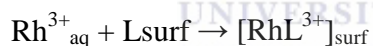
Figure 34. Steps in Adsorptive Stripping voltammetry Electroanalysis (Adapted from Wang *et al.*, 1996).

The techniques consist of 3 steps: First, metal ion are deposited onto an electrode which is held at a suitable potential. The solution is stirred during this step to maximize the amount of metal deposited. Secondly, stirring is stopped so that the solution will become steady. Thirdly, the metal deposited is stripped from the electrode by scanning the potential. The observed current during the stripping step can be related to the amount of the metal in the solution. The stripping step may consist of a negative or a positive potential scans, creating either cathodic or anodic current respectively. Hence, Cathodic Stripping Voltammetry and Anodic Stripping Voltammetry are two specific stripping techniques.

The aim of the stripping voltammetric experiments in this thesis was to drop coat rGO-SbNPs on the surface of a carbon surfaces, insert in a solution containing complexing ligands (DMG), to achieve lower detection limit compared to the similar methods published before. The mechanism of adsorption was described by Wang et al (1996) as:

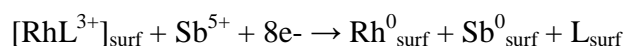
The metal M^{n+} reacts with a ligand L to form the complex in solution, in the case of PGMs, e.g Rh^{3+} .

Accumulation at open circuit:



The complex is then adsorbed onto the electrode surface

Reduction:



The adsorbed metal is stripped back to the solution

Oxidation (stripping):



L: DMG

Sodium acetate buffer (0.2 M, pH = 5.2) solution was used as voltammetric background electrolyte.

Chapter 4

Synthesis and Characterisation of Reduced Graphene Oxide Antimony Nanoparticles

4.1 Introduction

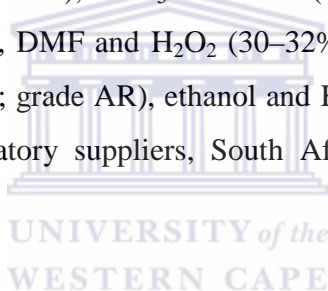
This chapter demonstrates some aspects on synthesis and characterisation of nanocomposite of carbon and antimony using polyvinyl alcohol as a stabiliser which combines high surface area and superior hybrid properties. The general aim of characterisation is to confirm and improve ideas and models of the materials synthesised. Well-defined models and structures not only tell things about a specific point in a reaction chain, but details about the precursor (graphite), possible products (modifications), and also about the reactions and procedures between them. Taking into account the importance of these materials, many studies aimed at improving the synthesis process have been conducted. A brief discussion on processing of nanocomposite is also presented. The present experimental design is to synthesise nanocomposite of reduced graphene oxide and antimony nanoparticles to be used as thin films for planar and disc carbon electrodes for enhancing sensing of different toxic metal pollutants in the environment. Reduced graphene oxide was used as a support for nanoparticles of antimony. This nanocomposite will effectively enhance electron transfer and promote response in sensing platform for toxic metal ions. The synthetic process of reduced graphene oxide was done using the modified Hummers method while antimony pentachloride was reduced with sodium borohydride into nanoparticles of antimony using polyvinyl-alcohol as a stabiliser. The systematic investigation of morphology was done by scanning electron microscope and high resolution-transmission electron microscope which revealed the synthesis of product possesses of reduced graphene oxide antimony nanoparticles. Elemental analysis has been done with energy dispersive X-ray spectroscopy on the high resolution-transmission electron microscope which proved expected elements in the nanocomposite. The detailed structural characterisation was performed by Fourier transform infrared spectroscopy and Raman spectroscopy. The

investigation of the electrochemical behaviour of reduced graphene oxide antimony nanoparticles coated on glassy carbon electrodes was carried out by voltammetric and impedance techniques. The impedance spectroscopy gave some support for the analyses for the material by evaluate the physical elements in the form of an electrical circuit model. Doing so, we can understand the double layer and the Faradaic components of the system.

4.2 Experimental section

4.2.1 Chemicals and reagents

Graphite (fine powder synthetic), SbCl_5 and PVA (99%) were purchased from Sigma-Aldrich, USA. HCl fuming (32%), DMF and H_2O_2 (30–32%; grade AR) were purchased from Merck, South Africa. H_2SO_4 (98%; grade AR), ethanol and KMnO_4 (grade AR) were purchased from Kimix Chemical and laboratory suppliers, South Africa. All chemicals were used as received.



4.2.2 Synthesis of reduced graphene oxide

rGO was exfoliated from natural graphite flake via a simplified Hummer's method. In a typical synthesis, graphite powder (1,2 μM ; 2g) and NaNO_3 (1 g) were subjected to an oxidative treatment with KMnO_4 in concentrated H_2SO_4 (120 mL) under constant stirring in an ice bath. The KMnO_4 (7.5 g) solution was added slowly with stirring and cooling, so that the temperature of the mixture was not allowed to reach 20 °C. The mixture was then stirred in water bath at 35 °C for 2 h, and distilled water (920 mL) was added. Upon oxidation, graphite oxide was exfoliated to GO, resulting in a brownish gel-like solution. After 15 min, the reaction was terminated by the addition of a large amount of distilled water (2 L) and 30% H_2O_2 solution (10 mL), in order to reduce the residual KMnO_4 . The colour changed from dark brown to bright yellow indicating the formation of graphene oxide. The mixture was then filtered and washed with a 1:10 HCl solution (3 L) in order to remove any metal ions.

In Hummer's method the final step is washing with acetone and distilled water until the pH was neutral. The resulting GO was dried in a vacuum oven (60 °C) to get a loose, light brown powder. Finally, rGO was prepared by dispersing 10 mg of the prepared GO in a 30 ml DMF/water (9:1 v/v) solution, while slowly adding drop wise 2 mL of 0.118 M aq. NaBH₄ for 1 h. Thereafter, the mixture was ultra-sonicated for 1 h. The rGO dispersion was then washed with ethanol and repeatedly with deionised water to remove the remaining NaBH₄ and dried at 60 °C for 4 h in a vacuum oven (Tang *et al.*, 2013; Gao *et al.*, 2011).

4.2.3 Synthesis of Antimony nanoparticles

Antimony nanoparticles were prepared by drop wise adding a solution of 0.175 M SbCl₅ into PVA used as a stabiliser, activated with DMF. NaBH₄ was used as a reducing agent. Typically, 1.8 M NaBH₄ aqueous solution was added all at once into the mixture of 3 g PVA, 10 mL DMF and 0.175 M SbCl₅ constant stirring then allowed to age in darkness at room temperature for 8 days. Finally the nanoparticles were refluxed and the powder was washed, separated and dried at ambient temperatures for 2 h.

UNIVERSITY of the
WESTERN CAPE

4.2.4 Preparation of nanocomposite

The composite of rGO support containing SbNPs have been synthesised for the first time in this study. Briefly synthesis of the reduced graphene oxide impregnated antimony nanocomposite was performed using PVA as a stabiliser.

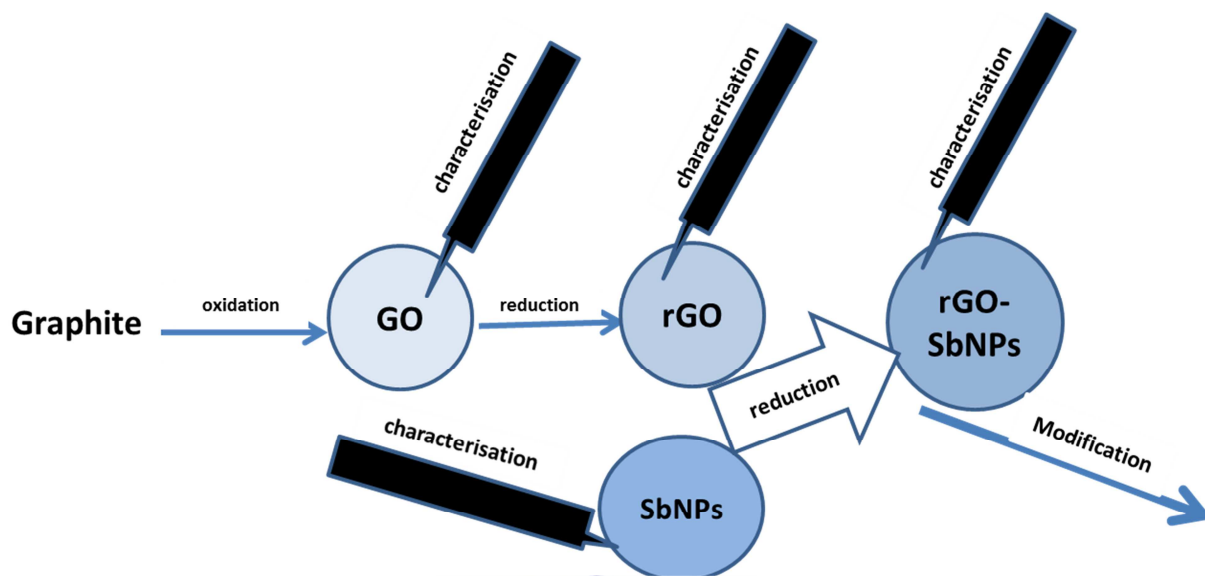


Figure 35. Scheme illustrating the examination and characterisation of rGO-SbNPs composites.

Thus, a suspension containing a ratio in weight of 10:4 (rGO/PVA), *i.e.* 100 mg of rGO and 40 mg of PVA were loaded in 250 mL round bottomed flask charged with 100 mL of ethanol pure grade and sonicated for 20 min. An excess of sodium borohydride (80 mg of NaBH_4) was then added in this suspension and sonicated for a further 20 min. A solution containing 0.118 M (2mL of SbCl_5) was slowly dropped onto the mixture, which was kept under constant stirring. Once the reaction was complete, the rGO-SbNPs nanocomposite was dispersed using an ultrasonic probe for 1 h. Finally, the rGO-SbNPs was filtered through a 0.45 μm Millipore nylon filter membrane under a vacuum and washed with ultrapure water. The formed nanocomposite was then dried in a vacuum for 24 h at 60 °C.

4.2.5 Preparation of the electrodes

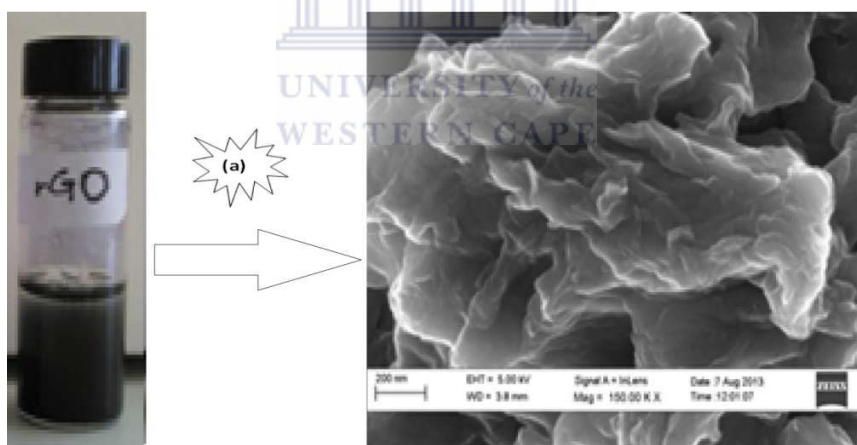
Prior to modification, the GC electrode surface was first polished with 0.3 μm alumina slurries, rinsed thoroughly with double-distilled water, sonicated for 5 min in ethanol and 5 min in water, and dried in air. A nanocomposite of rGO-SbNPs was prepared by dispersing 1 mg of

the rGO–SbNPs in 1.0 mL of DMF by ultrasonication agitation for about 10 min. A 5 μ L aliquot of this dispersion was dropped onto the GC electrode surface and left to dry overnight. After modification the surface of the electrode was carefully washed with distilled water. For comparison, a GC electrode was modified with rGO, SbNPs and rGO-SbNPs, which was individually characterised using voltammetry.

4.3. Results and discussion

4.3.1 Scanning Electron Microscope (SEM)

The morphology of the rGO, SbNPs, and rGO-SbNPs were characterised using SEM and the results are depicted in Figure 1(a), (b) and (c).



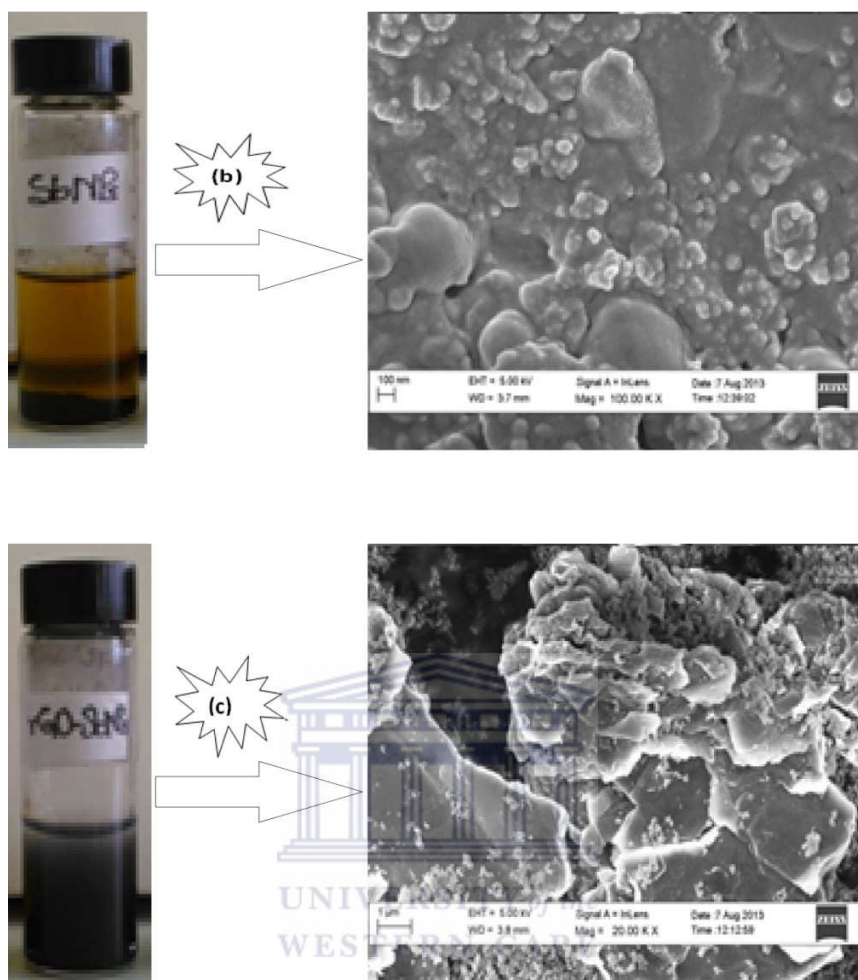


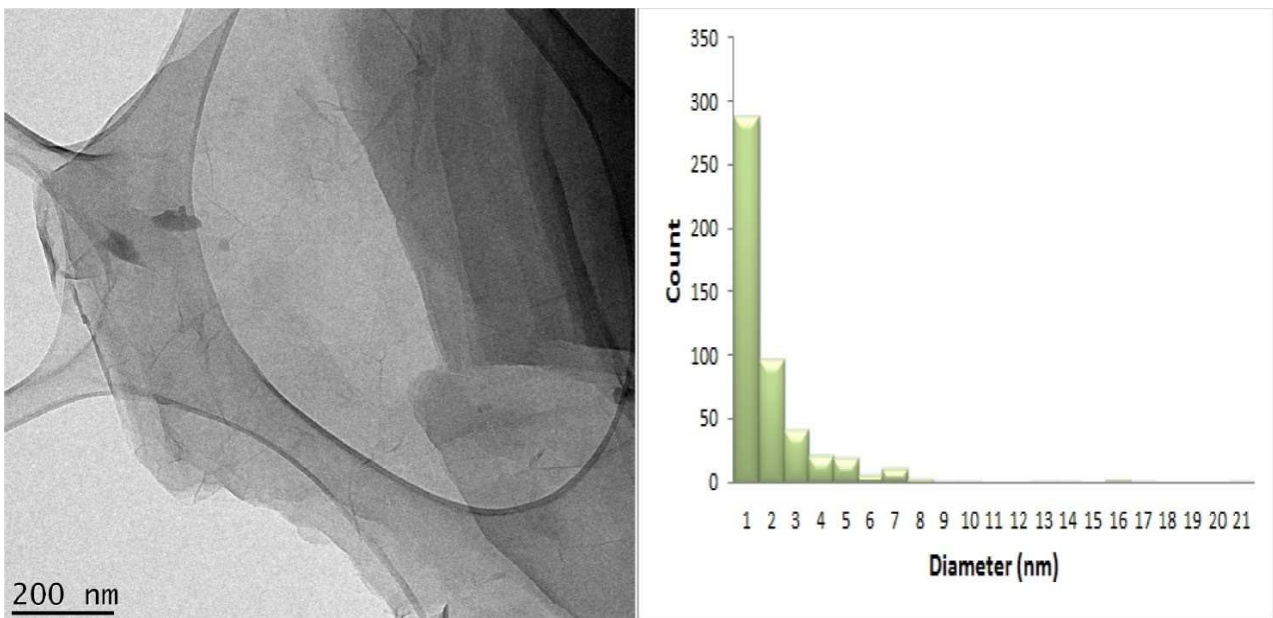
Figure 36. SEM image of (a) rGO, (b) SbNPs and (c) rGO-SbNPs with images showing ethanol dispersions of antimony nanoparticles (SbNPs), reduced graphene oxide antimony nanoparticles (rGO-SbNPs) and reduced graphene oxide (rGO).

A schematic diagram is shown in Figure 36 for better understanding and comparison of the structures of the synthesised composites. The rGO, SbNPs and the nanocomposite of rGO-SbNPs can also be observed by the change in colour in the picture images. The surface morphology judgment of the rGO, SbNPs and the nanocomposite of rGO-SbNPs were performed by SEM as shown in Figure 36 (a-c). Figure 36 (a) shows the SEM image of rGO revealing the typical curled morphology that the graphene intrinsically owns, consisting of a thin wrinkled paper-like structure. These results of rGO are in agreement with the studies done by (Fana *et al.*, 2011; Liana *et al.*, 2010; Meyer *et al.*, 2007).

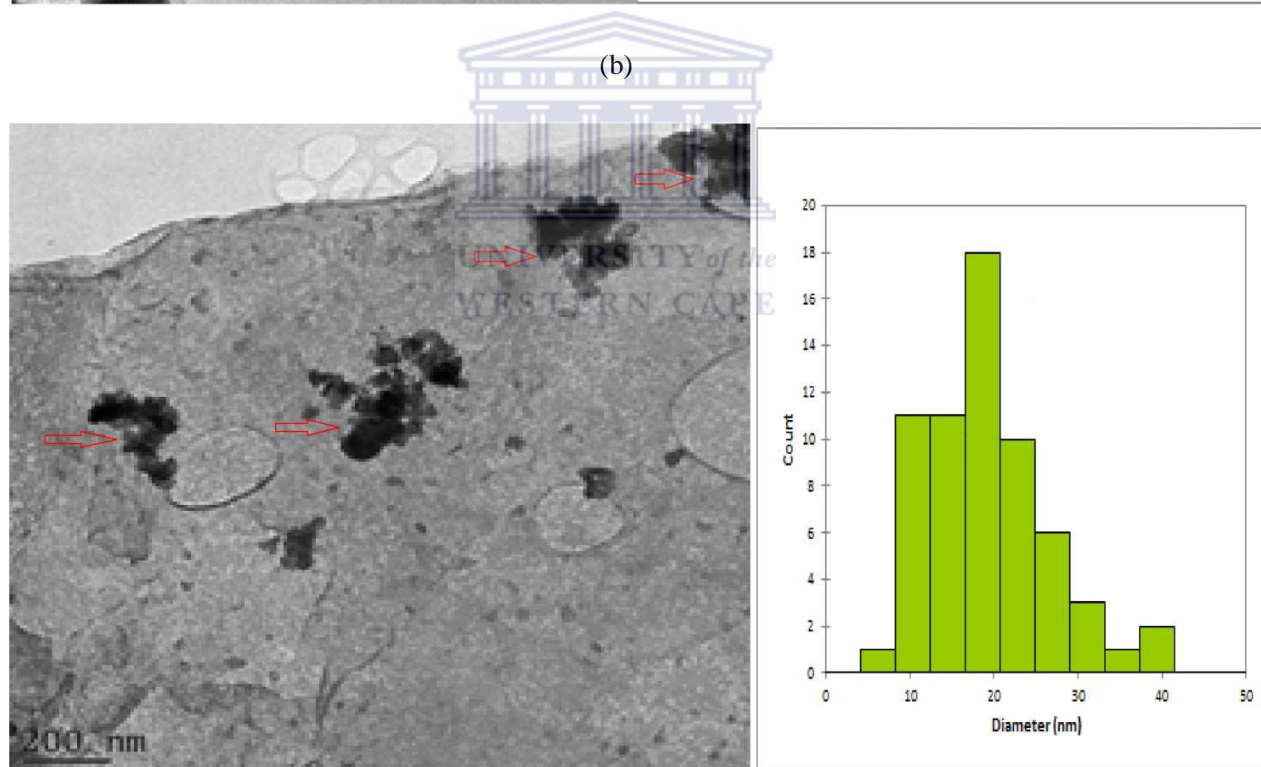
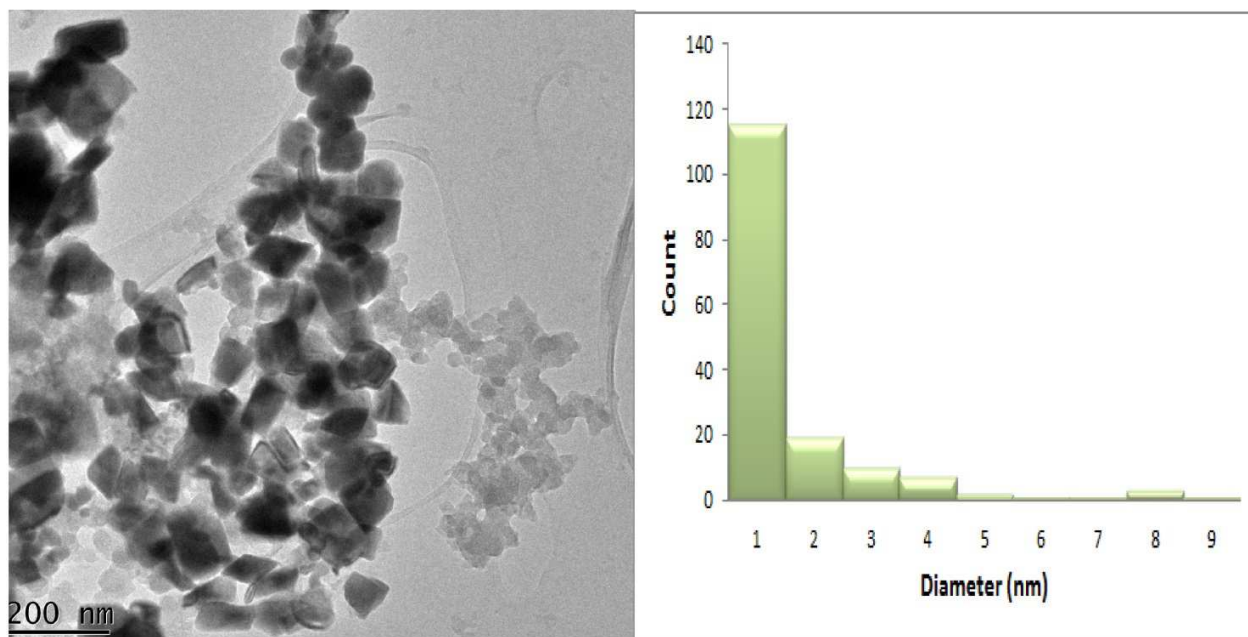
Figure 36(b) shows the SEM image of SbNPs, for which it can be seen that the morphology are spherical with different sizes. This means that the growth begins at different stages and period. The rGO with uniformly SbNPs distributed over the whole surface was observed in Figure 36 (c). The SbNPs can be seen as white spots on the rGO surface, which clearly indicates their coupling. On closer inspection of the SEM image, it appears in a flake-like shape. These thin edges heat up and ignite faster than the rest of the metal powder particle flakes, because of this edginess and the fact that they offer the greatest surface area, are generally the most reactive metal powder particle shape. The surface also exhibits uniform porosity in their structures, which is an important factor for sensing applications. Controlled and optimised process parameters are essential requirements to obtain desired results.

4.3.2 Transmission Electron Microscope

To further confirm the structure of the nanocomposite of rGO sheet, SbNPs and the nanocomposite of rGO-SbNPs, HRTEM analysis were carried out showing the comparative and the images are depicted in Figure 37 (a), (b) and (c).



(a)



(c)

Figure 37. HRTEM images of (a) rGO (b) SbNPs and (c)rGO-SbNPs and the corresponding nanoparticles size distribution.

HRTEM images of rGO sheet, SbNPs and the nanocomposite of rGO-SbNPs (Figure 37) reveal that nanoparticles are polydisperse in size as illustrated in the corresponding histogram. Figure 37 (a) shows the HRTEM image of rGO sheets, which illustrate the flake-like shapes of rGO. The transparent nature of the graphene implies that it is fully exfoliated into single or few-layer sheets. The selected region of HRTEM images revealed that the particles in rGO sheets have the size distribution between 1 and 16 nm with an average size distribution of 1 nm (Figure 37 a), These HRTEM results of rGO are in close agreement with the previous findings (Meyer *et al.*, 2007).

The results for HRTEM also indicate that the SbNPs consist of agglomerates of small grains due to a lack of stabilisation and the results are depicted in Figure 37(b). Figure 37(b) image also shows agglomerates of small grains and some dispersed nanoparticles, which are more or less crystalline. The selected region of HRTEM images revealed that the SbNPs have the size distribution between 1 and 8 nm with an average size distribution of 1 nm in Figure 37(b). Figure 37 (c) depicts a typical HRTEM image of the rGO sheets covered with SbNPs. The SbNPs appear distributed randomly as dark dots on a lighter shaded support in this image. These nanoparticles occupy the whole surface of the graphene sheets. The closely packed distribution of the SbNPs over the rGO nanosheet (indicated by red arrow) is also visible from the corresponding HRTEM image in Figure 37 (c). The nanoparticles remain closely associated with each other and these associations can be rationalised as the “nano-centres”. The latter shows a nanoparticles size distribution centred at about 20 nm with size distributions between 5 nm and 40 nm. The synthesis process led to a narrower particle size distribution being the average diameter at about 1 nm for rGO sheets, SbNPs and 20nm for rGO-SbNPs nanocomposite, as depicted by the corresponding histograms. The HRTEM results for rGO-SbNPs were confirmed with the EDX spectra images depicted in Figure 38. Further energy-dispersive X-ray (EDX) examination during HRTEM analysis in Figure 38 confirms the presence of antimony in the nanocomposite.

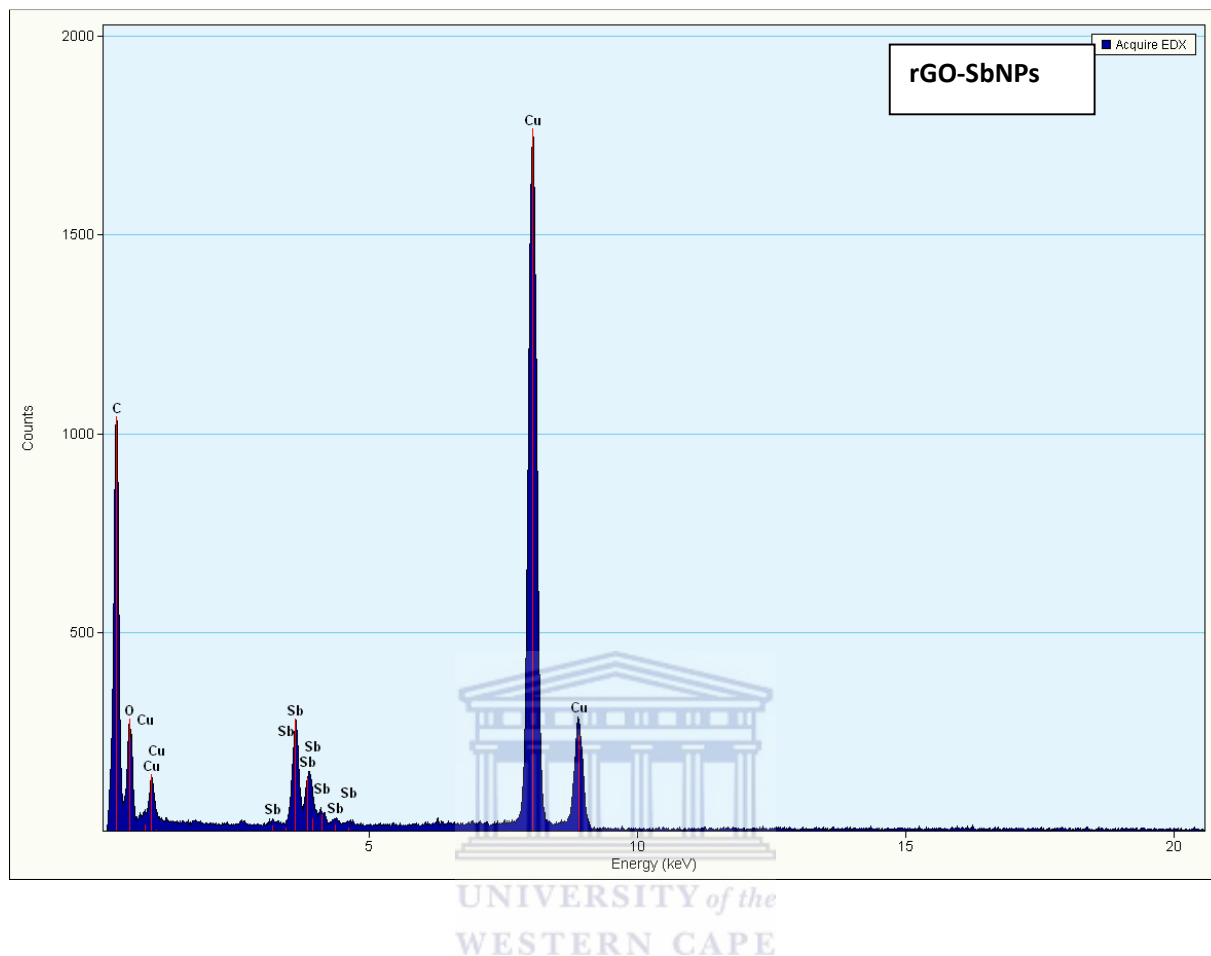


Figure 38. Typical EDX plot obtained for rGO-SbNPs nanocomposite.

The EDX profile of the rGO-SbNPs shows well defined peaks that contain mainly the element Sb, apart from the initial C and O that can be ascribed as rGO and the occurrence of Cu peaks that is ascribed to the grid used in mounting. This confirms the successfully incorporation of rGO supported SbNPs composite. As expected, the graphene gave carbon and oxygen in the spectrum, while Sb confirms the presence of antimony in the composite material.

4.3.3 Fourier Transmittance Infra-Red Spectroscopy

Figure 39 displays the comparative FTIR transmittance spectra of rGO, rGO-SbNPs composite, SbNPs and the GO. The spectra are shifted downwards for easy viewing.

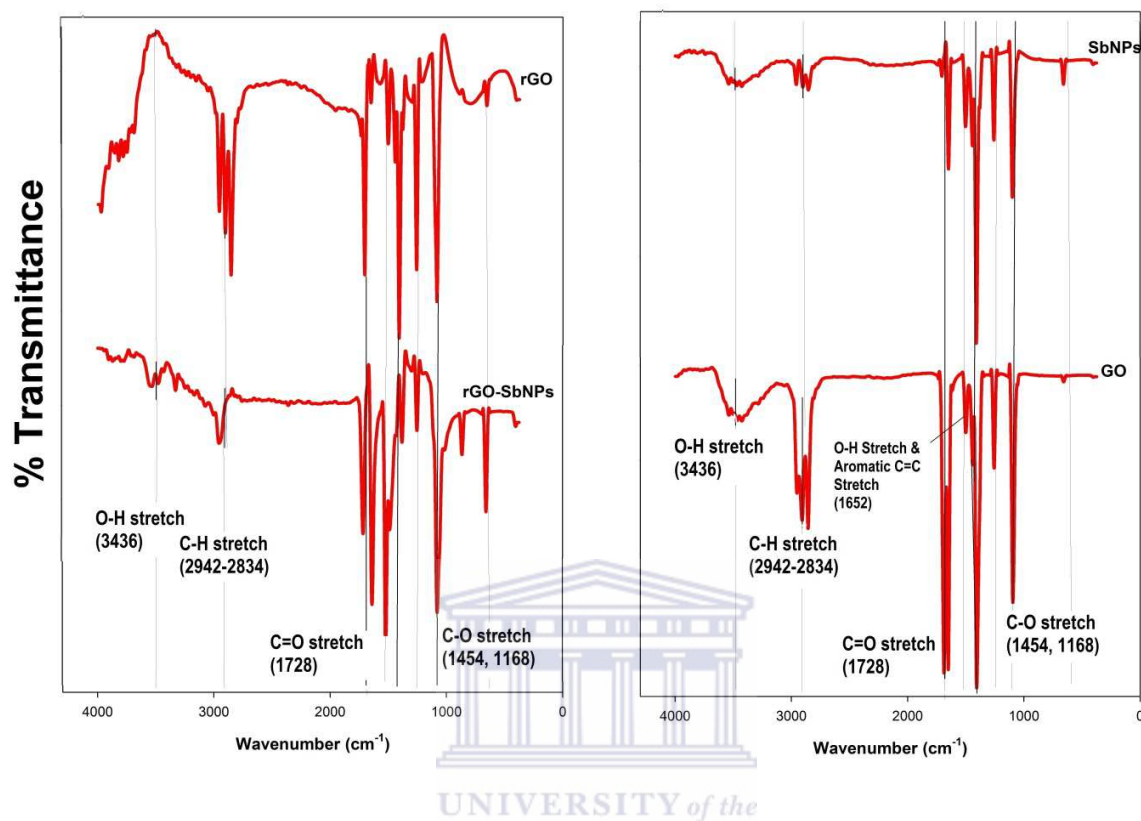


Figure 39. Results obtained for the individual FT-IR spectra of GO, SbNPs, rGO-SbNPs and rGO compounds.

The broad band at 3400 cm^{-1} of GO and SbNPs belongs to the $\nu(\text{-OH})$ vibration and a noticeable decrease in peak intensity at 3400 cm^{-1} in the case of rGO and rGO-SbNPs, implies that a large fraction of the O–H groups was removed. The C–H symmetric and asymmetric stretching vibration frequency modes at 2834 and 2942 cm^{-1} has been seen for GO and rGO. The appearances of these C–H symmetric and asymmetric stretching vibration frequency modes at 2834 and 2942 cm^{-1} in the SbNPs and rGO-SbNPs has been observed to be very small. The band at 1652 cm^{-1} is significant to the deformation vibration of O–H groups. The $\nu(\text{C=O})$ at 1728 cm^{-1} is assigned to the carbonyl and carboxyl moieties. Bending frequencies for $-\text{CH}_3$ asymmetric and $-\text{CH}_3$ symmetric have been identified at 1454 and 1145 cm^{-1} , respectively and 1065 cm^{-1} is assigned to the $\nu(\text{C-O})$ band of the epoxy group. The peak of $\nu(\text{C-O})$ at 1065 cm^{-1} remained unchanged, whereas the $\nu(\text{C-O})$ peak at 1454 cm^{-1} in rGO-SbNPs decreased, which indicates that

the carbonyl group was partially removed upon chemical reduction. These results of GO and rGO are in agreement with the findings (Wu *et al.*, 2012; Choi *et al.*, 2010). The rGO-SbNPs nanocomposite shows different absorption peaks compared to rGO and SbNPs. This means that there is new bond formed or strong chemical interaction occurring within the nanocomposites.

4.3.5 Raman Spectra

The results obtained for the Raman spectra for each of the composites synthesised in this study are shown in Figure 40.

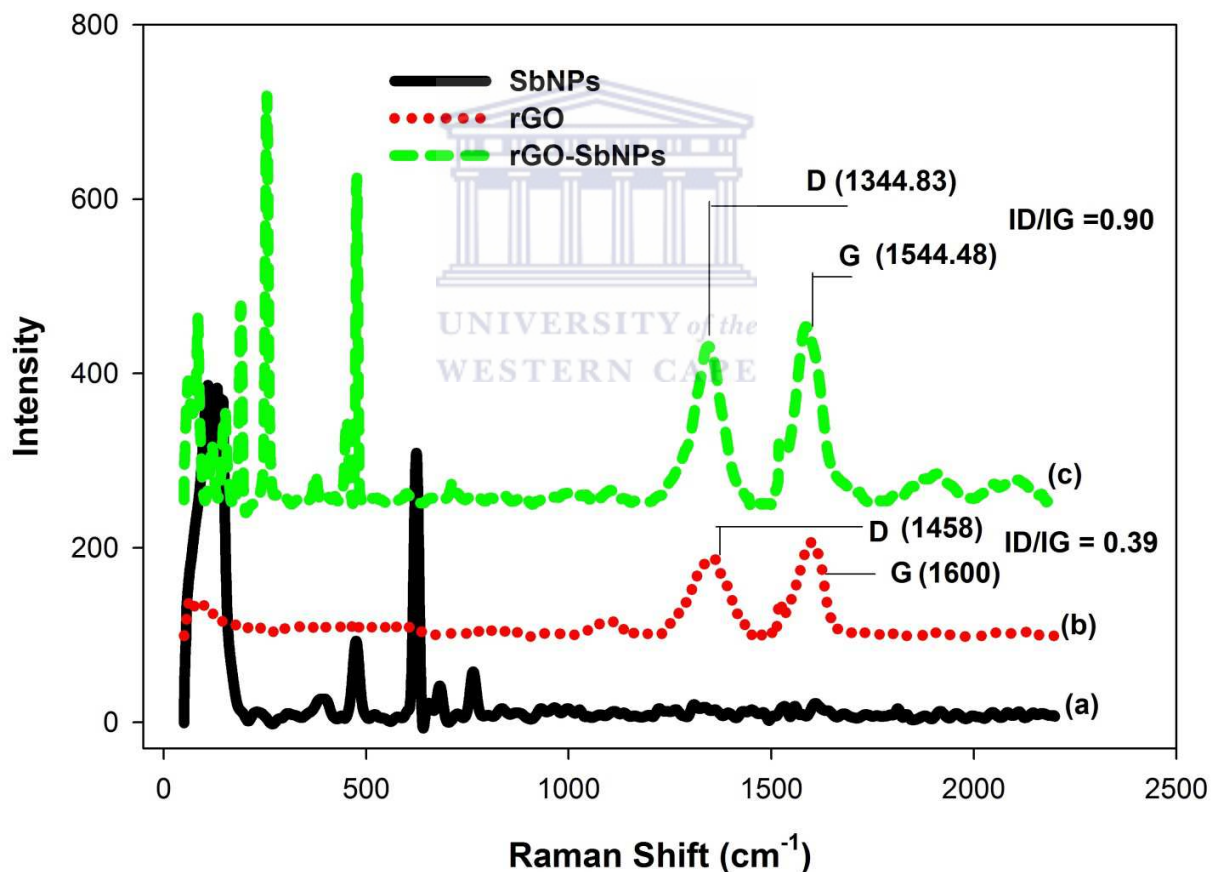


Figure 40. Comparative Raman spectra of rGO, rGO-SbNPs and SbNPs compounds.

The typical features for carbon in Raman spectra are the G-line obtained around 1600 cm⁻¹ and the D-line obtained around 1350 cm⁻¹ in the spectra. The G-line is usually assigned to the E_{2g} phonon of C sp² atoms, while the D-line is a breathing mode of κ-point phonons of A_{1g} symmetry. Extensive studies have determined that the positions, intensities and widths of these bands are dependent on the ordering of the sp² sites in varying compositions of amorphous and crystalline carbon compounds (Vix-Guter *et al.*, 2005; Ferrari and Robertson, 2000).

The corresponding D and G bands in the Raman spectrum of rGO appeared at 1458 cm⁻¹ and 1600 cm⁻¹, respectively while in the Raman spectrum of rGO-SbNPs appeared at 1345 cm⁻¹ and 1584 cm⁻¹, respectively. It is common to all sp² carbon lattices and arises from the stretching of C-C bond. The intensity of the D band is related to the size of the in-plane sp² domains (Guo *et al.*, 2012). The increase of the D peak intensity indicates forming more sp² domains. Moreover, the relative strength of D band compared to G band depends strongly on the amount of disorder in the graphitic materials (Wang *et al.*, 2008). In this case, the D/G intensity ratio of rGO (*ID/IG*) was 0.37, slightly smaller than that of rGO-SbNPs (*ID/IG* = 0.90). This suggest that new (or more) graphitic domains are formed and the sp² cluster number is increased (Guo *et al.*, 2012; Pimenta *et al.*, 2007).

The size of in-plane crystallites is also an important parameter for characterising graphene related materials. For instance, the electrical resistivity is considered to partly arise from the hopping of charge carriers between the crystallite zones (Guo *et al.*, 2012). Obviously, the crystallite size *L_a* should be somehow related to the D peak in the Raman spectrum since it expresses disorder/defect in a system. *L_a* can be expressed by the following equation (Pimenta *et al.*, 2007; Ferrari and Robertson, 2000).

$$L_a = 4.4 \cdot \frac{IG}{ID} \quad \text{Eqn. 4.1}$$

where *IG* and *ID* are the intensities of the G and D peak, respectively. This simplified relation allows the direct calculation of *L_a* from the Raman spectrum. The *L_a* 11.88 and 4.95 for

rGO and rGO-SbNPs, respectively were calculated which suggests larger crystalline zone in the rGO. One may therefore consider rGO-SbNPs to be the nanocomposite best suited for further study of various chemical and electrochemical properties.

We found that the rGO in Figure 40 (a) gave a similar Raman spectrum in terms of the shapes and positions of Raman peaks as can be seen in Figure 40. These results agreed very well with that obtained by Ferrari *et al.* (2007) and the studies by Das *et al.* (2008). Raman spectrum obtained from the synthesised SbNPs, indicating that the main features of the wave-number are observed at about 110 ; 140 ; 578 ; 624 ; 655 ; 681 and 764 cm^{-1} . These results are in fairly agreement with previous findings (Zeng *et al.*, 2004)for the Sb_2O_3 nanoparticles. Figure 40 (b) shows the Raman spectrum of the newly synthesised rGO-SbNPs composite, which is clearly reproducing the Raman spectrum of both of the individual rGO and SbNPs Raman spectra, thereby confirming the structure of the rGO-SbNPs composite.

4.3.5 UV Vis Spectra

The successful synthesis of SbNPs, rGO, rGO-SbNPs compositewas confirmed by UV-visible spectroscopy as shown in Figure 41.



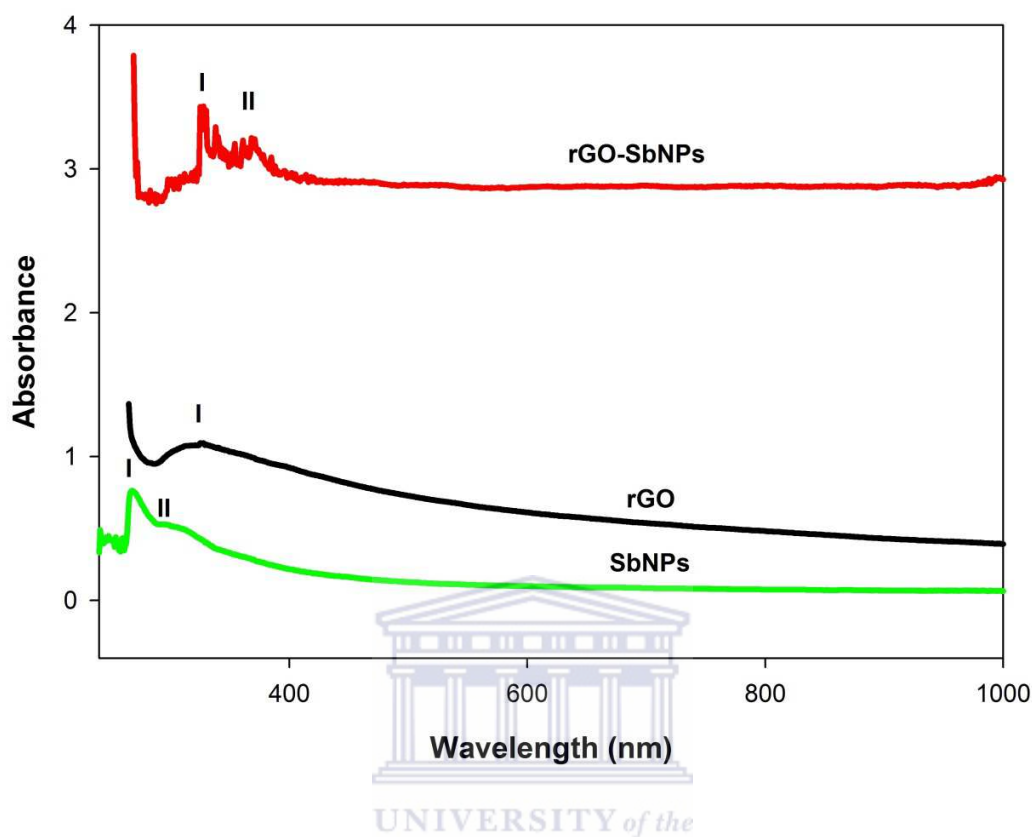


Figure 41. UV-Vis absorption spectra of SbNPs, rGO and rGO-SbNPs compounds.

The UV-visible spectrum of antimony nanoparticles (SbNPs) in DMF shows a characteristic absorption peak at 270 nm and a weak shoulder at 290 nm (Firdhouse and Lalitha, 2013). From different studies it was found that the rGO showed an absorption peak at around 260 nm (Zhu *et al.*, 2012). From our studies we found the UV-visible spectrum of reduced graphene in DMF shows one characteristic absorption peak at 300 nm corresponding to C=O bonds (Firdhouse and Lalitha, 2013) as shown in Figure 41. The absorption spectrum of rGO-SbNPs nanocomposite showed a characteristic absorption peak at 320 and 360 nm.

4.4 Electrode reactions and Electrode Capacitance

The reaction processes that are expected to occur in cyclic voltammetry and electrochemical impedance spectroscopy are explained in Figure 42.

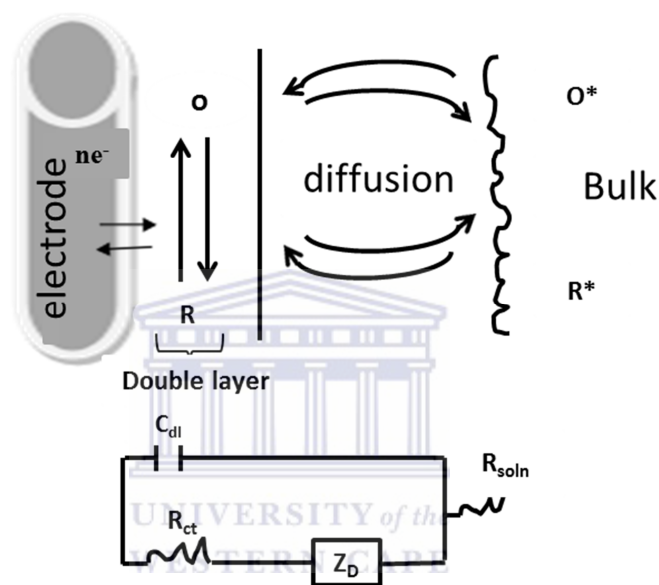


Figure 42. Schematic illustration of transport and kinetic phenomena in electrolytic reactions, drawn along with its equivalent impedance circuit.

Figure 42 describes the process that occurs in simple electrode reactions. In the case of reduction, a species (o) capable of receiving an electron from the electrode diffuses to the surface, receives an electron and diffuses away from the surface. Current at the surface is generated by the transfer of electrons from the electrode to the redox species. In solution current is carried by migrations of ions. Although we need to be aware of capacitive current in cyclic voltammetry, the real power of this technique lies in its ability to investigate mechanisms and potentials of electrode reactions (<http://docslide.us/documents/voltametria-ciclica-2.html>).

In the electro-circuit above, R_s is the solution resistance between the electrodes which is typically much smaller than the other components. R_{ct} is the charge transfer resistance which accounts for the ability of the redox compound to interact with the electrode surface via electron transport. C is the capacitance between the electrode and the charged ions in solution. This capacitance is known as the double layer capacitance which exists between any metal placed in an electrolyte solution. Z_D is an element called the Warburg impedance which accounts for the effects of diffusion in the system. The Warburg impedance itself has both a real and imaginary component and is frequency dependent. The most critical component in the system is the charge transfer resistance R_{ct} . This value is very sensitive to the addition of biomolecules onto the surface of the electrode as they disrupt the charge transport between the redox compound in solution and the metal. The sensitivity of R_{ct} to the conditions on the electrode surface makes impedance spectroscopy one of the best methods to use for detection of binding events on the surface of the working electrode (<http://docslide.us/documents/voltametria-ciclica-2.html>).



4.5. Comparative studies on electrochemical activity

4.5.1. Cyclic Voltammetry

In order to obtain substantial information about electrochemical processes, cyclic voltammetry was used and the results are depicted in Figure 43. Thermodynamic information is related to the formal potentials.

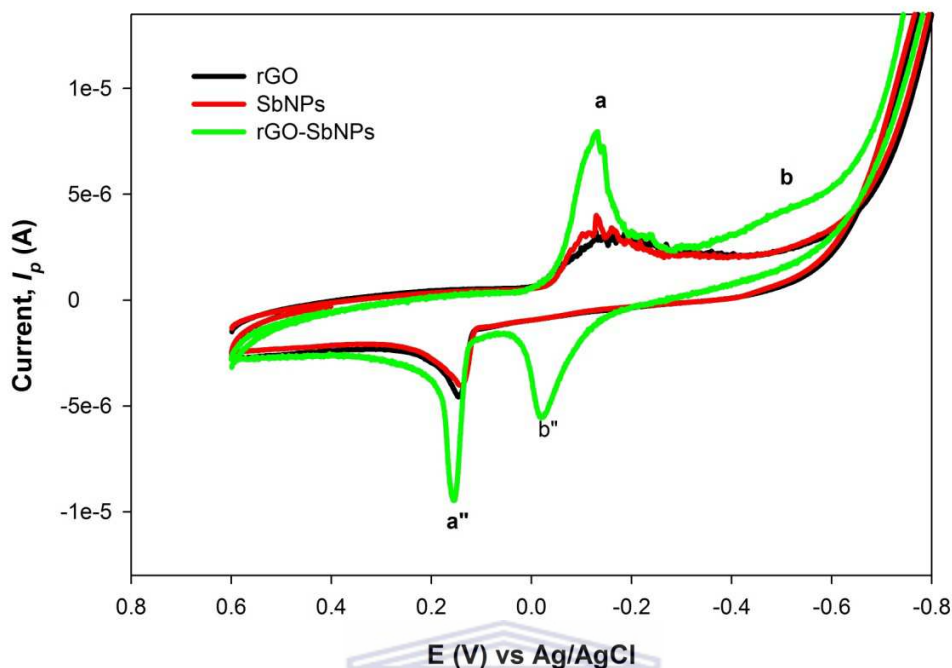


Figure 43. The CVs obtained for a GCE, compared to a rGO modified electrode, SbNPs modified electrode and to a rGO-SbNPs modified. The potential was scanned between 0.6 and -1.0 V (vs. Ag/AgCl) in a 0.1 M HCl solution.

The CV for the responses of the individual rGO, SbNPs and novel nano rGO-SbNPs composites are shown in Figure 43, evaluated in 0.1 M HCl solution at scan rate 50 mV s^{-1} ($S/N = 3$). For the purpose of this study CV remains mostly a qualitative technique as charging current limits CV sensitivity. Therefore, in order to quantify trace metal pollutants at low concentration level, a more effective electro-analytical method was employed. For this reason AdDPCSV, with its selective sampling nature and effective pre-concentration technique was used. The negative current region in the CV curves indicates the cathodic reduction and positive current region refers to the anodic oxidation. The electron transfer behaviour studies at these electrodes using CV of redox couples exhibits well-defined redox peaks. An interesting observation was made for the appearance of a pair of each anodic and cathodic peaks in the CV of the rGO-SbNPs composite. Peaks a and a'' are assigned to oxidation of antimony and reduction of antimony surface oxide, respectively. Formation of b and b' redox peaks were also observed in earlier studies, which is likely due to the experimental conditions and was not fully explained by Hocevar *et al.* (2007). The peak at band b' might be associated to the hydrolysis of antimony and

is pH related, including the scanning effect in a wider potential window according to the previous findings (Hocevar *et al.*, 2007). Anshrafi *et al.* (2012) suggested that very acidic medium of hydrochloric acid must be used to avoid hydrolysis of Sb since in 0.01 and 0.1 M HCl solutions, a peak corresponding to re-oxidation of antimony was observed in previous studies (Anshrafi *et al.*, 2012).

Mares *et al.* (2013) also observed a similar behavior to our studies, the second cathodic peak that occurred at -0.1 V (vs. Ag/AgCl), before the main peak of Sb and assigned to underpotential deposition (UPD) of antimony. This process is a surface-limited reaction of Sb atoms deposited on the substrate, with a partial covering of the electrode surface. The redox response of the rGO-SbNPs was associated with a larger peak current compared to other compounds evaluated. The better electrochemical responses exhibited by rGO-SbNPs can be attributed to the synergistic activities of rGO and SbNPs. Electrodes modified with rGO are well reported for electrocatalysis and sensing applications (Shao *et al.*, 2010). Table 6 summarises all the values (potential and current) referred to above for each electrode.

Table 6. Summary of the values obtained for $E_{p,a}$ and $E_{p,c}$ peak potential, I_p and ΔE by GCE modified with rGO, SbNPs and rGO-SbNPs compounds using CV.

Working Electrode	$E_{p,a}$ / V	$E_{p,c}$ / V	ΔE / V	$I_{p,a}$ (μ A)	$I_{p,c}$ (μ A)	$I_{p,a}/I_{p,c}$
rGO/GC	-0.156	0.145	0.011	3.93	-5.62	0.70
SbNPs/GC	-0.139	0.137	0.002	4.05	-4.07	1.00
rGO-SbNPs/GC	-0.148	0.156	0.008	5.42	-9.50	0.57

The results for the rGO and SbNPs scans appeared with anodic and cathodic peaks at around -0.156 V; -0.139 V and 0.145 V; 0.137 V (vs Ag/AgCl), respectively while that for rGO-SbNPs appeared with a pair of anodic peaks at around -0.148 V; -0.454 V (vs Ag/AgCl) with sharp return pair of cathodic peaks at around 0.156 V; -0.24 V (vs Ag/AgCl). The redox couples exhibited reversible to quasi-reversible behaviour with peak current ratios of the anode relative to cathode at around 0.56 – 1.0, indicating it was a perfect reversible system. The ΔE for redox couples found to be 0.011 V; 0.002V and 0.008 mV (vs Ag/AgCl) for rGO, SbNPs and rGO-

SbNPs, respectively. Considering that, it becomes so difficult to unequivocally establish the rate of electron transfer for any of these electrodes. Redox peak (b) was not highly reversible, showing a weak anodic component.

4.5.1.1 Effects of scan rates

To investigate the performance and electrochemical behaviour of the rGO-SbNPs/GC sensor, cyclic voltammetry analysis was performed at various scan rates in the potential range between 0.6 to -1.0 V (vs. Ag/AgCl) in 0.1 M HCl solution and the results are depicted in Figure 44.

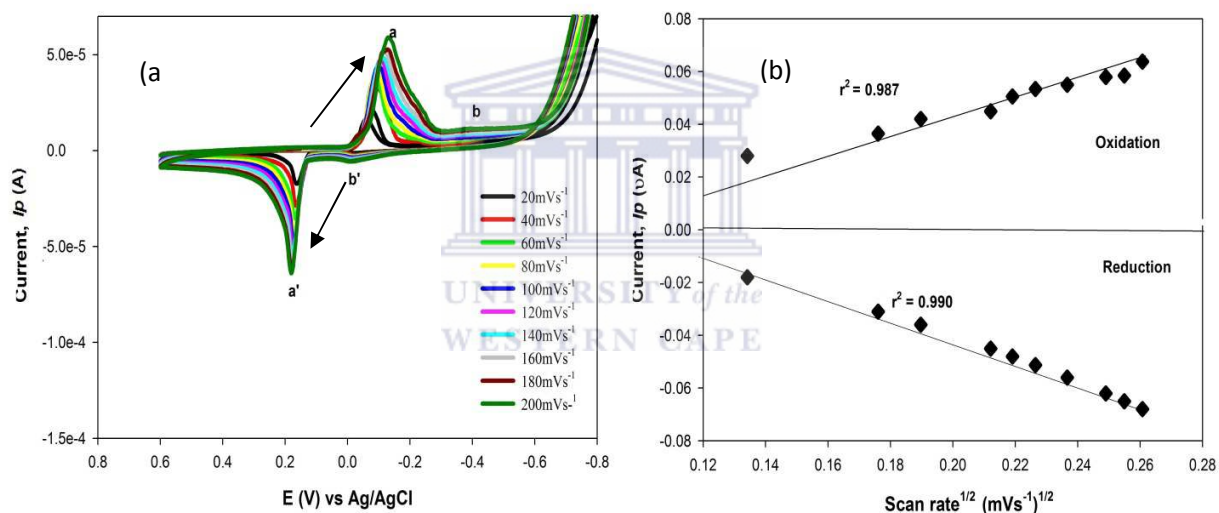


Figure 44. The results obtained for voltammetric scan rate studies of the rGO-SbNPs / GC sensor in a 0.1 M HCl solution at scan rates from 20 to 200 mV s⁻¹. The potential was scanned between 0.6 to -1.0 mV (vs. Ag/AgCl).

The results obtained for the voltammetric scan rate studies of the GCE/rGO-SbNPs sensor in a 0.1 M HCl solution at scan rates from 20 to 200 mV s⁻¹ (vs Ag/AgCl) (scanning potential window +0.6 to -1.0V (vs Ag/AgCl)) are shown in Figure 44. From the CV results in Figure 44, it was observed that two defined pairs of redox couples, (a/a') and (b/b') were obtained with couple (a/a') showing relatively higher anodic and cathodic currents, compared to that of (b/b').

The redox couples were obtained in the potential range from 0.2 to -0.6 V (vs. Ag/AgCl), with the first well-defined redox couple of (a/a') recorded at $E_{p,a} = -0.170$ V, $E_{p,c} = 0.180$ V (vs. Ag/AgCl). The (b/b') redox couple was recorded at around $E_{p,a} = -0.4$ V, $E_{p,c} = -0.05$ V (vs. Ag/AgCl). Inspection of the CV reveals that for both redox couples of (a/a') and (b/b'), the $I_{p,a}$ and $I_{p,c}$ peak currents increased with increasing scan rate. The $E_{p,a}$ shifted towards more negative potentials, while the $E_{p,c}$ shifted towards more positive potentials. The difference in potential shifts (ΔE) was 0.56 and 0.18 V (vs. Ag/AgCl) for anodic and cathodic peak potentials, respectively. The difference of $E_{p,a}$ and $E_{p,c}$ were found to be, $\Delta E = 0.71$ V at a scan rate of 100 mV s^{-1} , which was expected for a fast electron transport dynamic process.

This value is slightly higher than the standard difference for a one-electron transfer reaction, which is 0.059 V. The current ratio between the peaks I_a/I_c was 1.05. These results also demonstrate a quasi-reversible redox process obtained for the rGO-SbNPs composite. In cyclic voltammetry, we are also given the opportunity to directly observe the stability of the electrochemically generated product by current ratio. The dependence of peak current ratio with scan rate was examined for the entire scan rates studied and showed the stability of the GCE/rGO-SbNPs sensor to be consistent. The influence of the square root of the scan rate results on both the anodic and cathodic current is shown in Figure 44 (b). The peak current increases linearly with the square root of the scan rate and for the anodic current the corresponding linear equation is $I_p = 0.003 \text{ V}^{1/2} + 0.0014$ with a correlation coefficient (r^2) of 0.987. In the case of cathodic current the corresponding linear equation is $I_p = 0.401 \text{ V}^{1/2} + 0.038$ with a correlation coefficient (r^2) of 0.990. These observations indicate that the rGO-SbNPs sensor platform is electroactive and the peak currents are diffusion controlled (Somerset *et al.*, 2011; Wang *et al.*, 2010).

4.5.2 Impedance Spectroscopy

The change in the interfacial electron-transfer properties on modifying the electrode surface was evaluated by electrochemical impedance spectroscopy (EIS), with the results presented in Figure 45. In Figure 45 the Impedance Nyquist plot is shown in the left, while on the right the admittance Nyquist plot is shown. The graphs contain the EIS results for all of the

rGO, SbNPs and the rGO-SbNPs, employing 0.1 M HCl solution with A.C. potential modulation amplitude of 5 mV and for frequencies ranging between 100 kHz to 0.1 Hz.

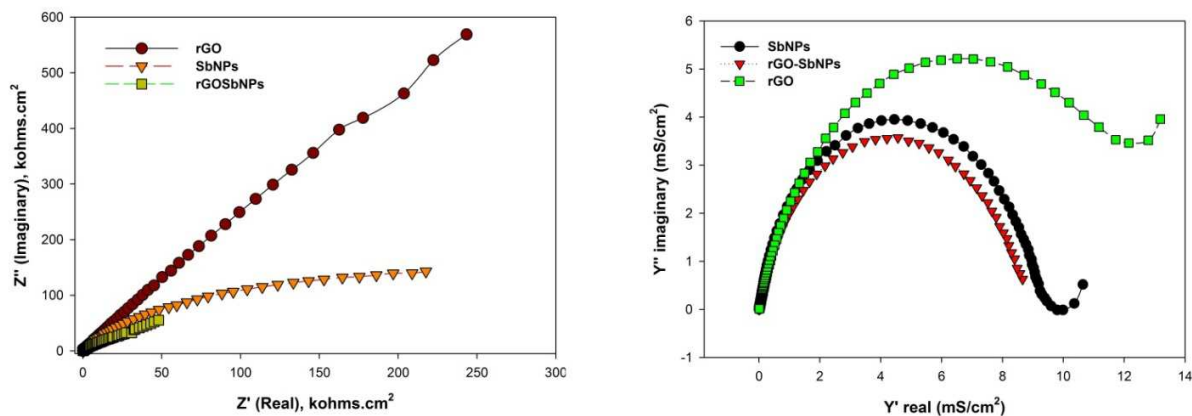


Figure 45. Nyquist Impedance and nyquist admittance plots for the rGO-SbNPs compound in 0.1 M HCl solution.

EIS was employed in this study in helping to understand the kinetics of the electrochemical process taking place at the electrode surface by measuring the total impedance of the system over a wide frequency range (Liu *et al.*, 2012; Ting *et al.*, 2011; Shan *et al.*, 2009). EIS analyses were performed using rGO and SbNPs samples to compare the results and responses to that of rGO-SbNPs nanocomposite. The impedance demonstrate predominantly charge diffusion as corroborated by semi circle in admittance plot as seen in Figure 45. The missing Warburg curves indicate that the electrodes have short ion diffusion paths, which facilitate the efficient access of electrolyte ions to the surfaces of the modified electrodes for each of the composites investigated (Mishra *et al.*, 2011).

Figure 45 shows typical comparative Nyquist plots of the modified electrodes for each of the three composites investigated. Impedance Z and admittance Y are two inverse transfer functions linked by the following very simple relation:

$$Z = \frac{1}{Y} \quad (\text{Eqn. 4.2})$$

The most employed plot for EIS analysis is the Impedance Nyquist plot. This is a plot of the imaginary component (Z'') of the impedance against the real component (Z') and it allows an easier prediction of the equivalent electronic circuit (Scully *et al.*, 1993). However, it does not represent the frequency dependence and therefore it is complemented by the Bode plot. The (C_{dl}) double layer capacitance and (R_{ct}) charge-transfer resistance in absence of mass transport and reaction intermediates are the key electrical parameters to determine the impedance change for analysis of the system kinetics required to observe the change in dielectric properties of the nanocomposite under investigation (Zia *et al.*, 2013). Z_w is the diffusion or Warburg resistance. It can be seen that GCE/rGO-SbNPs has little higher interfacial charge-transfer resistance than in the case of GCE/rGO and GCE/SbNPs. This is evident from the values of charge transfer resistance.

Table 7. Circuit elements for R_p , R_s , C_{dl} and CPE obtained by fitting equivalent circuit in Figure 42.

Equivalent circuit Parameter (units)	rGO	%Error	SbNPs	%Error	rGO-SbNPs	%Error
R_s ($k\Omega \cdot cm^2$)	135.2	1.2979	109.1	0.6546	82.36	0.71855
R_p ($k\Omega \cdot cm^2$)	846.2	6.7612	749.6	12.086	47.3	13.233
C_{dl} ($F \cdot cm^2$)	5.0763×10^{-6}	6.7612	9.599×10^{-7}	1.6412	-----	
$CPE-T$ ($F \cdot cm^2$)	-----		-----		1.66×10^{-6}	2.2117
$CPE-P$	-----		-----		0.7184	0.7612

Table 7 shows the circuit elements values obtained by applying the equivalent circuit analysis in the Nyquist plots of Figure 45. The simple Randle's equivalence circuit fitting at GCE/rGO, GCE/SbNPs and GCE/rGO-SbNPs can be observed in Table 7. R_s is the solution resistance, R_p – the polarisation resistance, C_{dl} – the double layer capacitance, R_{ct} – the charge transfer resistance in absence of mass transport and reaction intermediates, CPT – the constant phase element. The constant phase element (CPE) is comprised by two components; $CPE-T$ and $CPE-P$. $CPE-T$ is a pseudo capacitance which is called Q and $CPE-P$ is related to the semi-circle in the Nyquist plot (depressed semicircle), normally used for the notation 'n'. By using $CPE-P$ and $CPE-T$ and resistance, one can calculate the true capacitance for the electrodes. If $CPE-P$ equals approximately to 1, then the CPE turns theoretically to a capacitor, C (Gonullu *et al.*, 2014; Carrara *et al.*, 2005). $R_p = R_{ct}$ when there are no mass transport limitations and electrochemical reactions involve no adsorbed intermediates and nearly instantaneous charge transfer control

prevails and $R_p = R_{ct} + Z_w$ in the case of mass transport limitations. Solution resistance is often a significant factor in the impedance of an electrochemical cell. The R_s between the reference electrode and the working electrode must be considered. The resistance of an ionic solution depends on the ionic concentration, type of ions, temperature and the geometry of the area in which current is carried. An electrical double layer exists at the interface between an electrode and its surrounding electrolyte, characterized by existence of a charge excess on metal that attracts ions of opposite charges from solution. The simplest model of the electrolyte region is that of a line charge at a fixed distance from electrode surface (Helmholtz model) similar to a simple parallel-plate capacitor. The value of the double layer capacitance depends on many variables including electrode potential, temperature, ionic concentrations, types of ions, oxide layers, electrode roughness, impurity adsorption, etc. A charge transfer takes place at the interface; in the direct reaction, electrons enter in the metal and metal ions diffuse into the electrolyte.

The charge transfer resistances were found to be 711 k Ω , 639.9 k Ω and 34.6 k Ω for each of GCE/rGO/, GCE/SbNPs/ and GCE/rGO-SbNPs, respectively. It is worth noting that the lowest charge transfer resistance was for GCE/rGO-SbNPs. This could be explained by the different electron transport mechanisms within the GCE/rGO-SbNPs. In the case of GCE/rGO, electron transport occurs only on the surface particle-to-particle network by hopping within the GCE/rGO thin film, which is considered as a slow transfer mechanism. However, an electron in the rGO-SbNPs structure, the introduction of the rGO also supplies 2D conductive networks, enhances the wetting of the active material, and disperses the nanoparticles, leading to improved rate capability. This in turn causes a shorter pathway and compensates for fast electron transfer and thus, provides higher charge collection efficiency (Yao *et al.*, 2011).

From Table 7, the sequence of the values of R_{ct} for the different electrodes are GCE/rGO > GCE/SbNPs > GCE/rGO-SbNPs. This demonstrates that the GCE/rGO-SbNPs electrode has a higher electrochemical activity than the GCE/rGO and GCE/SbNPs. These results clearly indicate that the incorporation of graphene can improve the electrochemical properties of SbNPs. In Table 8 the results for the kinetic parameters of the nanocomposite of rGO, SbNPs and rGO-SbNPs are shown.

Table 8. Kinetics parameters of rGO, SbNP and rGO-SbNPs modified electrodes obtained in 0.1 M HCl solution.

Kinetics parameters	rGO/GCE	SbNPs/GCE	rGO-SbNPs/GCE
$\omega(\text{rad s}^{-1})$	277.00	1628.66	1739.30
$\tau(\text{s rad}^{-1})$	3.61×10^{-3}	6.14×10^{-4}	5.75×10^{-5}
$i_o (A)$	2.78×10^{-5}	3.14×10^{-5}	6.79×10^{-4}
$k_{et} (\text{cm s}^{-1})$	4.07×10^{-8}	4.60×10^{-8}	9.94×10^{-7}

Next, this study interrogated the electron transfer kinetics (time constant (τ), heterogenous rate constant (k_{et}) and exchange current (i_o) occurring at these electrodes, since the EIS analysis provides a more detailed description of an electrochemical system compared to cyclic voltammetry (Chang *et al.*, 2006). The results presented in Table 8 have shown that the heterogeneous rate constant (k_{et}) value increased as follows: GCE/ rGO-SbNPs > GCE/SbNPs \approx GCE/rGO, this agreed very well with the CV results shown in Figure 43. The value of exchange current calculated showed a higher value in GCE/rGO-SbNPs, compared to GCE/rGO and GCE/SbNPs, proving the faster flow of charge in the novel composite synthesised in this study.

4.6 Summary

This chapter demonstrated the successful synthesis and characterisation of the novel rGO-SbNPs composite, for further application in an electrochemical sensor for PGMs stripping analysis. This chapter has also shown the synthesis and characterisation of rGO, SbNPs and nanocomposite of rGO-SbNPs, which are potentially useful in sensors and related fields. The products of these reactions have been extensively characterised by electron microscopy, spectroscopic and electrochemical techniques. The results for the aforementioned analysis have shown that the products have a nanocomposite structure ideal for sensor applications. By incorporating nanomaterials in sensors, great promise has been achieved since these materials can be utilised to capture the pollutant or amplify the signal associated with its detection. Both of these capabilities are important for trace level detection of various pollutants.

The TEM-EDX spectra confirmed the presence of the graphene and antimony in the novel rGO-SbNPs composite. The cyclic voltammetric results clearly indicated that the peak current was much higher for the GCE/rGO-SbNPs composite, compared to the individual results

of GCE/rGO and GCE/SbNPs, respectively. This observation was also supported by the EIS results of the GCE/rGO-SbNPs composite. It could be deduced from the EIS results that the combined effect of rGO and SbNPs enhanced the electron transfer in the rGO-SbNPs composite. The value for R_{ct} is surface dependent, with the GCE/rGO-SbNPs having the lower charge transfer, which is consistent with the findings from the CV analysis. The equivalent circuit model that incorporated the CPE, yielded satisfactory results as evident from the percentage error values obtained in the calculations. On the other hand, EIS provided evidence on successful incorporation of rGO and SbNPs as it showed lower electron transfer resistance. The CV results offered a better current response for the GCE/rGO-SbNPs composite, compared to the individual results of GCE/rGO and GCE/SbNPs, respectively. The proposed modified electrode has high surface activity due to being modified with composite nano-particles, which could amplify the response current. Further work should be undertaken to optimise the composition and microstructure of the composite.



Chapter 5

Investigations of Redox behaviour of PGMs using rGO-SbNPs nanosensors

5.1 Introduction

In this chapter comparative study on the electrochemical behaviour of PGMs at GCE/rGO-SbNPs and SPCE/rGO-SbNPs has been investigated in NaOAc buffer by cy CV. The size and shape of the electrode surface has an effect on the voltammetric response of the electrode. Cyclic voltammetric characteristics, associated with the positions of peak potentials (E_a and E_c) and current ratios (I_a/I_c), are measured with scan rates. The peak current observed in the modified electrodes is dependent on both the porosity and nature and number of sites involved in partitioning the complex into film. The values of diffusion coefficient for different electrodes have been calculated from electrochemical data. The investigation focuses essentially on these effects, the different electrochemical cells (Epsilon electrochemical analyzer (BASi instruments, USA, model CV-27) and a commercially available miniaturized potentiostat (PalmSens®) in order to understand the role of electrode material, its surface modification, solvent and analyte in an electrochemical cell on cyclic voltammograms.

5.2 Materials and Methods

5.2.1 Reagents

All the PGMs under investigation were procured from Fluka (Germany), *i.e.* the standards for platinum (Pt), palladium (Pd) and rhodium (Rh) (1000 mg/L atomic absorption standard solution) and DMG. The antimony pentachloride was provided by Aldrich (Germany). All other reagents used were provided by Merck (South Africa) and included sodium acetate, ammonia with a purity of ca. 25% ammonium chloride, hydrochloric acid with purity 32% and nitric acid

with purity 55%. Glacial acetic acid and ethanol (95%) were purchased from Kimix (South Africa).

5.2.2 Instrumentation

Cyclic voltammetric experiments were performed with a BAS cyclic voltammograph (USA, model CV-27) equipped with three electrode system connecting with a Houston X-Y recorder (Model-100). The three electrodes used in the experiments were a working glassy carbon electrode, the electrode set-up consist of a conventional three electrode configuration, which comprised a platinum (Pt) working electrode, a Pt wire as counter electrode and silver/silver chloride (Ag/AgCl) as a reference electrode. Alumina micro polish and polishing pads (Buehler, IL, USA) were used for electrode polishing. All the experiments were carried out at different scan rates. 0.2 M NaOAc buffer solution has been used as supporting electrolyte with a fixed temperature of 25 °C. Other measurements were performed using a PalmSensportable potentiostat / galvanostat, with the PS Trace program and accessories (PalmSens® Instruments BV, 3992 BZ Houten, The Netherlands), interfaced to a microcomputer controlled by PS 2.1 software for data acquisition and experimental control. The measurements were performed in a conventional electrochemical cell of 20.0 ml, SPCE with 4 mm diameter provided by Dropsens (Oviedo, Spain) as working electrodes ([www. Dropsen.com](http://www.Dropsen.com)).

5.2.3 Preparation of graphene impregnated with antimony nanoparticles

The rGO-SbNPs were obtained by refluxing antimony pentachloride in a mixture of 10:4 graphene and polyvinyl alcohol in ethanol containing sodium borohydride. The suspensions were then centrifuged for 1h under constant stirring, and the supernatants were taken. The drop coating of the rGO-SbNPs on the GCE and SPCE was done in the way as suggested by Ntsendwana *et al.*, (2012). After drying properly the electrode was finally dipped into the NaOAc buffer for overnight

5.3. Results and discussion

5.3.1 Voltammetric evaluation of graphene-antimony nanomaterials

The comparative behaviour of cyclic voltammetric behavior of SPCE/rGO-SbNPs and GCE/rGO-SbNPs in 0.2 M NaOAc buffer at 60 mV s^{-1} scan rate is shown. In Figure 46 below the results for the CV comparison of the unactivated SPCE, activated SPCE and SPCE/rGO-SbNPs and GCE/rGO-SbNPs electrode evaluated in 0.2 M NaOAc buffer (pH = 4.8) solution are shown.

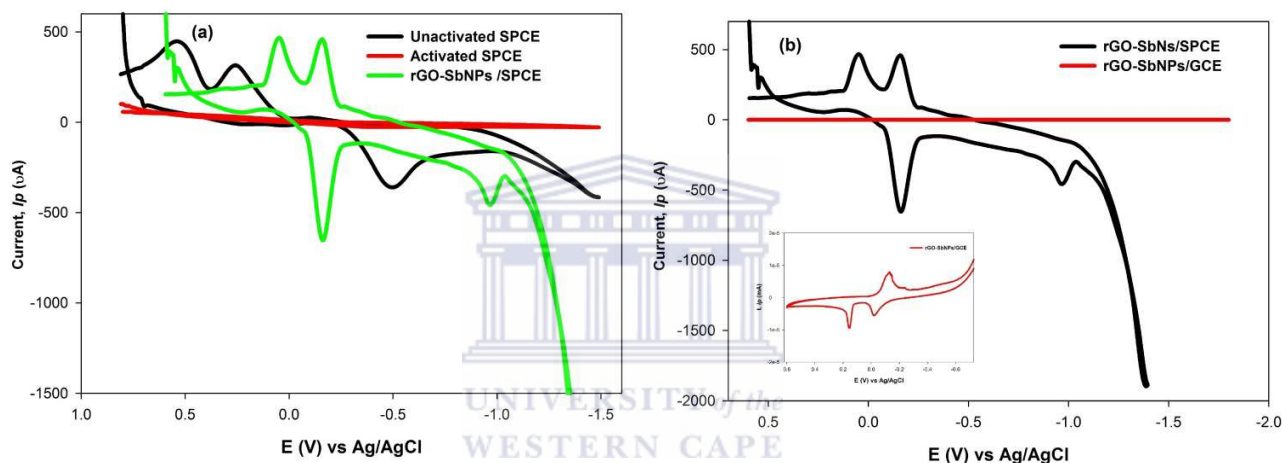


Figure 46. Overlay of (a) activated and unactivated SPCE and modified SPCE, (b) GC/rGO-SbNPs and SPC/rGO-SbNPs electrodes in 0.2 M NaOAc (pH = 4.8) solution.

For the results in Figure 46 (a) the SPCE was cycled at the potential from 0.4 V to -1.8 V (vs. Ag/AgCl) in 0.2 M NaOAc buffer at a rate of 10 mV s^{-1} for the first cycle, then pre-treated using the same specifications as for the unactivated SPCE measurement. As we seen in Figure 46 (a) oxidation and reduction signals of the redox couple were obtained when the electrode was measured directly as received from the manufacturer (unactivated SPCE).

This process was applied to remove any organic compounds or other contaminants that may be present in the carbon ink from the printing process. Pre-treatment and activation can make the surface more amenable to electron transfer by increasing the amount of active sites. After these measurements, rGO-SbNPs composite was drop coated and dried on the SPCE surface followed with other measurement as seen in Figure 46 (a). The reason for these

measurements was to compare the behaviour of the SPCE directly from the manufacture, the activated SPCE and the modified SPCE before proceeding with this study. The overlay of these electrodes are shown in Figure 46 (a).

This study was conducted using SPCE and GCE. In Figure 46 (b) the SPCE/rGO-SbNPs and GCE/rGO-SbNPs active surface areas were compared in terms of current signal. Before measurement the GCE was thoroughly polished on a Büehler pad using various sizes of alumina powder and rinsed with copious amounts of deionized water. Subsequent to the polishing step, the GCE was sonicated in 20% ethanol for 2 minutes to remove residual alumina, followed by rinsing with more deionised H₂O and air dried. An interesting observation was made for the appearance of a pair of anodic and cathodic peaks each in the CV of both GCE and SPCE. The voltammetric peak might be the results of a modifier used. From these results it was deduced that the maximum, I_p value is obtained at the SPCE/rGO-SbNPs surface. The difference of signal between the two voltammograms was due to the difference of surface area between the SPCE/rGO-SbNPs and GCE/rGO-SbNPs sensors. The peaks that appeared on both electrodes are the results of a modifier.

5.3.2 Effect of Supporting Electrolyte.

In Figure 47 the effect of different supporting electrolytes on the carbon electrode was assessed in two ways: (i) the effect on the current response magnitude, and (ii) the effect on cyclic voltammogram resolution.

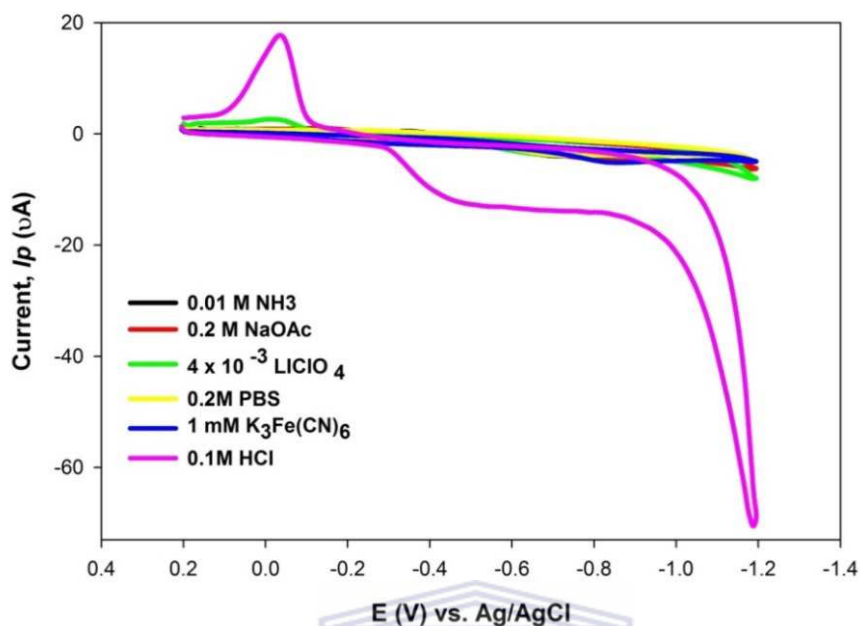


Figure 47. CV for the GCE/rGO-SbNPs sensor in different electrolytes at a scan rate of 10 mV s^{-1} in: 0.2 M NH_3 buffer (pH = 9.2); 0.2 M NaOAc buffer (pH = 4.8); 4×10^{-3} M LiClO_4 ; 0.2 M PBS buffer (pH = 7.4); 1 mM $\text{K}_3\text{Fe}(\text{CN})_6$ and 0.1 M HCl solutions.

Not only can the course of a reaction depend on the electrode material but it can also depend on the choice of solvent and supporting electrolyte. The supporting electrolyte may be an inorganic salt such as potassium chloride or nitrate, a mineral acid or a base. Supporting electrolytes can serve in three main purposes (Kissinger & Heineman, 1994). Firstly, it provides the necessary ions to enable electric charge to pass through the electrochemical cell and lower the resistance of the cell. Secondly, it minimises the migration of analyte caused by the electric field and thirdly, it influences the resolution and the half-wave potential of the analyte (Kissinger & Heineman, 1994). From the different electrolytes investigated in this study, it was found that 0.1 M HCl solution gave better resolution in both oxidation and reduction peaks. In contrast, the use of 0.1 M HCl resulted to the electrode surface collapsing. For graphene, it is reported that PB (pH = 7.4) is the ideal electrochemical supporting electrolyte documented (Ibrahim *et al.*, 2001). For the purpose of this study we have performed our experiments focusing in three media, *i.e.* NaOAc buffer (pH = 4.8), NH_3 buffer (pH = 9.2) and PB (pH = 7.4) solutions. The detailed results of these buffered solutions will be dealt with in the next chapter.

5.3.3 rGO-SbNPs Redox Chemistry in 0.1 M HCl.

Figure 48 shows a comparison of GCE/rGO-SbNPs and SPCE/rGO-SbNPs sensors at the different scan rates. Scan rate defines the speed of the potential sweep during data acquisition. Scan rate is one of the most important parameters that affect the redox properties of the substrates in cyclic voltammetry experiments. In reality the concept of an inert electrode is idealistic, given that the surface of an electrode has to exert an influence on the electrode reaction (perhaps small) and can form bonds with species in solution (formation of oxides, adsorption, etc.) (Brett, 2013).

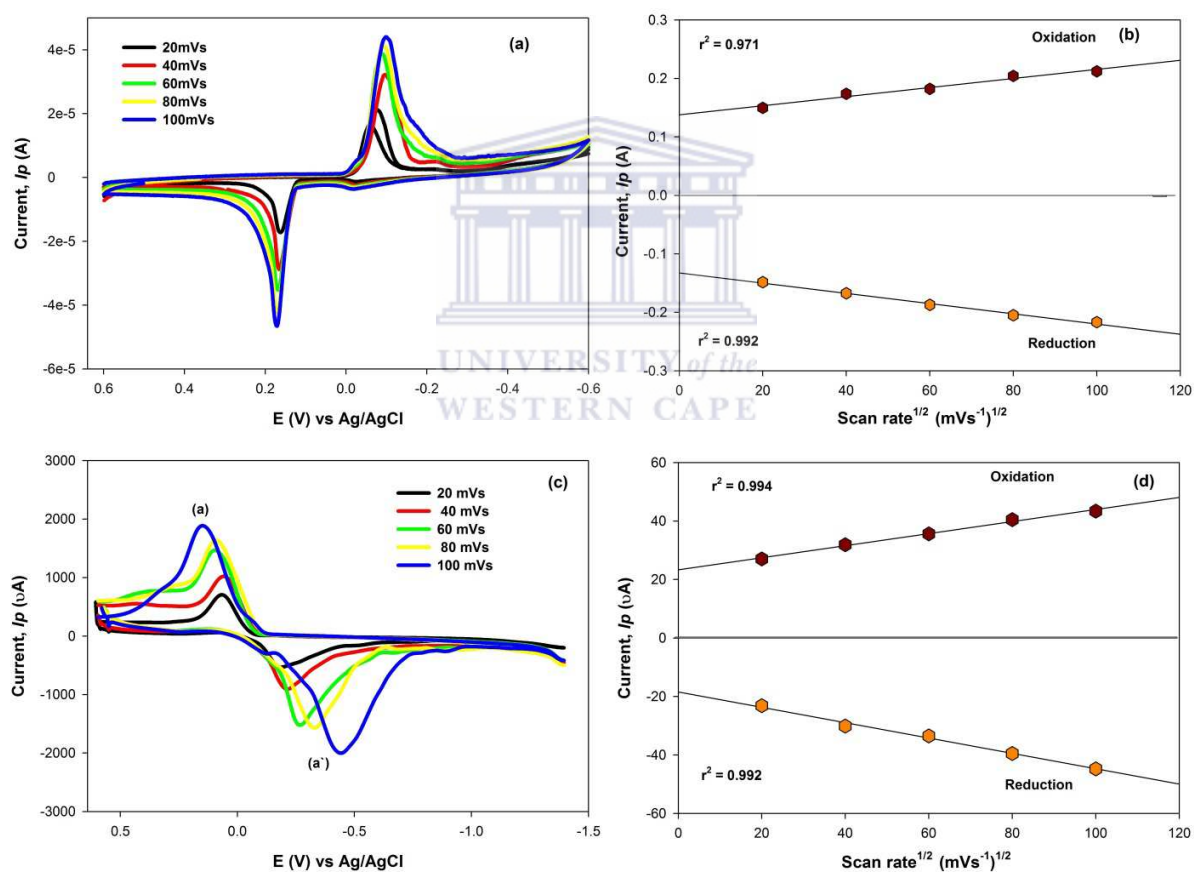


Figure 48. CV of rGO-SbNPs evaluated at modified (a) GCE, and (c) SPCE in aqueous 0.1 M HCl electrolyte; while in (b) and (d) the graphs of peak current vs. square root of scan rate is shown.

In order to understand the electrochemical behaviour of r.GO-SbNPs on SPCE and GCE, the various scan rates between 20 and 300 mV s^{-1} were measured by the CV method by using 0.1M HCl electrolytes for both electrodes. Figure 48 shows the CV plots at various scan rates between 20 and 100 mV s^{-1} . The results in Figure 48(b) and (d) give the peak current (I_p) as a function of square root of the scan rate ($v^{1/2}$) and the corresponding linear fitting. The relationship between scan rate (v) and I_{pa} / I_{pc} or I vs $v^{1/2}$ is often used as diagnostic criteria for identifying the nature of the electrode process. Here, I_{pa} and I_{pc} are anodic peak current and cathodic peak currents in a cyclic voltammograms, respectively. CV were used to study the electrochemical properties of the rGO-SbNPs-modified electrodes. It was performed in order to investigate the kinetics of the electrode reactions and verify whether diffusion is the only controlling factor for mass transport or not. Figure 48 illustrates the scan rate dependence of the GCE/rGO-SbNPs and SPCE/rGO-SbNPs electrodes, respectively. The anodic and cathodic peaks can be assigned to the oxidation of antimony and reduction of antimony at the surface, respectively. Mares *et al.*, (2006) observed the similar behaviour using antimony telluride on Pt and glassy carbon electrodes and diagnosed that the redox peak observed may be due to oxidation of Sb and reduction of Sb (Mares *et al.*, 2013).

Our results are consistent with the studies done by Svancara *et al.*, (2007) using antimony film electrode that has investigated the effect of different cathodic vertex potentials upon CV behaviour of antimony at the surface of the electrode. As can be clearly observed, in the case of SPCE/rGO-SbNPs the current signal is higher for both anodic and cathodic peaks compared to that of GCE/rGO-SbNPs. This was due to the greater electroactive surface area for SPCE compared to GCE. Another observation made was a normal peak shift for the GCE/rGO-SbNPs. CV shapes that are distorted at SPCE/rGO-SbNPs resulted to a decrease in potential at scan rates higher than 100 mV s^{-1} (scan rates CVs above 100 mV s^{-1} are not shown). We have also observed an anodic shift in the CV results of GCE/rGO-SbNPs and a large cathodic shift in that of SPCE/rGO-SbNPs. The large cathodic shift in the peak potential at the SPCE/rGO-SbNP agrees with slow electron transfer kinetics (Mardegan *et al.*, 2012). The decrease in current is much more important for the modified carbon at higher scan rates, indicating poorer kinetics. The GCE/rGO-SbNPs/GC exhibit excellent cycling rate stability up to very high scan rates such as 300 mV s^{-1} . A non-linear relationship would indicate an adsorption dependent redox reaction. Nevertheless, slight shifts in peak potential were observed with increasing scan rate indicating

some kinetic limitations. According to Isikli and Diaz, (2012) previously, Bélanger *et al.* reported that for covalently bound species the decrease of the total capacitance becomes much more important for the highest anthraquinone loaded electrodes and at high scan rates (Isikli and Diaz, 2012; Pognon *et al.*, 2011). In our results in the case of SPCE/rGO-SbNPs, we have seen a decrease in peak current at higher scan rates which means that the SPCE was rGO-SbNPs loaded.

According to the Randles-Sevcik equation, the plot of I_{pa} versus $v^{1/2}$ should be linear curve for a diffusion controlled process. Anodic and cathodic peak currents were plotted against square root of scan rate, as shown in Figure 3. We have correlation coefficient of ($R^2 = 0.992$ and $R^2 = 0.971$) for linear of current vs scan rate for GCE/rGO-SbNPs. SPCE/rGO-SbNPs gave a correlation coefficient of ($R^2 = 0.992$ and $R^2 = 0.994$). These results confirm the diffusion-controlled electron transfer in the range $20 - 100 \text{ mVs}^{-1}$ for SPCE/rGO-SbNPs. These results indicate that the determining step of reaction is mass transport to both the rGO-SbNPs/GCE and rGO-SbNPs/SPCE surfaces. One would expect that the peak current value, I_p , should linearly increase with the elevated potential scan rate as it is theoretically predicted for a surface-confined electrochemical process (Antonio *et al.*, 2013). However, we found that I_p is proportional to the square-root of the potential scan rate as predicted by the Randles–Sevcik equation. In our case, the electroactive species have to reach the electrode surface by diffusion in order for electron transfer to offer. It means that the electron transfer is controlled by mass transport, although the whole process is governed by diffusion. A summary of the results collected for the calculations slopes of the scan rate studied and correlation coefficient for SPCE/rGO – SbNPs and GCE/rGO – SbNPs are shown in Table 9.

Table 9. Summary of results for the slope and R^2 for carbon nanoparticle electrodes investigated.

Modified Electrode	Current	Slope	R^2
		(sqrt scan rate)	(sqrt scan rate)
SPCE/rGO-SbNPs	Anodic	8.0×10^{-3}	0.971
GCE/rGO-SbNPs	Anodic	2.06×10^{-1}	0.994

In conclusion rGO-SbNPs can act as an electron transfer medium and enhance the electrochemical reaction. The introduction of rGO-SbNPs on the GC and SPC electrode surfaces facilitates the conduction pathway at the modified electrode surface.

5.4 Electrochemical calculations

Scan rate studies of the GCE/rGO-SbNPs and SPCE/rGO-SbNPs sensors were performed in a 0.1 M HCl solution, in order to calculate the surface concentration of the nanoparticle films on the GC and SPC electrodes in accordance with Brown–Anson analysis, using a plot of peak current (I_p) against scan rate (ν) with the results calculated using Equation 5.1 (Somerset *et al.*, 2006).

5.4.1 Brown-Anson analysis

The electroactive surface area (A) of the modified electrodes tested was determined using the Randles-Sevcik plot described by the following equation:

$$I_p = \frac{n^2 \cdot F^2 \cdot A \cdot \Gamma}{4 \cdot R \cdot T} \quad (\text{Eqn. 5.1})$$

Where n represents the number of electrons transferred in the redox reaction, F is the Faraday constant (96,584 C mol⁻¹), Γ is the surface concentration of the rGO-SbNPs film (mol cm⁻²), A is the surface area of the electrode (0.0177 cm²), ν is the scan rate (mVs⁻¹), R is the gas constant (8.314 J mol⁻¹ K⁻¹), and T is the temperature of the system (298 K).

5.4.1.1. Number of electrons in nanocomposite matrices

Equation 5.2 was used for calculating the number of electrons in each of the carbon electrodes modified with rGO-SbNPs (Bard and Faulkner, 2001):

$$|E_p - E_{p/2}| = 2.20 \frac{R \cdot T}{n \cdot F} \quad (\text{Eqn. 5.2})$$

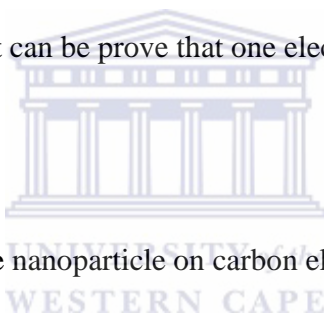
Where F is the Faraday constant ($96,485 \text{ C mol}^{-1}\text{e}^{-}$), R is the universal gas constant ($8.314 \text{ J.K}^{-1}.\text{mol}^{-1}$), T is the absolute temperature of the system ($25 \text{ }^{\circ}\text{C} = 298.15 \text{ K}$), and n is the number of electrons.

A summary of the results collected for the calculations of the number of electrons involved in the nanoparticle matrix, is shown in Table 10.

Table 10. Summaries of results for the number of electrons for different nanoparticle carbon electrodes matrices at the scan rate 40 mV s^{-1} .

	Current	Scan rate (mVs^{-1})	No. of electrons
SPCE/rGO - SbNPs	Anodic	40	1
GCE/rGO-SbNPs	Anodic	40	1

According to these results it can be prove that one electron is participating in the redox process



5.4.1.2 Surface concentration of the nanoparticle on carbon electrodes

In the next step, the true surface area of the electro-active species modified on the GCE and SPCE was determined experimentally, by cyclic voltammetry according to established methods (Bard & Faulkner, 2001). The geometric surface area only account for a theoretical and flat surface area, whereas experimental calculation takes into account the topographical variances of the surface. Using Randel-Sevcik plots of peak current vs. scan rate (or square root of scan rate), the data needed to perform Brown-Anson analysis were collected. The Brown-Anson equation is given in Equation 5.3 (Zanello, 2003):

$$I_p = \frac{n^2 \cdot F^2 \cdot A \cdot \Gamma^*}{4RT} \cdot \nu \quad \text{Eqn. 5.3}$$

Where the slope is equal to:

$$\text{Slope} = \frac{n^2 \cdot F^2 \cdot A \cdot \Gamma^*}{4RT} \quad \text{Eqn. 5.4}$$

Where F is the Faraday constant (96,485 C. mol⁻¹.e⁻), R is the universal gas constant (8.314 J.K⁻¹.mol⁻¹), T is the absolute temperature of the system (25 °C = 298.15 K), A is the surface area of the electrode, and n is the number of electrons.

When comparing the results for SPCE/rGO-SbNPs and GCE/rGO-SbNPs surfaces, the following result has been found and are summarised in Table 11.

Table 11. Summaries of results for the surface concentration of carbon nanoparticle electrodes.

	Current	Scan rate (mVs⁻¹)	Surface Concentration (Γ)
SPCE/rGO - SbNPs	Anodic	40	1.66×10^6
GCE/rGO-SbNPs	Anodic	40	4.01×10^3

Using Brown-Anson equation, the surface coverage, Γ , was calculated and the results are presented in Table 11. When comparing the results, it was found that SPCE/rGO-SbNPs has the highest surface concentration than GCE/rGO-SbNPs. This behaviour suggests that the carbon surfaces are different when the nanoparticles were drop coated. The results suggest that the surface area of SPCE was 3000 times more than that of GCE and leads to a more favorable exposure of rGO-SbNPs and a higher electrochemically effective surface area.

5.4.1.3 Electron transport diffusion coefficient for carbon nanoparticle electrodes

The electron transport diffusion coefficient, D_e (in cm²s⁻¹), was calculated from the Randle-Sevcik plot of peak current (I_p) versus square root of scan rate ($v^{1/2}$). Using the Randle-Sevcik data and Equation 5.3 (Bard and Faulkner, 2001), the following Equation 5.5 was obtained for the determination of D_e :

$$I_p = 2.69 \times 10^5 \cdot n^{3/2} \cdot A \cdot D_e^{1/2} \cdot C \cdot v^{1/2} \quad \text{Eqn. 5.5}$$

Where F is the Faraday constant ($96,485 \text{ C}\cdot\text{mol}^{-1}\cdot\text{e}^{-}$), R is the universal gas constant ($8.314 \text{ J}\cdot\text{K}^{-1}\cdot\text{mol}^{-1}$), T is the absolute temperature of the system ($25 \text{ }^{\circ}\text{C} = 298.15 \text{ K}$), A is the surface area of the electrode, and n is the number of electrons. The result from a plot of I_p vs $v^{1/2}$ is then used and the slope is equal to:

$$\text{Slope} = 2.69 \times 10^5 \cdot n^{3/2} \cdot A \cdot D_e^{1/2} \cdot C \quad \text{Eqn. 5.6}$$

In a similar method as for SPCE/rGO-SbNPs, the diffusion coefficient of the of the GCE/rGO-SbNPs was also calculated. A summary of the results are shown in Table 12.

Table 12. Summaries of results for electron transport diffusion coefficients in nanoparticle matrices.

	Current	Scan rate (mVs^{-1})	Diffusion coefficient (D_e)
SPCE/rGO - SbNPs	Anodic	40	1.60×10^{-9}
GCE/rGO-SbNPs	Anodic	40	1.48×10^{-12}

We have calculated diffusion coefficients of the SPCE/rGO-SbNPs and GCE/rGO-SbNPs sensors, at a scan rate of 40 mV s^{-1} . It can be observed that the diffusion coefficient for SPCE/rGO-SbNPs is higher than GCE/rGO-SbNPs (Table 12). This finding seems to indicate that a restriction for the electron transport also occurs on carbon surfaces. It implies faster diffusion mechanism in the case of SPCE/rGO-SbNPs.

5.4.1.4 Thickness of the nanoparticle carbon electrodes films

The thickness of the nanoparticle film obtained by drop coating on the electrode was also calculated. The following equation from Iwuoha *et al.* (1997) was used in the calculation, where a plot of peak current (I_p) versus square root of scan rate ($v^{1/2}$), gives the slope of the curve equal to Equation 5.7.

$$\frac{I_{p,c}}{v^{1/2}} = \frac{0.4463 \cdot (nF)^{3/2} \cdot A \cdot D_e \cdot \Gamma^*}{L \cdot (RT)^{1/2}} = \text{slope} \quad \text{Eqn. 5.7}$$

where F is the Faraday constant ($96,485 \text{ C}\cdot\text{mol}^{-1}\cdot\text{e}^{-}$), R is the universal gas constant ($8.314 \text{ J}\cdot\text{K}\cdot\text{mol}^{-1}$), T is the absolute temperature of the system ($25 \text{ }^{\circ}\text{C} = 298.15 \text{ K}$), A is the surface area of the electrode, D_e is the electron transport diffusion coefficient, n is the number of electrons, Γ^* is the surface concentration of the electro-active species, and L is the thickness of the polymer film (cm).

Thus, when values are substituted into Equation 5.7, the slope is then equal to Equation 5.8:

$$\frac{0.4463 \cdot (nF)^{3/2} \cdot A \cdot D_e \cdot \Gamma^*}{L \cdot (RT)^{1/2}} = \text{slope} \quad \text{Eqn. 5.8}$$

In a similar method as for SPCE/rGO-SbNPs, the film thickness of the GCE/rGO-SbNPs was also calculated. A summary of the results are shown in Table 13.

Table 13. Summaries of results for the thickness of the nanoparticle film.

	Current	Scan rate (mVs⁻¹)	Thickness of the Film (L) cm
SPCE/rGO - SbNPs	Anodic	40	1.60×10^{-9}
GCE/rGO-SbNPs	Anodic	40	1.48×10^{-12}

The thickness of the SPCE/rGO-SbNPs and GCE/rGO-SbNPs film was calculated and the results in table 13 show the highest film thickness at SPCE/rGO-SbNPs. Referring to the results in Table 13, SPCE/rGO-SbNPs sensors has a better sensitivity than GCE/rGO-SbNPs film.

5.5 Redox behaviour of GCE/rGO-SbNPs sensor in acetate buffer solution

In this section the investigations carried out on the redox behaviour of Pd(II), Pt(II) and Rh(III) in 0.2 M NaOAc buffer (pH = 5.2) solution using GCE/rGO-SbNPs sensor are discussed. These studies are of great relevance to develop electroanalytical methodologies for PGMs

determination using nanoparticles modified electrodes. Figure 49 shows the effect of scan rate on the reduction peak for PGMs. Redox peaks were assessed through CVs of PGMs in a quiescent solution of 0.2 M NaOAc buffer (pH = 5.2), in the presence of DMG by employing a scan rate ranging from 20 to 300 mV s^{-1} .

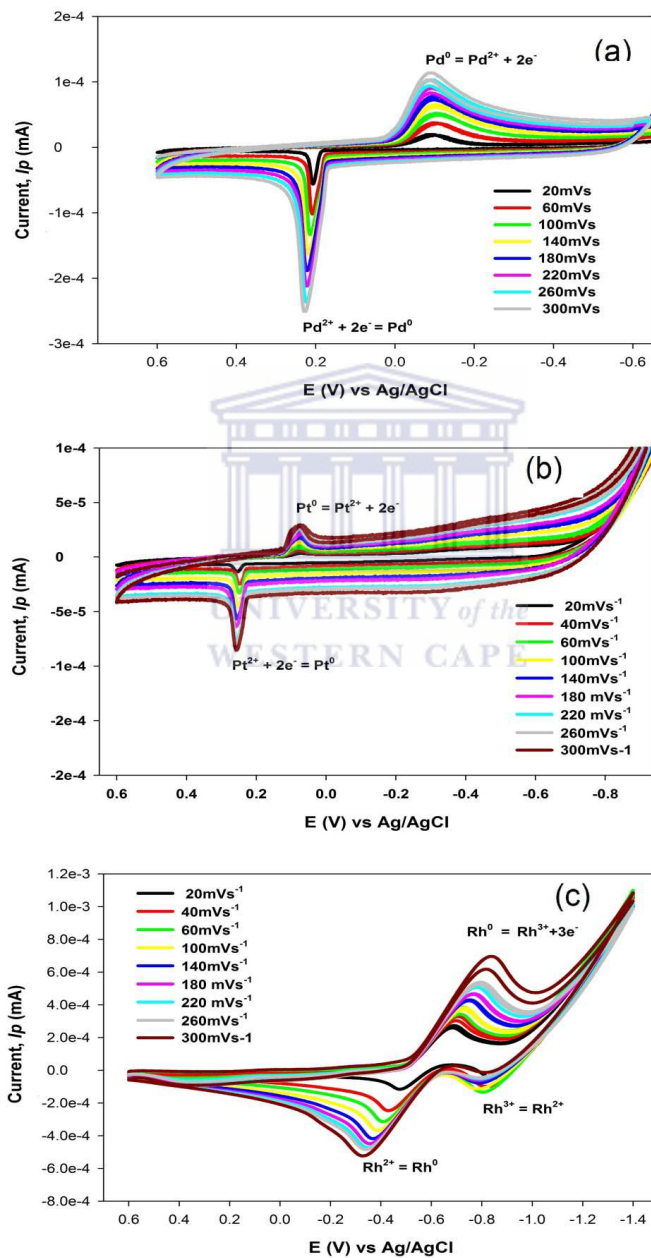


Figure 49. CV results obtained for the scan rate studies performed on a GCE/rGO-SbNPs sensor in the presence of Pt(II), Pd(II) and Rh(III) in a 0.2 M NaOAc buffer solution with 1×10^{-5} DMG.

The electrochemical behaviour of the GCE/rGO-SbNPs sensor in the presence of Pd(II), Pt(II) and Rh(III) was initially examined by using cyclic voltammetry (CV). The electrocatalytic activity of the rGO-SbNPs composite toward PGMs at different scan rates in 0.2M NaOAc buffer (pH = 5.2) solution before applying the sensor for stripping voltammetry, was investigated. In the following sections, we will try to identify the peak positions for the different PGMs in 0.2 M NaOAc buffer (pH = 5.2), in the presence of DMG since it will be used as a complexing agent for stripping voltammetric studies. The GCE/rGO-SbNPssensor showed a pair of stable redox peaks towards Pd(II) and Pt(II) activity. These peaks increased with increasing scan rate. The anodic peak around -0.1V (vs. Ag/AgCl) may be assigned to the oxidation of Pd(0) to Pd(II) and the reversed peak at potential around 0.2 V (vs. Ag/AgCl) may be assigned to the reduction of Pd²⁺ to Pd(0). For Pt(II), a pair of stable redox peaks appeared in the anodic region at 0.086V and 0.20 V (vs. Ag/AgCl) anodic and cathodic peaks, respectively. These peaks increased with increasing scan rate. The anodic peak may be assigned to the oxidation of Pt(0) to Pt(II) and the reversed peak may be assigned to the reduction of Pt(II) to Pt(0). The Rh(III) is irreversibly oxidised in a single multi electron-transfer step and the anodic peak potential is located at around E = -0.85 V (vs. Ag/AgCl) for all scan rates. This reaction is labeled as Rh(0) to Rh(III) in Figure 49. Two reduction peaks are associated with the formation of two different types of Rh(III) complexes. These complexes would probably correspond to the reduction of Rh(III) to Rh(II) for the first complex, while the second one would correspond to the Rh(III) to Rh transformation. These Peaks are located at around E = -0.90 V (vs. Ag/AgCl) for Rh(III) to Rh(III) and -0.45 V (vs. Ag/AgCl) for Rh(III) to Rh(0).

The I_{pa} for Rh(HDMG)₃ is almost the same for I_{pc} of the second reduction peak, while the I_{pa} for the first reduction peak is almost half of the second reduction peak with decrease in current at higher scan rates. Similar CVs were obtained by Kadish *et al.* (1992). The data for all the peaks with different scan rate ratios are shown in Table 14. It is evident from the Figure 49 results that the reduction peaks are sharper and more significant than the corresponding oxidation peaks for both Pd(II) and Pt(II). Both oxidation and reduction peak potentials for Rh(III) are almost the same hence, the reduction peaks were systematically studied using adsorptive differential pulse stripping voltammetry (AdDPSV) in order to achieve the desired detection limit in the following chapter.

Table 14. Results for the E_{pa} and E_{pc} , ΔE_p , and $E_{1/2}$ for the PGMs collected in 0.2 M NaOAc (pH = 5.2) solution at the GCE/rGO-SbNPs sensor surface.

PGMs	$mV s^{-1}$	E_{pa}/V	E_{pc}/V	$\Delta E/V$	$I_{pa}/\mu A$	$I_{pc}/\mu A$	I_{pa}/I_{pc}
Pd(II)	20	-0.09	0.21	0.30	20.7	-56.0	0.35
	40	-0.09	0.21	0.30	21.5	-57.0	0.38
	100	-0.10	0.21	0.31	53.0	-132.0	0.40
	140	-0.10	0.22	0.32	74.7	-176.0	0.42
	180	-0.10	0.22	0.32	87.1	-200.0	0.45
	260	-0.09	0.22	0.32	105.9	-236.0	0.45
	300	-0.09	0.23	0.33	115.7	-254.0	0.46
Pt(II)	20	0.086	0.25	0.61	5.3	-13.6	0.39
	40	0.086	0.25	0.61	12.1	-32.6	0.37
	100	0.086	0.25	0.61	16.3	-45.8	0.36
	140	0.084	0.25	0.59	21.6	-61.6	0.35
	180	0.084	0.26	0.58	24.6	-72.0	0.34
	260	0.084	0.26	0.58	27.6	-80.0	0.35
	300	0.080	0.26	0.54	29.1	-85.0	0.34
Rh(III)	20	-0.84	-0.90	0.06	274.3	-49.0	5.59
	40	-0.83	-0.90	0.07	333.2	-138.0	2.41
	100	-0.83	-0.90	0.07	386.1	-116.0	3.33
	140	-0.86	-0.90	0.04	390.6	-84.0	4.65
	180	-0.89	-0.90	0.03	452.1	-64.0	7.06
	260	-0.89	-0.90	0.01	564.0	-50.0	11.28
	300	-0.84	-0.92	0.08	696.0	-10.0	69.60
2nd Rh(III) Reduction Peak							
	20		-0.47	0.37		-216.0	1.27
	40		-0.41	0.41		-318.0	1.05
	100	(2 nd E_{pc})	-0.39	0.44	(2 nd I_{pc})	-368.0	1.05
	140		-0.38	0.48		-427.0	0.92
	180		-0.35	0.54		-475.0	0.95
	260		-0.35	0.54		-484.0	1.17
	300		-0.33	0.51		-528.0	1.32

V = Scan rate; E_{pa} = Anodic peak potential; E_{pc} = Cathodic peak potential; I_{pa} = Anodic peak current; I_{pc} = Cathodic peak current; ΔE = Peak potential separation.

Table 14 presents the peak potentials measured at different scan rates for the redox system of PGMs. There is a small negligible shift in peak potentials in the 0.2M NaOAc buffer (pH = 5.2) solution compared to the 0.1M HCl (pH = 1.4) solution. The E_{pc} , E_{pa} , I_{pa} , I_{pc} , peak current ratio (I_{pa}/I_{pc}) and ΔE_p are compiled in Table 14.

To better understand the reaction mechanism, analysis of the peak potentials versus increasing scan rate was performed. In practice, the theoretical value of $(0.059/n)$ V for ΔE_p is seldom observed.

This value is independent of the scan rate for fast electron transfer. The ΔE_p is also useful in the determination of n-values, as a two-electron transfer ($n = 2$) will give about 29 mV for the reversible case. For all the PGMs, Pt(II), Pd(II) and Rh(III) the results show a quasi-reversible system which is characterized by $\Delta E_p > 0.059.2/n$ V, with the values that are not increasing with increasing scan rate. In contrast, the increasing values of ΔE_p as a function of increasing scan rate indicate the presence of electrochemical irreversibility. A peak current ratio I_{pa}/I_{pc} is also a useful measure of the departure from reversibility in the cyclic voltammograms (Li and Albery, 1991; Cheung *et al.*, 1990; Cervini *et al.*, 1992). Ideally this ratio should be unity. Considering the peak current ratio, peak separation, and other factors discussed above it can be said that the redox system in PGMs complexes is quasi-reversible and the charge transfer process is diffusion controlled. However, it seems that the electrochemical process is partially controlled by adsorption for Rh(III). In fact, ΔE_p should be null for an electrochemical process which occurs from the species in the adsorbed state. We have seen the ΔE_p values of approximately null for Rh(III).

The peak current ratio was also evaluated by plotting the I_{pa}/I_{pc} versus the scan rate. Figure 50 shows that with increasing scan rate the peak current ratio stabilises accordingly.

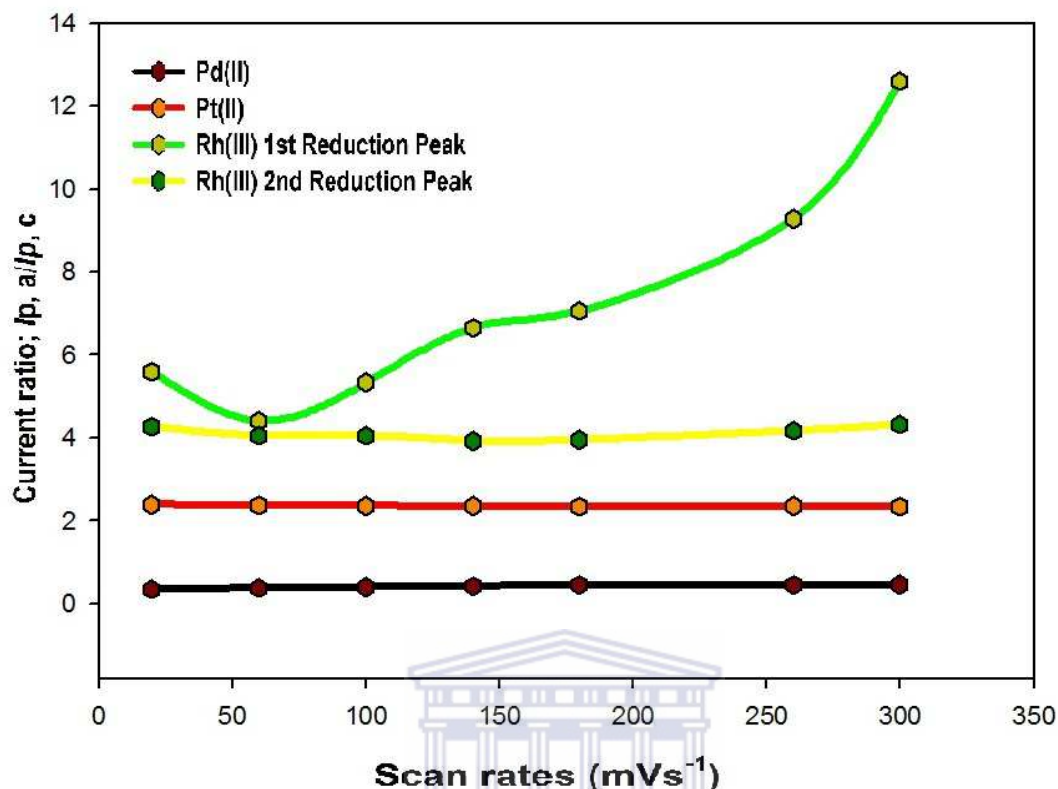


Figure 50. The dependence of peak current ratio with scan rate of Pd(II), Pt(II) and Rh(III) on the GCE/rGO-SbNPs, evaluated in 0.2 M NaOAc buffer solution.

In cyclic voltammetry, we are given the opportunity to directly observe the stability of the electrochemically generated product by current ratio. The dependence of peak current ratio with scan rate is shown in Figure 50. The ratio of the oxidation peak current to its corresponding reduction counterpart, (I_{pa}/I_{pc}) is less than a unity for Pd(II) and Pt(II). Whereas we obtained greater than unity for the first Rh(III) reduction peak, which corresponds to a quasi-reversible system and we managed to obtain unity for the second reduction peaks. In addition, I_{pa}/I_{pc} is less than unity (since only a fraction of the molecules that were reduced on the forward scan are available for re-oxidation on the reverse scan).

The results show that as the scan rate increases, the I_{pa}/I_{pc} ratio remain the same, indicating that this couple is a typical quasi-reversible charge transfer system, while for the first Rh(III) reduction peak we have experienced a value that is almost unity. The median scan rate of 60 mV s^{-1} was assigned as standard scan rate for future measurements.

5.6 Summary

In this chapter we firstly compared the behaviour of the GCE/rGO-SbNPs and SPCE/rGO-SbNPs sensors in 0.2M NaOAc buffer (pH = 5.2) solution and the maximum, I_p value was obtained at the SPCE/rGO-SbNPs sensor. rGO-SbNPs was dropcoated on different supports: carbon (SPCE and GCE). It was hypothesised that the SPCE/rGO-SbNPs sensor will give high current signal compared with that of the GCE/rGO-SbNPs sensor. As was clearly observed, in the case of the SPCE/rGO-SbNPs sensor the current signal is higher for both anodic and cathodic peaks, compared to that of the GCE/rGO-SbNPs sensor. This was due to the greater electroactive surface area for SPCE compared to GCE. True surface area as well as film thickness of the electro-active species modified on the SPCE/rGO-SbNPs and a GCE/rGO-SbNPs sensor surface was determined experimentally. The SPCE/rGO-SbNPs has shown better results compared to GCE/rGO-SbNPs. The redox behaviours of Pd(II), Pt(II) and Rh(III) in the presence of DMG have been studied in 0.2M NaOAc buffer (pH = 5.2) solution using the GCE/rGO-SbNPs sensor. The GCE/rGO-SbNPs sensor showed potential affinity toward PGMs and therefore, the feasible redox reaction of PGMs and the enhancement in the peak current can be attributed to the high electrocatalytic activity. The Pt(II) redox couple is a reversible system and provides a fair indication of the basic kinetic performance of the GCE/rGO-SbNPs sensor. These observations revealed that the PGMs reduction process is more favourable at the GCE/rGO-SbNPs sensor. Considering the results obtained for the peak current ratio, peak separation, and other factors discussed above it can be said that the redox system in PGMs is quasi-reversible and the charge transfer process is diffusion controlled. We directly observe the stability of the electrochemically generated product by current ratio for all the selected PGMs. It was found that peak current ratio was consistent to all scan rates.

Chapter 6

Optimisation and Application of GCE/rGO-SbNPs and SPCE/rGO-SbNPs Sensors

6.1 Introduction

Soil is a critical natural resource that plays a key role in determining human well-being, providing key ecosystem services, supporting food production, and the natural recycling of carbon (C) and essential nutrients in the environment. Although soils are recognised to be critically important, our knowledge of the concentration of naturally-occurring elements in soils is limited (Smith *et al.*, 2009).

In this chapter we report the optimisation and application of nano-carbon electrodes (GCE/rGO-SbNPs and SPCE/rGO-SbNPs) as much cheaper alternatives to ICP-MS spectroscopic analysis for the detection of PGMs. PGMs detection in soil and dust was studied so as to evaluate the performance of our novel developed sensor platforms using adsorptive differential pulse cathodic stripping voltammetry (AdDPCSV). Direct analysis of soil and analysis of extracts was performed by Inductive coupled plasma (ICP-MS) spectrophotometry, which was compared to the stripping voltammetric analysis.

6.2 Materials and Methods

6.2.1 Chemicals and reagents

All the PGMs under investigation were procured from Fluka (Germany), *i.e.* the standards for platinum (Pt), palladium (Pd) and rhodium (Rh) (1000 mg/L atomic absorption standard solution) and dimethylglyoxime (DMG). Graphite (fine powder synthetic), antimony (V) chloride were provided by Aldrich (Germany). All other reagents used were provided by Merck (South Africa) and included sodium acetate, ammonia with a purity of ca. 25% ammonium

chloride, hydrochloric acid with purity 32% and nitric acid with purity 55%. Glacial acetic acid and ethanol (95%) were purchased from Kimix (South Africa).

rGO-SbNPs were obtained by refluxing antimony pentachloride in a mixture of 10:4 graphene and polyvinyl alcohol in ethanol containing sodium borohydride. Graphite (fine powder synthetic), antimony (V) chloride, dimethylglyoxime (99%) and polyvinyl alcohol (99%) were purchased from Sigma-Aldrich, USA. Hydrochloric acid fuming (32%), N,N dimethylformamide (DMF) and hydrogen peroxide (32%; Grade AR) were purchased from Merck, South Africa. Ethanol Grade AR was purchased from Kimix Chemical and laboratory suppliers, South Africa. All chemicals were used as received.

6.2.2 Apparatus

All experiments were performed with Epsilon analyser (BASi Instruments, West Lafayette, IN, USA) connected to a personal computer using cyclic voltammetry (CV) and differential pulse stripping voltammetry (DPSV) equipped with three electrode system. The electrode set-up consisted of a conventional three electrode configuration, which comprised a glassy carbon (GC) working electrode, a Pt wire as counter electrode and silver/silver chloride (Ag/AgCl) as a reference electrode. Alumina micro polish and polishing pads (Buehler, IL, USA) were used for electrode polishing.

A PalmSensportablepotentiostat / galvanostat, with the PS Trace program and accessories (PalmSens® Instruments BV, 3992 BZ Houten, The Netherlands), interfaced to a microcomputer controlled by PS 2.1 software for data acquisition and experimental control was also used. The measurements were performed in a conventional electrochemical cell of 20.0 ml, employing with 4 mm diameter provided by Dropsens (Oviedo, Spain) as working electrodes. The measurement of pH values during the experiments was carried out by means of a microprocessor pH meter with custom buffers (the model HI 221 series, Hanna, instruments). All experiments were performed at a controlled room temperature of 20 ± 1 °C (Silwana *et al.*, 2014; Somerset *et al.*, 2009).

6.2.3 Preparation of nanocomposite

The composite of rGO support SbNPs nanoparticles have been synthesised for the first time. Briefly synthesis of the rGO-SbNPsnanocomposite was performed using PVA as a stabiliser. Thus, a suspension containing a ratio in weight of 10:4 (rGO/PVA), *i.e.* 100 mg of rGO and 40 mg of PVA were loaded in 250 mL round bottomed flask charged with 100 mL of ethanol pure grade and sonicated for 20 min. An excess of sodium borohydride (80 mg of NaBH_4) was then added in this suspension and sonicated for a further 20 min. A solution containing 0.118M (2 ml of SbCl_5) was slowly dropped onto the mixture, which was kept under constant stirring. Once the reaction was complete, the rGO-SbNPsnanocomposite was dispersed using an ultrasonic probe for 1 h. Finally, the rGO-SbNPs was filtered through a 0.45 μm Millipore nylon filter membrane under a vacuum and washed in the ultrapure water. The formed nanocomposite was then dried in a vacuum for 24 h at 60 °C.

6.2.4. Preparation of the electrodes

Prior to modification, the GC electrode surface was polished with various concentrations of alumina slurries, rinsed thoroughly with double-distilled water, sonicated for 5 min in ethanol and 5 min in water, and dried in air. A nanocomposite of rGO-SbNPs was prepared by dispersing 1 mg of the rGO-SbNPs in 1.0 mL of DMF by ultrasonication agitation for about 10 min. A 5 μL aliquot of this dispersion was dropped onto the GC electrode surface and left to dry overnight. After modification the surface of the electrode was carefully washed with distilled water. Finally, this was followed using voltammetric stripping measurements of the analyte solution and employing AdDPSV in the cathodic scanning direction.

6.2.5 Analytical procedure for the determination of PGMs

Before each voltammetric titration process, the presence of PGMs was checked by recording the AdDCSV of the blank buffer solution. The electrode surface was activated by 10 replicate direct current sweeps from + 0.6 to - 1.5 V (vs. Ag/AgCl) with scan rate 50 mV s^{-1} in 0.2 M acetate buffer (pH = 4.8) solution. The solution was then exchanged by a sample solution

containing the same supporting electrolyte purged by pure nitrogen gas for 5 min. The procedure used to obtain AdDCSV was as follows: A 5 ml of 0.2 M NaOAc buffer (pH = 5.2) solution containing 5×10^{-5} M DMG was transferred into the voltammetric cell. The stirrer was switched on and the solution was purged with nitrogen gas for 5 min. Then the analyte was pre-concentrated for 120 s at - 1.2 V (vs. Ag/AgCl) whilst stirring the solution at 200 rpm. At the end of the accumulation time the stirrer was switched off. After resting for 10 s, the AdDPCSV was performed, with the potential scanned from + 0.6 to - 1.5 V (vs. Ag/AgCl) at a scan rate 90 mV s^{-1} . When further metal solution was added to the cell, the solution was deoxygenated with nitrogen before performing further voltammetric analysis. The peak current was used for the construction of calibration curves for each metal investigated.

6.3. Results and Discussion

6.3.1 Influence of Supporting Electrolytes

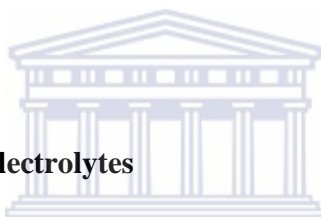


Figure 51 shows the influence of different buffer solution on cyclic voltammogram of rGO-SbNPs on a GCE/rGO-SbNPs sensor at a scan rate 10 mV s^{-1} .

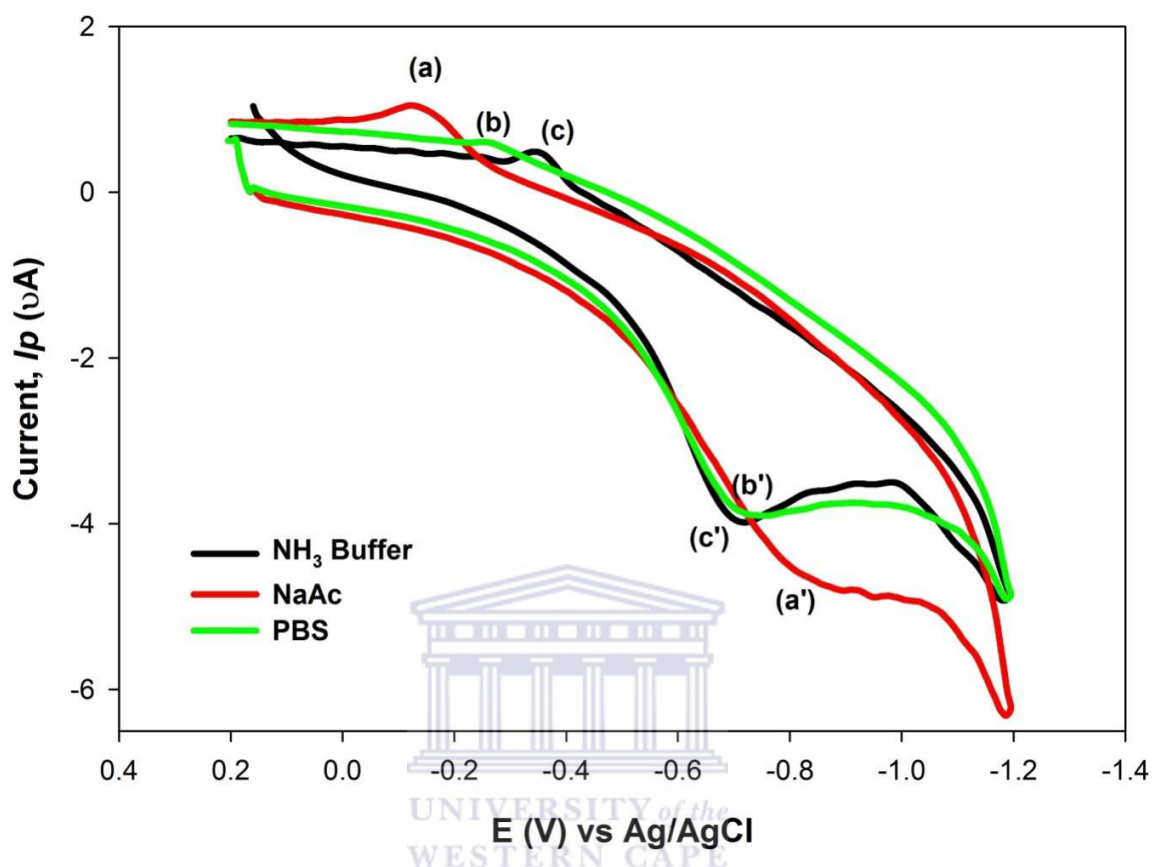


Figure 51. Effect of different buffers at concentration on CVs of the GCE/rGO-SbNPs sensor at a scan rate of 10 mV s^{-1} in: (a) 0.2M NH_3 buffer (pH = 9.2); (b) 0.2 M NaOAc buffer (pH = 4.8); and (c) 0.2 M PB (pH = 7.4) buffer solutions.

Figure 51 shows the CVs of GCE/rGO-SbNPs sensor in: (a) 0.2M NaOAc buffer (pH = 4.8); (b) 0.2M NH_3 buffer (pH = 9.2); and (c) 0.2M PB buffer (pH = 7.4) solutions at the scan rate of 10 mV s^{-1} . Preliminary investigation of the rGO-SbNPs was performed using CV in different types of supporting electrolytes as seen in Figure 47 of the previous chapter. The supporting electrolytes examined included 0.01 M NH_3 buffer (pH = 9.2), 0.2 M NaOAc buffer (pH = 4.8), 0.1 M HCl, 1 mM $\text{K}_3\text{Fe}(\text{CN})_6$, and 4×10^{-3} M LiClO_4 solutions (Figure 47).

It is noteworthy to mention here that the highest cyclic voltammetric signal was achieved in 0.1 M HCl solution, but performing electrochemical experiments in the same medium lead to the electrode surface collapse. Thus, we excluded the 0.1 M HCl, 1 mM $\text{K}_3\text{Fe}(\text{CN})_6$, and 4×10^{-3}

3M LiClO_4 solutions in our investigation and continue focusing on buffered solutions of the same concentration as shown in Figure 51. For the purpose of this experiment buffered solution were chosen since most of the literature has used phosphate buffer on graphene related sensors. Another reason, buffer system is required when pH control is essential. Three media, namely 0.2 M NH_3 buffer (pH = 9.2), 0.2 M NaOAc buffer (pH = 4.8) and 0.2 M PB buffer (pH = 7.4) solutions were tested to clarify their repercussion on the quantitative results as supporting media. From the different electrolytes investigated, it was found that all the ions in these acids show interactions on the carbon rGO-SbNPs surface. Additionally, the acetate buffer was outstanding in terms of resolution and peak current signal in both oxidation and reduction peaks. All the experiments in this study were performed using 0.2 M NaOAc buffer solution. Wei *et al.* (2012) observed the same response using a nanocomposite of Tin Oxide-Reduced Graphene Oxide ($\text{SnO}_2\text{-rGO}$) in three different supporting electrolytes: 0.1 M $\text{NH}_3\text{Cl-HCl}$, phosphate buffer, and acetate buffer solutions (Wei *et al.*, 2012).



6.3.2 Complexing reagent

Complexing reagent studies were performed using the chemical modification previously determined for the detection of PGMs. The concentration of DMG and alizarin red were varied in the previous investigation done by Silwana *et al.* (2014). The DMG chelating agent showed merit results for the determination of Pd(II), Pt(II) and Rh(III) in standard solutions. Following the previous investigation of the suitable complex reagent as well as concentration between alizarin red and DMG for PGMs, the performance of the GCE/rGO-SbNPs sensor was tested at the above mentioned conditions (Silwana *et al.*, 2014; van der Horst *et al.*, 2012).

6.3.3 Influence of pH

The electrochemical behaviour of rGO-SbNPs on the GCE and SPCE was studied in 0.2M NaOAc buffer solutions in the pH 4 to 6 range, as depicted in Figure 52.

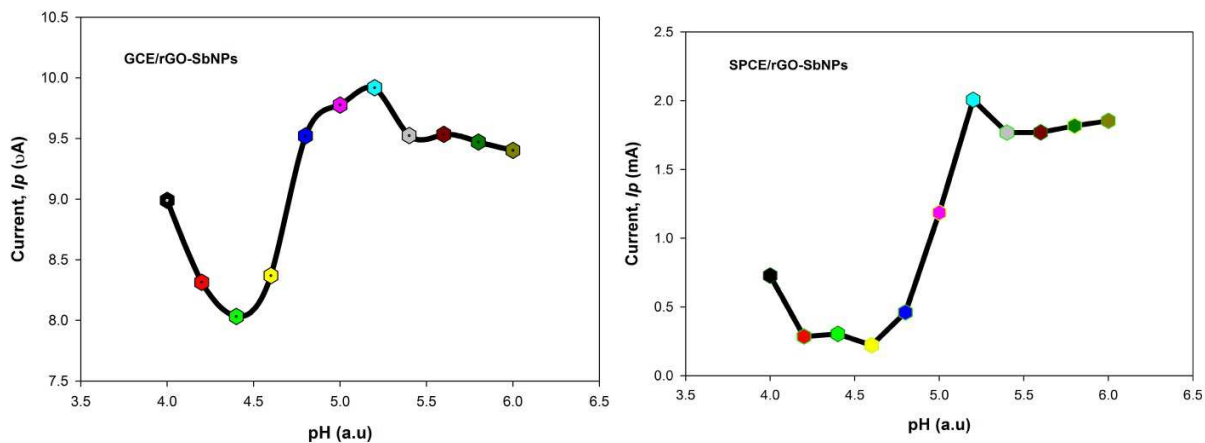


Figure 52. Influence of the pH value on the stripping current of GCE/rGO-SbNPs and SPCE/rGO-SbNPs in 0.2M NaOAc buffer (pH = 4.8) solution.

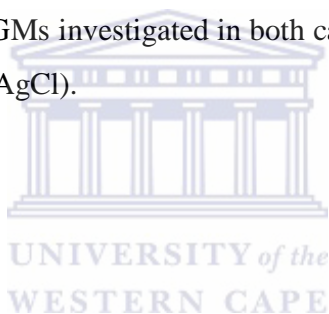
The effect of pH value is very important and is essential to select a proper pH value. The second step of this chapter was to investigate the influence of pH on the peak current of the GCE/rGO-SbNPs and SPCE/rGO-SbNPs sensors respectively, in the pH 4.0 to 6.0 range (Figure 52). The peak current increased with pH until it reached its maximum at pH = 5.2 for both sensors and then began to decrease slightly. An increase in peak current signal as pH increase has been observed from 4.6 to 5.2. Furthermore, beyond pH = 5.2, the peak current magnitude decreased gradually with increasing pH. From these results, the functional pH range of the both novel working electrodes was taken to be between 4.6 and 6.0 with the optimal pH appearing at 5.2. A pH = 5.2 was then chosen for the whole study conducted. The peak current decreased observed higher than pH = 5.2, could be ascribed to the decreasing proton concentration in the buffer system. From Figure 52, it is evident that the GCE/rGO-SbNPs and SPCE/rGO-SbNPs sensors are comparable with optimal pH obtained at pH = 5.2.

6.3.4 Deposition potential optimisation studies

The deposition potential is applied to the working electrode to cause the material of interest to be deposited onto the surface of the working electrode. The solution is generally stirred during deposition to maximise analyte-electrode contact. The selection of the deposition

potential depends upon whether the material to be determined is oxidised or reduced. As discussed by other authors (Gonzalez *et al.*, 2004), the deposition potential (E_d) at which the metal ion is able to deposit on the electrode surface is critical. Thus, the choice of the deposition potential can provide some selectivity in the measurement in order to obtain maximum sensitivity and optimum results. The potential applied during electrolysis step for deposition of metal ion should be at least 0.3 V less negative than the reversible potential calculated from the Nernst equation (Wang, 1985).

The voltammetric analysis of Pd(II), Pt(II) and Rh(III) as dimethylglyoxime (DMG) complexes on the respective GCE/rGO-SbNPs and SPCE/rGO-SbNP sensors was determined as a function of deposition potential (E_d) in sodium acetate buffer (pH = 5.2) solution and plotted against the peak current (I_p) values to make it easy to select the optimal deposition potential. Figure 53 represent the comparative results obtained for the optimisation of the deposition potential for all three PGMs investigated in both carbon nanoparticles sensor platform at a range of -0.1 to -1.2 V (vs. Ag/AgCl).



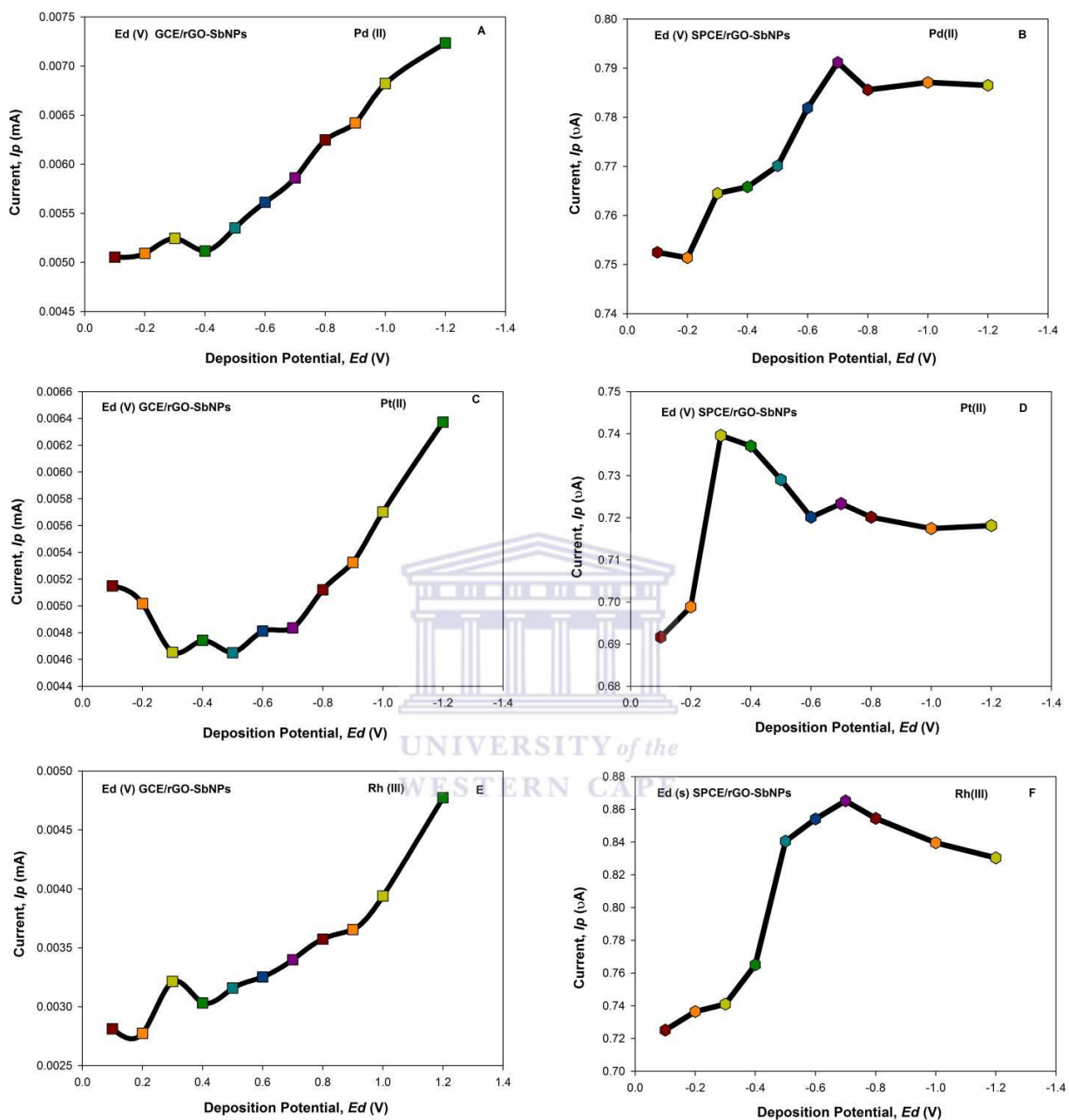


Figure 53. Results obtained for effects of E_d upon the peak current responses to 1 ng L^{-1} of Pd(II) (A), Pt(II) (C), Rh(II) (E) on GCE/rGO-SbNPs and Pd(II)(B), Pt(II) (D), Rh(II) (F) on SPCE/rGO-SbNPs evaluated in the presence of 0.2 M NaOAc buffer ($\text{pH} = 5.2$) solution.

In Figure 53(A), the results obtained for the Pd(II) peak current on a GCE/rGO-SbNPs sensor is displayed, indicating that the I_p values increased as the deposition potential became

more negative. The highest I_p was found at E_d of -1.2 V (vs. Ag/AgCl), which indicates that at this potential strong adsorption of Pd(II) takes place on the electrode surface. In Figure 53 (B), the results obtained for the Pd(II) peak current on a SPCE/rGO-SbNPs sensor are displayed, indicating that the I_p values increased as the deposition potential became more negative. A highest I_p was found at E_d of -0.7 V (vs. Ag/AgCl), which indicates that at this potential strong adsorption of Pd(II) takes place on the electrode surface.

In Figure 53(C), the results obtained for the Pt(II) peak current on a GCE/rGO-SbNPs sensor are displayed, indicating that the I_p values increased as the deposition potential became more negative. A highest I_p was found at E_d of -1.2 V (vs. Ag/AgCl) which indicates that at this potential, strong adsorption of Pt(II) takes place on the electrode surface. In Figure 53(D), the results obtained for the Pt(II) peak current on a SPCE/rGO-SbNPs sensor are displayed, indicating that the I_p values increased as the deposition potential from -0.1 V (vs. Ag/AgCl) and decreases beyond -0.3 V (vs. Ag/AgCl). A highest I_p was found at E_d of -0.3 V (vs. Ag/AgCl), which indicates that at this potential, strong adsorption of Pt(II) takes place on the electrode surface.

In Figure 53(E), the results obtained for the Rh(III) peak current on a GCE/rGO-SbNPs sensor are displayed, indicating that the I_p values increased as the deposition potential became more negative. A highest I_p was found at E_d of -0.7 V (vs. Ag/AgCl) which indicates that at this potential, strong adsorption of Rh(III) takes place on the electrode surface. In Figure 53(F), the results obtained for the Rh(III) peak current on a SPCE/rGO-SbNPs sensor are displayed, indicating that the I_p values increased as the deposition potential up to -0.7 V (vs. Ag/AgCl) and decreases beyond this value. A highest I_p was found at E_d of -0.7 V (vs. Ag/AgCl) which indicates that at this potential, strong adsorption of Pt(II) takes place on the electrode surface. After analysis of the results shown in Figure 53, it was decided that a deposition potential of -1.2 V (vs. Ag/AgCl) and -0.7 V (vs. Ag/AgCl) for GCCE/rGO-SbNPs and SPCE/rGO-SbNPs sensors, respectively will be used as an optimum value for the rest of the experiments conducted in this chapter.

6.3.5 Deposition time optimisation studies

Under the optimised deposition potential conditions, the effect of varying the deposition time was investigated and the results are shown in Figure 54. The experimental conditions were Pd(II), Pt(II) and Rh(III) = 1 ng L⁻¹, [DMG] = 1×10⁻⁵M, pH = 5.2 (0.2 M NaOAc buffer) solution and $E_d = -1.2$ V (vs. Ag/AgCl) in the range from 30 – 300 seconds.

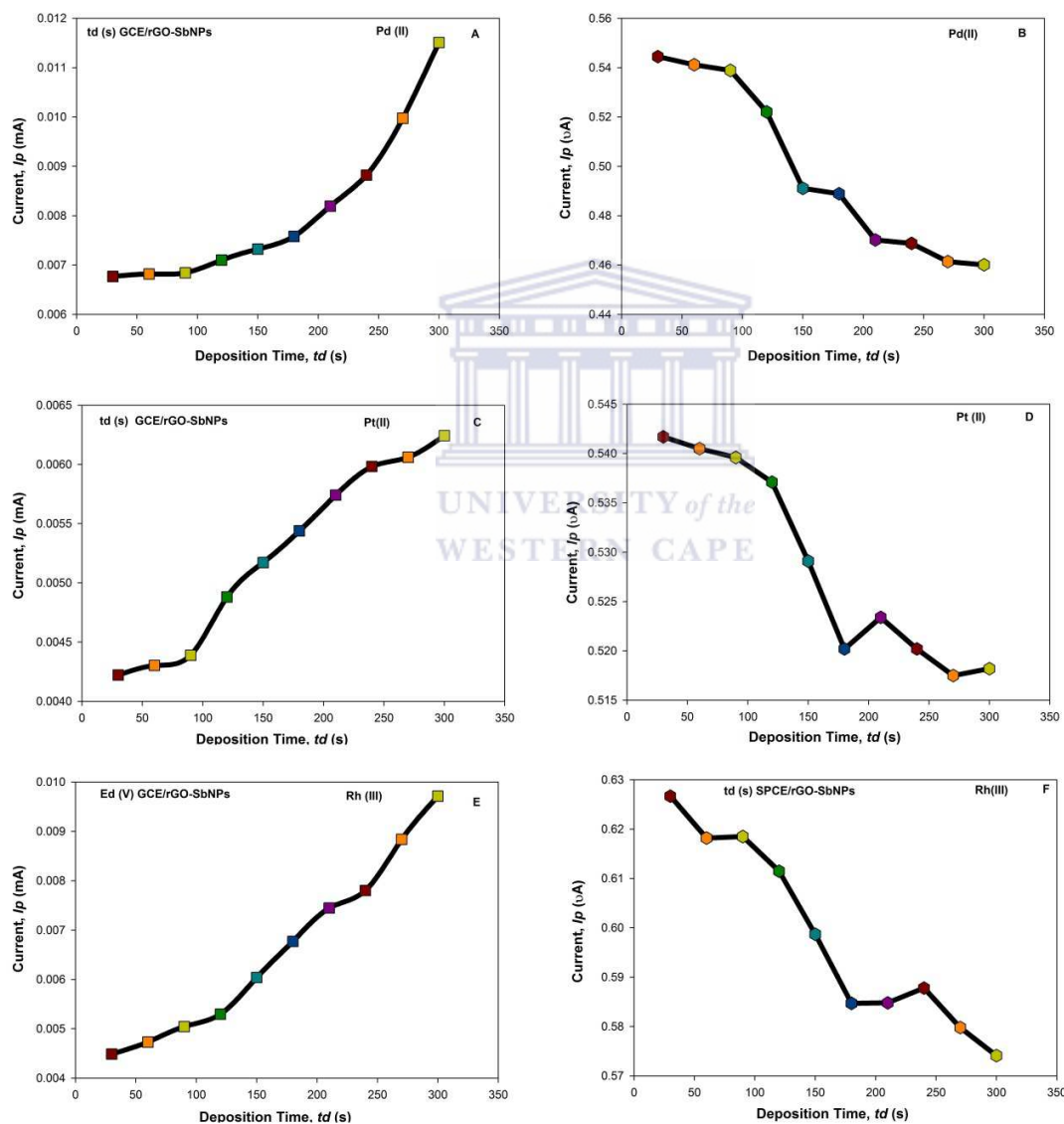


Figure 54. Effects of t_d upon the response to 1 ng L⁻¹ (A) Pd(II), (C) Pt(II), (E) Rh(III) on a GCE/rGO-SbNPs sensor and (B) Pd(II), (D) Pt(II), (F) Rh(III) in the presence of 0.2 M NaOAc buffer (pH = 5.2) solution.

Deposition time (t_d) is another important stripping voltammetric parameter, which should be precisely controlled during the stripping experiment. In Figure 54 (A), (C), and (E) the results obtained for the PGMs peak current on a GCE/rGO-SbNP sensor are displayed, indicating that the I_p values increased as the deposition time increases. The stripping current was found to increase with the expanding deposition time in the considered range, indicating an enhancement of PGMs complex uptakes at the electrode surface. On the basis of this study, 120 s was regarded as a good compromise between sensitivity and time-consuming for all further measurements.

In Figure 54 (B), (D), (F), the results obtained for the PGMs peak current on a SPCE/rGO-SbNPs sensor are displayed with the unusual behaviour, indicating that not too much difference found for the I_p values for the first 30 - 120 s. The slowly decreases in peak current signal which is due to the complete coverage of the electrode surface for the selected PGMs (Wang, 1985). However, when the t_d is longer than 120s, the I_p gradually decreases. This is an indication of saturation of the electrode surface at the long deposition periods and, thus, confirms the involvement of adsorption during the preconcentration step. Hence, in performing standard additions or calibration, electrode saturation may be avoided by using deposition periods less than 100 s (Shams *et al.*, 2004). Taking into consideration the suggestion done by Sham *et al.* (2004), therefore, a step having a deposition time of 90 s was chosen to further studies.

In summary, since there was not too much difference in peak current signal for deposition potential up to 120 s for both nanoparticle sensor, beyond which a gradually decrease in peak current signal for the SPCE and the GCE sensors were observed. Both sensors perform the opposite way with increase in peak current as the t_d increases. Hence, 90 s and 120 s were taken as the optimised t_d for PGMs determination using the SPCE/rGO-SbNPs and GCE/rGO-SbNPs sensors, respectively. Further investigation should be addressed on the unusual behaviour of the SPCE/rGO-SbNPs sensor.

6.3.6 Stirring Period optimisation studies

Figure 55 shows the influence of the electrode rotation rate (stirring speed) on the PGMs stripping peak currents using 120 s for deposition time.

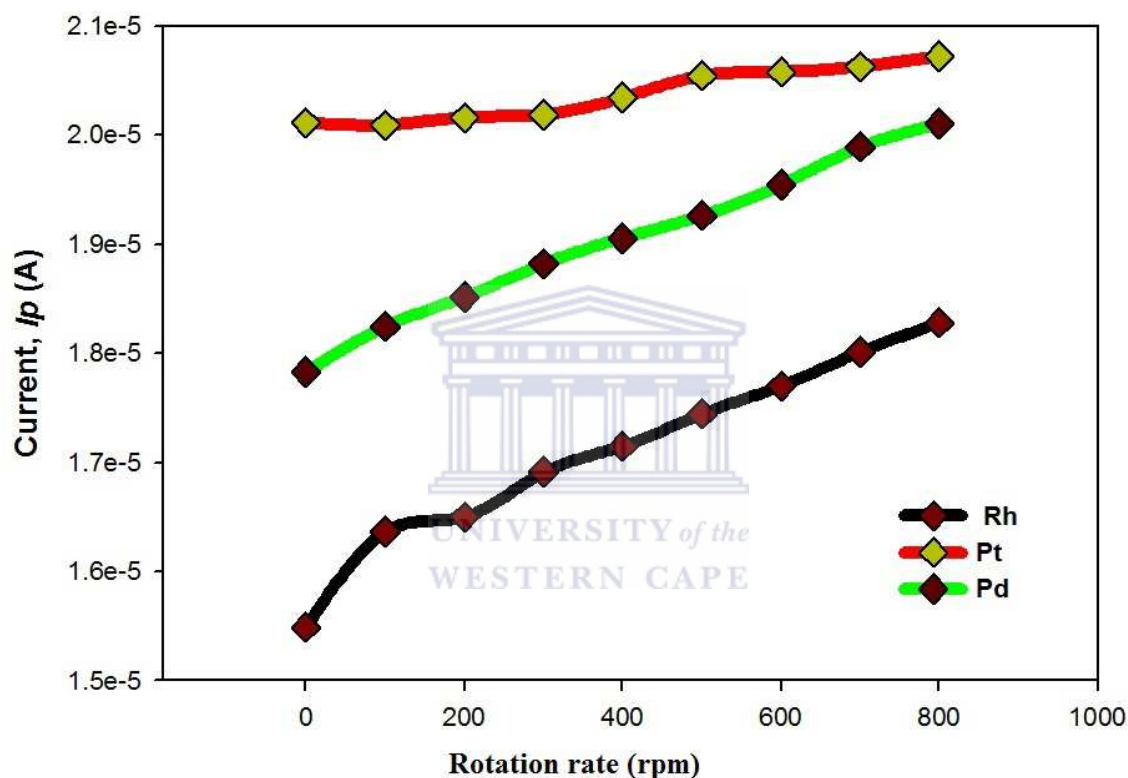


Figure 55. Influence of electrode rotation rate on Pd(II), Pt(II) and Rh(III) stripping peak currents obtained in a 1 ng L^{-1} of PGMs, 0.2 M NaOAc ($\text{pH} = 5.2$) solution, containing $1 \times 10^{-5} \text{ M DMG}$ solution, $E_d = -1.2 \text{ V}$ (vs. Ag/AgCl); $t_d = 120 \text{ s}$.

When cathodic stripping voltammetry is accomplished the solution is stirred during the first two steps at a repeatable rate. The first step is a cleaning step that is characterised by the potential being held at a more oxidising potential than the analyte of interest for a period of time in order to fully remove it from the electrode. In the second step, the potential is held at a lower potential, low enough to reduce/oxidise the analyte and deposit it on the electrode. After the second step, the stirring or rotation of the electrode is stopped, and the electrode is kept at the

lower/higher potential. The last step involves raising the working electrode to a higher potential (anodic), and stripping (oxidising) the analyte. As the analyte is oxidised, it releases electrons which are measured as a current. This aspect is similar when anodic stripping voltammetry is used (Mardegan, 2013).

Figure 55 shows that the peak currents increased gradually with increasing electrode rotation rate indicating an increase in the amount of Pd(II), Pt(II) and Rh(III) on the electrode. The graphs also show that no saturation occurred even when very high speed was utilised and this situation is demonstrated by increase with peak current up to 800 rpm. However, based on the peak resolution and reproducibility, the peak currents were better at lower rates of electrode rotation. Hence, a stirring speed rate of 200 rpm was chosen.

6.3.7 Stability testing of the GCE/rGO-SbNPs sensor

The GCE modified with a rGO-SbNPs film showed that the best analytical parameters were studied for stability. The stability of GCE/rGO-SbNPs sensor was investigated in 0.2M NaAOC buffer (pH = 5.2) solution by measuring 0.1 ng L⁻¹ of each of the PGM-(DMG)_x complexes using cathodic adsorptive stripping voltammetry in the potential range from + 0.6 to - 1.5 V (vs. Ag/AgCl) at a scan rate of 120 mVs⁻¹ for every 5days (Figure 56).

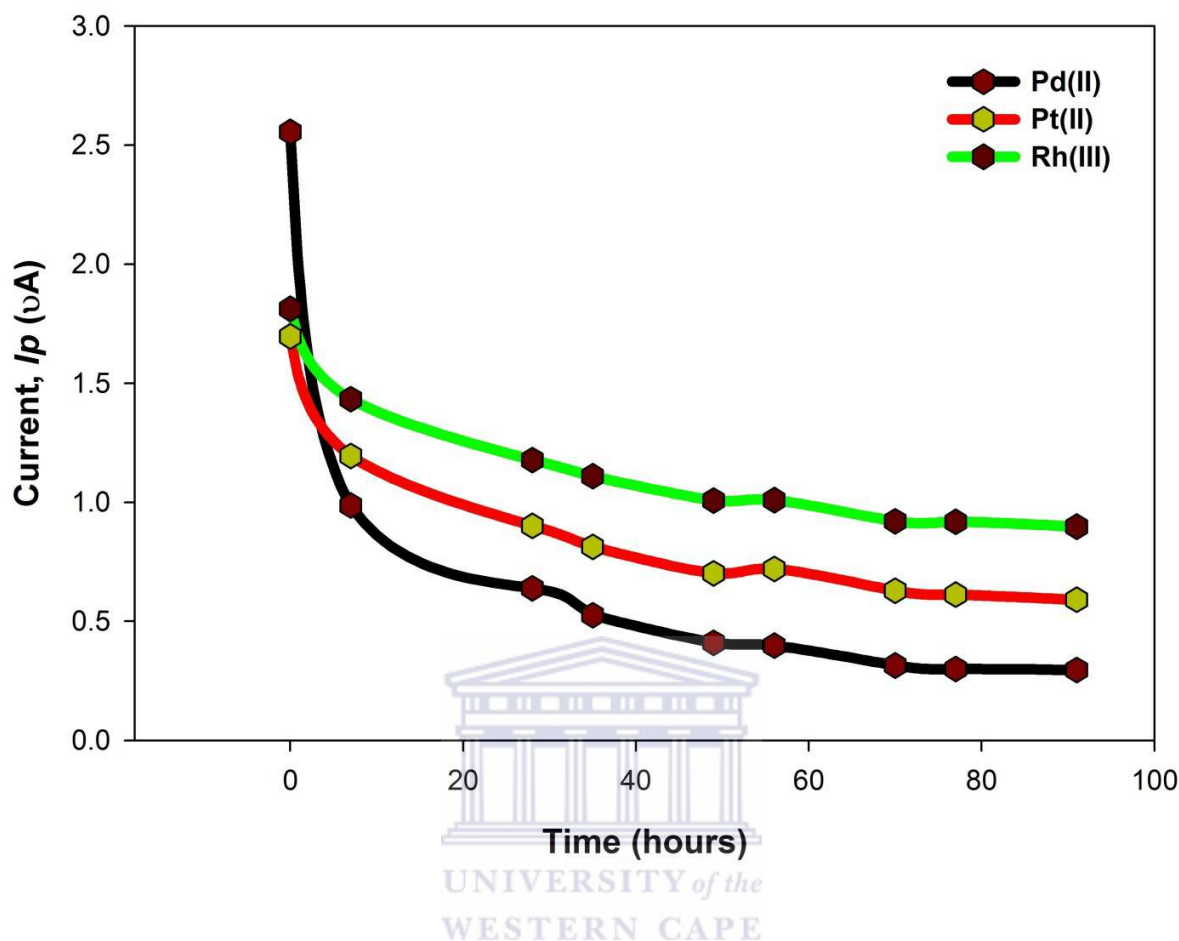


Figure 56. Results obtained for stability testing of the GCE/rGO-SbNPs sensor in 0.2 M NaOAc buffer (pH = 5.2) solution containing 0.1 ng L^{-1} of selected PGMs with 1×10^{-5} DMG concentration, $E_d = -1.2 \text{ V}$ (vs. Ag/AgCl) and $t_d = 120 \text{ s}$.

Figure 56 shows that the peak current results obtained for the selected PGMs was plotted against time for each of the PGMs [HDMG]_x complexes investigated.

Stability studies were also performed. The prepared sensors were stored for up to 98 h when needed, for the results collected and reported in this section. The results have shown close similarities in the peak current for the entire duration of the experiment, with slight current decreases between 0 and 56 h obtained at the beginning of the experiment. For all the PGMs-[DMG]_x complexes investigated, a stable decrease in peak current was observed between 70 and 98 hrs (Figure 56).

In summary, after evaluation of the results for each of the PGMs complexes the stability has shown over a period of 70 to 98 h.

6.3.8 Analytical features of the adsorptive stripping voltammetry procedure

An electro-analytical method for the analysis of PGMs in soil and dust samples using adsorptive differential pulse cathodic stripping voltammetry (AdDPCSV) with DMG as complexing agent on the GCE/rGO-SbNPs and SPCE/rGO-SbNPs sensors is finally proposed and the optimum conditions of this method are presented in Table 15.

Table 15. Summary of the optimal conditions for PGMs determination with the respective GCE/rGO-SbNPs and SPCE/rGO-SbNPs sensor platforms and DMG as complexing agent.

Sensor	Step	Condition / Analysis			Unit
		Pd(II)	Pt(II)	Rh(III)	
	<i>Reduction step</i>				
	pH	5.2	5.2	5.2	
	Reduction potential				
GCE/rGO-SbNPs		-1.2	-1.2	-1.2	V
SPCE/rGO-SbNPs		-0.7	-0.7	-0.7	V
	<i>Reduction time</i>				
GCE/rGO-SbNPs		120	120	120	s
SPCE/rGO-SbNPs		90	90	90	s
	Concentration of Buffer		0.2		M
	Complexing agent		Dimethylglyoxime (DMG)		
	Stirring speed		200		rpm
	<i>Measurement step</i>				
	Measuring technique	Adsorptive Differential Pulse Stripping Voltammetry			
	Method Calibration	Standard addition			

Cell volume	25	mL
Buffer	Sodium Acetate buffer solution	
Potential window	Sweep potential from +0.6 to -1.5 V	

The results obtained showed that a deposition time of 120 s and deposition potential of -1.2 V (vs. Ag/AgCl) gave well defined peaks for the GCE/rGO-SbNPs sensor and a deposition time of 90s and deposition potential of - 0.7 V (vs. Ag/AgCl) for the SPCE/rGO-SbNPs sensor. Table 15 provides a summary of the optimal conditions for the adsorptive differential pulse stripping voltammetric (AdDPCSV) evaluation of Pd(HDMG)₂, Pt(HDMG)₂ and Rh(HDMG)₃. These parameters were applied in the next stage of the investigation for the analysis of the PGMs in various matrices.

Thus, the procedure was as follows. The sample containing each of the selected PGMs was conditioned by addition of 0.2 M NaOAc buffer (pH = 5.2) solution and added 1×10^{-5} M DMG solution. After that, 1 ml of sample was put into the voltammetric cell and the buffer was added. The solution was de-oxygenated for 150 s with high purity nitrogen and the adsorption PGMs was done using a preconcentration potential of -1.2V (vs. Ag/AgCl) under stirring conditions of 200 rpm for 120 s. After an equilibration time of 10 s, the adsorbed metal complex was stripped and voltammogram was recorded in the quiescent solution by scanning cathodically (direction). Scans of each experiment were repeated triplicate with a new developed sensor. The metal analysis was performed by standard addition method.

6.3.9 Calibration curves

To better understand the electro-analytical characteristics of our sensors, we performed AdDPCSV measurements of different concentrations of the selected PGMs under the chosen optimum conditions. Before assessing the performance of the developed nanosensors in environmental samples, the most suitable carbon electrode to use needed to be addressed. This was ascertained in two ways:

- Compare PGMs detection and reproducibility for GCE/rGO-SbNPs and SPCE/rGO-SbNPs sensors.
- Compare sensitivity and linear ranges for PGMs quantification through standard curves (in 0.2 M NaOAc; pH= 5.2 solution) as determined in proposed procedure.

Figure 57 displays the results for GCE/rGO-SbNPs and SPCE/rGO-SbNPs sensors obtained for the Pd(HDMG)₂ complex with increasing in peak current as concentration increases.

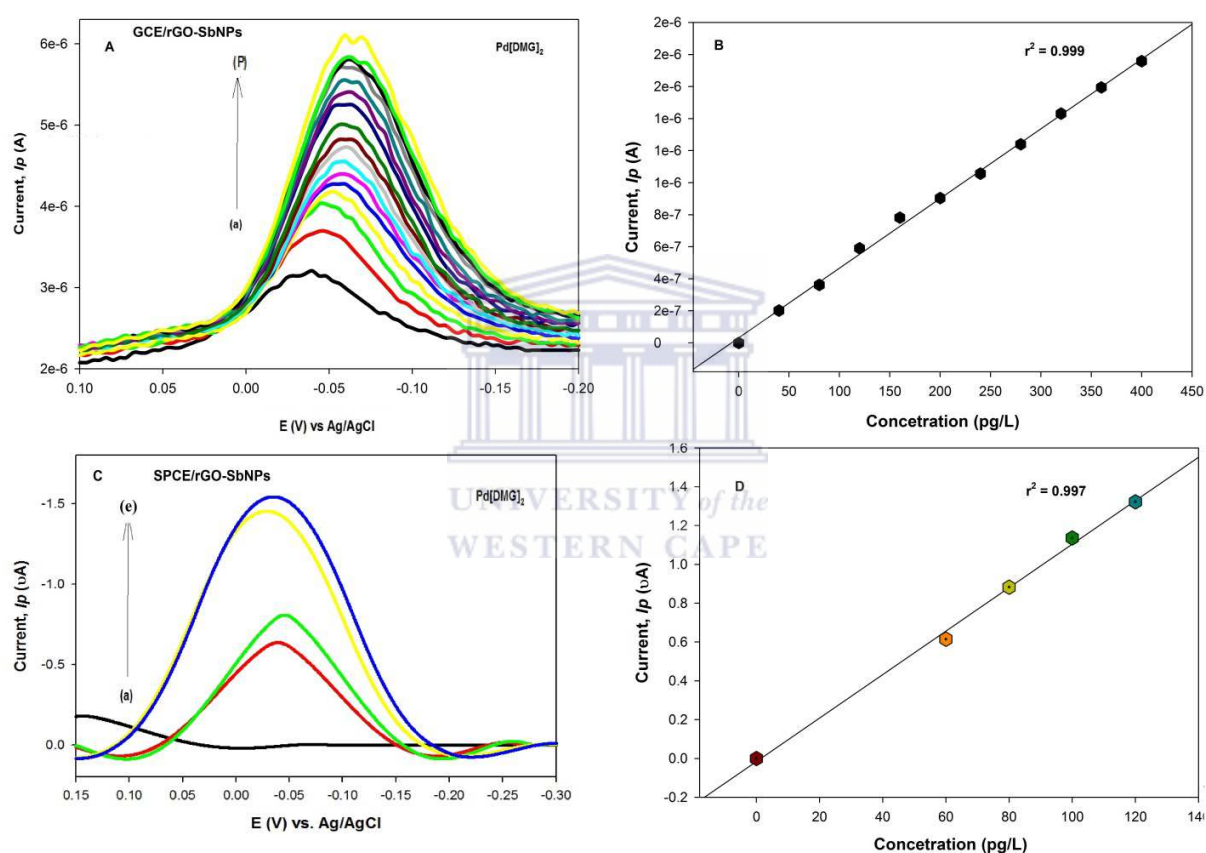


Figure 57. Results obtained for the AdDPCSV analysis for the increasing concentrations of Pd(HDMG)₂ evaluated using the GCE/rGO-SbNPs and SPCE/rGO-SbNPs sensors, respectively in 0.2 M NaOAc buffer (pH = 5.2) solution with 0.00, 40, 80, 120, 160, 200, 240, 280, 360, 400 Pd(II) $\mu\text{g L}^{-1}$ concentrations; with $E_d = -0.7$ V (vs. Ag/AgCl); $t_d = 90$ s for SPCE/rGO-SbNPs sensor and $E_d = -1.2$ V; $t_d = 120$ s for GCE/rGO-SbNPs sensor.

Calibration plots were obtained under the optimised conditions with consecutive additions of 1×10^{-8} ppb of Pd(II) and the corresponding equation for this dependence is shown

on each graph. The peak at approximately -0.05 V vs (Ag/AgCl) increases linearly with $\text{Pd}(\text{HDMG})_2$ concentration for both electrodes in the range $0 - 400 \text{ pg L}^{-1}$ for the GCE/rGO-SbNPs and SPCE/rGO-SbNPs sensors, respectively as shown in Figure 57. Calibration plots showed good linear correlation for the concentration range between $0 - 400 \text{ pg L}^{-1}$ as obtained for the GCE/rGO-SbNPs sensor and between $0 - 100 \text{ pg L}^{-1}$ obtained for the SPCE/rGO-SbNPs sensor. The SPCE/rGO-SbNPs sensor also produced a slight initial increase in current response, but for the concentrations greater than 120 pg L^{-1} a more significant decrease in current was observed, suggesting a saturation of the thin film has occurred.

Figure 58 displays the results for the respective GCE/rGO-SbNPs and SPCE/rGO-SbNPs sensors obtained for the $\text{Pt}(\text{HDMG})_2$ complex with increasing peak current as concentration increased.

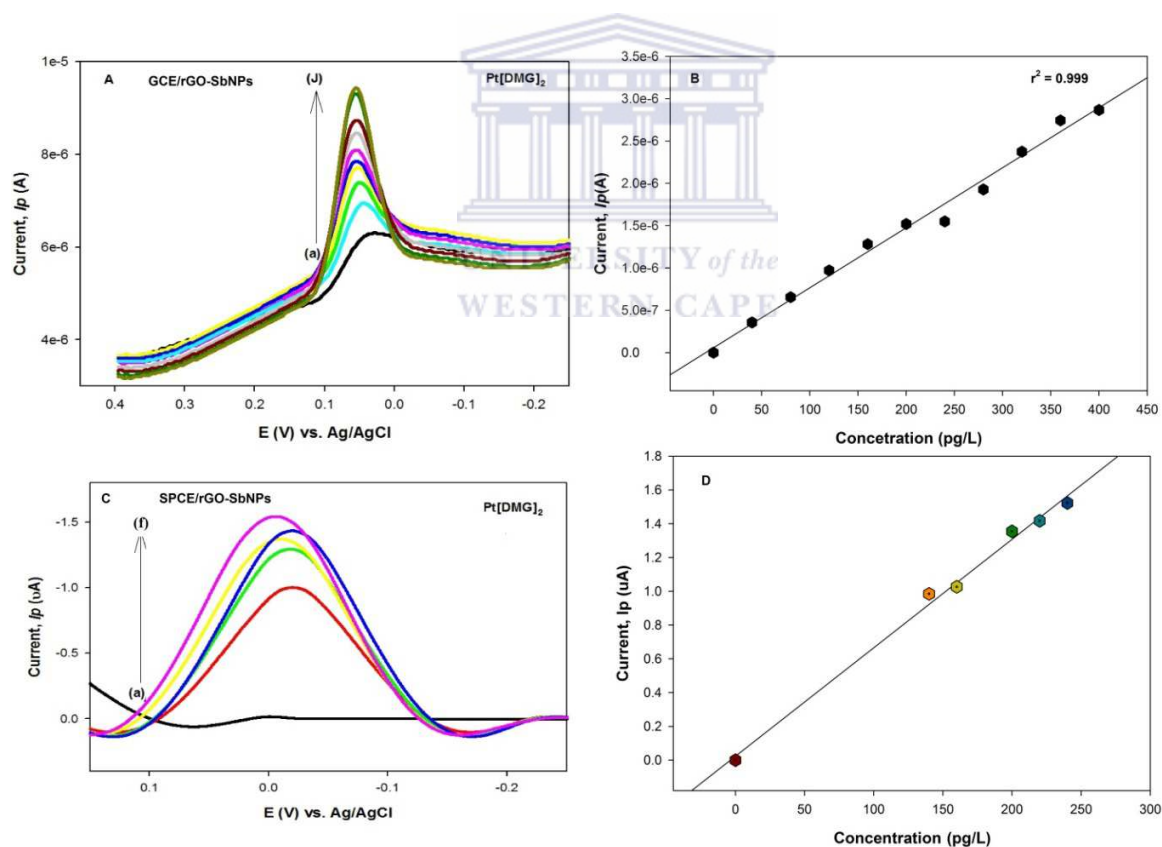


Figure 58. Results obtained for the AdDPCSV analysis for the increasing concentrations of $\text{Pt}(\text{HDMG})_2$ evaluated using the GCE/rGO-SbNPs and SPCE/rGO-SbNPs sensors, respectively in 0.2 M NaOAc buffer ($\text{pH} = 5.2$) solution with $0.00, 40, 80, 120, 160, 200, 240, 280, 360, 400 \text{ Pt(II) pg L}^{-1}$ concentrations; with $E_d = -0.7 \text{ V}$; $t_d = 90\text{s}$ for SPCE/rGO-SbNPs sensor and $E_d = -1.2 \text{ V}$ (vs. Ag/AgCl); $t_d = 120\text{s}$ for GCE/rGO-SbNPs sensor.

The voltammograms shown in Figure 58 (A) and (C) has a stripping potential at approximately 0.02 V (vs. Ag/AgCl) and -0.01 (vs. Ag/AgCl) that slightly shift to positive potentials for a SPCE/rGO-SbNP sensor, as the concentration was increased. A good linear increase in the peak current was observed and is reflected in the calibration curve shown in Figure 58 (B) and (D). The calibration curve was linear over the concentration range studied from 0 to 400 $\mu\text{g L}^{-1}$ and 0 – 120 $\mu\text{g L}^{-1}$ of Pt(HDMG)₂ for GCE/rGO-SbNPs and SPCE/rGO-SbNPs sensors, respectively.

Figure 59 displays the results for respective GCE/rGO-SbNPs and SPCE/rGO-SbNPs sensors obtained for the Rh(HDMG)₃ complex with increasing peak current as concentration increased.

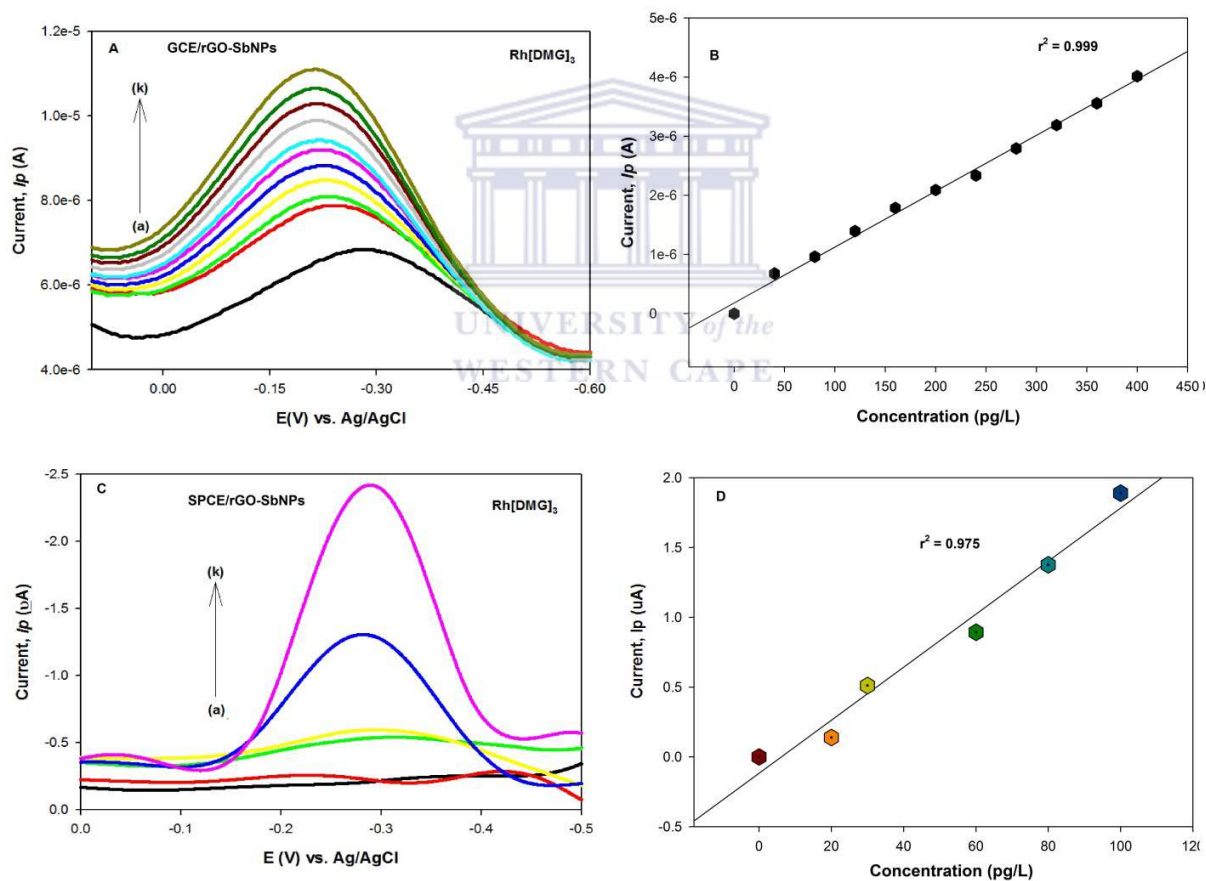


Figure 59. Results obtained for the AdDPCSV analysis for the increasing concentrations of Rh(HDMG)₃ evaluated using the GCE/rGO-SbNPs and SPCE/rGO-SbNPs sensors, respectively in 0.2 M NaOAc buffer (pH = 5.2) solution with 0.00, 40, 80, 120, 160, 200, 240, 280, 360, 400 Rh(III) $\mu\text{g L}^{-1}$ concentrations; with $E_d = -0.7$ V ; $t_d = 90$ s for SPCE/rGO-SbNPs sensor and $E_d = -1.2$ V ; $t_d = 120$ s for GCE/rGO-SbNPs sensor.

Figure 59 shows the responses of Rh(HDMG)₃ analysis at the respective GCE/rGO-SbNPs and SPCE/rGO-SbNPs sensors in 0.2 M acetate buffer (pH= 5.2) solution. Adsorptive stripping voltammograms obtained for the Rh(HDMG)₃ complex with increasing peak current as concentration increased is displayed (Figure 59). The voltammograms shown has a stripping potential at approximately -0.25 V and -0.30 (vs. Ag/AgCl) for the GCE/rGO-SbNPs and SPCE/rGO-SbNPs sensors, respectively. A good linear increase in the peak current was observed and is reflected in the calibration curves shown in Figure 59 (B) and (D).

In summary, the evaluation of the results for each of the carbon electrodes modified with nanoparticles has shown an increase in current as concentration increased up to 400 $\mu\text{g L}^{-1}$ and 120 $\mu\text{g L}^{-1}$ for GCE/rGO-SbNPs and SPCE/rGO-SbNPs sensors, respectively.

Table 2 summarises the current responses and reduction potentials for each of the PGMs analysed with the rGO-SbNPs modified electrodes (GCE/rGO-SbNPs and SPCE/rGO-SbNPs) in 0.2 M NaOAc buffer (pH = 5.2) solution.

Table 16. Summary of the comparative current responses and potentials for the cathodic reduction of Pd(HDMG)₂, Pt(HDMG)₂ and Rh(HDMG)₃ at the GCE/rGO-SbNPs and SPCE/rGO-SbNPs sensors, respectively.

Sensor	Current $ I_{pc} $ (μA)			Potential $ E_{pc} $ (V)		
	Pd(II)	Pt(II)	Rh(III)	Pd(II)	Pt(II)	Rh(III)
GCE/rGO-SbNPs	4.18	8.54	8.06	-0.05	0.04	0.25
SPCE/rGO-SbNPs	1.38	1.89	1.38	-0.05	0.01	-0.30

Each of the GCE/rGO-SbNPs and SPCE/rGO-SbNPs sensors was assessed under identical conditions and the only difference applied was the use of optimised parameters for E_d and t_d . With a potential window scanned in the cathodic direction between 0.6 V and -1.5 V (vs. Ag/AgCl) applied for both electrodes, some observations were made. By taking a proper look at the calibration curves the SPCE/rGO-SbNPs sensor current signal increased with concentration in a range up to 120, 240, and 80 $\mu\text{g L}^{-1}$ for Pd(II), Pt(II) and Rh(III), respectively. At concentrations above the above values, the saturation of the SPCE/rGO-SbNPs sensor surface occurred. We have selected the concentration values which gave increasing current signals for the SPCE/rGO-SbNPs sensor and also correspond to that for the GCE/rGO-SbNPs sensor. This

resulted with concentrations of 120, 240, and 80 $\mu\text{g L}^{-1}$ for Pd(II), Pt(II) and Rh(III), respectively.

These values were used for the comparative current and potential responses for the cathodic reduction of PGMs using both sensors constructed. The SPCE/rGO-SbNPs sensor platform yielded the lowest current response with a reduction potential almost the same as that of the GCE/rGO-SbNPs sensor. Although we have seen high current responses for the GCE/rGO-SbNPs sensor, we cannot conclude that it showed merit results since there were sensitivity issues we needed to deal with, which was not the case for the SPCE/rGO-SbNPs sensor. Since the SPCE/rGO-SbNPs sensor reached saturation at low concentration values, this problem can be overcome by using smaller concentrations than the ones used in this study. This might help to improve the current results obtained.

As the rGO-SbNPs nanofilm was proven to be suitable for PGMs detection, it was then decided to investigate their simultaneous measurement at the GCE surface. The results of this experiment are displayed in Figure 60 -62.

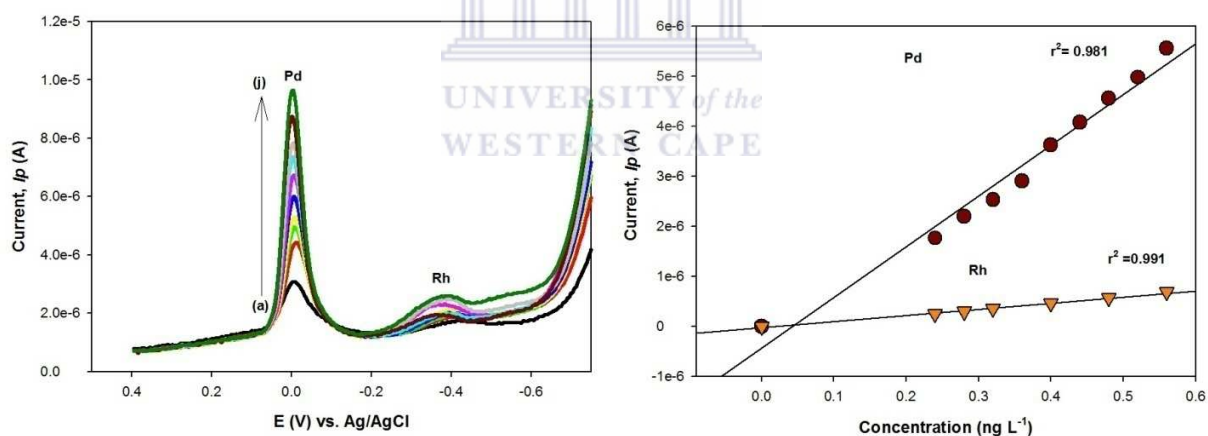


Figure 60. AdDPCSV analysis for the simultaneous determination of Pd-Rh-(HDMG)_x complexes at 0.00, 120, 160, 200, 240, 280, 320, 360, 400 $\mu\text{g L}^{-1}$ concentrations using a GCE/rGO-SbNPs sensor; $E_d = -1.2$ V (vs. Ag/AgCl) and $t_d = 120$ s with a corresponding linear calibration curve also shown.

The simultaneous determination of Rh(HDMG)₃ and Pd(HDMG)₂ is possible using the GCE/rGO-SbNPs sensor, but the current for the Rh(HDMG)₃ peak is smaller than that of Pt(HDMG)₂ evaluated for the same concentration. This simultaneous determination of these two elements was done successfully and the Pd(HDMG)₂ stripping peak has been observed at -0.04 V

(vs. Ag/AgCl), followed by the stripping peaks obtained at potential - 0.38 V (vs. Ag/AgCl) for Rh(HDMG)₃. It was obvious that the stripping peak currents for Rh(HDMG)₃ were lower. The reason might be due to a competition between these two elements for binding sites on the electrode surface. A good linear increase in the peak current was observed for both Pd(II) and Rh(III) that is reflected in the calibration curve.

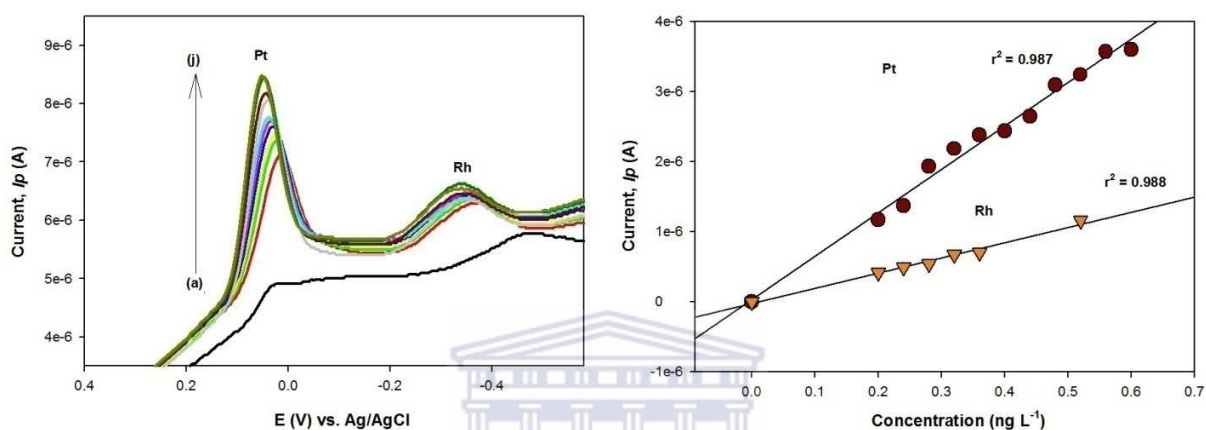


Figure 61. AdDPCSV analysis for the simultaneous determination of Pt-Rh-(HDMG)_x complexes at 0.00, 120, 160, 200, 240, 280, 320, 360, 400 $\mu\text{g L}^{-1}$ concentrations using a GCE/rGO-SbNPs sensor; $E_d = -1.2$ V (vs Ag/AgCl) and $t_d = 120$ s with a corresponding linear calibration curve also shown.

Figure 61 displays the results obtained for the simultaneous determination of Pt(HDMG)₂ and Rh(HDMG)₃ complexes. The simultaneous determination of Rh(HDMG)₃ and Pt(HDMG)₂ is possible but the current responses for the Rh(HDMG)₃ peak is smaller than that obtained for the Pt(HDMG)₂ complex for the same concentrations evaluated. This simultaneous determination of Pt(II) and Rh(III) was done successfully and the Pt(HDMG)₂ stripping peaks has been observed at 0.02V (vs. Ag/AgCl), followed by the stripping peaks obtained at potential -0.35 V (vs. Ag/AgCl) for Rh(III). A good linear increase in the peak current was observed that is reflected in the calibration curves (Figure 61).

I then became very ambitious and explored the simultaneous determination of Pt(II), Pd(II) and Rh(III) at the GCE surface. Figure 62 displays the results obtained for the simultaneous determination of Pt(HDMG)₂, Pd(HDMG)₂ and Rh(HDMG)₃ complexes at the GCE/rGO-SbNPs sensor surface.

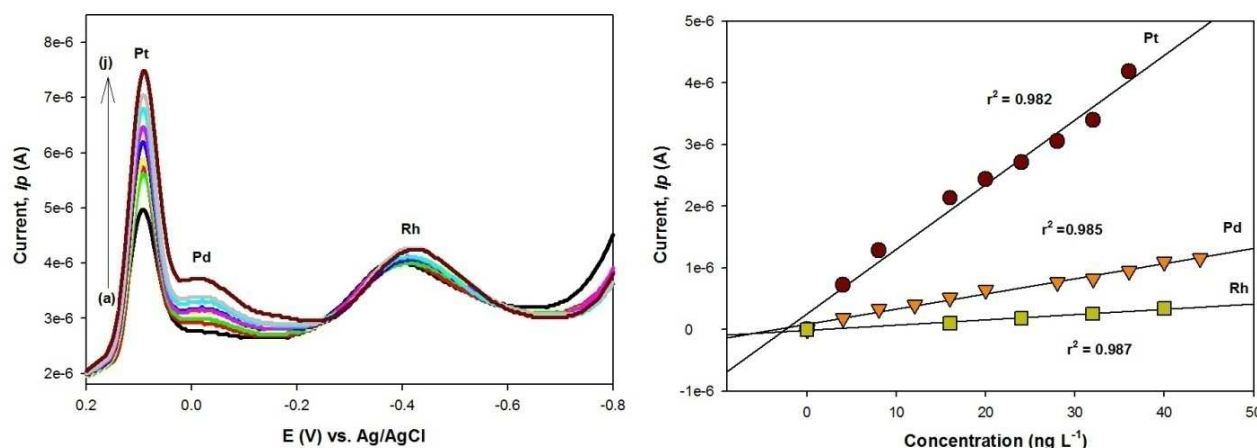


Figure 62. AdDPCSV analysis for the simultaneous determination of Pt-Pd-Rh-(HDMG)_x complexes at 0.00, 120, 160, 200, 240, 280, 320, 360, 400 $\mu\text{g L}^{-1}$ concentrations using a GCE/rGO-SbNPs sensor; $E_d = -1.2$ V (vs. Ag/AgCl) and $t_d = 120$ s with a corresponding linear calibration curve also shown.

Increasing the concentration of DMG appears to result in more favourable complexation / adsorption for the simultaneous determination of all three PGMs. The simultaneous determination of Pt(HDMG)₂, Pd(HDMG)₂ and Rh(HDMG)₃ was possible by increasing the concentration of the DMG but the current for Rh(HDMG)₃ peak was smaller than that of Pt(HDMG)₂ for the same concentration. This simultaneous determination of these three precious metals was done successfully. The Pd(HDMG)₂ stripping peak has been observed at -0.02 V (vs. Ag/AgCl) while the Pt(II) stripping peak has been observed at 0.09 V (vs. Ag/AgCl), followed by the stripping peaks obtained at potential -0.45 V (vs. Ag/AgCl) for Rh(III). A good linear increase in the peak current was observed that is reflected in the calibration curve (Figure 62).

In Table 17 the results obtained from the calibration plots for the PGM-(HDMG)_x complexes analysed with the GCE/rGO-SbNPs and SPCE/rGO-SbNPs sensor are displayed. The stripping voltammograms were obtained with the experimental conditions outlined in Table 1.

Table 17. Calibration data for the determination of PGMs in the presence of [DMG] = 1×10^{-5} M as chelating agent, using the GCE/rGO-SbNPs and SPCE/rGO-SbNPs sensor, with a supporting electrolyte of NaOAc buffer (pH = 5.2) solution.

Sensor	PGM	Regression	R ²
GCE/rGO-SbNPs			
	Pd(II)	$y = 4 \times 10^{-6}x + 8 \times 10^{-8}$	0.999
	Pt(II)	$y = 6 \times 10^{-6}x + 1 \times 10^{-7}$	0.999
	Rh(III)	$y = 8 \times 10^{-6}x + 3 \times 10^{-7}$	0.999
SPCE/rGO-SbNPs			
	Pd(II)	$y = 3.733x + 0.015$	0.997
	Pt(II)	$y = 6.420x + 0.024$	0.994
	Rh(III)	$y = 6.448x - 0.165$	0.974
GCE/rGO-SbNPs (Simultaneous Calibration curves)			
	Pd – Rh	$y = 1 \times 10^{-5}x - 4 \times 10^{-7}$ (Pd)	0.981 (Pd)
	Pd – Rh	$y = 1 \times 10^{-6}x - 3 \times 10^{-8}$ (Rh)	0.991 (Rh)
	Pt – Rh	$y = 6 \times 10^{-6}x + 3 \times 10^{-8}$ (Pt)	0.982 (Pt)
	Pt – Rh	$y = 2 \times 10^{-6}x - 3 \times 10^{-8}$ (Rh)	0.988 (Rh)
	Pt – Pd– Rh	$y = 1 \times 10^{-7}x - 3 \times 10^{-7}$ (Pt)	0.982 (Pt)
	Pt – Pd– Rh	$y = 2 \times 10^{-8}x - 9 \times 10^{-8}$ (Pd)	0.985 (Pd)
	Pt – Pd– Rh	$y = 8 \times 10^{-9}x - 1 \times 10^{-8}$ (Rh)	0.987 (Rh)

From all the results for the AdDPCSV studies listed in the above table, it was evident that all PGMs are reduced and adsorbed onto the GCE/rGO-SbNPs and SPCE/rGO-SbNPs sensor surfaces and gave cathodic peaks and anodic peaks for the stripping voltammetric analysis. In both cases (*i.e.* single and simultaneous determination), the slope of the linear regression equation of the calibration plot was the highest for platinum. Standard additions for each of the

PGMs analysed showed that the peak current increases with increasing concentrations. Due to these properties, an adsorptive cathodic stripping voltammetric technique was developed to obtain a more sensitive method for the determination of trace levels of PGMs. The results of the calibration plots are proof of this successful AdDPCSV analysis and the summary of the corresponding regression equations for this dependence are given in Table 17. Using the results in Table 3 and by comparing the sensitivity of the respective GCE/rGO-SbNPs and SPCE/rGO-SbNPs sensors, the highest sensitivity for the detection of PGMs was observed by using the SPCE/rGO-SbNPs sensor. Further correlation to the aforementioned sensitivity was obtained through the determination of the respective limits of detection (LOD), calculated using equation in Table 17. Table 18 summarises these findings.

6.3.10 Comparison of calculated results for different sensor platforms

Validation of the method was examined via evaluation of linearity (LR), limit of detection (LOD), limit of quantification (LOQ), accuracy, repeatability and reproducibility. The reproducibility, accuracy and sensitivity of the GCE/rGO-SbNPs and SPCE/rGO-SbNPs sensors was examined by a comparison of correlation coefficient, linearity and standard deviation and detection limit as tabulated in Table 18.

The limit of detection was evaluated as the minimum detectable concentration, which is the lowest concentration of analyte that can be distinguished at a stated level of probability, from a sample not containing the analyte or any one of the analyte (PGMs standards) solutions at the lowest working concentration. The limits of detection (LOD) were calculated using the formulae for;

$$LOD = \frac{3 \times SD}{m} \quad \text{Eqn. 6.1}$$

Where SD is the standard deviation and m is the slope of the linearity (Somerset *et al.*, 2009).

Table 18. Results obtained for the analytical parameters of applying the individual GCE/rGO-SbNPs and SPCE/rGO-SbNPs sensors in the AdDPCSV analysis of Pd(HDMG)₂, Pt(HDMG)₂ and Rh(HDMG)₃ in 0.2 M acetate buffer (pH = 5.2) solution as the supporting electrolyte.

Sensor	Property	Pd(II) ($\mu\text{g L}^{-1}$)	Pt(II) ($\mu\text{g L}^{-1}$)	Rh(III) ($\mu\text{g L}^{-1}$)
GCE /rGO-SbNPs				
	R ²	0.999	0.999	0.999
	LR	0 –240	40 – 400	40 - 400
	LOD	0.45	0.49	0.49
	LOQ	0.029	0.018	0.016
	Sensitivity	5.7×10^{-7}	8.5×10^{-7}	1.1×10^{-6}
	%RSD	4.2	2.6	2.8
SPCE /rGO-SbNPs				
	R ²	0.961	0.983	0.974
	LR	60 – 120	0 – 240	30 - 80
	LOD	0.42	0.26	0.34
	LOQ	1.38	0.86	1.14
	Sensitivity	0.93	1.61	1.45
	%RSD	23.94	26.96	27.98

LR: Linear range; LOD: detection limit; LOQ: Limit of quantification; Sensitivity in (A/($\mu\text{g.L}^{-1} \cdot \text{mm}^2$))

UNIVERSITY of the
WESTERN CAPE

Table 18 shows the comparison of the LR, LOD, LOQ values and the %RSD obtained for both the GCE/rGO-SbNPs and SPCE/rGO-SbNPs sensors, respectively. The sensitivity of the proposed method was evaluated, both the limit of detection (LOD) and limit of quantification (LOQ) values under the proposed experimental conditions as outlined in Table 18

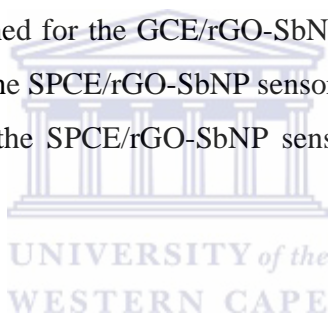
In this study intercepts of regression lines were used to calculate standard deviation. By comparing the responses and results of the two sensors applied in AdDPCSV analysis, the results indicated that both sensors exhibit good detection limits. The SPCE/rGO-SbNPs sensor obtained better sensitivity responses with slightly better detection limits compared to the GCE/rGO-SbNPs sensor. On the other hand the same electrode shows poorer %RSD with a narrower linear range. The GCE/rGO-SbNPs sensor has shown a wider linear range compared to the SPCE/rGO-SbNPs sensor. The results obtained has further indicated that the use of the adsorptive differential pulse techniques offer a more sensitive technique for the single and simultaneous determination of PGMs, when compared to traditional ICP-MS spectrometry. The

deposition time for the stripping analysis used was 120 s, adding to the better results obtained in a shorter analysis times.

However, we still need to do a follow-up study in future since we have obtained an unusual trend for the deposition time of the SPCE/rGO-SbNPs sensor. These observation shows evidence that the carbon electrodes modified with antimony nanoparticles can be able to detect PGMs at very low concentration levels.

The criterion for the choice of carbon electrode used in this study was based on the performance of the disc and screen-printed electrodes in the specific application of PGMs detection. The sensitivity was calculated from the slope of the calibration graph divided by the geometric area of GCE (7.06 mm²) electrode. The sensitivity of the GCE/rGO-SbNPs sensor was found to be 5.7×10^{-7} , 8.5×10^{-7} , 1.1×10^{-6} A/(pg.L⁻¹*mm²) for Pd(II), Pt(II) and Rh(III), respectively, while for the SPCE/rGO-SbNP sensor, it was found to be 0.93, 1.61, 1.45 A/(pg.L⁻¹*mm²). The smaller values obtained for the GCE/rGO-SbNPs sensor is therefore an indication of poorer sensitivity compared to the SPCE/rGO-SbNP sensor.

These results proved that the SPCE/rGO-SbNP sensor was very sensitive compared to GCE/rGO-SbNP sensor.



6.3.11 Repeatability

The accuracy of the method is defined as the closeness of agreement between the experiment result and the true value (Chan *et al.*, 2004). It is determined by calculating the percentage of relative error between the measured mean concentrations and the added concentrations (Torriero, 2004). In order to determine the accuracy of the proposed method, a recovery study was performed by the addition of an amount of three different concentrations of PGMs into the voltammetric cell and measuring the peak currents of respective concentrations. The actual amount of PGMs found in the cell was calculated using the obtained regression equation as shown in Table 19. The average values obtained for the % recoveries are reported in Table 19 where the errors are expressed as standard deviations. Recovery values between 88.8% and 111.6% were obtained for the GCE/rGO-SbNPs sensor, while values between 93.3% and

103.9% were obtained for the SPCE/rGO-SbNP sensor. The aforementioned results confirmed that the AdDPCSV method applied in this study for PGMs determination was relatively accurate.

Table 19. Mean values for recovery of PGMs standard solution ($n = 3$).

Sensor	Amount Added ($\mu\text{g L}^{-1}$)	Amount Found ($\mu\text{g L}^{-1}$)			%Recovery \pm SD
GCE/rGO-SbNPs					
Pd	40	45.9	51.4	29.4	105.0 \pm 11.45
Pt		45.4	66.5	22.0	111.58 \pm 27.34
Rh		49.9	54.3	28.1	110.10 \pm 37.92
	80	73.4	67.9	89.9	96.33 \pm 14.03
		78.1	78.1	73.4	95.66 \pm 2.71
		84.4	67.4	71.7	93.13 \pm 8.84
	120	84.4	100.9	117.4	88.81 \pm 9.39
		96.8	106.1	106.1	91.94 \pm 5.17
		111.0	67.4	71.74	93.93 \pm 8.3
SPCE/rGO-SbNPs					
Pd	40	59.1	70.5	47.6	98.5 \pm 11.45
Pt		53.3	69.3	61.3	102.17 \pm 8.0
Rh		58.5	55.5	55.4	94.11 \pm 1.76
	80	81.9	76.2	81.9	100.0 \pm 3.29
		80.0	76.9	83.1	93.28 \pm 4.62
		77.3	77.3	69.3	99.96 \pm 3.05
	100	99.1	93.3	104.8	99.06 \pm 5.75
		109.3	93.3	109.3	103.96 \pm 9.24
		104.3	101.5	92.3	99.37 \pm 6.27

For the determination of precision of the developed method, the reproducibility of the method was evaluated through calculating the relative standard deviation (%RSD) of the measurements of five solutions containing 120 $\mu\text{g L}^{-1}$ of PGMs ions by using three replicates for each measurement. The adsorptive deposition on the GCE/rGO-SbNPs sensor under the optimized conditions resulted in reproducible measurements with relative good %RSD values of 4.2%, 2.55% and 2.67% for Pd(HDMG)₂, Pt(HDMG)₂ and Rh(HDMG)₃, respectively. The adsorptive deposition on the SPCE/rGO-SbNPs sensor under the optimised conditions resulted in

reproducible measurements with poor %RSD values of 23.94%, 26.96% and 27.98% for Pd(HDMG)₂, Pt(HDMG)₂ and Rh(HDMG)₃, respectively. The results are summarised in Table 18.

The reproducibility can be said is good only when the %RSD is less than 10%. Over 10%, reproducibility is not poor, but at the same time it is also not good. Reproducibility is poor if %RSD is over 15% (Prichard, 1996). We have observed a relative good reproducibility for the GCE/rGO-SbNPs sensor, while the SPCE/rGO-SbNPs sensor gave poor reproducibility. Despite the SPCE/rGO-SbNPs sensor showing the highest sensitivity and a better detection limit, the results obtained indicate that a better reproducibility and wider linear range were reached using the GCE/rGO-SbNPs sensor. Considering these results the GCE/rGO-SbNPs sensor was chosen for analytical application and PGMs determination in environmental samples.

Table 20 shows the results obtained in this study as it was compared to that of previous reports of electrodes for PGMs detection by stripping voltammetry in other studies.

Table 20. Comparison of results obtained in the present study with other data in which modified stripping voltammetric techniques were applied for the determination of PGMs in standard solutions or environmental samples are listed.

Sensor	Method	Linear range	LOD	Reference
GCE/rGO-SbNPs	AdDPCSV	Pd(II): 0–400 $\mu\text{g L}^{-1}$	0.45 $\mu\text{g L}^{-1}$	This work
		Pt(II): 0–260 $\mu\text{g L}^{-1}$	0.49 $\mu\text{g L}^{-1}$	
		Rh(III): 40–400 $\mu\text{g L}^{-1}$	0.49 $\mu\text{g L}^{-1}$	
SPCE/rGO-SbNPs	AdDPCSV	Pd(II): 60–120 $\mu\text{g L}^{-1}$	0.42 $\mu\text{g L}^{-1}$	This work
		Pt(II): 0–240 $\mu\text{g L}^{-1}$	0.26 $\mu\text{g L}^{-1}$	
		Rh(III): 30–80 $\mu\text{g L}^{-1}$	0.34 $\mu\text{g L}^{-1}$	
GCE/Bi-AgF	AdDPSV	Pt(II): 0.02–0.1 ng L^{-1}	0.2 ng L^{-1}	(Van der Horst <i>et al.</i> , 2015)
SPCE/BiF	AdDPSV	Pd(II): 0–0.1 $\mu\text{g L}^{-1}$	0.008 $\mu\text{g L}^{-1}$	(Silwana <i>et al.</i> , 2014)
		Pt(II): 0.02–0.1 $\mu\text{g L}^{-1}$	0.006 $\mu\text{g L}^{-1}$	
		Rh(III): 0–0.08 $\mu\text{g L}^{-1}$	0.006 $\mu\text{g L}^{-1}$	
GCE/BiF	AdDPSV	Pd(II): 0–2.5 $\mu\text{g L}^{-1}$	0.12 $\mu\text{g L}^{-1}$	(Van der Horst <i>et al.</i> , 2012)
		Pt(II): 0–3.5 $\mu\text{g L}^{-1}$	0.04 $\mu\text{g L}^{-1}$	
		Rh(III): 0–3.0 $\mu\text{g L}^{-1}$	0.23 $\mu\text{g L}^{-1}$	
HDME	AdSV	Pt(II): 8–48 pM L^{-1}	4.38 pM L^{-1}	(Somerset <i>et al.</i> ,

				2010)
Hg(Ag)FE	AdSV	Pd(II): 1–50 $\mu\text{g L}^{-1}$	0.15 $\mu\text{g L}^{-1}$	(Bobrowski <i>et al.</i> , 2009)
CPE/DMG	CSV	Pd(II): 2.4×10^{-7} –6.0 $\times 10^{-6}$ M	6.2×10^{-8} M	(Dalvi <i>et al.</i> , 2008)
CGMDE	AdSV	Pt(II): 1.0–195 $\mu\text{g L}^{-1}$	0.03 $\mu\text{g L}^{-1}$	(Huszalet <i>et al.</i> , 2005)

The detection limit of the proposed method has been compared with that of the other previously reported methods for the determination of PGMs by stripping voltammetry shown in Table 20. It is evident that the proposed electrochemical methods developed in this study shows results with high sensitivity and lower detection limit, indicating that both the GCE and SPCE sensor platforms modified with nanoparticles can be used as a sensor for the sensitive electrochemical detection of Pt(II), Pd(II) and Rh(III) in environmental samples. The results are summarised in Table 20.

Van der Horst *et al.* (2015) conducted measurements of platinum by adsorptive stripping voltammetry using a GCE/Bi-AgF sensor and obtained a detection limit of 0.20 ng L^{-1} under a 60s accumulation time. However, there are no publications reporting the determination of PGMs at nanoparticle-based electrodes except the studies done by van der Horst *et al.* (2015).

In summary, this research has shown that the GCE/rGO-SbNPs and SPCE/rGO-SbNPs sensors tested in this study has a better detection limit compared to the literature and could improve the performance of an electrochemical sensor for better detection of the PGMs in environmental samples. Considering all these results simultaneous detection were also evaluated, showing promising results.

6.3.12 Interference studies of PGMs

Precise and selective measurement of PGMs present in real sample matrices is a challenging task, as there are other commonly encountered cations and anions normally present in the real samples along with PGMs can pose a serious problem for electrochemical analysis.

In this work interferences were investigated under the optimum conditions described in Table 21, while the results obtained for these investigations are shown in Figures 63 – 65.

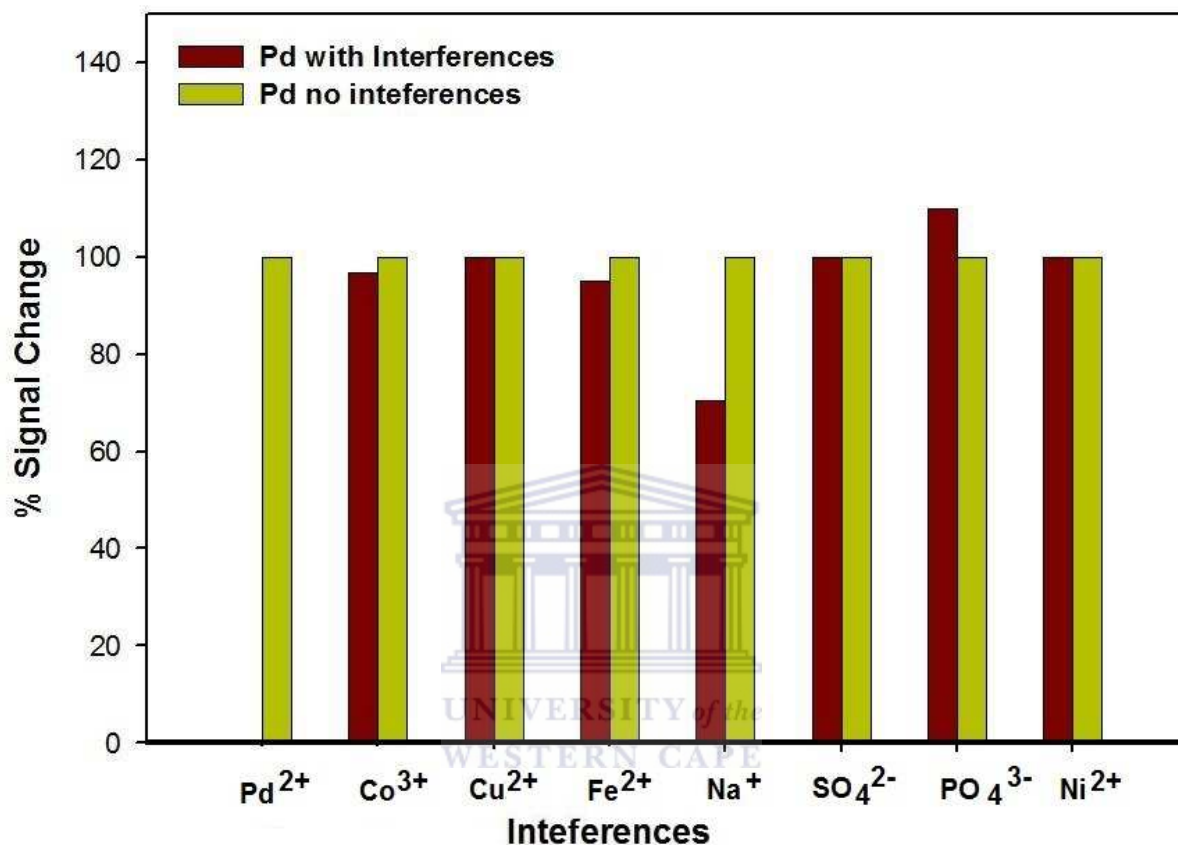


Figure 63. The AdDPSV results obtained for the effect of interfering ions on the stripping voltammetric results for Pd(HDMG)₂ using the GCE/rGO-SbNPs sensor in ratio 1:4 (PGM: interference) with 0.2 M NaOAc buffer (pH = 5.2) solution containing 1 × 10⁻⁵ DMG solution.

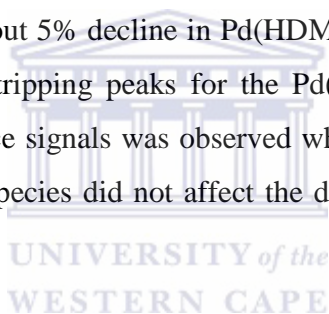
Interferences can distort or obscure analytical signal by reacting with the analyte of interest or blocking the surface of working electrode. This behaviour usually cause one of the stripping peaks to be depressed when compared with the peak height obtained in the absence of the second metal (Nguyen, 2013)

Therefore, it was useful to examine the effects of different interferences using our novel GCE/rGO-SbNPs sensor. This will provide some guidance as to what types of environmental soil and dust sample are suitable for analysis using the proposed method. Possible interfering ions of iron (Fe²⁺), nickel (Ni²⁺), cobalt (Co²⁺), sodium (Na⁺) and copper (Cu²⁺) were tested using a 4:1

ratio of each metal ion possibly coexisting with selected PGMs. Interferences arising from oxygen containing inorganic ions of phosphate (PO_4^{3-}) and sulphate (SO_4^{2-}) that are expected to co-exist in PGMs were also evaluated. Stripping current signals were recorded at each different interference concentration and normalised with the stripping current obtained when there is no interference presents (base value).

Figure 63 illustrate the behaviour of the GCE/rGO-SbNPs sensor in the presence of ions such as Fe^{2+} , Ni^{2+} , Co^{2+} , Na^+ , Cu^{2+} , PO_4^{3-} and SO_4^{2-} and the $\text{Pd}(\text{HDMG})_2$ complex. The peak of $\text{Pd}(\text{HDMG})_2$ was monitored and compared to that without any interferences added. In the case of Co^{2+} , Fe^{2+} and Na^+ it was observed that these ions only caused the stripping current of $\text{Pd}(\text{HDMG})_2$ to drop by 5% , 5% and 30%, respectively as shown in Figure 63.

Although Co^{2+} and Fe^{2+} appeared to have an interfering effect toward stripping analysis of $\text{Pd}(\text{HDMG})_2$ compared to Na^+ , the severity of Co^{2+} and Fe^{2+} interference was still at tolerable level as these ions only lead to about 5% decline in $\text{Pd}(\text{HDMG})_2$ stripping signals. The presence of the PO_4^{3-} ions increased the stripping peaks for the $\text{Pd}(\text{HDMG})_2$ complex as observed in Figure 63. Insignificant interference signals was observed when Cu^{2+} , Ni^{2+} and SO_4^{2-} co-exist in the sample, indicating that these species did not affect the determination of $\text{Pd}(\text{HDMG})_2$ in the buffer solution selected.



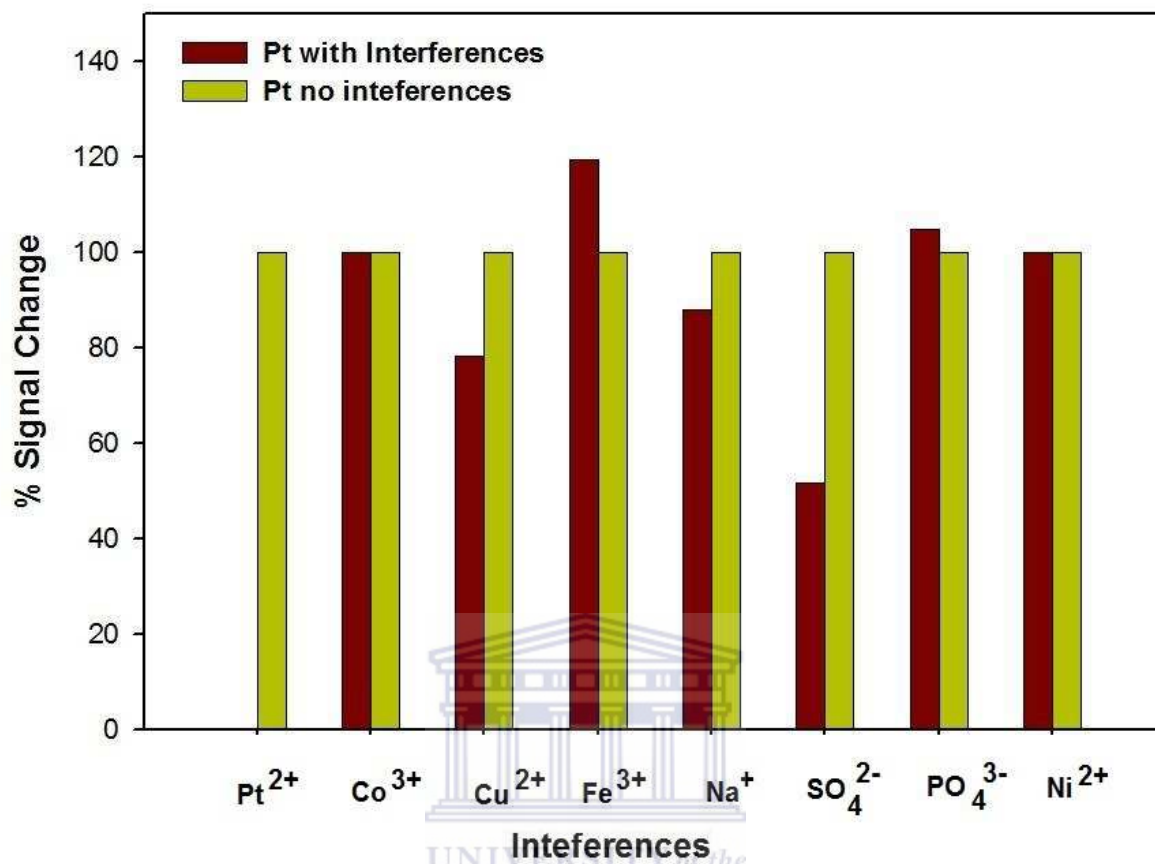


Figure 64. The AdDPCSV results obtained for the effect of interfering ions on the stripping voltammetric results for Pt(HDMG)₂ using the GCE/rGO-SbNPs sensor in ratio 1:4 (PGM:interference) with 0.2 M NaOAc buffer (pH = 5.2) solution containing 1×10^{-5} DMG solution.

In the case of the Pt(HDMG)₂ complex, the results displayed in Figure 64 was obtained for the interferences of Fe²⁺, Ni²⁺, Co²⁺, Na⁺, Cu²⁺, PO₄³⁻ and SO₄²⁻ in a Pt(HDMG)₂ complex. The peak of Pt(HDMG)₂ was monitored and compared to that without any interferences added. The results for Cu²⁺, Na⁺ and SO₄²⁻ only caused the stripping current of Pt(HDMG)₂ to drop by 22%, 12% and 48%, respectively (Figure 64). The presence of the Fe²⁺ and PO₄³⁻ ions increased the stripping peaks for the Pt(HDMG)₂ complex as observed in Figure 64. Insignificant interference signals were observed when Co²⁺ and Ni²⁺ coexist in the sample indicating that these species did not affect the determination of Pd(HDMG)₂ in the buffer solution selected.

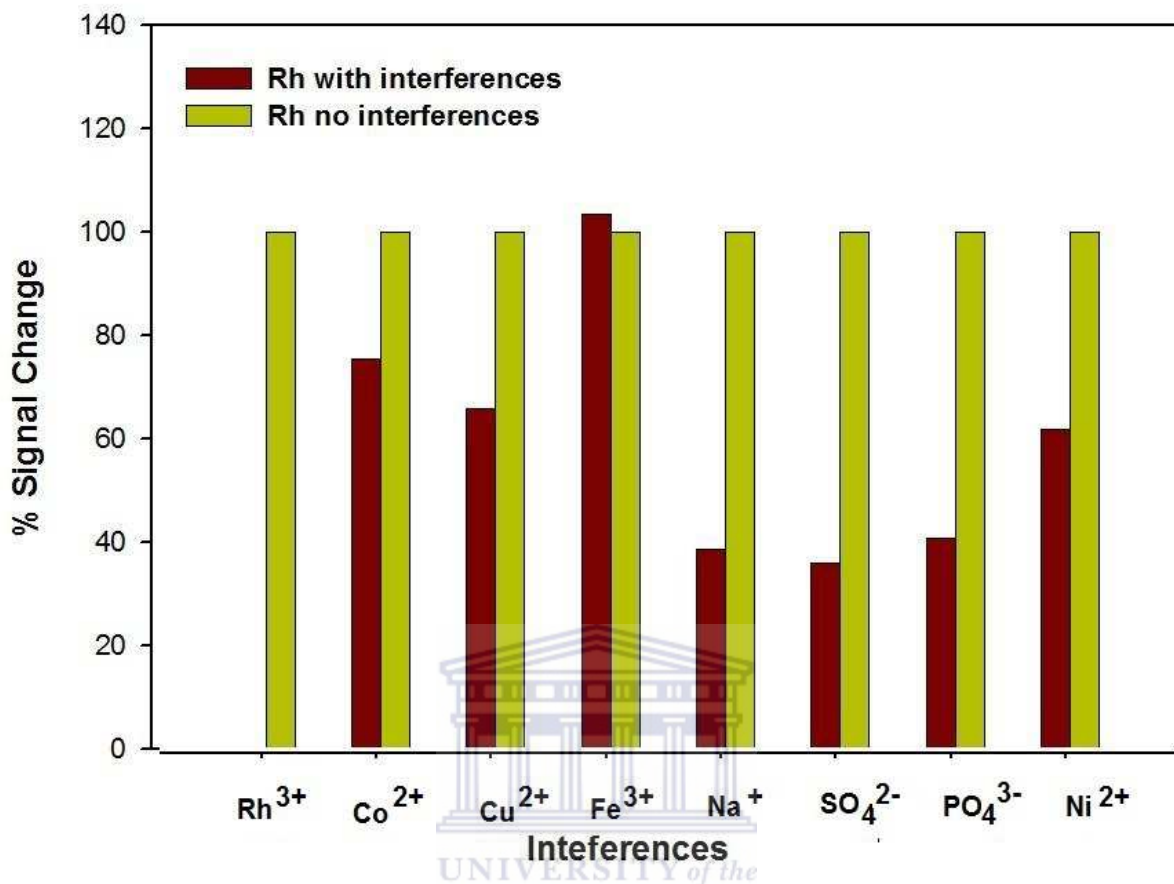


Figure 65. The AdDPSV results obtained for the effect of interfering ions on the stripping voltammetric results for Rh(HDMG)₃ using the GCE/rGO-SbNPs sensor in ratio 1:4 (PGM: interference) with 0.2 M NaOAc buffer (pH = 5.2) solution containing 1×10^{-5} DMG solution.

The Rh(HDMG)₃ complex was strongly affected by the addition of Ni²⁺, Co²⁺, Na⁺, Cu²⁺, PO₄³⁻ and SO₄²⁻ interfering ions, as can be observed in Figure 65. The presence of these ions diminished the stripping peaks for the Rh(HDMG)₃ complex while Fe²⁺ ions increased the stripping peaks for the Rh(HDMG) complex. The summary of the effect of interferences on PGMs are tabulated in Table 21.

Table 21. Results obtained for the interferences and resulting % signal change in 0.2 M NaOAc buffer (pH = 5.2) solution as the supporting electrolyte.

Interferences	PGMs(% Signal Change)		
	Pd(II)	Pt(II)	Rh(III)
Co ²⁺	5 % decrease	no effect	25% decrease
Fe ²⁺	5 % decrease	25%increase	3% increase
Cu ²⁺	no effect	22% decrease	34% decrease
Ni ²⁺	no effect	48%decrease	38% decrease
Na ⁺	30 decrease	12% decrease	39% decrease
SO ₄ ²⁻	no effect	48% decrease	64% decrease
PO ₄ ³⁻	10% increase	5%increase	59%decrease

In summary, the results obtained indicate that Co²⁺ and Ni²⁺ presence caused negligible effects and SO₄²⁻ presence increased the stripping current. The presence of Co²⁺, Fe²⁺ and Na⁺ caused a decrease to approximately 10% or less of its original value in the Pd(HDMG)₂ stripping current. It was observed that the peak of Pt(HDMG)₂ decreased to 22%, 12% and 48% of its original value when Cu²⁺, Na⁺ and SO₄²⁻ interferences were present in the measurement solution, respectively. The presence of Co²⁺ and Ni²⁺ caused negligible effects on the Pt(HDMG)₂ stripping current, while the presence of Fe²⁺ and PO₄³⁻ in the measurement solution increased the stripping peak current. The Rh(HDMG)₃ stripping current was strongly affected with all the interfering ions present in the measurement solution, except for excess Fe²⁺ that caused the stripping peak current to increase. Overall, for both the Pd(HDMG)₂ and Pt(HDMG)₂ complexes, all the interfering ions did not exhibit any significant interfering behaviour even at a 1:4 ratio (metal: interference) concentration. However, in the case of Cu²⁺, SO₄²⁻ and Na⁺ some interfering signals were observed for the Pd(HDMG)₂ and Pt(HDMG)₂ complexes, respectively. The Rh(HDMG)₃ complex, on the other hand exhibited strong interfering behaviour at a more significant level compared to the previously mentioned metals. To avoid the effect of interferences, for real sample analysis a dilution of the samples before experimental

determination is recommended. In this way, if the samples contain high concentration of cations, the interfering effect may be minimised.

6.4 Application of Analytical Techniques in Real Samples

The evaluation of the analytical performances of this new methodology was also conducted in environmental samples, since the main application is focused on environmental sample analysis. The roadside soil and dust samples of the Stellenbosch area in the Western Cape Province (South Africa) were sampled for analysis. This part also discusses in detail the results obtained for the unknown samples analysed using AdDPCSV and ICP-MS techniques, respectively.

6.4.1 Study Area

Soil and dust samples were collected on the Bottelary road that joins the R304 road into Stellenbosch (Figure 66). Sampling sites and corresponding samples were labelled BOT1 to BOT4. Secondly, samples were collected at sampling sites on the Old Paarl road that joins the R44 (or Adam Tas Road) that also runs into Stellenbosch. These sampling sites and corresponding samples were labelled OP1 to OP4 (Figure 66).

For the sampling procedure and the purpose of illustrating PGMs deposition from the catalytic car converters of vehicles passing the roadside, distance between sampling sites was 100 m in Stellenbosch area at 10 cm depths using hand auger and brush for collection of the dust samples. To avoid contamination during the collection and processing of sample material, nitrile gloves were worn at all times. The samples were placed into double zip-locked plastic bags labelled BOT1- BOT4, OP1 - OP4 to represent Bottelary and Old Paarl sites, respectively. The samples were transported to the laboratory immediately and stored in the fridge at 4 °C until analysis. The working environment was also kept clean to avoid any cross-contamination.

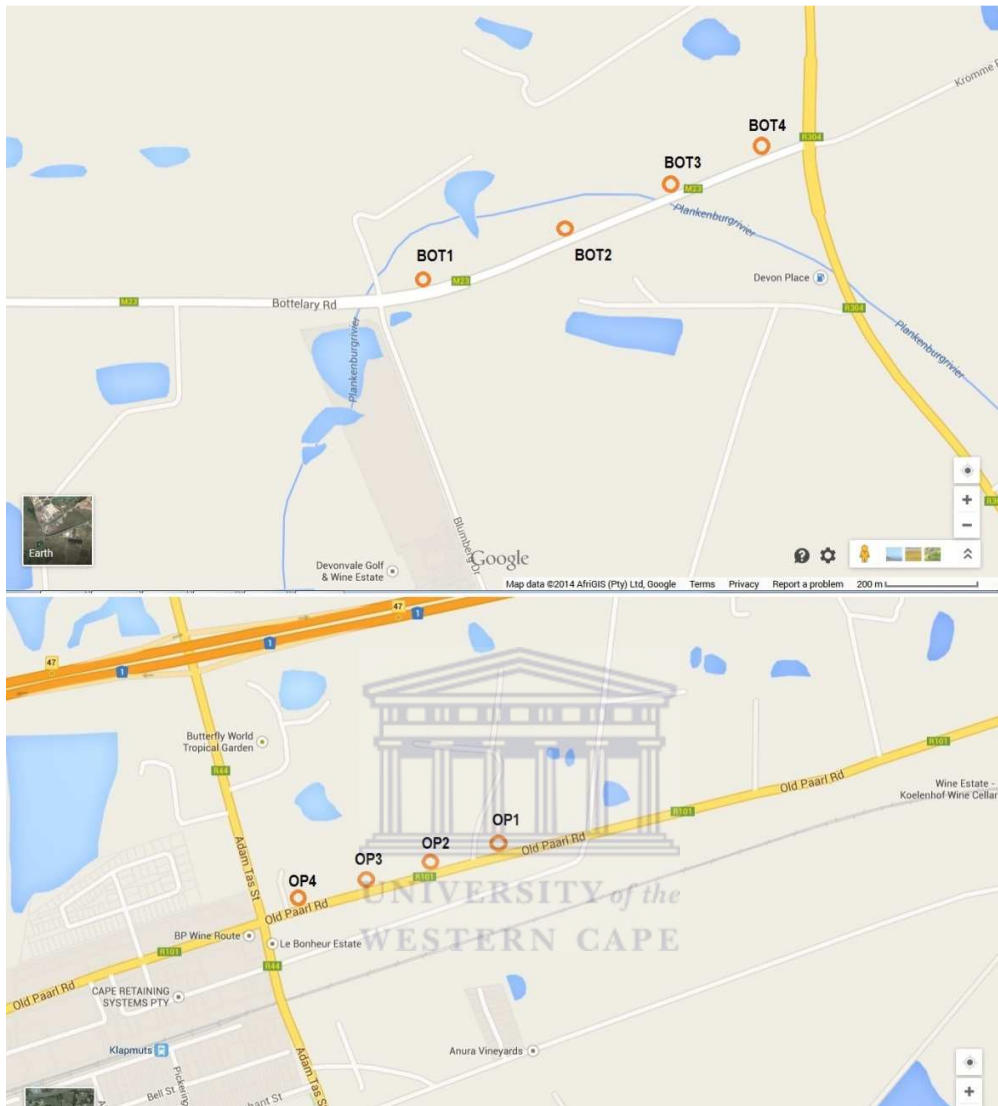


Figure 66. Maps showing the location of the sampling sites on the Bottelary Road and Old Paarl Road, major routes into the town of Stellenbosch, South Africa.

6.4.2 Sample Analysis Procedures

Heavy metal mobility and bioavailability in soil depend strongly on the mineralogical and chemical forms in which they occur (Baeyenet *al.*, 2003). Therefore, measurement of total metal concentrations is useful to estimate the heavy metal burden since their mobility depends on ways of binding. For this reason, sequential extraction procedures are commonly applied because they

provide information on the fractionation of metals in the different lattices of the soil sample, which serves as a good compromise to give information on environmental contamination risk (Marguiet *et al.*, 2004, Nadaska *et al.*, 2004). The procedures used for the determination of the PGMs in soil and dust samples are described in the next section.

6.4.2.1 ICP-MS spectrophotometric analysis.

Sequential Extraction: Sequential extraction schemes were first developed for soils and then extended to sediments. The sequence is designed so that the most reactive phases are removed first and the severity of the extractants increases with each step. For the purpose of this study Tessier procedure sequential extraction protocol was utilised. It is a five-step method, separating metal-contaminants into five fractions: the exchangeable fraction, the carbonatic fraction, the reducible (bound to Fe-Mn Oxides) fraction, the oxidisable (bound to organic matter) fraction, and residue fraction. All materials associated with the metal extraction were thoroughly acid-cleaned and rinsed with deionised water before use according to internationally recommended protocols (Somerset *et al.*, 2015, Li *et al.*, 2010). Sequential extraction procedures are among the most common methods for assessing trace metal speciation in contaminated soils and sediments (Okoro *et al.*, 2012, Li *et al.*, 2010; Morera *et al.*, 2001). In this study it was the metal fractionation that was investigated by sequential extraction procedures (SEPs).

Furthermore, in all of the analyses Milli-Q-water and Milli-Q washed equipment was used. These preparations should ensure that the samples were not additionally contaminated during the processing. The precision and purity of the analyses was controlled by using triplicates of samples and simultaneously processed blanks. This should detect if the measured PGMs (Pd, Pt, Rh) were added during the sample preparation by accident.

Total acid digestion: Samples were air-dried and sieved using a 2 mm mesh. The dried-soil was further broken down, pulverised with a pestle and mortar and sieved samples were homogenised by coning and quartering and stored. For recovery of the metals, the samples were digested using a modified version of XP1500 Method. This modified procedure accomplished a total digestion of the entire sample matrix so that the crustal elements could be quantified. Approximately 0.5 g of each of the sieved soil samples were weighed into a conical flask and

digested with an acid mixture consisting of 69% nitric, 70% hydrochloric acids, and 30% hydrogen peroxide. Afterwards, 10 ml de-ionised water was added to the content and demented into a 50 volumetric flask after additional water rinsing and decanted and made up to the mark with deionised water. A blank was similarly prepared without soil sample. A 0.45 μm filter was used to filter the dilute acid mixture into ICP vials. The extract solution was analysed for using ICP-MS model 205. There are 3 metals (Pd, Pt and Rh) analysed by ICP-MS that are chosen as representatives for discussing the metal mobility and contamination. In ICP-MS, plasma is applied to atomise and ionise the sampled elements, thus the species are identified by their mass-to-charge ratio. A variable speed peristaltic pump was used to deliver both standard and sample solutions to the nebulizer. The concentration of heavy metals was then determined by means extrapolation from a calibration plot. Comparing with other spectroscopic techniques, ICP-MS has a lower detection limit (better than sub ng/L) suitable for trace metals analysis under a wide dynamic range (Rosen, 2004).

6.4.2.2 Adsorptive stripping voltammetry analysis on GCE/rGO-SbNPs sensor

We have developed the novel electrochemical sensor based on nanoparticles using GCE and SPCE transducer surfaces. Both the GCE/rGO-SbNPs and SPCE/rGO-SbNPs sensors have shown a good detection limit for the detection of PGMs in environmental samples. Because of the uncertainties on the SPCE sensor, GCE was the one chosen for environmental sample analysis. Finally, the proposed method was applied to the AdDPCSV determination of PGMs in a soil and dust samples. The behaviour of the selected PGMs was studied in a potential range between + 0.6 to - 1.5 V (vs. Ag/AgCl). The stripping voltammetric sample preparation required was the addition of buffer and complexing agent and, where necessary, sample dilution. For each of the PGMs investigated, the calibration curve was prepared by a series of standard addition of PGMs to a 0.2 M sodium acetate buffer (pH = 5.2) solution. The actual amount of PGMs found in the soil and dust samples were calculated using the obtained regression equation ($y = mx + c$). The determination of PGMs in environmental samples was performed with an adapted procedure from Locatelli (2006). The detailed method is discussed in the following section.

Initially, the analysis of the environmental samples was performed in a 10 ml voltammetric cell vial containing 1 ml of water sample and 9 ml of acetate buffer (pH = 5.2)

solution, with 1×10^{-5} DMG and using the developed AdDPSV procedure. The amount of sample was determined through the standard addition method using standard solutions containing appropriate concentrations of Pd(II), Pt(II) and Rh(III) (Silwana *et al.*, 2014, Van der Horst *et al.*, 2012).

6.4.3 PGMs analysis in soil samples by using ICP-MS

Table 22 shows the results obtained for the total metal concentrations ($\mu\text{g g}^{-1}$ for Pt, Pd, Rh) obtained by acid digestion of the soil samples collected at the eight sampling sites, using ICP-MS spectrophotometric technique.

Table 22. Results obtained for the total concentrations of PGMs in the in soil samples, using the acid digestion procedure and ICP-MS analysis.

Site ID	Pd ($\mu\text{g g}^{-1}$)	Pt ($\mu\text{g g}^{-1}$)	Rh ($\mu\text{g g}^{-1}$)
OP1	926	25	19
OP2	763	17	14
OP3	9.3	15	13
OP4	673	9	8
BOT1	809	8	6
BOT2	529	7	16
BOT3	768	11	9
BOT4	825	20	6

The total concentration of PGMs in the samples collected at the OP sites ranged from 673 – 926 $\mu\text{g g}^{-1}$ for Pd, 7 – 25 $\mu\text{g g}^{-1}$ for Pt, and 6 – 19 $\mu\text{g g}^{-1}$ for Rh. The order found for the presence of PGMs were OP1 > OP3 > OP2 > OP4; followed by OP1 > OP2 > OP3 > OP4; and OP1 > OP2 > OP3 > OP4 for Pd, Pt and Rh, respectively. Pd had the highest concentration in the soil samples at

all the four OP sites, followed by Pt while Rh had the lowest concentrations. The sequence for PGMs concentration in the soil samples was as follows: Pd > Pt > Rh.

The total concentrations of PGMs in the samples collected at BOT sites ranged from 529 – 825 $\mu\text{g g}^{-1}$ for Pd, 7 – 20 $\mu\text{g g}^{-1}$ for Pt, and 6 – 16 $\mu\text{g g}^{-1}$ for Rh. The order found for the presence of PGMs were BOT4 > BOT1 > BOT3 > BOT2; followed by BOT4 > BOT3 > BOT1 > BOT2; BOT2 > BOT3 > BOT4 = BOT1 for Pd, Pt and Rh, respectively. Pd has the highest concentration in the soil samples at all the four BOT sites, followed by Pt while Rh had the lowest concentrations. The sequence for PGMs concentration is as follows: Pd > Pt > Rh with Pt and Rh showing the same sequence. Pd has shown highest concentration for both OP and BOT sites.

This total concentration of metal in the soil matrix obtained above often does not accurately represent their characteristic and toxicity (Okoro *et al.*, 2012). In order to understand their actual and potential environmental effect, a sequential extraction procedure was used on the soil samples, followed with ICP-MS analysis of the extracts. The results obtained for PGMs concentrations in the extracted samples are shown in Table 23.

Table 23. Results obtained for the sequential extraction of total metal concentrations in soil samples obtained using ICP-MS spectrophotometric analysis.

Site ID	Fraction	Pd ($\mu\text{g g}^{-1}$)	Pt ($\mu\text{g g}^{-1}$)	Rh ($\mu\text{g g}^{-1}$)
OP1	Carbonate-bound	0.02	0.01	0.005
	Fe-Mn oxides bound	0.02	0.01	0.01
	Organic bound	0.01	0.004	0.002
OP2	Carbonate-bound	0.03	0.02	0.01
	Fe-Mn oxides bound	0.17	0.03	0.02
	Organic bound	0.02	0.01	0.01
OP3	Carbonate-bound	0.04	0.01	0.02
	Fe-Mn oxides bound	0.15	0.04	0.03
	Organic bound	0.03	0.03	0.02
OP4	Carbonate-bound	0.08	0.05	0.03
	Fe-Mn oxides bound	0.08	0.06	0.04
	Organic bound	0.05	0.03	0.004
BOT1	Carbonate-bound	0.03	0.01	0.004
	Fe-Mn oxides bound	0.01	0.004	0.003
	Organic bound	0.01	0.01	0.005

BOT2	Carbonate-bound	0.06	0.03	0.02
	Fe-Mn oxides bound	0.03	0.02	0.01
	Organic bound	0.02	0.01	0.01
BOT3	Carbonate-bound	0.34	0.04	0.26
	Fe-Mn oxides bound	0.06	0.05	0.04
	Organic bound	0.04	0.02	0.02
BOT4	Carbonate-bound	0.06	0.05	0.04
	Fe-Mn oxides bound	0.13	0.07	0.05
	Organic bound	0.04	0.04	0.04

Table 23 presents the results obtained for sequential extraction of the soil samples. The results obtained for the carbonate-bound extracts for sites OP1 – OP4 shows that the concentration of Pd(II), Pt(II) and Rh(III) ranged from 0.005 – 0.06 $\mu\text{g g}^{-1}$. The results for the Fe-Mn oxide bound extracts for sites OP1 – OP4 shows that the concentration of Pd, Pt and Rh ranged from 0.01 – 0.19 $\mu\text{g g}^{-1}$. The results for the organic bound extract showed that the concentration of Pd, Pt and Rh ranged from 0.001 – 0.01 $\mu\text{g g}^{-1}$.

The OP1 site order of mobility of the metals in the first fraction is Pd > Pt > Rh. Furthermore, similar mobility orders of the elements for the Fe-Mn oxide bound and the organic bound extracts were Pd > Pt = Rh and Pd > Pt > Rh, respectively.

The OP2 site order of mobility of the metals in the first fraction was Pd > Pt > Rh. Furthermore, similar mobility orders of the elements for the second and the third fractions were Pd > Pt > Rh and Pd > Pt = Rh, respectively.

The OP3 site order of mobility of the metals in the first fraction was Pd > Pt > Rh. Furthermore, similar mobility orders of the elements for the second and the third fractions are Pd > Pt > Rh and Pd = Pt > Rh, respectively.

The OP4 site order of mobility of the metals in the first fraction is Pd > Pt > Rh. Furthermore, similar mobility orders of the elements for the Fe-Mn oxide bound and the organic matter are Pd > Pt > Rh and Pd > Pt > Rh, respectively.

In overall Pd seemed to be the most mobile element in all fractions with higher concentrations found in Fe-Mn bound extract.

In the case of the BOT1 – BOT4 sites, the results for the carbonated bound extracts were as follow: the concentrations of Pd(II), Pt(II) and Rh(III) ranged from 0.004 – 0.34 $\mu\text{g g}^{-1}$. The

results for the Fe-Mn oxide bound extract showed that the concentrations of Pd, Pt and Rh ranged from 0.003 – 0.08 $\mu\text{g g}^{-1}$.

The results for the organic bound extracts showed that the concentrations of Pd(II), Pt(II) and Rh(III) ranged from 0.005 – 0.05 $\mu\text{g g}^{-1}$. The BOT1 site order of mobility of the metals in the first fraction was Pd > Pt > Rh. Furthermore, similar mobility orders of the elements for the Fe-Mn oxide bound extracts and the organic bound extracts were Pd > Pt = Rh and Pd > Pt > Rh, respectively.

The BOT2 site order of mobility of the metals in the first fraction was Pd > Pt > Rh. Furthermore, similar mobility orders of the elements for the Fe-Mn oxide bound extracts and the organic bound extracts were Pd > Pt > Rh and Pd > Pt = Rh, respectively.

The BOT3 site order of mobility of the metals in the first fraction was Pd > Pt > Rh. Furthermore, similar mobility orders of the elements for the Fe-Mn oxide bound extracts and the organic bound extracts were Pd > Pt > Rh and Pd > Pt = Rh, respectively.

The BOT4 site order of mobility of the metals in the first fraction was Pd > Pt > Rh. Furthermore, similar mobility orders of the elements for the Fe-Mn oxide bound extracts and the organic bound extracts were Pd > Pt > Rh and Pd > Pt = Rh, respectively.

In overall Pd seemed to be the most mobile element in all fractions with higher concentrations found in carbonated bound extracts.

6.4.4 PGMs analysis in dust samples using ICP-MS

Table 24 presents the results of the total metal concentrations ($\mu\text{g g}^{-1}$ of Pt, Pd, Rh) obtained by direct acid digestion in the dust samples collected at the eight sampling sites, using the ICP-MS spectrophotometric technique.

Table 24. Results obtained for the total concentrations of PGMs obtained in the direct acid digestion of the dust samples.

Site ID	Pd ($\mu\text{g g}^{-1}$)	Pt ($\mu\text{g g}^{-1}$)	Rh ($\mu\text{g g}^{-1}$)
OP1	926	25	19

OP2	763	17	14
OP3	9.3	15	13
OP4	673	9	8
BOT1	809	8	6
BOT2	529	7	16
BOT3	768	11	9
BOT4	825	20	6

The total concentrations of PGMs in the OP1 – OP4 sites obtained ranged from 673 – 926 $\mu\text{g g}^{-1}$ for Pd, 31 – 90 $\mu\text{g g}^{-1}$ for Pt, and 28 – 45 $\mu\text{g g}^{-1}$ for Rh. The order found for the presence of PGMs were OP1 > OP3 > OP2 > OP4; followed by OP4 > OP2 > OP1 > OP3; and OP4 > OP2 > OP1 > OP3 for Pd, Pt and Rh, respectively.

Pd had the highest concentration in all the four OP1 – OP4 sites, followed by Pt while Rh has the least values. The sequence for PGMs concentration was as follows: Pd > Pt > Rh with Pt and Rh showing the same sequence of order for the OP1 – OP4 sites.

The total concentrations of PGMs in the BOT1 – BOT4 sites obtained ranged from 529 – 825 $\mu\text{g g}^{-1}$ for Pd, 24 – 45 $\mu\text{g g}^{-1}$ for Pt, and 11 – 20 $\mu\text{g g}^{-1}$ for Rh. The order found for the presence of PGMs were BOT4 > BOT1 > BOT3 > BOT2; followed by BOT2 > BOT3 = BOT4 > BOT1; and BOT2 > BOT3 = BOT4 > BOT1 for Pd, Pt and Rh, respectively.

Pd had the highest concentration in all the four BOT1 – BOT4 sites, followed by Pt while Rh has the least values. The sequence for PGMs concentration was as follows: Pd > Pt > Rh with Pt and Rh showing the same sequence.

The results obtained for both the OP and BOT sites have further shown that Pd had the highest concentration for both the OP and BOT sites.

The results obtained for the dust samples were very similar to the results obtained for the soil samples with the same order obtained for Pd. The results obtained for the sequential extraction procedure are also presented in Table 25.

Table 25. Results obtained for the sequential extraction of the dust samples and analysis using ICP-MS spectrophotometry.

Site ID	Fraction	Pd ($\mu\text{g g}^{-1}$)	Pt ($\mu\text{g g}^{-1}$)	Rh ($\mu\text{g g}^{-1}$)
OP1	Carbonate-bound	0.04	0.02	0.01
	Fe-Mn oxides bound	0.15	0.02	0.01
	Organic bound	0.02	0.01	0.004
OP2	Carbonate-bound	0.07	0.04	0.03
	Fe-Mn oxides bound	0.06	0.04	0.03
	Organic bound	0.03	0.02	0.01
OP3	Carbonate-bound	0.09	0.05	0.04
	Fe-Mn oxides bound	0.15	0.06	0.05
	Organic bound	0.05	0.05	0.03
OP4	Carbonate-bound	0.11	0.07	0.05
	Fe-Mn oxides bound	0.09	0.08	0.06
	Organic bound	0.06	0.05	0.03
BOT1	Carbonate-bound	0.06	0.02	0.005
	Fe-Mn oxides bound	0.02	0.01	0.01
	Organic bound	0.02	0.02	0.01
BOT2	Carbonate-bound	0.08	0.04	0.03
	Fe-Mn oxides bound	0.04	0.03	0.02
	Organic bound	0.05	0.03	0.03
BOT3	Carbonate-bound	0.09	0.05	0.04
	Fe-Mn oxides bound	0.08	0.06	0.04
	Organic bound	0.06	0.05	0.04
BOT4	Carbonate-bound	0.10	0.06	0.05
	Fe-Mn oxides bound	0.09	0.08	0.07
	Organic bound	0.08	0.06	0.05

Table 25 represents the results obtained for the OP1 – OP4 sites in the sequential extraction procedure. The results for the carbonated bound extracts showed that the concentration of Pd(II), Pt(II) and Rh(III) ranged from 0.01 – 0.1 $\mu\text{g g}^{-1}$. The results for the Fe-Mn oxide bound extracts obtained for the OP1 – OP4 sites showed that the concentration of Pd, Pt and Rh ranged from 0.01 – 0.15 $\mu\text{g g}^{-1}$. The results for the organic bound extract showed that the concentration of Pd, Pt and Rh ranged from 0.004 – 0.03 $\mu\text{g g}^{-1}$.

The OP1 site order of mobility of the metals in the carbonated bound extract was Pd > Pt > Rh. Furthermore, similar mobility orders of the elements for the Fe-Mn oxide bound extracts and the organic bound extracts were Pd > Pt > Rh and Pd > Pt > Rh, respectively.

The OP2 site order of mobility of the metals in the carbonated bound extracts was Pd > Pt > Rh. Furthermore, similar mobility orders of the elements for the Fe-Mn oxide bound extracts and the organic bound extracts were Pd > Pt > Rh and Pd > Pt > Rh, respectively.

The OP3 site order of mobility of the metals in the carbonated bound extract was Pd > Pt > Rh. Furthermore, similar mobility orders of the elements for the Fe-Mn oxide bound extracts and the organic matter extracts were Pd > Pt > Rh and Pd = Pt > Rh, respectively.

The OP4 site order of mobility of the metals in the first fraction was Pd > Pt > Rh. Furthermore, similar mobility orders of the elements for the Fe-Mn oxide bound extracts and the organic bound extracts were Pd > Pt > Rh and Pd > Pt > Rh, respectively.

In overall the results obtained for Pd seemed to be the most mobile element in all fractions with higher concentrations found in the Fe-Mn oxide bound extracts.

In case of the BOT sites the results for the carbonated bound extracts were as follow: the concentration of Pd, Pt and Rh ranged from 0.0 – 0.10 $\mu\text{g g}^{-1}$.

The results for the Fe-Mn oxide bound extracts showed that the concentration of Pd, Pt and Rh ranged from 0.010 – 0.09 $\mu\text{g g}^{-1}$.

The results for the organic bound extracts showed that the concentration of Pd, Pt and Rh ranged from 0.01 – 0.05 $\mu\text{g g}^{-1}$.

The BOT1 site order of mobility of the metals in the first fraction was Pd > Pt > Rh. Furthermore, similar mobility orders of the elements for the second and the third fractions were Pd > Pt = Rh and Pd > Pt > Rh, respectively.

The BOT2 site order of mobility of the metals in the first fraction was Pd > Pt > Rh. Furthermore, similar mobility orders of the elements for the second and the third fractions were Pd > Pt > Rh and Pd > Pt = Rh, respectively.

The BOT3 site order of mobility of the metals in the first fraction was Pd > Pt > Rh. Furthermore, similar mobility orders of the elements for the second and the third fractions were Pd > Pt > Rh and Pd > Pt > Rh, respectively.

The BOT4 site order of mobility of the metals in the first fraction was Pd > Pt > Rh. Furthermore, similar mobility orders of the elements for the second and the third fractions were Pd > Pt > Rh and Pd > Pt > Rh, respectively.

The overall evaluation showed that the results for Pd indicate that it seems to be the most mobile element in all fractions with higher concentrations found in the carbonated bound extracts.

In summary, in the environmental studies for the determination of different ways of binding gives more information of trace metal mobility, as well as on the availability or toxicity. A comprehensive comparison of the total concentration in analysis involving direct digestion methods and sequential extraction for eight selected soil and dust samples has been studied. The results obtained from the analysis of soils collected from Bottelary and Old Paarl road sampling sites indicated that the total concentrations of PGMs for the direct digestive procedure were higher than those of sequential extraction in both soil and dust samples. The PGMs pollution in soils near highways or similar environments may be attributed to emissions from catalytic car converters. In addition, Pd has shown the highest total metal concentration for both soil and dust samples. At the same time, according to the results obtained by sequential extraction procedure, it is obvious that Pd can be identified in abundant amounts in the Fe-Mn oxide bound and carbonated bound extracts for both soil and dust samples.

6.4.5 PGMs analysis in soil samples using AdDPCSV.

Next, the stripping voltammetric method optimised in this study was applied to the determination of PGMs in environmental soil samples. There are many methods for determination of PGM but only a few studies reporting voltammetric analysis of PGMs in soil and sediment samples (Zereini *et al.*, 2000.) The sequential extraction method for evaluating different fractions in sediments or soil samples for its metal content have been applied in this study (Li *et al.*, 2010; Morera *et al.*, 2001).

This was further done to determine in which fraction of the soil extraction process, the highest yield of PGMs with minimum matrix effect, can be determined. For quantitative determination of the PGMs, calibration curves were obtained from the results obtained and the corresponding equations for this dependence are given below.

Table 26. Results obtained for the sequential extraction of speciation metal concentrations in soil samples obtained using AdDPSV analysis.

Site ID	Fraction	Pd ($\mu\text{g g}^{-1}$)	Pt ($\mu\text{g g}^{-1}$)	Rh ($\mu\text{g g}^{-1}$)
OP1	Carbonate-bound	0.96 ± 0.01	0.93 ± 0.01	0.42 ± 0.01
	Fe-Mn oxides bound	1.14 ± 0.05	0.94 ± 0.01	0.94 ± 0.01
	Organic bound	0.99 ± 0.01	0.92 ± 0.01	0.90 ± 0.01
OP2	Carbonate-bound	0.98 ± 0.01	0.96 ± 0.03	0.92 ± 0.02
	Fe-Mn oxides bound	1.17 ± 0.01	0.84 ± 0.06	0.94 ± 0.03
	Organic bound	0.97 ± 0.03	0.97 ± 0.01	0.96 ± 0.01
OP3	Carbonate-bound	0.96 ± 0.02	0.96 ± 0.03	0.99 ± 0.01
	Fe-Mn oxides bound	1.17 ± 0.01	0.84 ± 0.06	0.98 ± 0.01
	Organic bound	0.98 ± 0.01	0.97 ± 0.01	0.98 ± 0.04
OP4	Carbonate-bound	0.98 ± 0.03	0.97 ± 0.01	0.96 ± 0.01
	Fe-Mn oxides bound	1.17 ± 0.03	0.97 ± 0.01	0.97 ± 0.01
	Organic bound	0.99 ± 0.01	0.97 ± 0.01	0.97 ± 0.01
BOT1	Carbonate-bound	1.04 ± 0.01	0.94 ± 0.01	0.86 ± 0.03
	Fe-Mn oxides bound	0.98 ± 0.01	0.96 ± 0.01	0.96 ± 0.06
	Organic bound	0.94 ± 0.01	0.96 ± 0.01	0.76 ± 0.01
BOT2	Carbonate-bound	1.31 ± 0.01	0.99 ± 0.04	0.99 ± 0.01
	Fe-Mn oxides bound	0.98 ± 0.01	0.97 ± 0.01	0.98 ± 0.03
	Organic bound	0.94 ± 0.01	0.98 ± 0.01	0.75 ± 0.04
BOT3	Carbonate-bound	4.00 ± 0.01	0.95 ± 0.01	0.95 ± 0.01
	Fe-Mn oxides bound	0.98 ± 0.03	0.98 ± 0.01	0.97 ± 0.01
	Organic bound	0.97 ± 0.05	0.97 ± 0.03	1.21 ± 0.01
BOT4	Carbonate-bound	0.92 ± 0.06	0.90 ± 0.01	0.86 ± 0.08
	Fe-Mn oxides bound	0.98 ± 0.01	0.96 ± 0.02	0.86 ± 0.06
	Organic bound	0.98 ± 0.01	0.98 ± 0.01	0.75 ± 0.03

Analysis of the results in Table 26 for sites OP1 – OP4 and BOT1 – BOT4 has been conducted to understand the prevalence of the PGMs at these sampling sites. The results obtained for the samples collected at these sites showed that the concentration of Pd(II), Pt(II) and Rh(III) ranged from 0.4 – 4.0 ng g⁻¹. These results were much lower and showed better detection with AdDPCS analysis, compared to the results obtained for ICP-MS analysis in sections 6.4.3 and 6.4.5.

The results for the Fe-Mn oxide bound extracts for sites OP1 – OP4 and BOT1 – BOT4 showed that the concentration of Pd(II), Pt(II) and Rh(III) ranged from 0.86 – 1.14 ng g⁻¹.

The results for the organic bound extracts for sites OP1 – OP4 and BOT1 – BOT4 showed that the concentration of Pd(II), Pt(II) and Rh(III) ranged from 0.75 – 1 ng g⁻¹. It was again observed that the results for Pd(II) seemed to be the highest in the extracted fractions, indicating that Pd(II) was the most mobile element in all fractions investigated with higher concentrations found in the carbonated bound and Fe-Mn oxide bound extracts.

6.4.6 PGMs analysis in dust samples using AdDPCSV

Table 27 presents the results for the speciation of the metal concentrations (ng g⁻¹ Pt(II), Pd(II), Rh(III)) obtained by adsorptive stripping voltammetry analysis of the dust samples.

Table 27. Results obtained for the sequential extraction of speciation metal concentrations in dust samples obtained using AdDPCSV analysis.

Site ID	Fraction	Pd ($\mu\text{g g}^{-1}$)	Pt ($\mu\text{g g}^{-1}$)	Rh ($\mu\text{g g}^{-1}$)
OP1	Carbonate-bound	0.99 ± 0.01	0.93 ± 0.01	0.40 ± 0.01
	Fe-Mn oxides bound	0.99 ± 0.01	0.98 ± 0.01	0.15 ± 0.01
	Organic bound	1.05 ± 0.01	0.99 ± 0.01	0.93 ± 0.02
OP2	Carbonate-bound	1.35 ± 0.01	0.93 ± 0.02	0.70 ± 0.01
	Fe-Mn oxides bound	0.99 ± 0.01	0.97 ± 0.05	0.42 ± 0.06
	Organic bound	0.97 ± 0.03	0.95 ± 0.01	0.89 ± 0.01
OP3	Carbonate-bound	1.35 ± 0.01	0.92 ± 0.01	0.70 ± 0.01
	Fe-Mn oxides bound	0.99 ± 0.03	0.98 ± 0.01	0.25 ± 0.01
	Organic bound	1.00 ± 0.02	0.98 ± 0.01	0.95 ± 0.01
OP4	Carbonate-bound	1.30 ± 0.01	0.96 ± 0.01	0.72 ± 0.03
	Fe-Mn oxides bound	0.97 ± 0.03	0.96 ± 0.02	0.34 ± 0.03
	Organic bound	1.00 ± 0.02	0.98 ± 0.02	0.95 ± 0.04
BOT1	Carbonate-bound	0.98 ± 0.01	0.93 ± 0.01	0.80 ± 0.01
	Fe-Mn oxides bound	0.98 ± 0.01	0.87 ± 0.04	0.24 ± 0.02
	Organic bound	1.01 ± 0.01	0.99 ± 0.02	0.92 ± 0.01
BOT2	Carbonate-bound	0.99 ± 0.01	0.99 ± 0.01	0.80 ± 0.01
	Fe-Mn oxides bound	0.98 ± 0.02	0.89 ± 0.03	0.13 ± 0.05
	Organic bound	1.12 ± 0.01	0.99 ± 0.01	0.30 ± 0.02

BOT3	Carbonate-bound	0.97 ± 0.01	0.92 ± 0.01	0.17 ± 0.01
	Fe-Mn oxides bound	0.97 ± 0.01	0.94 ± 0.01	0.40 ± 0.03
	Organic bound	1.20 ± 0.01	0.95 ± 0.01	0.60 ± 0.01
BOT4	Carbonate-bound	0.96 ± 0.02	0.89 ± 0.02	0.10 ± 0.01
	Fe-Mn oxides bound	0.97 ± 0.01	0.91 ± 0.02	0.88 ± 0.03
	Organic bound	1.18 ± 0.01	0.96 ± 0.01	0.47 ± 0.01

The results obtained showed some similarities to the results obtained for the soil samples with palladium leading with higher concentrations in both of the sampling sites (OP1 – OP4 and BOT1 – BOT4).

The results for Pd(II) in the samples collected from sites OP1 – OP4 were the highest in the carbonate bound extract, followed by the organic bound extract, and the least in the Fe-Mn oxide bound extract.

The Pt(II) results for sites OP1 – OP4 were slightly higher in the the Fe-Mn oxide bound extract, followed closely by the organic bound extract, and the least in the carbonate bound extract.

The Rh(III) results for sites OP1 – OP4 were the highest in the organic bound extract, followed by the carbonate bound extract, and the least in the Fe-Mn oxide bound extract.

The results obtained for the OP1 – OP4 sites have shown varied mobility of the PGMs in the different extracts evaluated. The trend observed indicated that the decreasing order of PGMs concentrations were Pd(II) > Pt(II) > Rh(III).

The analysis of the results obtained for sites BOT1 – BOT4 showed that the Pd(II) concentrations in the organic bound extracts were the highest, followed by the carbonate bound and Fe-Mn oxide bound extracts that were relatively similar to each other.

Analysis of the Pt(II) results for sites BOT1 – BOT4 showed that these concentrations were the highest in the organic bound extracts, followed by the carbonate bound extract, with the least concentrations observed in the Fe-Mn oxide bound extracts.

In the case of the Rh(III) results for sites BOT1 – BOT4, it was observed that these concentrations were the highest in the carbonate bound extracts for sites BOT1 and BOT2, followed by the Fe-Mn oxide bound extract for site BOT4 and the organic bound extract for site

BOT3. The lowest concentrations were observed in the Fe-Mn oxide bound extracts for sites BOT1 and BOT2, including the carbonate bound extract for sites BOT3 and BOT4.

For sites BOT1 – BOT4, the decreasing order of PGMs concentrations were also Pd(II) > Pt(II) > Rh(III).

The results obtained has further indicated that the use of the adsorptive differential pulse techniques offer a more sensitive technique for the determination of PGMs, when compared to traditional ICP - MS spectrometry. The deposition time for the stripping analysis used was 120 s, adding to the better results obtained in a shorter analysis times.

6.5 Summary

In summary the results obtained in this work have demonstrated that the newly constructed GCE/rGO-SbNPs sensor can be successfully employed for the PGMs determination in soil and dust samples. The use of nanoparticle sensors implies a series of advantages with respect to spectroscopic methods, which may result in the decreasing of cost and time.

The results obtained in this chapter have further demonstrated that the proposed electrochemical methods developed in this study shows results with high sensitivity and lower detection limit, indicating that both the GCE and SPCE sensor platforms modified with nanoparticles can be used as a sensor for the sensitive electrochemical detection of Pt(II), Pd(II) and Rh(III) in environmental samples.

The SPCE/rGO-SbNPs sensor obtained better sensitivity responses with slightly better detection limits compared to the GCE/rGO-SbNPs sensor. On the other hand the same electrode shows poorer %RSD with a narrower linear range.

The GCE/rGO-SbNPs sensor has shown a wider linear ranger compared to the SPCE/rGO-SbNPs sensor. The results obtained has further indicated that the use of the adsorptive differential pulse techniques offer a more sensitive technique for the single and simultaneous determination of PGMs, when compared to traditional ICP-MS spectrometry. The deposition time for the stripping analysis used was 120 s, adding to the better results obtained in a shorter analysis times.

The practical analytical utility of GCE/rGO-SbNPs was assessed by measurements of soil and dust samples and the results are not completely different with the results from ICP-MS. The mobility order for PGMs on the adsorptive stripping voltammetry is the same as the ICP-MS results. However, it should be highlighted that lower and more sensitive LODs were obtained for the voltammetric analysis, compared to the ICP-MS spectroscopic analysis.



Chapter 7

Conclusion and Recommendations

7.1 General Discussion and Conclusions

The high demand for simple, fast, accurate, and sensitive detection methods in environmental analysis has led to the development of novel electrochemical sensors. The glassy carbon electrode (GCE) and screen-printed carbon electrode (SPCE) were chosen because of its broad potential window, low background current, rich surface chemistry, low cost, chemical inertness, and suitability for the detection of trace levels of metal ions. Accordingly, the aim of this thesis work was to develop novel and improved electrochemical sensors based on nanoparticles exploiting the electrocatalytic effect of nanomaterials in general. PGMs were chosen as a target species due to the increasing contribution of exhaust emissions from vehicles to the presence of these metals in environmental samples.

The introduction of catalytic converter technology to cars has alleviated gaseous exhaust emissions, but in turn has resulted in emissions of the three platinum group metals (PGMs), e.g. Pd, Pt and Rh, contained in the automobile catalysts. The present literature survey showed that the concentrations of these metals have increased significantly in the last decades in diverse environmental matrices; like airborne particulate matter, soil, roadside dust and vegetation, rivers, coastal and oceanic environment. The details for each chapter are as follows.

In Chapter 1, the goals of this study were introduced focussing on the development of electrochemical sensors based on nanoparticles and its application for the detection of PGMs in environmental matrices. The method involved the modification of carbon electrodes (GCE and SPCE). The next step was to sample road side soil and dust samples to analyse for its PGMs content, thereby achieving the goals of our study. By using the adsorptive stripping voltammetry technique, the importance of the emergent field of nanocomposite functional materials has provided suitable to achieve the results of the study. The results indicated that the developed sensors are effective and reliable to detect PGMs in soil and dust samples.

Chapter 2 established the literature review on electrochemical sensing with nanoparticles. In this chapter the state of the art in modifying electrochemical sensors and the methods for preparation of nanoparticles were reviewed. The literature review and theory relative to the chemistry of this project were presented by a detailed description of the relevant work done by previous studies and researchers.

Chapter 3, detailed the experimental protocol of the synthesis of the nanocomposite of rGO-SbNPs and other related materials. Synthesis of rGO-SbNPs were successfully demonstrated, and has been achieved using rGO and antimony nanoparticles to obtain the synthesised nanocomposite of rGO-SbNPs by chemical method employing PVA as a capping agent. Graphite and antimony pentachloride were used as the starting materials. Individual nanoparticles of rGO, SbNPs and the nanocomposite of rGO-SbNPs were also produced using a chemical method. The phase formation has been investigated microscopically, spectroscopically and electrochemically. It was observed that substantial differences exist between these materials as observed in microscopy, structural and electrochemical behaviours.

In Chapter 4 the novel synthesis and characterisation of the nanocomposite of rGO-SbNPs was presented. The results for the characterisation of the obtained nanocomposite were presented. The rGO-SbNPs were obtained from the chemical integration of rGO and SbNPs and characterised by SEM, HRTEM, EDX, UV-VIS, FTIR, Raman spectra, CV and EIS techniques. All the results revealed that rGO-SbNPs contains the structural characteristics of the individual rGO and SbNPs nanoparticles. According to SEM analysis, the rGO contained uniformly SbNPs distributed over the whole surface of the nanocomposite. The SbNPs can be seen as white spots on the rGO surface, which clearly indicates their coupling. From HRTEM results, the antimony nanoparticles occupy the whole surface of the graphene sheets. Furthermore, energy-dispersive X-ray (EDX) examination confirmed the presence of antimony in the nanocomposite. From the FTIR study the compositional comparison among composites and individual materials has also been studied. The rGO-SbNPs nanocomposite showed different absorption peaks compared to the individual rGO and SbNPs compounds. The Raman spectrum of the newly synthesised rGO-SbNPs composite was confirmed, including that of both of the individual rGO and SbNPs Raman spectra.

The electrochemistry of a rGO-SbNPs film in acidic solution showed the presence of redox species over a broad potential range. From CV analysis, the results showed that the

combined effect of rGO and SbNPs enhanced the electron transfer for the rGO-SbNPs compounds. This observation was also supported by EIS analysis and results obtained.

In Chapter 5 a description of the redox investigation obtained on PGMs using rGO-SbNPs in sensor analysis, was provided. For the application purpose, current-voltage characteristics and electrochemical studies have been performed in NaOAc buffer (pH = 5.2) solution, in order to compare the carbon modified nanosensors (SPCE/rGO-SbNPs and GCE/rGO-SbNPs). The results have proved that rGO-SbNPs acted as an electron transfer medium and enhanced the electrochemical reaction in both carbon nanosensors. The introduction of rGO-SbNPs on the GC and SPC electrode surfaces facilitates the conduction pathway at the modified electrode surface. True surface area as well as film thickness of the electro-active species modified on the SPCE/rGO-SbNPs and GCE/rGO-SbNPs sensor surfaces was determined experimentally. From the studies performed in this chapter, the SPCE/rGO-SbNPs sensor was found to be more sensitive than the GCE/rGO-SbNPs sensor.

Chapter 6 demonstrated the application of the SPCE/rGO-SbNPs and GCE/rGO-SbNPs sensors for the detection of PGMs in environmental samples. This novel sensor application for the determination of PGMs in roadside dust and soil samples, was successfully demonstrated with the aforementioned constructed sensors.

To this end, this study has provided a detailed examination of the optimisation of GCE/rGO-SbNPs and SPCE/SbNPs sensors for PGMs analysis. Specifically, the optimisation of supporting electrolytes, pH, deposition potential, deposition time and stirring conditions were thoroughly investigated. The nanocomposite materials displayed enhanced response times to detect target analytes. The GCE/rGO-SbNPs sensor in combination with adsorptive differential pulse cathodic stripping voltammetry (AdDPCSV) were successfully used for the determination of Pd(II), Pt(II) and Rh(III) with good detection limits of 0.45, 0.49, and 0.49 $\mu\text{g L}^{-1}$, respectively.

The accuracy of the method was obtained by calculating the average values for % recoveries. Recovery values between 91.9% and 111.6% were obtained, confirming that the method was relatively accurate. For the determination of precision of the developed method, the reproducibility of the method was evaluated through the percent relative standard deviation (%RSD). The adsorptive deposition on a GCE/rGO-SbNPs sensor under the optimised

conditions resulted in reproducible measurements with relative good %RSD values of 4.2%, 2.55% and 2.67% for Pd(HDMG)₂, Pt(HDMG)₂ and Rh(HDMG)₃, respectively.

The SPCE/rGO-SbNPs sensor in combination with adsorptive differential pulse cathodic stripping voltammetry were employed for the detection of Pd(II), Pt(II) and Rh(III) with excellent limits of detection limits of 0.42, 0.26, and 0.34 $\mu\text{g L}^{-1}$, respectively and apparent recovery factors (very close to 100 %). The adsorptive deposition on a SPCE/rGO-SbNPs sensor under the optimised conditions resulted in reproducible measurements with poor %RSD values of 23.94%, 26.96% and 27.98% for Pd(HDMG)₂, Pt(HDMG)₂ and Rh(HDMG)₃, respectively.

By comparing the responses and results of the two carbon nanoparticle sensors applied in AdDPCSV analysis of PGMs, the results indicated that both sensors exhibit good detection limits. The SPCE/rGO-SbNPs sensor obtained better sensitivity responses with a slightly better detection limit compared to the GCE/rGO-SbNPs sensor. On the other hand, the precision of the SPCE/rGO-SbNPs sensor was not satisfactory. The GCE/rGO-SbNPs sensor was characterised by extreme wide linear range, very good RSD % and apparent recovery factors compared to the SPCE/rGO-SbNPs sensor, offering its application to real samples. From the results, there are some uncertainties surrounding the SPCE/rGO-SbNPs sensor and further investigations need to be performed in real samples.

Interferences were also evaluated, showing promising results. ICP-MS analysis coupled with a sequential extraction procedure (SEP), compared to direct acid digestion method and AdDPCSV voltammetry have been investigated as methods for analysis of PGMs in soil and dust samples. ICP-MS is commonly used for analysis of most of the elements of particular interest in this study and therefore it was with this technique that comparison has been made. The AdDPCSV analysis proved to be a much more satisfactory method of high sensitivity for PGMs analysis. The Pd(II), Pt(II) and Rh(III) were successfully determined at concentrations as low as 0.26 $\mu\text{g L}^{-1}$.

7.2 Future Recommendations

The selective detection of the PGMs has been achieved. It could be envisaged that further work can be conducted on the simultaneous determination of PGMs with the constructed sensors.

Each time when the SPCE/rGO –SbNPs was used different calibration curves were obtained. Detailed surface studies can be done to understand the changes occurring on the surface of the sensor. Improving the better mixing of the nanocomposite mixture is also required. The findings outlined in this thesis could prove beneficial to not only the environmental studies, but have ramifications for other industries suffering with pollutants.

Further investigations into the results outlined in this thesis could yield valuable additional information, and see the processes and materials move closer to commercial application. Future developments will consider the production of our own screen-printed carbon electrodes to further improve the top insulation ink (that we think may be a problem) in order to modify the effect of shear force on the prepared surface.

The utilisation of SPCE/rGO-NPs sensors for further developmental work into the construction of electrode surfaces is highly recommended, based on the satisfactory and promising outcomes shown in the detection limit obtained. The SPCE/rGO-NPs sensor also requires further study in order to boost the precision of the sensor results. This is most likely to be achieved by limiting the amount of the nanocomposite when preparing the suspension drop-coated on the electrode surface. Perhaps by finding a suitable solvent due to the possibilities of organic solvent not suitable for SPCE. This may be achieved by further investigating the unusual behaviour of the decrease of deposition time observed. The long-term stability of these electrodes also needs further investigation.

Chapter 8

References

8.1 References

Abbaspour, A., Ghaffarinejad, A. (2009). Method for Preparation of a Sol-Gel-Derived Carbon Ceramic Electrode Using Microwave Irradiation. *Analytical Chemistry*, 81: 3660-3664.

Ajayan, P.M., Schadler, L.S., Braun, P.V. (2003). *Nanocomposite Science and Technology*. Wiley-VCH Verlag GmbH, Weinheim, Germany.

Ajayan, P.M. (1999). Nanotubes from Carbon. *Chemical Reviews*, 99: 1787-1799.

Ajayan, P.M., Iijima, S. (1991). Wetting and de-wetting transitions of small metal particles on substrates under electron irradiation. *Journal of Colloid and Interface Science*, 147: 281-285.

Alexandre, M. and Dubois, P. (2000). Polymer-layered silicate nanocomposites: preparation, properties and uses of a new class of materials. *Materials Science and Engineering: R: Reports*, 28: 1-63.

Alloway, B.J., Jackson, A.P., Morgan, H. (1990). The accumulation of cadmium by vegetables grown on soils contaminated from a variety of sources. *Science of the Total Environment*, 91: 223-236.

Alvarez-Icaza, M., Bilitewski, U. (1993). Mass production of biosensors. *Analytical Chemistry*, 65(11): 525A-533A.

Alwarappan, S., Erdem, A., Liu, C., Li, C.Z. (2009). Probing the Electrochemical Properties of Graphene Nanosheets for Biosensing Applications. *Journal of Physical Chemistry C*, 113: 8853-8857.

Amy, F., Chabal, Y.J. (2003). Interaction of H, O₂, and H₂O with 3C-SiC surfaces. *Journal of Chemical Physics*, 119(12): 6201-6209.

Anderson, G.P., King, K.D., Gaffney, K.L., Johnson, L.H. (2000). Multi-analyte interrogation using the fiber optic biosensor. *Journal of Biosensors & Bioelectronics*, 14 (10-11): 771-777.

Andres, R.P., Bielefeld, J.D., Henderson, J.I., Janes, D.B., Kolagunta, V.R., Kubiak, C.P., Mahoney, W.J., Osifchin, R.G. (1996). Self-assembly of a two-dimensional superlattice of molecularly linked metal clusters. *Science*, 273(5282): 1690-1693.

Andrievskii, R. A. (2003). Directions in Current Nanoparticle Research. *Powder Metallurgy and Metal Ceramics*, 42(11): 624–629.

Anne Andrew Research Group, Response and Excitation form of Cronoamperometry. <http://www.serotonin.ucla.edu>, accessed on 4 June 2014.

Antiohos, D., Pingmuang, K., Romano, M., Beirne, S., Romeo, T., Aitchison, P., Minett, A., Wallace, G., Phanichphant, S. (2013). Manganosite–microwave exfoliated graphene oxide composites for asymmetric supercapacitor device applications. *Electrochimica Acta*, 101: 99–108.

Arancibia, V., Nagles, E., Gomez, M., Rojas, C. (2012). Speciation of Cr (VI) and Cr (III) in water samples by adsorptive stripping voltammetry in the presence of pyrogallol red applying a selective accumulation potential. *International Journal of Electrochemical Science*, 7: 11444–11455.

Arancibia, V., Alarcón, L., Segura, R. (2004). Supercritical fluid extraction of cadmium as Cd–oxine complex from human hair Determination by square wave anodic or adsorptive stripping voltammetry. *Analytica Chimica Acta*, 502: 189–194.

Ashrafi, A.M and Vytřas, K. (2012). Determination of Trace Bismuth(III) by Stripping Voltammetry at Antimony-Coated Carbon Paste Electrode. *International Journal Electrochemical Science*, 7: 68–67).

Arotiba, O.A., Songa, E.A., Baker P.G E., Iwuoha, I. (2009). Dendrimeric gold- poly(propylene imine) electrochemical DNA nanobiosensor. *Chemistry Today*, 27: 55–58.

Atkins, P. (1998). *Molecular Quantum Mechanics*. 4th Ed., Oxford University Press Inc., New York.

Attar, A., Ghica, M.E., Amine, A., Brett, C.M.A. (2014). Comparison of Cobalt Hexacyanoferrate and Poly(Neutral Red) Modified Carbon Film Electrodes for the Amperometric Detection of Heavy Metals Based on Glucose Oxidase Enzyme Inhibition, *Analytical Letters*, DOI: 10.1080/00032719.2014.952372

Attia, S.M., Wang, J., Wu., G., Shen. J. (2002). Review on Sol-Gel Derived Coating: Process, Techniques and Optical Applications. *Journal of Material Science Technology*, 18(3): 211–217.

Baeyens, W., Monteny, F., Leermakers, M., Bouillon, S. (2003). Evaluation of sequential extractions on dry and wet sediments. *Analytical Bioanalytical Chemistry*, 376: 890-901.

Balanta, A., Godard, C., Claver, C. (2011). Pd nanoparticles for C–C coupling reactions. *Chemical Society Reviews*.40: 4973–4985.

Banks, C.E and Compton, R.G. (2006). New electrodes for old: from carbon nanotubes to edge plane pyrolytic graphite. *Analyst*, 131: 15–21.

Banks, C.E., Moore, R.R, Davies, T.J, Compton, R.G. (2004). Investigation of modified basal plane pyrolytic graphite electrodes: definitive evidence for the electrocatalytic properties of the ends of carbon nanotubes. *Chemical Communications*, 16: 1804–1805.

Barau, A., Budarin, V., Caragheorgheopol, A., Luque, R., Macquarrie, D.J., Prella, A., Teodorescu, V.S., Zaharescu, M. (2008). A simple and efficient route to active and dispersed silica supported palladium nanoparticles. *Catalysis Letters*, 124(3-4): 204–214.

Barbooti, M. (2015). *Environmental Applications of Instrumental Chemical Analysis*. Apple Academy Press, Inc. Canada.

Bard, A.J. and Faulkner, L.R. (2001). *Electrochemical Methods: Fundamentals and Applications*, 2nd Ed. John Wiley & Sons, Inc., New York, USA.

Baldwin, R.P. and Thomsen, K.N. (1991). Chemically modified electrodes in liquid chromatography detection: A review. *Talanta*, 38: 1–16.

Barek., J., Fogg, A.G., Muck, A., Zima, J. (2001). Polarography and Voltammetry at Mercury Electrodes. *Critical Reviews in Analytical Chemistry*, 31(4): 291–309.

Barth, J.V., Costantini, G., Kern, K. (2005). Engineering atomic and molecular nanostructures at surfaces. *Nature*, 437: 671-679.

Basavaraja, C., Kim, W. J., Kim, Y. D., Huh, D. S. (2011). Synthesis of polyanilinegold/graphene oxide composite and microwave absorption characteristics of the composite films. *Materials Letters*, 65(19-20): 3120–3123.

Baumann, T., Muller, S., Niessner, R. (2002). Migration of dissolved heavy metal compounds and PCP in the presence of colloids through heterogeneous calcareous gravel and a homogeneous quartz and - pilot scale experiments. *Water Research*, 36: 1213–1223.

Beaudry, P. (2010). Louis De Broglie: The wave and particle paradox. http://amatterofmind.org/Pierres_pdf, accessed on 7 November 2013.

Berger, C., Song, Z., Li, T., Li, X., Ogbazghi, A.Y., Feng, R., Dai, Z., Marchenkov, A.N., Conrad, E.H., First, P.N., de Heer, W.A. (2004). Ultrathin epitaxial graphite: two-dimensional electron gas properties and a route toward graphene-based nanoelectronics. *Journal of Physical Chemistry B*, 108(52): 19912–19916.

Bettmer, J., Jakubowski, N., Prange, A. (2006). Elemental tagging in inorganic mass spectrometric bioanalysis. *Analytical and Bioanalytical Chemistry*, 386: 7–11.

Birke, C., Peter, H.H., Langenberg, U., Muller-Hermes, W.J.R., Peters J.H., Heitmann, J., Leibold, W., Dallugge, H., Krapf, E., Kirchner, H. (1981). Mycoplasma contamination in human

tumor cell lines: effects on interferon induction and susceptibility to natural killing. *Journal of Immunology*, 127: 194–98.

Birwland, W.P. (1999). *Soil and Geomorphology*. 3rd Ed., Oxford University press, New York, 301–3.

Bo, Y., Yang, H.Y., Hu, Y., Yao, T.M., Huang, S.S. (2011). A novel electrochemical DNA biosensor based on graphene and polyaniline nanowires. *Electrochimica Acta*, 56: 2676–2681.

Bobrowski, A., Gawlicki, M., Kapturski, P., Mirceski, V., Spasovski, F., Zarebski, J. (2009). The silver amalgam film electrode in adsorptive stripping voltammetric determination of palladium(II) as its dimethyldioxime complex. *Electroanalysis*, 21(1): 36–40.

Bockris, J. O'M. (1999). *Modern Aspects of Electrochemistry*. Kluwer Academic, New York, USA.

Bond A.M. (1994). Past, present and future contributions of microelectrodes to analytical studies employing voltammetric detection: A review. *Analyst*, 119: 1R–21R.

Bonnemann H and Richards, R.M. (2001). Nanoscopic Metal Particles-Synthetic Methods and Potential Applications. *European Journal of Inorganic Chemistry*, 2001(10): 2455–2480.

Boukhvalov, D.W, Katsnelson, M.I. (2008). Modeling of graphite oxide. *Journal of American Chemical Society*, 130(32): 10697–701.

Bowman M.J., Booth A.D. (1997). A Review of Methods for the Examination of Magnetic Domain Structure. *Materials Characterization*, 39: 139–167.

Brett, C. M. A and Oliveira-Brett, A. M. (2013). *Electrochemistry Principles, Methods and Applications*. 2nd Ed.; Oxford University Press: Oxford, UK.

Brett, C.M.A and Brett, A.M.O. (1993). *Electrochemistry-principles, methods, and applications*. Oxford University Press, Oxford, UK.

Brett, C.M.A. (2001). Electrochemical sensors for environmental monitoring: ‘Strategy and examples’. *Journal of Pure Applied. Chemistry*, 73(12): 1969–1977.

Bronstein, L.M., Chernyshov, D.M., Volkov, I.O., Ezernitskaya, M.G., Valetsky, P.M., Matveeva, V.G., Sulman, E. M. (2000). Structure and Properties of Bimetallic Colloids Formed in Polystyrene-block-Poly-4-vinylpyridine Micelles: Catalytic Behavior in Selective Hydrogenation of Dehydrolinalool. *Journal of Catalysis*, 196(2): 302–314.

Brust, M., Kiely, C.J (2002). Some recent advances in nanostructure preparation from gold and silver particles: a short topical review. *Colloids Surface A*, 202: 175–186.

Budarin, V.L., Clark, J.H., Luque, R., Macquarrie, D.J., White, R.J. (2008). Palladium nanoparticles on polysaccharide derived mesoporous materials and their catalytic performance in C-C coupling reactions. *Green Chemistry*, 10: 382–387.

Buffle, J., Horvai, G. (2000). *In Situ Monitoring of Aquatic Systems: Chemical Analysis and Speciation General Concepts*. John Wiley & Sons Ltd, Chichester, UK.

Burda, L., Chen, X., Narayanan, R., El-Sayed, M.A. (2005). Chemistry and properties of nanocrystals of different shapes. *American Chemical Society, Chemistry revised*, 105(4): 1025–1102.

Butler, O.T., Cairns, W., Cook, J.M., Davidson, C.M. (2011). Atomic spectrometry update. Environmental analysis. *Journal of Analytical Atomic Spectrometry*, 26: 250–286.

Butt, H-J., Cappella, B., Kappl, M. (2005). Force measurements with the atomic force microscope: Technique, interpretation and applications. *Surface Science Reports*, 59: 1–152.

Cai, H., Wang, Y.Q., He, P.G., Fang, Y.H. (2002). Electrochemical detection of DNA hybridization based on silver-enhanced gold nanoparticle label. *Analytica Chimica Acta*, 469: 165–172.

Campelo, J.M., Luna, D., Luque, R., Marinas, J.M., Romero, A.A. (2009). Sustainable Preparation of Supported Metal Nanoparticles and Their Applications in Catalysis. *Chemsuschem*, 2: 18–45.

Cao, G. (2004). *Nanostructures and Nanomaterials, synthesis, properties and applications*. Imperial College Press, London, UK.

Carotenuto, G., and Nicolais, L. (2003). Size-controlled synthesis of thiol-derivatized gold clusters. *Journal of Materials Chemistry*, 13: 1038–1041.

Carrara, S., Bavastrello, V., Ricci, D., Stura, E., Nicolini, C. (2005). Improved nanocomposite materials for biosensor applications investigated by electrochemical impedance spectroscopy. *Sensors and Actuators B*, 109: 221–226.

Cass, A.E.G. (1990). *Biosensors: A practical Approach*. IRL Press, Oxford University Press. Oxford, UK.

Chalmers, J.M and Griffiths, P.R. (2002). *Handbook of Vibrational Spectroscopy*. John Wiley & Sons, Chichester, UK.

Chan, C.C., Lam, H., Lee, Y.C., Zhang, X-M. (2004). *Analytical Method Validation and Instrument Performance Verification*, Wiley-Interscience, New York.

- Chang, S-Y. Hong, J-S. Yoo, Park, S-M. (2006). Determination of Electron Transfer Kinetic Parameters by Fourier Transform Electrochemical Impedance Spectroscopic Analysis. *Journal of Physical Chemistry B*, 110: 19380–19385.
- Chang, Y-T.; Hseu, Z-Y.; Zehetner, F. (2014). Evaluation of hyto-availability of Heavy Metals to Chinese Cabbage (*Brassica chinensis* L.) in Rural Soils. *The Scientific World Journal*, 2014. ID 309396.
- Chapman, P.M, Allen, H.E, Z'Graggen, M.N. (1996). Evaluation of bioaccumulation factors in regulating metals. *Environmental Science and Technology*, 30(10): 448A–452A.
- Chatreewongsin, U. (2000). Metal extraction from soil samples by chelation in a microwave system. Published PhD Thesis, Institute and State University Blacksburg, Virginia, USA.
- Chaturvedi, S., Dave, P. N., Shah, N.K. (2012). Applications of nano-catalyst in new era. *Journal of Saudi Chemical Society*, 16(3): 307–325.
- Chen, P-Y., Luo, C-H., Chen, M-C., Tsai, F-J., Chang, N-F., Shih, Y. (2011). Screen-Printed Carbon Electrodes Modified with Cobalt Phthalocyanine for Selective Sulfur Detection in Cosmetic Products. *International Journal Molecular Science*, 12: 3810–3820.
- Chen, F., Tao, N.J. (2009). Electron transport in single molecules: From benzene to graphene. *Accounts of Chemical Research*, 42(3): 429-38.
- Chen, M.Q., Wang, J., Zhang, M.X., Chen, M.G., Zhu, X.F., Min, F.F., Tan, Z.C. (2008). Catalytic effects of eight inorganic additives on pyrolysis of pine wood sawdust by microwave heating. *Journal of Analytical and Applied Pyrolysis*, 82(1):145–150.
- Chirenje, T., Ma, L.Q., Clark, C., Reeves, M. (2003). Cu, Cr and As distribution in soils adjacent to pressure-treated decks, fences and poles. *Journal of Environmental Pollution*, 124: 407–417.
- Choi, W., Lahiri, I., Seelaboyina, R., Kang, Y.S. (2010). Synthesis of Graphene and Its Applications: A Review. *Critical Reviews in Solid State and Material Science*, 35: 52–71.
- Christian, P., Von der Kammer, F., Baalousha, M., Hofmann, T. (2008). Nanoparticles: structure, properties, preparation and behaviour in environmental media. *Ecotoxicology*, 17: 326–343.
- Chuan, M.C., Shu, G.Y., Liu, J.C. (1996). Solubility of heavy metals in a contaminated soil: Effects of redox potential and pH. *Water, Air, and Soil Pollution*, 90: 543–556.
- Chung, D. (2002). Review Graphite. *Journal of Material Science*, 37(8): 1475–1489.
- Chushak, Y.G and Bartell, L.S. (2003). Freezing of Ni-Al bimetallic nanoclusters in computer simulations. *Journal of Physical Chemistry B*, 107(16): 3747–3751.

Ciszewski, M., Mianowski, A., Nawrat, G., Szatkowski, P. (2014). Reduced graphene oxide supported antimony species for high-performance supercapacitor electrodes. *ISRN Electrochemistry*, 2014, 1D 826832.

Ciucu, A.A. (2014). Chemically Modified Electrodes in Biosensing. *Journal of Biosensors & Bioelectronics*, 5: 154, doi: 10.4172/2155-6210.1000154.

Claesson, P.M., Ederth, T., Bergeron, V., Rutland, M.W. (1996). Techniques for measuring surface forces. *Advances in colloid and interface science*, 67: 119–183.

Cofre P., Brinck K. (1992). Determination of gallium by anodic stripping square-wave voltammetry Detection of a Ga-Zn intermetallic compound and its destruction by Sb in an NaSCN-NaClO₄ supporting electrolyte. *Talanta*, 39: 127–136.

Compagnone, D., Baldini, F., Natale, C.D. (2015). Sensors: Proceedings of the Second National Conference on Sensors, *Technology & Engineering*, Rome.

Compton, O.C., Nguyen, S.T. (2010). Graphene oxide, highly reduced graphene oxide, and graphene: versatile building blocks for carbon-based materials. *Small*, 6(6): 711–23.

D'amore, J.J., Al-abed, S.R., Scheckel, K.G., Ryan, J.A. (2005). Methods of Speciation of Metals in Soils. *Journal of Environmental Quality*, 34(5): 1707–1745.

Dailly, A., Schneider, R., Billaud, D., Fort, Y., Ghanbaja, J. (2003). Nanometric antimony powder synthesis by activated alkaline hydride reduction of antimony pentachloride. *Journal of Nanoparticle Research*, 5: 389–393.

Dalvi, A.A., Satpati, A.K., Palrecha, M.M. (2008). Simultaneous determination of Pt and Rh by catalytic adsorptive stripping voltammetry, using hexamethylene tetramine (HMTA) as complexing agent. *Talanta*, 75(5): 1382–1387.

Dan, Y., Lu, Y., Kybert, N.J., Luo, Z., Johnson, A.T.C. (2009). Intrinsic response of graphene vapor sensors. *Nano Letters*, 9(4): 1472–1475.

Das, A., Pisana, S., Chakraborty, B., Piscanec, S., Saha, S.K., Waghmare, U.V., Novoselov, K.S., Krishnamurthy, H.R., Geim, A.K., Ferrari, A.C., Sood, A.K. (2008). Monitoring dopants by Raman scattering in an electrochemically top-gated graphene transistor. *Nature Nanotechnology*, 3: 210–215.

Dekanski, A., Stevanovic, J., Stevanovic, R., Nikolic, B. Z., Jovanovic, V.M. (2001). Glassy carbon electrode 1: Characterization and electrochemical activation. *Carbon*, 39: 1195–1205.

Denney, R.C., Sinclair, R. (1993). *Visible and Ultraviolet Spectroscopy. Analytical Chemistry by open learning series*, John Wiley and Sons, Canada.

Deshpande, S., Patil S., Kuchibhatla, S., Seal, S. (2005). Size dependency variation in lattice parameter and valency states in nanocrystalline cerium oxide. *Applied Physics Letters*, 87: 133–113.

Dhand, V., Rhee, K.Y., Kim, H. J., Jung, D.H. (2013). A Comprehensive Review of Graphene Nanocomposites: Research Status and Trends. *Journal of Nanomaterials*, 2013: ID 763953.

Doumett, S., Lamperi, L., Checchini, L., Azzarello, E., Mugnai, S., Mancuso, S., Petruzzelli, G., Del Bubba, M. (2008). Heavy metal distribution between contaminated soil and *Paulowniatomentosa*, in a pilot-scale assisted phytoremediation study: Influence of different complexing agents. *Chemosphere*, 72(10): 1481–1490.

Dresselhaus M.S., Dresselhaus, G., Eklund, P. (1996). *Science of Fullerenes and Carbon Nanotubes*. Academic Press, San Diego, USA.

Dreyer, D. R., Park, S., Bielawski, C. W., Ruoff, R.S. (2010). The chemistry of graphene oxide. *Chemical Society Reviews*, 39(1): 228–240.

Dropsens Technologies, Spain (2012). www.dropsens.com, Accessed on 1. August 2013.

Du Toit, (2002). Analytical Techniques to Fulfill Air Pollution Monitoring Requirements. *African Pulp and Paper Week*, International Convention Centre, Durban, SA.

Du, P.C., Mu, B., Wang, Y.J., Shi, H.G., Xue, D.S., Liu, P., (2011). Facile approach for temperature-responsive polymeric nanocapsules with movable magnetic cores. *Material Letters*, 65: 1579–1581.

Dube, A., Zbytniewski, R., Kowalkowski, T., Cukrowska, E., Buszewski, B. (2001). Adsorption and Migration of Heavy Metals in Soil. *Polish Journal of Environmental Studies*, 10(1): 1–10.

Dubiella-Jackowska, A. Polkowska, Ż. Namieśnik, J. (2007). Platinum Group Elements: A Challenge for Environmental Analytcs. *Polish Journal of Environmental Studies*, 16(3): 329–345.

Dunlap, M and Adaskaveg, J.E. (1997). *Introduction to the Scanning Electron Microscope Theory, Practice, & Procedures. Facility for Advance Instrumentation*. U.C. Davis, California, USA.

Economou A. (2005). Bismuth-film electrodes: recent developments and potentialities for electroanalysis. *TrAC Trends in Analytical Chemistry*, 24: 334–340.

Economou A., Fielden P.R. (2005). Mercury film electrodes: developments, trends and potentialities for electroanalysis. *Analyst*, 128: 205–213.

Economou, A., Fielden, P.R. (2003) Mercury film electrodes: developments, trends and potentialities for electroanalysis. *Analyst*, 128: 205–213.

Eggins, B.R. (2002). *Chemical Sensors and Biosensors Analytical Techniques in the Sciences*, 2nd Edition, John Wiley & Sons

Electron microscopes, House Ear Institute, *Advance Hearing Science*. (2001). <http://www.hei.org/research/aemi/emt.htm>. Last accessed 24 February, 2014.

El Mhammedi M.A., Achak M., Hbid M., Bakasse M., Hbid T., Chtaini A. (2009). Electrochemical determination of cadmium(II) at platinum electrode modified with kaolin by square wave voltammetry. *Journal of Hazardous Materials*, 170: 590–594.

EL-Sayed, M.A. (2004). Small Is Different: Shape-, Size-, and Composition-Dependent Properties of Some Colloidal Semiconductor Nanocrystals. *Account of Chemical Research*, 37: 326–333

Endo, M., Kim, Y. A., Ezaka, M., Osada, K., Yanagisawa, T., Hayashi, T., Terrones, M., Dresselhaus, M.S. (2003). Selective and Efficient Impregnation of Metal Nanoparticles on Cup-Stacked-Type Carbon Nanofibers. *Nano Letters*, 3: 723–726.

Esteban, M., Casassas, E. (1994). Stripping electroanalytical techniques in environmental analysis. *Trends in Analytical Chemistry*, 13: 110–117.

Fana, Y., Liua, J-H., Yang, C-P., Yua, M., Liua, P. (2011). Graphene–polyaniline composite film modified electrode for voltammetric determination of 4-aminophenol. *Sensors and Actuators B*, 157: 669–674.

Fang, Y.X., Guo, S.J. Zhu, C.Z. Zhai, Y.M., Wang, E.K. (2010). Self-Assembly of Cationic Polyelectrolyte-Functionalized Graphene Nanosheets and Gold Nanoparticles: A Two-Dimensional Heterostructure for Hydrogen Peroxide Sensing. *Langmuir*, 26(13): 11277–11282.

Faridbod, F., Gupta, V.K., Zamani, H.A. (2011). Electrochemical Sensors and Biosensors. *Endocrinology and International Journal of Electrochemistry* . ID 352546, 2 pages.

Farrell-Poe, K. (2000). Water Quality and Monitoring “A river is the report card for its watershed.” - Alan Levere, *Connecticut Department of Environmental Protection*, Hartford, US.

Fedlheim, D.L and Foss, C.A. (2004). *Metal Nanoparticles: Synthesis, Characterization, and Applications*. In: G Schmid, ed. *Clusters and Colloids. From Theory to Applications*, 459–544, New York: VCH.

Fergusson, P.L., Chandler, G.T. (1998). A laboratory and field comparison of sediment polycyclic aromatic hydrocarbon accumulation by the cosmopolitan estuarine polychaete *Streblospio benedicti* (Webster). *Marine Environmental Research*, 45: 387–401.

Fernández-Ujados, M., Trapiella-Alfonso, L., Costa-Fernández, J. M., Pereiro, R., Sanz-Medel, A. (2013). One-step aqueous synthesis of fluorescent copper nanoclusters by direct metal reduction. *Nanotechnology*, 24(49): 495601.

- Ferrando, R., Jellinek, J., Johnston, R.L. (2008). Nanoalloys: from theory to applications of alloy clusters and nanoparticles. *Chemical Reviews*, 108(3): 845–910.
- Ferrari, A.C., Bonaccorso, F., Fal'ko, V., Novoselov, K.S., Roche, S. (2015). Science and technology roadmap for graphene, related two-dimensional crystals, and hybrid systems. *Nanoscale*, 7: 4598–4810.
- Ferrari, A.C. (2007). Raman spectroscopy of graphene and graphite: Disorder, electron-phonon coupling, doping and nonadiabatic effects. *Solid State Communication*, 143: 47–57.
- Ferrari, A.C., Robertson, J. (2000) Interpretation of Raman Spectra of Disordered and Amorphous Carbon. *Physical Reviews. B*, 61: 14095–14107.
- Ferraro, J.R., Nakamoto, K., Brown, C.W. (2003). *Introductory Raman Spectroscopy*, 2nd, Ed., Elsevier, Hingham, MA, USA.
- Fifield, F.W. and Haines, P.W. (2000). *Environmental Analytical Chemistry*, Blackwell Science, Oxford, UK.
- Filgueiras, A.V., Lavilla, I., Bendicho, C. (2002). Chemical sequential extraction for metal partitioning in environmental solid samples. *Journal of Environmental Monitoring*, 4: 823–857.
- Fiorito, P.A., Goncales, V.R., Ponzio, E.A., Cordoba de Torresi, S.I. (2005). Synthesis, characterization and immobilization of Prussian Blue nanoparticles. A potential tool for biosensing devices. *Chemical Communications*, 3:366–368.
- Fultz, B., Howe, J. (2013). *Transmission Electron Microscopy and Diffractometry of Materials*, Graduate Texts in Physics, Springer-Verlag Berlin Heidelberg, Germany.
- Gao, Y., Liu, L.Q., Zu, S.Z., Peng, K., Zhou, D., Han, B.H., Zhang, Z. (2011). The effect of interlayer adhesion on the mechanical behaviors of macroscopic graphene oxide papers. *ACS Nano*, 5(3): 2134–2141.
- Gao, W., Song, J. and Wu, N. (2004). Voltammetric Behavior and Square-wave Voltammetric Determination of Trepibutone at a Pencil Graphite Electrode. *Journal of Electroanalytical Chemistry*, 576(1): 1–7.
- Geim, A.K., Novoselov, K.S. (2007). The rise of graphene. *Nature Materials*, 6(3): 183–191.
- Gerringa, L.J.A., de Baar, H.J.W., Nolting, R.F., Paucot, H. (2001). The influence of salinity on the solubility of Zn and Cd sulphides in the Scheldt estuary. *Journal of Sea Research*, 46: 201–211.
- Ghosh, S., Bao, W., Nika, D., Pokatilov, E.P., Lau, C.N., Balandin, A.A. (2010). Dimensional crossover of thermal transport in few-layer graphene. *Nature Materials*, 9: 555–558.

- Gimmler, H., Carandang, J., Boots, A., Reisberg, E., Woitke, M. (2002). Heavy metal content and distribution within a woody plant during and after seven years continuous growth on municipal solid waste (MSW) bottom slag rich in heavy metals. *Journal of Applied Botany*, 76: 203–217.
- Gleyzes, C., Tellier, S., Astruc, M. (2002). Fractionation studies of trace elements in contaminated soils and sediments: a review. *Trends Analytical Chemistry*, 21: 451–467.
- Gao, X., Jang, J., Nagase, S. (2009). Hydrazine and thermal reduction of graphene oxide: reaction mechanisms, product structures, and reaction design. *Journal of Physical Chemistry C*, 114(2): 832–42.
- Goia, D.V. (2004). Preparation and Formation Mechanisms of Uniform Metallic Particles in Solutions. *Journal of Materials Chemistry*, 14 (4): 451–458.
- Goldstein, J. I., Newbury, D.E., Echlin, P. (1992). *Scanning Electron Microscopy and X-ray Microanalysis*, 2nd Ed. Plenum Press, New York and London.
- Goldstein, J. (2003). *Scanning Electron Microscopy and X-Ray Microanalysis*. Springer, New York, USA.
- Gong, J.M., Zhou, T., Song, D.D., Zhang, L.Z (2010). Monodispersed Au nanoparticles decorated graphene as an enhanced sensing platform for ultrasensitive stripping voltammetric detection of mercury(II). *Sensors & Actuators B*, 150(2): 491–497.
- González, J.G., Renedo, M., Lomillo, O.D., Martínez, J.A. (2004). Determination of gallium by adsorptive stripping voltammetry. *Talanta*, 62: 457–462.
- Gooding, J.J. (2005). Nanostructuring electrodes with carbon nanotubes: A review on electrochemistry and applications for sensing. *Electrochimica Acta*, 50(15): 3049–3060.
- Gosser Jr., D. K. (1993). *Cyclic Voltammetry/Simulation and Analysis of Reaction Mechanisms*, Wiley-VCH, New York, NY, USA.
- Goh, M.S., and M. Pumera. (2010). Single-, Few-, and Multilayer Graphene Not Exhibiting Significant Advantages over Graphite Microparticles in electroanalysis *Analytica.Chemistry*, 82(19): 8367–8370
- Gonullu, Y., Kelm, K., Mathur, S., Saruhan, B. (2014). Equivalent Circuit Models for Determination of the Relation between the Sensing Behavior and Properties of Undoped/Cr Doped TiO₂ NTs. *Chemosensors*, 2: 69-84.
- Gothberg, A., Greger, M., Holm, K., Bengtsson, B. (2004). Influence of nutrients on uptake and effects of Hg, Cd and Pb in *Ipo-moeaaquatica*. *Journal of Environmental Quality* 33: 1247–1255.

Grasselli, J.G. (1992). Analytical chemistry--feeding the environmental revolution? *Analytical Chemistry*, 64(13): 677A–685A.

Grieshaber, D., MacKenzie, R., Voros, J., Reimhult, E. (2008). Electrochemical Biosensors - Sensor Principles and Architectures. *Sensors*, 8: 1400–1458.

Guo, X., Small, J.P., Klare, J.E., Wang, Y., Purewal, M.S., Tam, I.W., Hong, B.H., Caldwell, R., Huang, L., O'Brien, S., Yan, J., Breslow, R., Wind, S.J., Hone, J., Kim, P., Nuckolls, C. (2006). Covalently Bridging Gaps in Single-Walled Carbon Nanotubes with Conducting Molecules. *Science*, 311: 356–359.

Guo, Y., Sun, X., Liu, Y., Wang, W., Qiu, H., Gao, J. (2012). One pot preparation of reduced graphene oxide (RGO) or Au (Ag) nanoparticle-RGO hybrids using chitosan as a reducing and stabilizing agent and their use in methanol electro-oxidation. *Carbon*, 50: 2513–2523.

Guo, Y.L., Zhao, X., Lanz, C., Weigel, D. (2011). Evolution of the S-locus region in Arabidopsis thaliana relatives. *Plant Physiology*, 157: 937–946.

Gupta, S.R.N (2014) Advances in Molecular Nanotechnology from Premodern to Modern Era. *International Journal of Materials Science and Engineering*, 2(2): 99–106.

Hadjipaschalis, I., Poullikkas, A., Efthimiou, A. (2009). Overview of current and future energy storage technologies for electric power applications. *Renewable and Sustainable Energy Reviews*, 13: 1513–1522.

Halvorson, R. A.; Vikesland, P. J. (2010). Surface-Enhanced Raman Spectroscopy (SERS) for Environmental Analyses. *Environmental Science & Technology*, 44 (20): 7749–7755.

Han, F.X., Banin, A., Su, Y., Monts, D.L., Plodinec, M.J., Kingery, W.L., Triplett G.E. (2002). Industrial age anthropogenic inputs of heavy metals into the pedosphere. *Science of Nature*, 89: 497–504.

Hanrahan, G.; Patil, D.G. & Wang, J. (2004). Electrochemical sensors for environmental monitoring: design, development and applications. *Journal Environmental Monitoring*, 6(8): 657–664.

Harris, P.J.F. (2005). New perspectives on the structures on the structure of graphitic carbons. *Critical Reviews Solid State Material Science*, 30: 235–253.

Harvey, D. (2013). Electrochemical cell for voltammetry. Images and video exchange forum. Accessed 20 January 2016.

Hassel, T. (2014). *Metal–Polymer Nanocomposites by Supercritical Fluid Processing*. In: L. Nicolais and G. Carotenuto (eds) *Nanocomposites: In Situ Synthesis of Polymer-Embedded Nanostructure*. John 1st Ed. Wiley & Sons, Inc., New York, USA.

Haward, S. (2007). "Atomic force microscope", Wills Physics laboratory, University of Bristol, Bristol, UK: <http://spm.phy.bris.ac.uk/techniques/AFM/>. Accessed on 24 August 2013.

Hayden, B.E., Pletcher, D., Suchsland, J.P. (2007). Enhanced activity for electrocatalytic oxidation of carbon monoxide on titania-supported gold nanoparticles. *Angewandte Chemie International Edition*, 46(19): 3530-3532.

Hedberg, Y., Gustafsson, J., Karlsson, H.L., Möller, L., Wallinder, I. (2010). Bioaccessibility, bioavailability and toxicity of commercially relevant iron and chromium based particles: in vitro studies with an inhalation perspective. *Particle and Fibre Toxicology*, 7(23): 1–14.

Heilmann, A. (2003). *Polymer Films with Embedded Metal Nanoparticles*, Springer, Berlin Heidelberg, New York, USA.

Hibino, H., Tanabe S., Mizuno, S., Kageshima, K. (2012). Growth and electronic transport properties of epitaxial graphene on SiC. *Journal of physics D: Applied physics*, 45: 154008.

Hill, E.W., Geim, A.K., Novoselov, K., Schedin, F., Blake, P. (2007). Graphene Spin Valve Devices. *IEEE Transactionson Magnetics*, 42: 2694–2696.

Hirata, M., Gotou, T., Horiuchi, S., Fujiwara, M., Ohba, M. (2004). Thin-filmparticles of graphite oxide 1: high-yield synthesis andflexibility of the particles. *Carbon*, 42(14): 2929–2937.

Hirner, A. (2006). Speciation of alkylated metals and metalloids in the environment. *Analytical and Bioanalytical Chemistry*, 385:555–567.

Hocevar ,S.B.,Švancara, I ., Ogorevc ,B., and Vytřas, K. (2007). Antimony Film Electrode for Electrochemical Stripping Analysis. *Analytical Chemistry*, 79(22): 8639–8643.

Hong, J., Zhao, Y-X., Xiao, B-L., Moosavi-Movahedi, A.A., Ghourchian , H., Sheibani, N. (2013). Direct Electrochemistry of Hemoglobin Immobilized on a Functionalized Multi-Walled Carbon Nanotubes and Gold Nanoparticles Nanocomplex-Modified Glassy Carbon Electrode. *Sensors*, 13: 8595–8611.

Hostetler, M.J., Templeton, A.C., Murray, R.W. (1999). Dynamics of place-exchange reactions on monolayer-protected gold cluster molecules. *Langmuir*, 15: 3782– 3789.

<http://compton.chem.ox.ac.uk/index.php?title=research&topic=fund>, Accessed on 15. August 2014.

<http://mrsec.wisc.edu/Edetc/index.html>, Accessed on 1. July 2014.

<http://mrsec.wisc.edu/Edetc/nanolab/silver/index.html>, Accessed on 1. July 2014.

http://www.doitpoms.ac.uk/tlplib/raman/raman_scattering.php, Accessed on 28. January 2015.

<http://www.files.chem.vt.edu/chem-ed/spec/uv-vis/array-spectrometer.html>, Accessed on 9. March 2013.

<http://www.nlectc.org/assistance/sem.html>, Accessed on 17. July 2014.

<https://spie.org/Documents/ConferencesExhibitions/PW2009-Final-Ir.pdf>, Accessed on 7. May 2015

Hu, Q. H., Wang, X., Chen, T. H., Wang Z., (2012). Synthesis of Ni/graphene sheets by an electroless Ni-plating method. *New Carbon Material*, 27(1): S35-41.

Huang, K.J., Niu, D.J., Liu, X., Wu, Z.W., Fan, Y., Chang, Y.F., Wu, Y.Y. (2011). Direct electrochemistry of catalase at amine-functionalized graphene/gold nanoparticles composite film for hydrogen peroxide sensor. *Electrochimica Acta*, 56(7): 2947–2953.

Huang, B., Li, Z.Y., Liu, Z.R., Zhou, G., Hao, S.G., Wu, J., Gu, B.L., Duan. W.H. (2008). Adsorption of gas molecules on graphene nanoribbons and its implication for nanoscale molecule sensor. *Journal of Physical Chemistry C*, 112(35): 13442–13446.

Huang, Y.F., Kuan, W.H., Lo, S.L., Lin, C.F. (2008). Total recovery of resources and energy from rice straw using microwave-induced pyrolysis. *Bioresource Technology*, 99: 8252–8258.

Huszal, S., Kowalska, J, Krzeminska, M., Golimowski, J.(2005). Determination of platinum with thiosemicarbazide by catalytic adsorptive stripping voltammetry. *Electroanalysis*, 17: 299–304.

Hutter, E.; Fendler, J. H.(2004). Exploitation of localized surface plasmon resonance, *Advanced Materials*, 16: 1685–1706.

Hwang, E.W., Adam, S., Das Sarma, S. (2007). Carrier transport in two-dimensional graphene layers, *Physical Reviews Letters*, 98, 186806.

Iijima, S. (1991). Helical microtubules of graphitic carbon. *Nature*, 354: 56–58.

Iijima, S.; Ichihashi, T. (1993). Single-Shell Carbon Nanotubes of 1-nm Diameter. *Nature*, 363: 603–605.

Isikli, S and Díaz, R. (2012). Substrate-dependent performance of supercapacitors based on an organic redox couple impregnated on carbon. *Journal of Power Sources*, 206: 53–58.

Ispas, C.R., Crivat, G., Andreessen, S. (2012). Review: Recent developments in enzyme based biosensors for biomedical analysis. *Analytical Letters*, 45(2-3): 168-186.

Iwashita, N., Park, C.R., Fujimoto, H., Shiraiishi, M., Inagaki, M. (2004). Specification for a standard procedure of X-ray diffraction measurements on carbon materials. *Carbon*, 42: 701–714.

- Janata, J. (2001). Peer Reviewed: Centennial Retrospective on Chemical Sensors: In the past 20 years, chemical sensors have become an accepted part of analytical chemistry. *Analytical Chemistry*, 73(5): 150 A–153 A.
- Janata, J., Josowick, M., Devaney, M. (1994). *Chemical sensors*. Analytical Chemistry, 66: 207R.
- Jenkins, S., Ayers, P., Kirk, S., Mori-S´anchez, P., Mart´ınPend´as, A. (2009). Bond metallicity of materials from real space charge density distributions. *Chemical Physics Letters*, 471(1–3): 174–177.
- Jeong, H-K, Lee, Y.P., Jin, M.H., Kim, E.S., Bae, J.J., Lee, Y.H. (2009). Thermal stability of graphite oxide. *Chemical Physics Letters*, 470(4– 6): 255–8.
- Jia, J., Cao, L., Wang, Z. (2007). Nafion/Poly(sodium 4-styrenesulfonate) mixed coating modified bismuth film electrode for the determination of trace metals by anodic stripping voltammetry. *Electroanalysis*, 19: 1845–1849.
- Jiang, Y.Y., Lu, Y.Z., Li, F.H., Wu, T.S., Niu, L., Chen, W. (2012). Facile electrochemical codeposition of “clean” graphene-Pd nanocomposite as an anode catalyst for formicacidelectrooxidation. *Electrochemistry Communications*, 19: 21–4.
- Kabata-Pendias, A. (2011). *Trace Elements in Soils and Plants*, 4th Ed. Taylor and Francis Group, CRC Press, New York, USA.
- Kabata-Pendias, A., Pendias, H. (1992). *Trace Elements in Soils and Plants*. 2nd Ed., CRC Press, Boca Raton, Florida, USA
- Kadish, K.M. Koh, P W., Tagliatesta, P., Sazou, D., Paolesse, R., Licocchia, S., Boschi, T. (1992). Electrochemistry of rhodium and cobalt corroles: Characterization of (OMC)Rh(PPh₃) and (OMC)Co(PPh₃) where OMC is the trianion of 2,3,7,8,12,13,17,18-octamethylcorrole. *Journal of Inorganic Chemistry*, 31(12): 2305–2313.
- Kampa, M and Castanas, E. (2008). Human health effects of air pollution. *Environmental Pollution*, 151(2): 362–367.
- Kaniyoor, A., Jafri, R. I., Arockiadoss, T., Ramaprabhu, S. (2009). Nanostructured Pt decorated graphene and multi walled carbon nanotube based room temperature hydrogen gas sensor. *Nanoscale*, 1(3): 382–386.
- Kaniyoor, A., Ramaprabhu, S. (2011). A Hybrid carbon nanostructured ensembles as chemiresistive hydrogen gas sensors. *Carbon*, 49(1): 227–236.
- Keeley, G.P., O’Neill, A., Holzinger, M., Cosnier, S., Coleman, J.N., Duesberg, G.S. (2011). DMF exfoliated graphene for electrochemical NADH detection. *Physical Chemistry Chemical Physics*, 13(17): 7747–7750.

- Kelly, J.F., Cotterell, M.G. (2002). Minimal Lubrication Machining of Aluminum Alloys. *Journal of Materials Processing Technology*, 120(1–3): 327–334.
- Kendall, K. and Kosseva, M.R. (2005). Adhesion of nanoparticles fouling glass surfaces. *Journal of Adhesion*, 81: 1017–1030.
- Kim, J., Cote, L.J., Huang, J. (2012). Two dimensional soft material: new faces of graphene oxide. *Account of Chemical Research*, 45(8): 1356–1364.
- Kim, K.S., Zhao, Y., Jang, H., Lee, S.Y., Kim, J.M., Kim, K.S., Ahn, J-H., Kim, P., Choi, J-Y., Hong, B.H. (2009). Large-scale pattern growth of graphene films for stretchable transparent electrodes. *Nature*, 457: 706–710.
- Kim, H.J., Park, H.S., Hyun, M.S., Chang, I.S., Kim, M., Kim, B.H. (2002). A mediator-less microbial fuel cell using a metal reducing bacterium: *Shewanella putrefaciens*. *Enzyme Microbial Technology*. 30 (2): 145–152.
- Kissinger, P.T and Heineman, W.R. (1996). *Laboratory techniques in electroanalytical chemistry*. Marcel Dekker, Inc; New York, USA.
- Kinoshita, K. (1996). Carbon: Electrochemical and Physicochemical Properties; Wiley: New ... ed.; Kissinger, P. T., Heineman, W. R., Eds.; Dekker: New York, USA.
- Kissinger, P. and Ridgway, T. (1996). "Small-amplitude controlled-potential techniques," in *Laboratory Techniques in Electroanalytical Chemistry*, Marcel Dekker, New York, USA.
- Kirkland, A.I. and Hutchison, J.L. (2006). Atomic resolution transmission electron microscopy. In *Science of Microscopy* (P. W. Hawkes and J. C. H. Spence, eds). Springer, New York, USA.
- Kleijn, S.E.F., Lai, S.C.S., Koper, M.T.M., Unwin, P.R. (2014). Electrochemistry of Nanoparticles. *Angewandte Chemie International Edition*, 53: 3558 – 3586.
- Kochmann, S., Hirsch, T., Wolfbeis, O. (2012). The pH Dependence of the Total Fluorescence of Graphite Oxide. *Journal of Fluorescence*, 22(3): 849–855.
- Kong, J., Franklin, N.R., Zhou, C., Chapline, M.G., Peng, S., Cho, K., Dai, H. (2000). Nanotube molecular wires as chemical sensors. *Science*, 287(5453): 622–625.
- Koptsik, S., Koptsik, G., Livantsova, S., Eruslankina, L., Zhmelkova, T., Vologdina, Z. (2003). Heavy metals in soils near the nickel smelter: chemistry, spatial variation, and impacts on plant diversity. *Journal of Environmental Monitoring*, 5: 441–450.
- Korotcenkov, G. (2008). The role of morphology and crystallographic structure of metal oxides in response of Conductometric type gas sensors. *Material Science and Engineering*, R61: 1–39.

Kostoff, R. N.; Koytcheff, R. G.; Lau, C. G. Y. (2008). Structure of the nanoscience and nanotechnology applications literature. *The Journal of Technology Transfer*, (33): 472–484.

Kovtyukhova, N.I. Ollivier, P.J.B., Martin, R., Mallouk, T.E., Chizhik, S.A., Buzaneva, E.V., Gorchinskiy, A.D. (1999). Layer-by-Layer Assembly of Ultrathin Composite Films from Micron-Sized Graphite Oxide Sheets and Polycations. *Chemistry Materials*, 11(3): 771–778.

Kreibig, U.; Vollmer, M. (1995). Optical Properties of Metal Clusters, *Springer Series in Material Science*, 25: 26-76, Springer-Verlag: Berlin, Germany.

Kuila, T. Bose, S., Mishra, A. K., Khanra, P. Kim, N. H Lee J.H. (2012). Chemical functionalization of graphene and its applications. *Progress in Material Science*, 57(7): 1061–105.

Kumar, R., Varandani, D., Mehta, B.R., Singh, V.N., Wen, Z.H., Feng, X.L., Mullen, K. (2011). Fast response and recovery of hydrogen sensing in Pd-Pt nanoparticle-graphene composite layers. *Nanotechnology*, 22(27): 275719.

Landman, U., Luedtke, W.D., Ringer, E.M. (1992). Atomistic mechanisms of adhesive contact formation and interfacial processes. *Wear*, 153(1): 3–30.

Lange, U., Hirsch, T., Mirsky, V.M., Wolfbeis, O.S. (2011). Hydrogen sensor based on a graphene-palladium nanocomposite. *Electrochimica Acta*, 56(10): 3707–3712.

Laschi, S., Franek, M., Mascini, M. (2000). Screen-printed electrochemical Immunosensors for PCB Detection. *Electroanalysis* 12(16): 1293–1298.

Leary, R., and Westwood, A. (2011). Carbonaceous nanomaterials for the enhancement of TiO₂ photocatalysis. *Carbon*, 49(3): 741–772.

Lee, M., Wei, X., Kysar, J.W., Hone, J. (2008). Measurement of the Elastic Properties and Intrinsic Strength of Monolayer Graphene. *Science*, 321(5887): 385–388.

Lewen, N., Methew, S., Schenkenberger, M., Raglione, T. (2004). A rapid ICP-MS screen for heavy metals in pharmaceutical compounds. *Journal of pharmaceutical and biomedical analysis*, 35(4): 739–752.

Li, L., Xu, Z., Wu, J. and Tian, G. (2010). Bioaccumulation of heavy metals in the earthworm *Eisenia fetida* in relation to bioavailable metal concentrations in pig manure. *Bioresource Technology*, 101: 3430–3436.

Li, M., Li, Y.T., Li, D.W., Long, Y.T. (2012). Recent developments and applications of screen-printed electrodes in environmental assays--a review. *Analytica Chimica Acta*, 734: 31–44.

Liana, P., Zhub, X., Lianga, S., Li, Z., Yang, W., Wang, H. (2010). Large reversible capacity of high quality graphene sheets as an anode material for lithium-ion batteries. *Electrochimica Acta*, 55: 3909–3914.

- Liang, X., Fu, Z., Chou, S.Y. (2007). Graphene Transistors Fabricated via Transfer-Printing In Device Active-Areas on Large Wafer. *Nano Letters*, 7(12): 3840–3844.
- Lim, H. S., Lee, J. S., Chon, H. T., and Sager, M. (2008). Heavy metal contamination and health risk assessment in the vicinity of the abandoned Songcheon Au–Ag mine in Korea. *Journal of Geochemical Exploration*, 96: 223–230.
- Lira, M., Santos, L., Azeredo, J., Yebra-Pimentel, E. and Oliveira, M. E. (2008). Comparative study of silicone-hydrogel contact lenses surfaces before and after wear using atomic force microscopy. *Journal of Biomedical Materials Research Part B: Applied Biomaterials*, 85: 361–367.
- Liu, S.Y., Xie, J., Pan, Q., Wu, C.Y., Cao, G.S., Zhu, T.J., Zhao, X.B. (2012) A wetchemical route for the decoration of CNTs with silver nanoparticles. *International Journal of Electrochemical Science*, 7: 354–362.
- Liz-Marzan, L.M. and Lado-Tourino, I. (1996). Reduction and Stabilization of Silver Nanoparticles in Ethanol by Nonionic Surfactants. *Langmuir*, 12: 3585–3589.
- Locatelli, C. (2006). Simultaneous square wave stripping voltammetric determination of platinum group metals (PGMs) and lead at trace and ultra-trace concentration level, application to surface water. *Analytica Chimica Acta*, 557: 70–77.
- Loryuenyong, V., Totepvimarn, K., Eimburanaprat, P., Boonchompoo, W., Achanai Buasri, A. (2013). Preparation and Characterization of Reduced Graphene Oxide Sheets via Water-Based Exfoliation and Reduction Methods. *Advances in Materials Science and Engineering*, ID 923403.
- Lost, R.M., Madurro, J.M., Brito-Madurro, A.G., Nantes, I.L., Caseli, L., Crespilho, F.N. (2011). Strategies of Nano-Manipulation for Application in Electrochemical Biosensors, *International Journal of Electrochemical Science*, 6: 2965–2997.
- Loux, N.T. and Savage, N. (2008). An assessment of the fate of metal oxide nanomaterials in porous media, water, air, and soil pollution. *Springer*, New York, NY, 194(1-4): 227–241.
- Lu, J.S. (2007). Effect of surface modifications on the decoration of multi-walled carbon nanotubes with ruthenium nanoparticles. *Carbon*, 45: 1599–1605.
- Luo, X.L., Morrin, A., Killard, A.J., Smyth, M.R. (2006). Application of nanoparticles in electrochemical sensors and biosensors. *Electroanalysis*, 18(4): 319–326.
- Ma, L.Q., Dong, Y. (2004). Effects of incubation on solubility and mobility of trace metals in two contaminated soils. *Environmental Pollution*, 130: 301–307.
- Macdonald, J.R. (2005). *Impedance Spectroscopy Theory, Experiment, and Applications*. 2nd Ed., John Wiley & Sons, Hoboken, New Jersey, USA.

- Mackay D, Fraser A. (2000). Bioaccumulation of persistent organic chemicals: mechanisms and models. *Environmental Pollution*, 110: 375–91.
- Manias E., (2001). Origins of the Materials Properties Enhancements in Polymer/Clay Nanocomposites. <http://zeus.plmsc.psu.edu/nano.html>, accessed on 12 July 2014.
- Marcano, D.C., Kosynkin, D.V., Berlin, J.M., Sinitskii, A., Sun, Z., Slesarev, A., Alemany, L.B., Lu, W., Tour. J.M. (2010). Improved Synthesis of Graphene Oxide. *ACS Nano*, 4(8): 4806–4814.
- Mardegan, A., Scopece, P., Lamberti, F., Meneghetti, M., Moretto, L.M., Ugo, P. (2013). Simultaneous Adsorptive Cathodic Stripping Voltammetric Determination of Nickel(II) and Cobalt(II) at an In Situ Bismuth-Modified Gold Electrode. *Electroanalysis*, 24(11): 2471–2479.
- Mardegan, A., Scopece, P., Lamberti, F., Meneghetti, M., Moretto, L.M., Ugo, P. (2012). Electroanalysis of Trace Inorganic Arsenic with Gold Nanoelectrode Ensembles. *Electroanalysis*, 24(4): 798–806.
- Mares, M.L., Golgovici, F., Visan, T. (2013). RDE voltammetry and impedance spectroscopy studies of Sb, Te and SbTe electrodeposition from choline chloride – urea ionic liquids. *Chalcogenide Letters*, 10(8): 259–272.
- Margui, E., Salvado, V., Queralt, I., Hidalgo, M. (2004). Comparison of three- stage sequential extraction Toxicity characteristic leaching tests to evaluate metal mobility in mining wastes. *Analytica Chimica Acta*, 524: 151–159.
- Martin-Gonzalez, M., Prieto, A., Gronsky, R., Sands, T., Stacy, A. (2003). High-Density 40 nm Diameter Sb-Rich Bi₂-xSbxTe₃ Nanowire Arrays. *Advanced materials*, 15(12): 1003-100.
- Masala, O., Seshadri, R. (2004). Synthesis routes for large volumes of nanoparticles, *Annual Review of Materials Research*, 34: 41–81.
- Mauter, M.S and Elimelech, M. (2008). Environmental Applications of Carbon-Based Nanomaterials. *Environmental Science and Technology*, 42(16): 5843–5859.
- McCreery, R. L. (2000). *Raman Spectroscopy for Chemical Analysis*. 4th Ed., John Wiley & Sons, Inc. New York, USA.
- McCreery, R.L. (2008). Advanced Carbon Electrode Materials for Molecular Electrochemistry. *Chemical Reviews*, 108: 2646–2687.
- McKenna, J.M., Chaney, R.L., Williams, F.M. (1993). The effect of cadmium and zinc interactions on the accumulation and tissue distribution of zinc and cadmium in lettuce and spinach. *Environmental Pollution*, 79: 113–120.

McLean, J.E., Bledsoe, B.E. (1992). Behaviour of metals in soils. USEPA Ground Water, Issue, EPA/540/S-92/018.

Mehrotra, R.C. (1992). *Chemistry, Spectroscopy and Application of Sol-Gel Glasses*, Springer-Verlag, Berlin, Heidelberg, Germany.

Mehta, A. (2012). Ultraviolet- visible (UV-Vis) spectroscopy derivation of Beer Lambert law. Analytical Chemistry. <http://pharmaxchange.info/press/2012/05/ultraviolet-visible-uv-vis-spectroscopy-limitations-and-deviations-of-beer-lambert-law>, accessed on 13 May 2012.

Metters, J.P., Kadara, R.O., Banks, C.E. (2011). New directions in screen printed electroanalytical sensors: an overview of recent developments. *The Analyst*, 136(6): 1067–76.

Meyer, J.C., Geim, A.K., Katsnelson, M.I., Novoselov, K.S., Booth, T.J., Roth, S. (2007). The structure of suspended graphene sheets. *Nature*, 446: 60–63.

Mishra, A.K., Ramaprabhu, S. (2011). Functionalized Graphene-Based Nanocomposites for Supercapacitor Application. *Journal of Physical Chemistry, C* 115: 14006–14013.

Mitchell, B.S. (2004). *An introduction to materials engineering and science: for chemical and materials engineers*. John Wiley & Sons, Inc. Hoboken, New Jersey, USA.

Mitchell, B.S. (2004). *An introduction to materials engineering and science: for chemical and materials engineers*. John Wiley & Sons, Inc. Hoboken, New Jersey, USA.

Mock, J.J., Smith, D.R., Schultz, S. (2003). Local Refractive Index Dependence of Plasmon Resonance Spectra from Individual Nanoparticles. *Nano Letters*, 3(4): 485–491.

Moldovan, M., Krupp, E.M., Holliday, A.E., Donard, O.F.X. (2004). High resolution sector field ICP-MS and multicollector ICP-MS as tools for trace metal speciation in environmental studies: a review. *Journal of Analytical Atomic Spectrometry*, 19: 815–822.

Montaser, A. (1998). *Inductively Coupled Plasma Mass Spectrometry*. Wiley VCH. New York, USA.

Monthieux, M.; Smith, B.W.; Burteaux, B.; Claye, A.; Fischer, J.E. & Luzzi, D.E. (2001). Sensitivity of single-wall carbon nanotubes to chemical processing: an electron microscopy investigation. *Carbon*, 39(8): 1251–1272.

Monticelli, D., Carugati, G., Castelletti, A., Recchia, S., Dossi, C. (2009). Design and development of a low cost, high performance UV digester prototype: Application to the determination of trace elements by stripping voltammetry. *Microchemical Journal*, (In press).

Morera, M.T., Echeverria, J.C., Mazkarian, C. and Garrido, J.J. (2001). Isotherms and sequential extraction procedures for evaluating sorption and distribution of heavy metals in soils. *Environmental Pollution*, 113: 135–144.

Morita, S., Giessib, F.J., Meyer, E. (2002). *Principle of NC-AFM, in Noncontact Atomic Force Microscopy*. Springer. Berlin, Heidelberg, Germany.

Moussa, S., Abdelsayed, V., Shall, M. S. (2011). Laser synthesis of Pt, Pd, CoO and Pd-CoO nanoparticle catalysts supported on graphene. *Chemical Physics Letters*, 510(4): 179–184.

Murali, R., Brenner, K., Yang, Y., Beck, T., Meindl, J.D. (2009). Resistivity of Graphene Nanoribbon Interconnects. *IEEE Electron Device Letters*, 30(6): 611–613.

Murray, R. (1992). *Molecular design of electrode surfaces*, John Wiley, New York, USA.

Murray, R.W., Ewing, A.G., Durst, R.A. (1987). Chemically modified electrodes: Molecular design for electroanalysis. *Analytical Chemistry*, 59: 379A–390A.

Nadaska, G., Polcova, K.J. Nova, L. (2009). Manganese fractionation analysis in specific Soil and Sediments Samples. *Biotechnolgy*, 9: 295–301.

Nair, R.R., Blake, P., Grigorenko, A.N., Novoselov, K.S., Booth, T.J., Stauber, T. Peres, N.M.R., Geim, A.K. (2008). Fine structure constant defines visual transparency of graphene. *Science*, 320(5881): 1308–1308.

Ndlovu, T., Arotiba, O.A., Krause, R.W., Mamba, B.B. (2010). Electrochemical detection of o-nitrophenol on a poly (propyleneimine) -gold nanocomposite modified glassy carbon electrode, *International Journal of Electrochemical Science*, 5: 1179–1186.

Nelms, S. (2005). *Inductively Coupled Plasma Mass Spectrometry Handbook*, Carlton, Victoria, Blackwell, Australia.

Nelms, S. (2005). *Inductively Coupled Plasma Mass Spectrometry Handbook*, Carlton, Victoria, Blackwell, Australia.

Neogi, A., Karna, S., Shah, R., Phillipose, U., Perez, J., Shimada, R., Wang, Z.M. (2014) Surface plasmon enhancement of broadband photoluminescence emission from graphene oxide. *Nanoscale*, 6(19): 11310–11315.

Neto, A.H.C., Guinea, F., Peres, N.M.R, Novoselov, K.S., Geim, A.K. (2009). The electronic properties of graphene. *Reviews of Modern Physics*, 81(1): 109–62.

Nguyen, N.H., Kulis, J., Sun, H-J., Jia, Z., van Beusekom, B., Levere, M.E., Wilson, D.A., Monteiro, M.J., Percec, V. (2013). A comparative study of the SET-LRP of oligo(ethylene oxide) methyl ether acrylate in DMSO and in H₂O. *Polymer Chemistry*, 4: 144–155.

Nguyen, P.K.Q. (2010). Cyclic voltammetric and square wave anodic stripping voltammetric analysis of lead and cadmium utilizing the novel titanium dioxide/ zirconium dioxide/ tween 80 carbon paste composite electrode. Published PhD Thesis, Wright State University, USA.

Nguyen, S.T., Ruoff, R.S. (2007). Synthesis of graphene-based nanosheets via chemical reduction of exfoliated graphite oxide. *Carbon*, 45(7): 1558–1565.

Nicolais, L. and Carotenuto, G. (2005). *Metal-Polymer Nanocomposites*, John Wiley & Sons, Inc. Hoboken, USA.

Noked, M., Soffer, A., Aurbach, D. (2011). The electrochemistry of activated carbonaceous materials: past, present, and future. *Journal of Solid State Electrochemistry*, 15(7-8): 1563–1578.

Nouri, J., Mahvi, A.H., Babaei, A., Ahmadpour, E. (2006). Regional pattern distribution of groundwater fluoride in the Shush aquifer of Khuzestan County Iran. *Fluoride*, 39(4): 321–325.

Novoselov, K.S., Geim, A.K., Morozov, S.V., Jiang, D., Zhang, Y., Dubonos, S.V., Grigorieva, I.V., Firsov, A.A. (2004). Electric field effect in atomically thin carbon films. *Science*, 306 (5696): 666–669.

Ntsendwana, B. Mamba, B.B, Sampath, S, Arotiba, O.A. (2012). Electrochemical Detection of Bisphenol A Using Graphene-Modified Glassy Carbon Electrode. *International Journal of Electrochemical Science*, 7: 3501–3512.

Obata, H., Yoshida, T., Ogawa, H. (2006). Determination of picomolar levels of platinum in estuarine waters: A comparison of cathodic stripping voltammetry and isotope dilution-inductively coupled plasma mass spectrometry. *Analytica Chimica Acta*, 580: 32–38.

Ohring, M. (1992). *The Materials Science of Thin Films*. 2nd Ed., Academic Press, San Diego, USA.

Oja, S.M., Wood, M., Zhang, B. (2012). Nanoscale Electrochemistry. *Analytical Chemistry*, 85, 473–486.

Okoro, H.K., Fatoki, O.S., Adekola, F.A., Ximba, B.J., Snyman, R.G. (2012). A Review of Sequential Extraction Procedures for Heavy Metals Speciation in Soil and Sediments. *Open Access Scientific Reports*, 1(3): 181–189.

Okuyama K, Lenggoro W, Iwaki T. (2004). MEMS, NANO and Smart Systems ICMENS 2004. Proceedings. 2004 International Conference on, 25-27 Aug 2004, pp 369–372.

Ozel, R.E., Hayat, A., Andreessen, S. (2015). Recent Developments in Electrochemical Sensors for the Detection of Neurotransmitters for Applications in Biomedicine. *Analytical Letters*, 48: 1044–1069.

Pandey, D., Reifengerger, R., Piner, R. (2008). Scanning probe microscopy study of exfoliated oxidized graphene sheets. *Surface Science*, 602(9): 1607–13.

Paredes, J.I., Villar-Rodil, S., Martinez-Alonso, A., Tascón, J.M.D. (2008). Graphene oxide dispersions in organic solvents. *Langmuir*, 24: 10560–10564.

Park S, Ruoff RS. (2009). Chemical methods for the production of graphenes. *Nature Nanotechnology*, 4: 217–224

Pei, S.F., Cheng, H.M. (2012). The reduction of graphene oxide. *Carbon*, 50: 3210–3228.

Perry, M., Li, Q., Kennedy, R.T. (2009). Review of recent advances in analytical techniques for the determination of neurotransmitters. *Analytical chemica Acta*, 653(1): 1-22.

Peralta-Videa., J.R., Lopeza, M.L., Narayana, M., Saupea, G., Gardea-Torresdeya, J. (2009). The biochemistry of environmental heavy metal uptake by plants: Implications for the food chain *The International Journal of Biochemistry & Cell Biology*, 41: 1665–1677

Pimenta, M.A., Dresselhaus, G., Dresselhaus, M.S., Cancado, L.G., Jorio, A., Saito, R. (2007). Studying disorder in graphite-based systems by Raman spectroscopy. *Physical Chemistry Chemical Physics*, 9 (11): 1276–1290.

Poole, C.P., & Owens, F.J. (2003). *Introduction to Nanotechnology*. Wiley Interscience: New Jersey, USA.

Pognon, G., Brousse, T., Demarconnay, L., Bélanger, D. (2011). Performance and stability of modified activated carbon. *Journal of Power Sources*, 196: 4117–4122.

Pradhan, N., Pal, A., Pal, T. (2002). Colloids and Surfaces A: *Physicochemical and Engineering Aspects*, 196(2–3): 247–257.

Prasad, P.N. (2004). *Nanophotonics*, Wiley, Hoboken, New Jersey, USA.

Prichard, E. Mackay, G.M. Points, J. (1996). *Trace Analysis: A Structured Approach to Obtaining Reliable Results*. Royal Society of Electrochemistry, Cambridge, UK.

Pujol L, Evrard D, Groenen-Serrano K, Freyssinier M, Ruffien-Cizsak A and Gros, P. (2014). Electrochemical sensors and devices for heavy metals assay in water: the French groups' contribution. *Frontiers in Chemistry*, 2(19) 1–24.

Pumera, M. (2009). The electrochemistry of carbon nanotubes: Fundamentals and applications. *Chemistry- A European Journal*, 15(20): 4970–4978.

Qi, D and Berger, A.J. (2006). Correction method for absorption-dependent signal enhancement by a liquid core optical fiber. *Applied Optics*, 45: 489–494.

Qureshi, A., Kang, W.P., Davidson, J.L., Gurbuz, Y. (2009). Review on carbon-derived, solid-state, micro and nano sensors for electrochemical sensing applications. *Diamond and Related Materials*, 18(12): 1401–1420.

Raj, C.R., Okajima, T., Ohsaka, T. (2003). Gold nanoparticle arrays for the voltammetric sensing of dopamine. *Journal of Electroanalytical Chemistry*, 543: 127–133.

- Rajeshwar, K., Ibanez, J.G., Swain, G.M. (1994). Electrochemistry and environment. *Journal of Applied Electrochemistry*, 24: 1077–1091.
- Randviir, E. P. and Banks, C. E. (2013). Electrochemical Impedance Spectroscopy: An Overview of Bioanalytical Applications. *Analytical Methods*, 5: 1098–1115.
- Rao, C.N.R., Sood, A.K., Subrahmanyam, K.S., Govindaraj, A. (2009). Graphene: the new two-dimensional nanomaterial. *Angewandte Chemie International Edition*, 48(42): 7752–7777.
- Rao, V., Simonov, P.A., Savinova, E.R., Plaksin, G.V., Cherepanova, S.V., Kryukova, G.N., Stimming, U. (2005). The influence of carbon support porosity on the activity of PtRu/Sibunit anode catalysts for methanol oxidation. *Journal of Power Sources*, 145(2): 178–187.
- Ratinac, K.R., Yang, W.R., Gooding, J.J., Thordarson, P., Braet, F. (2011). Graphene and related materials in electrochemical sensing. *Small*, 7: 1876–1902.
- Raut, H.K., Ganesh, V.A., Nair A.S., Ramakrishna, S. (2011). Anti-reflective coatings: A critical, in-depth review. *Energy & Environmental Science*, 4(10): 3779–3804.
- Ray, S. J., Andrade, F., Gamez, G., McClenathan, D., Rogers, D., Schilling, G., Wetzel, W. and Hieftje, G.M. (2004). Plasma-source mass spectrometry for speciation analysis: state-of-the-art. *Journal of Chromatography A*, 1050:3–34.
- Reimer, L. (1993). *Transmission electron microscopy: Physics of image formation and microanalysis*, 3rd Ed., Springer-Verlag, New York, USA.
- Robinson, J. T., Perkins, F. K., Snow, E. S., Wei, Z., Sheehan, P. E. (2008). Reduced graphene oxide molecular sensors. *NanoLetters*, 8(10): 3137–3140.
- Roco, M.C. Williams, S., Alivisatos P. (1990). *Nanotechnology Research Directions: IWGN Workshop Report - Vision for Nanotechnology R&D in the Next Decade*. WTEC, Loyola College in Maryland, Washington, USA.
- Rodrigues V., Bettini J., Silva, P.C, Ugarte, D. (2003). Evidence for spontaneous spin-polarized transport in magnetic nanowires. *Physical Review Letters*, 91: 96801.
- Rodriguez-Mozaz, S., Lopez de Alda ,M.J., Barceló, D. (2006). Biosensors as useful tools for environmental analysis and monitoring, *Analytical and Bioanalytical Chemistry*, 386: 1025–1041.
- Roduner, E. (2006). Size matters: Why nanomaterials are different. *Chemical Society Reviews*, 35: 583–592.
- Ronald L. Birke , Myung-Hoon Kim , Moses Strassfeld, (1981). Diagnosis of reversible, quasi-reversible, and irreversible electrode processes with differential pulse polarography. *Analytical Chemistry*, 53(6): 852–856.

Rosen, A.L. and Hieftje, G.M. (2004). Inductively coupled plasma mass spectrometry and electrospray mass spectrometry for speciation analysis: Applications and instrumentation. *Spectrochimica Acta Part B*, 59: 135–146.

Royal Society (2004). *Nanoscience and nanotechnologies: Opportunities and uncertainties*. The Royal Society and the Royal Academy of Engineering, London.

Royal Society (2006). *Response to Defra consultation on a Voluntary Reporting Scheme for nanomaterials*. The Royal Society and the Royal Academy of Engineering, London.

Roychowdhury, T. (2014). Investigation on the electrical and electrochemical properties of conducting polymer coated a CNT- bismuth ferrite nanocomposite. Published Master's Thesis, Jadavpur University Kolkata, India.

Ruus, A., Schaanning, M., Oxnevad, S., Hylland, K., (2005). Experimental results on bioaccumulation of metals and organic contaminants from marine sediments. *Aquatic Toxicology*, 72: 273–292.

Saito, R., Takeya, T., Kimura, T., Dresselhaus, G., Dresselhaus, M.S. (1998). Raman intensity of single-wall carbon nanotubes. *Physical Review B*, 57(7): 4145–4153.

Salimi, H. Mamkhezri, R., Hallaj, R. Soltanian, S. (2008). Electrochemical detection of trace amount of arsenic(III) at glassy carbon electrode modified with cobalt oxide nanoparticles. *Sensors and Actuators B: Chemical*, 129: 246–254.

Satti, A., Larpent, P., Gun'ko, Y. (2010). Improvement of mechanical properties of graphene oxide/ poly(allylamine) composites by chemical crosslinking. *Carbon*, 48(12): 3376–3381.

Schedin, F., Geim, A.K., Morozov, S.V., Hil, E.W., Blake, P., Katsnelson, M.I., Novoselov, K.S. (2007). Detection of individual gas molecules adsorbed on graphene. *Nature Materials*, 6(9): 652–655.

Schlenoff, J.B., Dubas, S.T. (2001). Mechanism of polyelectrolyte multilayer growth: Charge overcompensation and distribution. *Macromolecules*, 34(3): 592–598.

Schmid, G., Corain, B. (2003). Nanoparticulated Gold: Syntheses, Structures, Electronics, and Reactivities. *European Journal of Inorganic Chemistry*, 2003(17):3081–3098.

Scully, J.R., Silverman, D.C., Kendig, M.W. (1993). *Electrochemical Impedance: Analysis and Interpretation*, ASTM. Philadelphia, USA.

Shams, E., Abdollahi, H., Yekentaz, M., Hajian, R. (2004). H-point standard addition method in the analysis by differential pulse anodic stripping voltammetry: Simultaneous determination of lead and tin. *Talanta*, 63(2): 359–364.

Shan, C., Yang, H., Song, J., Han, D., Ivaska, A., Niu, L. (2009). Direct electrochemistry of glucose oxidase and biosensing for glucose based on graphene. *Analytical Chemistry*, 81: 2378–2382.

Shao, Y., Wang, J., Wu, H., Liu, J., Aksay, I.A., Lina, Y. (2010). Graphene Based Electrochemical Sensors and Biosensors: A Review *Electroanalysis*, 22 (10): 1027–1036.

Shao, Y., Wang, J., Wu, H., Liu, J., Aksay, I.A., Lina, Y. (2010). Graphene Based Electrochemical Sensors and Biosensors: A Review. *Electroanalysis*, 22 (10): 1027–1036.

Sharma, R.K., Agrawal, M., Marshall, F.M. (2004). Effects of waste water irrigation on heavy metal accumulation in soil and plants. Paper presented at a National Seminar. Bangalore University, India, Abstract 7, p. 8.

Sharma, S.K. (2012). *X-Ray Spectroscopy*, InTech Open Science, JanezaTrdine, Croatia.

Sharma, V., Anderson, D., Dhawan, A. (2012). Zinc oxide nanoparticles induce oxidative DNA damage and ROS-triggered mitochondria mediated apoptosis in human liver cells (HepG2). *Apoptosis*, 17: 852–870.

Shipway, A. N., Katz, E., Willner, I. (2000). Nanoparticle arrays on surfaces for electronic, optical and sensoric applications. *Chemphyschem*, 1: 18–52.

Silwana, B., van der Horst, C., Iwuoha, E., Somerset, V. (2014). Screen-printed carbon electrodes modified with a bismuth film for stripping voltammetric analysis of platinum group metals in environmental samples. *Electrochimica Acta*, 128: 119–127.

Sippel-Oakley, J., Wang, H.T., Kang, B.S., Wu, Z.; Ren, F., Rinzler, A.G., Pearton, S.J. (2005). Carbon nanotube films for room temperature hydrogen sensing. *Nanotechnology*, 16(10): 2218–2221.

Song, Y.S., Muthuraman, G, Chen, Y.Z, Lin, C.C., Zen, J.M. (2006). Screen-printed Carbon Electrode Modified with Poly(L-Lactide) Stabilized Gold Nanoparticles for Sensitive As(III) Detection. *Electroanalysis*, 18(18): 1763–1770.

Song, X., Zhang, W., and Yin, Z. (2004). A method for the synthesis of spherical copper nanoparticles in the organic phase. *Journal of Colloid and Interface Science*, 273: 463–469.

Skoog, A., Hall, P.O.J., Hulth, S., Paxeus, N., van der Loeff, M.R., Westerlund, S. (1996a). Early diagenetic production and sediment-water exchange of fluorescent dissolved organic matter in the coastal environment. *Geochimica et Cosmochimica Acta*, 60: 3421–3431.

Skoog, A., Wedborg, M., Fogelquist, E. (1996b). Photo bleaching of fluorescence and the organic carbon concentration in a coastal environment. *Marine Chemistry*, 55: 333–345.

Smith, S. R. (2009). A critical review of the bioavailability and impacts of heavy metals in municipal solid waste composts compared to sewage sludge. *Environment International*, 35: 142–156.

Somerset, V., Van der Horst, C., Silwana, B., Walters, C., Iwuoha, E. (2015). Biomonitoring and evaluation of metal concentrations in sediment and crab samples from the North-West Province of South Africa. *Water, Air, & Soil Pollution*. 226: 43.

Somerset, V. (2010). Development of an analytical sensor for the identification, quantitation and detection of heavy metal pollution with precious metal refinery wastewaters. *Research proposal to the WRC for funding*, NRE, CSIR. Pretoria, South Africa.

Somerset, V., Van der Horst, C., Silwana, B., Iwuoha, E. (2011). CSIR-NRE Internal Report, CSIR, Stellenbosch, Report No. CSIR/NRE/WR/IR/2011/0020/B.

Somerset, V., Iwuoha, E., Hernandez, L. (2009). Stripping Voltammetric Measurement of Trace Metal Ions at Screen-printed Carbon Paste Electrodes. *Procedia Chemistry*, 1: 1279–1282.

Somerset, V., Leaner, J., Mason, R., Iwuoha, E. and Morrin, A. (2010). Determination of inorganic mercury using a polyaniline and polyaniline-methylene blue coated screen-printed carbon electrode. *International Journal of Environmental Analytical Chemistry*, 90(9): 671–685.

Somerset, V., Leaner, J., Mason, R., Iwuoha, E., Morrin, A. (2009). Development and application of a poly(2,2'-dithiodianiline) (PDTDA)-coated screen-printed carbon electrode in inorganic mercury determination. *Electrochimica Acta*, 30: 31–37.

Somerset, V.S., Klink, M.J., Sekota, M.M.C., Baker, P.G.L. and Iwuoha, E.I. (2006). Polyaniline-Mercaptobenzothiazole Biosensor for Organophosphate and Carbamate Pesticides. *Analytical Letters*, 39: 1683–1698.

Stankovich, S., Dikin, D.A., Piner, R.D., Kohlhaas, K.A. Kleinhammes, A. Jia, Y. Wu, Y. Nguyen, S.T., Ruoff, R.S. (2007). Synthesis of graphene-based nanosheets via chemical reduction of exfoliated graphite oxide. *Carbon*, 45(7): 1558–1565.

Star, A., Han, T. R., Joshi, V., Gabriel, J. C. P., Gruner, G. (2004). Nanoelectronic carbon dioxide sensors. *Advanced Materials*, 16(22): 2049–2052.

Stohs, J.S., Bagchi, D., Hassoun, E., Bagchi, M. (2000). Oxidative Mechanisms in the Toxicity of Chromium and Cadmium Ions. *Journal of Environmental Pathology, Toxicology and Oncology*, 19: 201–213.

Stoller, M.D., Park, S., Zhu, Y., An, J., Ruoff, R.S. (2008). Graphene-based ultracapacitors. *Nano Letters*, 8(10): 3498–3502.

Stradiotto, N.R., Yamanaka, H., Zanoni, M.V.B. (2003). Electrochemical Sensors: A Powerful Tool in Analytical Chemistry. *Journal of Brazilian Chemical Society*, 14(2): 159–173.

Stuart, B. (1996). *Modern Infrared Spectroscopy*, John Wiley & Sons, New York and Chichester, UK.

Švancara, I., Galík, M., Vytrás, K. (2007). Stripping voltammetric determination of platinum metals at a carbon paste electrode modified cationic surfactants. *Talanta*, 72: 512–518)

Svancara, I., Vytras, K., Kalcher, K., Walcarius, A., Wang, J. (2009). Carbon paste electrodes in facts, numbers, and notes: A Review on the occasion of the 50-years jubilee of carbon paste in electrochemistry and electroanalysis. *Electroanalysis*, 21: 7–28.

Takahashi, T., Yu, Z., Chen, K., Kiriya, D., Wang, C., Takei, K., Shiraki, H., Chen, T., Ma, B., Javey, A. (2013). Carbon Nanotube Active-Matrix Backplanes for Mechanically Flexible, Visible Light and X-ray Imagers. *Nano Letters*, 13(11): 5425–5430.

Takahashi, S., Abiko, N., Anzai, J-I., Alwarappan, S., Erdem, A., Liu, C., Li, C-Z. (2009). Redox Response of Reduced Graphene Oxide-Modified Glassy Carbon Electrodes to Hydrogen Peroxide and Hydrazine. *Journal of Physical Chemistry C*, 113(20): 8853-8857.

Tang, Y., Allen, B.L., Kauffman, D.R., Star, A. (2009). Electrocatalytic activity of nitrogen-doped carbon nanotube cups. *Journal of American Chemical Society*, 131: 13200–13201.

Tapas K., Saswata, B., Partha, K., Ananta., K.M., Nam, H.K., Joong, H.L. (2012). Chemical functionalization of graphene and its applications. *Progress in Materials Science*, 57: 1061–1105.

Tasis, D., Tagmatarchis, N., Bianco, A., Prato, M. (2006). Chemistry of Carbon Nanotubes, *Chemistry Reviews*, 106: 1105–1136.

Terrones, H., Terrones, M., Charlier, J.-C (2004). Electron irradiation damage and sputtering from oxidized silicon particles supported on amorphous carbon., *Nano Letters*, 4: 805.

Tessonier, J.-P., Villa, A., Majoulet, O., Su, D. S., Schlög, R. (2009). Defect-Mediated Functionalization of Carbon Nanotubes as a Route to Design Single-Site Basic Heterogeneous Catalysts for Biomass Conversion. *Angewandte Chemie International Edition*, 48: 6543–6546.

Thiemann, M., Scheibler, E., Wiegand, K.W. (2000). *Nitric Acid, Nitrous Acid, and Nitrogen Oxides*, Wiley-VCH Verlag GmbH & Co. KGaA, Germany.

Thomas, J.M., Raja, R., Johnson, B.F.G., Hermans, S., Jones, M.D., Khimyak, T. (2003). Bimetallic catalysts and their relevance to the hydrogen economy. *Industrial & Engineering Chemistry Research*, 42: 1563–1570.

Ting, S.W., Periasamy, A.P., Chen, S.M., Saraswathi, R. (2011). Direct Electrochemistry of Catalase Immobilized at Electrochemically Reduced Graphene Oxide Modified Electrode for

Amperometric H₂O₂ Biosensor. *International Journal of Electrochemical Science*, 6: 4438–4453.

Torrey, J.D., Kirschling, T.L., Greenlee, L.F. (2015). Processing and Characterization of Nanoparticle Coatings for Quartz Crystal Microbalance Measurements. *Journal of Research of the National Institute of Standards and Technology*, 120: 1.

Torriero, A.A.J. Luco, J.M., Sereno, L., Raba, J. (2004). Voltammetric Determination of Salicylic Acid in Pharmaceuticals Formulations of Acetylsalicylic Acid. *Talanta*, 62: 247–254.

UNEP/GPA. (2006). *The State of the Marine Environment: Trends and processes*. The Hague, The Netherlands.

Uslu, B. and Ozkan, S.A. (2007). Solid Electrodes in Electroanalytical Chemistry: Present Applications and Prospects for High Throughput Screening of Drug Compounds. *Combinatorial Chemistry & High Throughput Screening Journal*, 10: 495–513.

Tyszczyk, K., Korolczuk, M., Grabarczyk, M. (2007). Application of gallium film electrode for elimination of copper interference in anodic stripping voltammetry of zinc. 71(5): 2098–101.

Ulrich, A., Moor, C., Vonmont, H., Jordi, H.R. and Lory, M. (2004). ICP–MS trace-element analysis as a forensic tool. *Analytical and Bioanalytical Chemistry*, 378: 1059–1068.

Van der Horst, C., Silwana, B., Iwuoha, E., Somerset, V. (2012). Stripping voltammetric determination of palladium, platinum and rhodium in freshwater and sediment samples from South African water resources. *Journal of Environmental Science and Health, Part A*, 47: 2084–2093.

Van der Horst, C., Silwana, B., Iwuoha, E., Somerset, V. (2015). Bismuth–silver bimetallic nanosensor application for the voltammetric analysis of dust and soil samples. *Journal of Electroanalytical Chemistry*, 752: 1–11.

Vanbroekhoven, K., Van Roy, S., Gielen, C.; Maesen, M., Diels, L., Seuntjens, P. (2006). Varying redox conditions changes metal behavior due to microbial activities. *Geophysical Research Abstract*, 8: 02292.

Van Cleef, M., Holt, S.A., Watson, G.S., Myhra, S. (1996). Polystyrene sphere on mica substrate: AFM calibration, tip parameters on scan artefacts. *Journal of Microscopy*, 81: 2–9.

Venugopal, G., Kim, S-J. (2011). Investigation of electrical transport characteristics of nanoscale stacks fabricated on thin graphite layer. *Thin Solid Films*, 519(20): 7095–7099.

Vix-Guter, C., Frackowiak, E., Jurewicz, K., Friebe, M., Parmentier, J., Bèguin, F. (2005). Electrochemical energy storage in ordered porous carbon materials. *Carbon*, 43: 1293–1302.

- Volpe, T., Schramke, V., Hamilton, G.L., White, S.A., Teng, G., Martienssen, R.A., Allshire, R.C. (2003). RNA interference is required for normal centromere function in fission yeast. *Chromosome Research*, 11: 137–146.
- Walt, D.R. (2002). Nanomaterials: Top-to-bottom functional design. *Nature Materials*, 1: 17–18.
- Wanekaya, A.K. (2011). Applications of nanoscale carbon-based materials in heavy metal sensing and detection. *The Analyst*, 136(21): 4383–4391.
- Wang, G., Zhang, L. Zhang, J. (2012). A review of electrode materials for electrochemical supercapacitors, *Chemical Society Reviews*, 41(2): 797–828.
- Wang, G., Yang, J., Park, J., Gou, X., Wang, B., Liu, H., Yao, J. (2008). Facile synthesis and characterization of graphene nanosheets. *Journal of Physical Chemistry C*, 112(22): 8192–8195.
- Wang Q., Li J-X., Li G-D., Cao X-J., Wang K-J., Chen J-S. (2007). Formation of CuS nanotube arrays from CuCl nanorods through a gas–solid reaction route. *Journal of Crystal Growth*, 299: 386–392.
- Wang, B., Zhang, J., Cheng, G., Dong, S. (2000). Amperometric enzyme electrode for the determination of hydrogen peroxide based on sol-gel/hydrogel composite film. *Analytica Chimica Acta*, 407: 111–118.
- Wang, H., Cui, H., Zhang, A., Liu, R. (1996). Adsorptive stripping voltammetric determination of tryptophan at an electrochemically pre-treated carbon-paste electrode with solid paraffin as a binder. *Analytical Communications*, 33: 275–277.
- Wang, J. (1985). *Stripping Analysis: Principles, Instrumentation, and Applications*, VCH Publishers, Inc. Deerfield Beach, Florida, USA.
- Wang, J. (1994). Decentralized electrochemical monitoring of trace metals: from disposable strips to remote electrodes. *Analyst*, 119: 763–766.
- Wang, J. (2006). *Analytical Electrochemistry*, 3rd edition, Wiley-VCH, Hoboken, USA.
- Wang, J.C. (2000). *Analytical Electrochemistry*. John Wiley & Sons, Chichester, UK.
- Wang, L., Bai, J., Huang, P., Wang, H., Zhang, L., Zhao, Y. (2006). Self-assembly of gold nanoparticles for the voltammetric sensing of epinephrine. *Electrochemistry Communications*, 8: 1035–1040.
- Wang, L., Li, Y., Yu, D.W., Katsunori, T., Masaru, T. (2008). Electron transmission and quantum current distribution of C70 molecule *Science in China Series G: Physics, Mechanics & Astronomy*, 51(2): 126–132.

- Wang, S., Jiang, S.P., Wang X. (2011.) Microwave-assisted one-pot synthesis of metal/ metal oxide nanoparticles on graphene and their electrochemical applications. *Electrochimica Acta*, 56 (9): 3338–3344.
- Wang, A.M., Doyle, M.V., Mark, M.F. (1989). Quantitation of mRNA by the polymerase chain reaction Proceedings of the National Academy. 86: 9717–9721.
- Wang, Y., Li, Y., Tang, L., Lu, J., Li, J. (2009). Application of graphene-modified electrode for selective detection of dopamine. *Electrochemistry Communications*, 11(4): 889–892.
- Wang, Y.Y., Ni, Z.H., Yu, T., Shen, Z.X., Wang, H.M. (2008). Raman Studies of Monolayer Graphene: The Substrate Effect. *Journal of Physical Chemistry C*, 112: 10637–10640.
- Watcharotone, S., Dikin, D.A., Stankovich, S., Piner, R., Jung, I., Dommett, G. H.B., Evmenenko, G., Wu, S.E., Chen, S.F., Liu, C.P., Nguyen, S.T., Ruoff, R.S. (2007). Graphenesilica composite thin films as transparent conductors. *Nano Letters*, 718: 88–1892.
- Wei, Y., Gao, C. Meng, F-L., Li, H-H Wang, L., Liu, J-H., Huang, X-J. (2012). SnO₂/Reduced Graphene Oxide Nanocomposite for the Simultaneous Electrochemical Detection of Cadmium(II), Lead(II), Copper(II), and Mercury(II): An Interesting Favorable Mutual Interference. *Journal of Physical Chemistry C*, 116: 1034–1041.
- Westbroek, P., Priniotakis, G., Kiekens, P. (2005). *Analytical Electrochemistry in Textiles*, Woodhead Publishing Ltd. and CRC Press LLC, Cambridge England, UK.
- White, R.J., Luque, R., Budarin, V.L., Clark, J.H., Macquarrie, D.J. (2008). Supported metal nanoparticles on porous materials. *Methods and Applications*. DOI: 10.1039/b802654h
- Wildgoose, G.G., Banks, C.E., Compton, R.G. (2006). Metal nanoparticles and related materials supported on carbon nanotubes: Methods and applications. *Small*, 2 (2): 182–196.
- Wilson, G.S., Ammam, M. (2007). In vivo biosensors. *FEBS Journal*, 274(21): 5452-5461.
- Willemse, C.M., Tlhomelang, K., Jahed, N., Baker, P. G., Iwuoha, E.I. (2011). Metallo-Graphene Nanocomposite Electrocatalytic Platform for the Determination of Toxic Metal Ions. *Sensors*, 11: 3970–3987.
- Williams, D.B., Carter C.B (1996). *Transmission Electron Microscopy: A Textbook for Materials Science*. Kluwer Academic / Plenum Publishers, New York, USA.
- Woolhouse, H. W. (1993). *Toxicity and tolerance in the response of plants to metals*. In: Lange O.L., P.S. Nobel, C.B. Osmond, and H. Ziegler (eds.) *Encyclopedia of Plant Physiology.: Physiological Plant Ecology*, 12: 245–300. Springer Verlag, Berlin, Germany.
- Wring, S.A., J.P. Hart, and B.J. Birch. (1991). Voltammetric behavior of SPCEs modified with mediators and their application as sensors for the determination of reduced glutathione. *Analyst*, 116: 123–129.

Wu, C., Yu, S-H., Chen, S., Liu, G., Liu, B. (2006). Large scale synthesis of uniform CuS nanotubes in ethylene glycol by a sacrificial templating method under mild conditions. *Journal of Material Chemistry*, 16: 3326–3331.

Wu, J., Pisula., W., Mullen, K. (2007). Graphenes as Potential Material for Electronics. *Chemistry Reviews*, 107(3): 718–747.

Wu, L., Feng, L., Ren, J., Qu, X. (2012). Electrochemical detection of dopamine using porphyrin-functionalized graphene. *Biosensors and Bioelectronics*, 34: 57–62.

Wu, Y., Zhang, T., Zheng, Z., Ding, X., Peng, Y. (2010). A facile approach to Fe₃O₄@Au nanoparticles with magnetic recyclable catalytic properties. *Materials Research Bulletin*, 45: 513–517.

Wuilloud, R.G. and Altamirano, J.C. (2006). Speciation Analysis of Non-Metallic Elements Using Plasma-Based Atomic Spectrometry for Detection. *Current Analytical Chemistry*, 2: 353–377.

Wum, P. (2012). *Inductively Coupled Plasma - Mass Spectrometer*. Washington: Washington University in St. Louis, USA.

www.asu.edu, accessed on 18 March 2015.

[www.geobacter.org/microbial nanowires](http://www.geobacter.org/microbial_nanowires), accessed on 7 November 2014.

www.scienceclarified.com/Ca-Ch/Carbon-Family.html, accessed on 3 September 2013.

Xia, F., Wang, H., Xiao, D., Dubey, M., Ramasubramaniam, M. (2014). Two-dimensional material nanophotonics. *Nature Photonics*, 8: 899–907.

Xiao, Y., Patolsky, F., Katz, E., Hainfeld, J.F., Willner, I. (2003). “Plugging into Enzymes”: nanowiring of redox enzymes by a gold nanoparticle. *Science*, 299, 1877–1881.

Xu, J-J., Zhao, W. LuO, X-L., Chen, H-Y. (2005). A sensitive biosensor for lactate based on layer-by-layer assembling MnO₂ nanoparticles and lactate oxidase on ion-sensitive field-effect transistors. *Chemical Communications*, 6: 792–794.

Xu, J.Z., Zhu, J.J., Wang, H., Chen, H.Y. (2003). Nano-sized copper oxide modified carbon paste electrodes as an amperometric sensor for amikacin. *Analytical Letters*, 36: 2723–2733.

Yang X., Feng, B., He, X., Li, F., Ding, Y., Fe, J. (2013). Carbon nanomaterial based electrochemical sensors for biogenic amines. *Microchimica Acta*, 180:9 35–956.

- Yang, S.B., Feng, X.L., Ivanovici, S., Mullen, K. (2010). Fabrication of graphene-encapsulated oxide nanoparticles: towards high-performance anode materials for lithium storage. *Angewandte Chemie International Edition*, 49: 408–8411.
- Yang, D., Velamakanni, A., Bozoklu, G., Park, S., Stoller, M., Piner, R.D. (2009). Chemical analysis of graphene oxide films after heat and chemical treatments by X-ray photoelectron and micro-Raman spectroscopy. *Carbon*, 47(1): 145–52.
- Yi, J., Lee, J.M., Park, W.I. (2011). Vertically aligned ZnO nanorods and graphene hybrid architectures for high-sensitive flexible gas sensors. *Sensors & Actuators B*, 155(1): 264–269.
- Yin, P.T., Kim, T-H., Choic, J-W., Lee, K-B. (2013). Prospects for graphene–nanoparticle-based hybrid sensors. *Chemistry Chemical Physics*, 15(31): 12785–12799.
- You, T., Niwa, O., Tomita, M. Hirono, S. (2003). Characterization of platinum nanoparticle-embedded carbon film electrode and its detection of hydrogen peroxide. *Analytical Chemistry*, 75: 2080–2085.
- Yu, A., Ramesh, P., Itkis, M.E., Bekyarova, E., Haddon, R.C. (2007). Graphite nanoplatelet epoxy composite thermal interface materials. *Journal of Physical Chemistry C*, 111(21): 7565–7569.
- Yu, H.S., Salgado, R., Sloan, S.W., Kim, J.M. (1998). Limit analysis versus limit equilibrium for slope stability. *Journal of Geotechnical and Geoenvironmental Engineering*, 124(1): 1–11.
- Zabet-Khosousi, A., Dhirani, A.A. (2008). Charge transport in nanoparticle assemblies. *Chemistry Reviews*, 108(10): 4072–124.
- Zahmakiran, M., Ozkar, S. (2011). Metal nanoparticles in liquid phase catalysis; from recent advances to future goals. *Nanoscale*, 3: 3462–3481.
- Zanello, P. (2003). *Inorganic Electrochemistry: Theory, Practice and Application*. Cambridge, UK:
- Zarzycki, J. (1997). Past and Present of Sol-Gel Science and Technology. *Journal of Sol-Gel Science and Technology*, 8: 17–22.
- Zen, J.M., Hsu, C.T., Kumar, A.S., Lyuu, H.J. Lin, K.Y. (2004). Amino acid analysis using disposable copper nanoparticle plated electrodes. *Analyst*, 129: 841–845.
- Zeng, D.W., Xie, C.S., Zhu, B.L., Song, W.L. (2004). Characteristics of Sb₂O₃ nanoparticles synthesized from antimony by vapor condensation method. *Material Letters*, 58: 312–315.
- Zhang, S., Zhang, L., Zhang, X., Yang, P., Cai, J. (2014). An efficient nanomaterial-based electrochemical biosensor for sensitive recognition of drug-resistant leukemia cells. *Analyst*, 139: 3629–3635.

Zhang, L.S., Wang, W.D., Liang, X.Q., Chu, W.S., Song, W.G., Wang, W., Wu, Z.Y. (2011). Characterization of partially reduced graphene oxide as room temperature sensor for H₂. *Nanoscale*, 3(6): 2458–2460.

Zhang, S., Wright, G., Yang, Y. (2000). Materials and techniques for electrochemical biosensor design and construction. *Biosensors and Bioelectronics*, 15(5–6), 273–282.

Zhou, K.F., Zhu, Y.H., Yang, X.L., Luo, J., Li, C.Z., Luan, S.R. (2010). A novel hydrogen peroxide biosensor based on Au-graphene-HRP-chitosan biocomposites. *Electrochimica Acta*, 55(9): 3055–3060.

Zhou, M., Zhai, Y., Dong, S. (2009). Electrochemical sensing and biosensing platform based on chemically reduced graphene oxide. *Analytical Chemistry*, 81(14): 5603–5613.

Zia, A.I., M. Syaifudin, A.R., Mukhopadhyay, S.C., Yu, P.L., AlBahadly, I.H., Gooneratne, C.P., Kosel, J., Liao, T-S. (2013). Electrochemical impedance spectroscopy based MEMS sensors for phthalates detection in water and juices. *Journal of Physics. Conference Series*, 439(1): 12026–12037.

Zidan, M., Zawawi, R.M., Erhayem, M., Salhin, A. (2014). Electrochemical Detection of Paracetamol Using Graphene Oxide -Modified Glassy Carbon Electrode. *International Journal of Electrochemical Science*, 9: 7605–7613.

Zhuo, Y., Yuan, R., Chai, Y., Zhang, Y., Wang, N., Li, X., Zhu, Q., Wang, N. (2005). An amperometric immunosensor based on immobilization of hepatitis B surface antibody on gold electrode modified gold nanoparticles and horseradish peroxidase. *Analytica Chimica Acta*, 548: 205–210.